



UNIVERSITA' DEGLI STUDI DI CAGLIARI
Facoltà di Scienze Matematiche Fisiche e Naturali
Dipartimento di Fisica

GRAPHENE UNDER STRAIN

A Combined Continuum-Atomistic Approach

EMILIANO CADELANO

PhD Thesis FIS/03
Novembre 2010

Relatore:

Prof. Luciano Colombo

Correlatore:

Dott. Stefano Giordano

Emiliano Cadelano: *Graphene under Strain*,
PhD Course in Condensed Matter Physics
XXIII Cycle., © October 2009

SUPERVISORS:
Luciano Colombo
Cagliari October 2009

Famiglia means family.
Family means nobody gets left behind, or forgotten.

Emi & Manu

Dedicated to the loving memory of my grandPa and grandMa
Benedetto Pinna and Agnese Pisu.

ABSTRACT

By combining continuum elasticity theory and atomistic simulations, we provide a picture of the elastic behavior of graphene, which was addressed as a two-dimensional crystal membrane. Thus, the constitutive nonlinear stress-strain relations for graphene, as well as its hydrogenated conformers, have been derived in the framework of the two-dimensional elastic theory, and all the corresponding linear and nonlinear elastic moduli have been computed by atomistic simulations. Moreover, we discuss the effects of an applied stretching on graphene lattice to its electronic band structure, in particular regards the concept of strain-induced band gap engineering. Finally, we focus on the emergence of a stretching field induced on a graphene nanoribbon by bending, providing that such an in-plane strain field can be decomposed in a first contribution due to the actual bending of the sheet and a second one due to the edge effects induced by the finite size of the nanoribbon.

SUMMARIO

Combinando la teoria dell'elasticità del continuo con calcoli eseguiti attraverso simulazioni atomistiche, si è affrontato lo studio del comportamento elastico del grafene, ovvero di una struttura cristallina bidimensionale a base carbonio. In tal modo, nell'ambito della teoria elastica bidimensionale, sono state derivate le equazioni costitutive non lineari per il grafene e per il suo composto con l'idrogeno, detto grafane; conseguentemente sono stati determinati per mezzo di simulazioni atomistiche tutti i relativi moduli elastici lineari e non lineari. Inoltre, abbiamo discusso gli effetti dovuti a deformazioni omogenee applicate al reticolo di grafene sulle sue bande elettroniche, con particolare attenzione al concetto di ingegnerizzazione della gap elettronica indotta da deformazione. Infine, discutiamo l'insorgenza di un campo di deformazione su un campione di grafene finito sottoposto a piegamento, evidenziando come tale campo possa essere decomposto in un contributo causato della flessione reale subita e in un secondo dovuto ai soli effetti di bordo.

PUBLICATIONS

Some ideas and figures have been discussed previously in the following publications

1. **Emiliano Cadelano**, Pier Luca Palla, Stefano Giordano, and Luciano Colombo, *Elastic properties of hydrogenated graphene*, Phys. Rev. B **82**, 235414 (2010).
2. Giulio Cocco, **Emiliano Cadelano**, Luciano Colombo *Gap opening in graphene by shear strain* Phys. Rev. B **81**, 241412(R) (2010) (selected for the July 2, 2010 issue of Virtual Journal of Nanoscale Science & Technology) (selected for Editors' Suggestions list in Physical Review B)
3. **Emiliano Cadelano**, Stefano Giordano, and Luciano Colombo, *Interplay between bending and stretching in carbon nanoribbons* Phys. Rev. B **81**, 144105 (2010)
4. **Emiliano Cadelano**, Pier Luca Palla, Stefano Giordano, and Luciano Colombo, *Nonlinear elasticity of monolayer graphene* Phys. Rev. Lett. **102**, 235502 (2009) (selected for the June, 22 2009 issue of Virtual Journal of Nanoscale Science & Technology)
5. Federico Bonelli, Nicola Manini, **Emiliano Cadelano**, and Luciano Colombo, *Atomistic simulations of the sliding friction of graphene flakes*, Eur. Phys. J. B **70**, 449,(2009)
6. Stefano Giordano, Pier Luca Palla, **Emiliano Cadelano**, and Michele Brun, *On the behavoir of elastic nano-inhomogeneities with size and shape differnt from thier hosting cavities*. In preparation

Feymann: "I am Feymann."
Dirac: "I am Dirac."
... (silence) ...
E.: "It must be wonderful to be the discover of that equation."
D.: "That was a long time ago"
... (pause) ...
D.: "What are you working?"
E.: "Mesons."
D.: "are you trying to discover an equation for them?"
E.: "It is hard."
D.: "One must try!"
1961, 12th Solvay.Congress

ACKNOWLEDGMENTS

This thesis project would not have been possible without the support of many people. I would like to express my gratitude to my supervisor, Luciano Colombo, whose expertise, understanding, and patience, added considerably to my graduate experience. I would like to thank the other members of my research group, Stefano Giordano, and Pier Luca Palla for the assistance they provided at all levels of the research project, and especially for their friendship. Discussions with Alessandro Mattoni, Giuseppe Fadda, Nicola Manini, and Giancarlo Cappellini are gratefully acknowledged. Appreciation also goes out to Matteo Dessalvi and the CASPUR staff for technical support and assistance. I acknowledge financial support by MIUR and the University of Cagliari and computational support by COSMOLAB (Cagliari, Italy) and CASPUR (Rome, Italy).

I would also like to thank my family for the support they provided me through my entire life. In particular, I thank a lot my lovely wife, Manuela, without whose love, and encouragement, I would not have finished this thesis.

Many thanks to everybody!

CONTENTS

1	THE GRAPHENE: WELCOME IN FLATLAND.	1
I THEORETICAL BACKGROUND 11		
2	THE TIGHT-BINDING SEMI-EMPIRICAL SCHEME	13
2.1	The Tight-Binding method	13
2.2	The Tight-Binding representation of carbon-base systems	21
3	DENSITY FUNCTIONAL THEORY	25
3.1	Density functional theory	25
3.1.1	Exchange and correlation energy approximations	28
3.1.2	Plane waves and Pseudopotentials	31
3.2	Density Functional Perturbation Theory	33
4	CONTINUUM MECHANICS AND NONLINEAR ELASTICITY	35
4.1	Lagrangian versus Eulerian formalism	35
4.2	Finite Strain Theory	38
4.3	Stress Theory	41
4.4	The Continuity equation	46
4.5	Balance equations	46
4.5.1	The Euler description	46
4.5.2	The Lagrange description	48
4.6	Nonlinear constitutive equations	50
4.7	The small-strain approximation	53
4.8	The Stiffness tensor and the Elastic moduli in two-dimensional systems.	60
4.9	The virial stress tensor	66
4.9.1	Physical meaning of the virial stress	70
4.9.2	The atomistic nonlinear Cauchy stress	71
4.9.3	Atomic stress for two-body interactions	72
II ELASTIC BEHAVIOR OF GRAPHENE 75		
5	THE GRAPHENE IS STRETCHED	77
5.1	Elastic properties of graphene	78
5.2	The computational approach	83
5.3	The stress-strain approach	86
6	ELASTIC PROPERTIES OF GRAPHANE	89
6.1	Graphane	89
6.2	Methods and computational setup	92
6.3	Structure and stability of graphane conformers	94
6.4	Linear elasticity	96
6.5	Nonlinear elasticity	103
7	GAP OPENING IN GRAPHENE BY SHEAR STRAIN	109

7.1	Introduction and motivation	109
7.2	The electronic structure of graphene	110
7.3	Some detail about the out-of-plane relaxation	117
8	THE BENDING OF GRAPHENE.	121
8.1	Bending in carbon nanoribbons	121
8.2	The bending rigidity theory	122
8.2.1	Continuum picture	122
8.2.2	Atomistic simulations	126
8.3	Simulation protocol and the calculated bending features	130
III	APPENDIX	135
A	APPENDIX	137
A.1	Derivative of a volume integral	137
A.2	Derivative of a surface integral	139
A.3	Novozhilov formulation of Lagrangian equations of motion.	141
A.4	Crystal symmetry condition	143
A.5	Virial stress and Periodic Boundary Conditions	145
A.6	Symmetry of the elastic moduli of Graphane conformers	147
A.6.1	Young Modulus	147
A.6.2	Poisson Ratio	151
A.7	Bending rigidity in nanotubes	153
A.8	Minimal surface of a bended membrane	157
	BIBLIOGRAPHY	163
	INDEX	171

ACRONYMS

DRY	Don't Repeat Yourself
TB	Tight Binding
TBMD	Tight Binding Molecular Dynamics
DFT	Density Functional Theory
DFPT	Density Functional Perturbation Theory
LDA	Local Density Approximation
GGA	Generalized Gradient Approximation
SEOC	Second Order Elastic Constant
TEOC	Third Order Elastic Constant
LCAO	Linear Combination of Atomic Orbitals
KS	Kohn-Sham
PP	PseudoPotential
PW	Plane Waves
PAW	Plane Augmented Waves
PBE	Perdew-Burke-Ernzerhof
BLYP	Becke-Lee-Yang-Parr
PW91	Perdew-Wang Becke
LSD	Local Spin Density

SYMBOLS

List of the most important tensor quantities used in the following chapters

$\hat{\mathbf{F}}$	deformation gradient
$\hat{\mathbf{G}}$	inverse deformation gradient
$\hat{\mathbf{L}}$	velocity gradient
\mathbf{J}	deformation Jacobian
$\hat{\mathbf{B}}$ and $\hat{\mathbf{C}}$	left and right Cauchy tensors
$\hat{\mathbf{U}}$ and $\hat{\mathbf{V}}$	left and right stretching tensors
$\hat{\mathbf{R}}$	rotation tensor
$\hat{\boldsymbol{\eta}}$	Green-Lagrange tensor
$\hat{\mathbf{e}}$	Almansi-Eulero tensor
$\hat{\mathbf{J}}_{\mathbf{L}}$	Lagrangian displacement gradient
$\hat{\mathbf{J}}_{\mathbf{E}}$	Eulerian displacement gradient
$\hat{\mathbf{D}}$	rate of deformation tensor
$\hat{\mathbf{W}}$	spin tensor
$\hat{\boldsymbol{\tau}}$	Cauchy stress tensor
$\hat{\boldsymbol{\tau}}^{1\mathcal{PK}}$	first Piola-Kirchhoff stress tensor
$\hat{\boldsymbol{\tau}}^{2\mathcal{PK}}$	second Piola-Kirchhoff stress tensor
$\hat{\mathbf{j}}$	small-strain displacement gradient
$\hat{\mathbf{e}}$	small-strain tensor
$\hat{\boldsymbol{\Omega}}$	local rotation tensor
$\hat{\mathbf{c}}$	stiffness tensor

THE GRAPHENE: WELCOME IN FLATLAND.

"True" said the Sphere "it appears to you a Plane because you are not accustomed to light and shade and perspective just as in Flatland a Hexagon would appear a Straight Line to one who has not the Art of Sight Recognition But in reality it is a Solid as you shall learn by the sense of Feeling"

Edwin A. Abbott "Flatland" (1884).

Graphene is the name given to a two-dimensional flat sheet of sp^2 -hybridized carbon atoms. Its extended honeycomb network is the basic building block of other important allotropes. It can be stacked to form three-dimensional graphite, rolled to form one-dimensional nanotubes, and wrapped to form zero-dimensional fullerenes. Long-range π -conjugation in graphene yields extraordinary thermal, mechanical, and electrical properties, which have long been the interest of many theoretical studies and more recently became an exciting area for experimentalists.

Indeed, some extraordinary properties of honeycomb carbon atoms are not really new. Abundant and naturally occurring, graphite has been known as a mineral for nearly 500 years. Even in the middle ages, the layered morphology and weak dispersion forces between adjacent sheets were utilized to make marking instruments, much in the same way that we use graphite in pencils today. More recently, these same properties have made graphite an ideal material for use as a dry lubricant, along with the similarly structured but more expensive compounds hexagonal boron nitride and molybdenum disulfide. High in-plane electrical ($104 \Omega^{-1} \text{ cm}^{-1}$) and thermal conductivity (3000 W/mK) enable graphite [1] to be used in electrodes and as heating elements for industrial blast furnaces. High mechanical stiffness of the hexagonal network (1060 GPa) is also utilized in carbon fiber reinforced composites [2, 3, 4]. The anisotropy of graphite's material properties continues to fascinate both scientists and technologists. The s , p_x , and p_y atomic orbitals on each carbon atom hybridize to form strong covalent sp^2 bonds, giving rise to 120° C-C-C bond angles and the familiar chicken-wire-like layers. The remaining p_z orbital on each carbon overlaps with its three neighboring carbons to form a band of filled π orbitals, known as the valence band, and a band of empty π^* orbitals, called the conduction band. While three of the four valence electrons on each carbon form the σ (single) bonds, the fourth electron forms one-third of a π bond with each of its neighbors producing

Graphene is the name given to a two-dimensional flat sheet of sp^2 -hybridized carbon atoms.

A brief history: from graphite to graphene

*The discover of
graphene*

a carbon-carbon bond order in graphite of one and one-third. With no chemical bonding in the normal direction, out-of-plane interactions are extremely weak. This includes the propagation of charge and thermal carriers, which leads to out-of-plane electrical and thermal conductivities that are both more than ~ 100 times lower than those of their in-plane analogues. While studies of graphite have included those utilizing fewer and fewer layers for some time, the field was delivered a jolt in 2004 [5, 6], when A. Geim, K. Novoselov, and co-workers at Manchester University first isolated single-layer samples from graphite. For this they are awarded the Nobel Prize in Physics 2010. This led to their Nobel Degree in Physics in 2010 and aroused interest in everybody else since its discovery.

*Main graphene
properties*

Initial studies included observations of graphene's ambipolar field effect, the quantum Hall effect at room temperature [7], and even the first ever detection of single molecule adsorption events. Furthermore, graphene is the thinnest known crystal in the universe and the strongest ever measured. Its charge carriers exhibit giant intrinsic mobility, have zero effective mass, and can travel for micrometers without scattering at room temperature. Electron transport in graphene is described by a Dirac-like equation, which allows the investigation of relativistic quantum phenomena in a benchtop experiment. Graphene can sustain current densities six orders of magnitude higher than that of copper, shows record thermal conductivity and stiffness, is impermeable to gases, and reconciles such conflicting qualities as brittleness and ductility. These properties generated huge interest in the possible implementation of graphene in a myriad of devices. These include future generations of high-speed and radio frequency logic devices, thermally and electrically conductive reinforced composites, sensors, and transparent electrodes for displays and solar cells.

*The Mermin-Wagner
Theorem*

The experimental isolation of single-layer graphene yielded access to a large amount of interesting physics, nevertheless two-dimensional crystals were thought to be thermodynamically unstable at finite temperatures. In fact, graphene is a material that should not exist. More than 70 years ago, Landau and Peierls [8, 9] shown that strictly two-dimensional crystals were thermodynamically unstable. Their theory pointed out that a divergent contribution of thermal fluctuations in low-dimensional crystal lattices should lead to such displacements of atoms that they become comparable to interatomic distances at any finite temperature. The argument was later extended by Mermin- Wagner [10] and it is strongly supported by experimental observations. Indeed, the melting temperature of thin films rapidly decreases with decreasing thickness, and the films become unstable (segregate into islands or decompose) at a thickness of, typically, dozens

of atomic layers. For this reason, atomic monolayers have so far been known only as an integral part of larger three-dimensional structures, usually grown epitaxially on top of monocrystals with matching crystal lattices. Without such a three-dimensional environment, two-dimensional materials were presumed not to exist, until 2004, when the common wisdom was brought into question by the experimental discovery of graphene and other free-standing two-dimensional atomic crystals (for instance, single-layer boron nitride). With the benefit of hindsight, the existence of such one-atom-thick crystals can be reconciled with theory. Indeed, it can be argued that the obtained two-dimensional crystallites are quenched in a metastable state because they are extracted from three-dimensional materials, whereas their small size ($\ll 1$ mm) and strong interatomic bonds ensure that thermal fluctuations cannot lead to the generation of dislocations or other crystal defects even at elevated temperature. A complementary viewpoint is that the extracted two-dimensional crystals become intrinsically stable by gentle crumpling in the third dimension. Such ripples lead to a gain in elastic energy but suppresses thermal vibrations, which above a certain temperature can minimize the total free energy [11].

Thermodynamic stability of graphene

Moreover, it is probably more unexpected the news that every time someone draws a line with a common pencil, the resulting mark includes bits of graphene. Indeed, graphene isolation was a funny accident as told by its discoverers. A PhD student was trying to make a large piece of graphite as thin as possible. The student sawed it till $50 \mu\text{m}$, but all further attempts led to graphite dust. Konstantin Novoselov once paid attention to work of researcher from a neighboring lab, who used well-known technique, called "scotch tape method", which is simply sticking the tape to graphite and ripping it off, for getting thin graphite layers. As told by Konstantin Novoselov at the International Forum RusNanoTech-2010, Moscow, it is possible to make graphene samples, having a piece of graphite, a scotch tape, and a mobile phone's screen as solid substrate. "Making good graphene needs two rules to be fulfilled", Novoselov said, "First is using quality graphite, and second is preparing the substrate". "Drinking vodka usually helps, because alcohol vapors can perfectly degrease the surface", the scientist advised, "You won't be able to see graphene you just made, but believe that it is really there".

How win a Nobel Prize

This simple mechanical exfoliation technique has been used by the Manchester group to isolate the two-dimensional crystals from three-dimensional graphite. Resulting single- and few-layer flakes were pinned to the substrate by only van der Waals forces and could be made free-standing by etching away the substrate. This minimized any induced effects and allowed scientists to probe graphene's intrinsic properties. Despite this intense interest

Beyond the simple mechanical exfoliation technique

and continuing experimental success by physicists, widespread implementation of graphene has yet to occur. This is primarily due to the difficulty of reliably producing high quality samples, especially in any scalable fashion. The challenge is double because performance depends on both the number of layers present and the overall quality of the crystal lattice. So far, the original approach of mechanical exfoliation has produced the highest quality samples, but the method is neither high throughput nor high-yield. In order to exfoliate a single sheet, van der Waals attraction between exactly the first and second layers must be overcome without disturbing any subsequent sheets. Therefore, a number of alternative approaches to obtaining single layers have been explored, a few of which have led to promising proof-of-concept devices. Alternatives to mechanical exfoliation include primarily three general approaches: chemical efforts to exfoliate and stabilize individual sheets in solution, bottom-up methods to grow graphene directly from organic precursors, and attempts to catalyze growth in situ on a substrate.

*Mechanical
properties of
graphene*

Graphene have mainly attracted interest for its unusual electron transport properties, but recently some attention has been paid also to mechanical properties of planar graphene sheets. In particular, Lee *et al.* in 2008 [12] measured the mechanical properties of a single graphene layer, demonstrating that graphene is the hardest material known, since the effective three-dimensional elastic modulus reaches a huge value of 1.0 TPa.

Moreover, the ultimate use of graphene sheets in integrated devices will likely require understanding of the mechanical properties that may affect the device performance and reliability as well as the intriguing morphology [13].

One typically assumes that the in-plane elastic moduli of a single-layer graphene are identical to those for the base plane of hexagonal crystal graphite. However, significant discrepancies have been reported between theoretical predictions for in-plane Young's modulus and Poisson's ratio of graphene and those derived from graphite [14]. It has also been noted that bending of a graphene sheet of a single atomic layer cannot be simply modeled using continuum plate or shell theories [15]. Further studies are thus necessary in order to develop a theoretically consistent understanding for the mechanical properties of graphene as well as their relationships with corresponding properties of carbon nanotubes and nanoribbons. A theoretical approach is developed in the present Thesis in order to predict the in-plane elastic properties of single-layer graphene based on an interplay between an atomistic Tight Binding simulations and a continuum elastic theory approach, providing a link between atomistic interactions and macroscopic elastic properties of crystals.

*Aims and scope of
this thesis*

While similar approaches have been developed previously [16], we herein emphasize the nonlinear elastic behavior under homogeneous deformation. Third-order elastic constants are important quantities characterizing nonlinear elastic properties of materials, and the interest in them dates back to the beginning of modern solid state physics. Third- and higher-order elastic constants are useful not only in describing mechanical phenomena when large stresses and strains are involved e.g., in heterostructures of optoelectronic devices, but they can also serve as a basis for discussion of other anharmonic properties. The applications include phenomena such as thermal expansion, temperature dependence of elastic properties, phonon-phonon interactions, etc.

Thus, by combining continuum elasticity theory and tight-binding atomistic simulations, we work out the constitutive nonlinear stress-strain relation for graphene stretching elasticity and we calculate all the corresponding nonlinear elastic moduli. We show in Chapter 5 some results which represent a robust picture on the elastic behavior and provide the proper interpretation of recent experiments of Lee *et al.* [12]. In particular, we discuss the physical meaning of the effective nonlinear elastic modulus there introduced and we predict its value in good agreement with available data. Moreover, a hyperelastic softening behavior is observed and discussed, so determining the failure properties of graphene.

The defect-free and highly ordered, crystals of graphene are the thinnest objects possible and, simultaneously, 100 times stronger than structural steel, making them the strongest material in nature. Such an unusual combination of extreme properties makes this two-dimensional crystal attractive for a wide variety of applications. However, in terms of electronic applications, sometimes graphene is a little too conductive. Graphene is so highly conductive that it is hard to create graphene-based transistors suitable for applications in integrated circuits. In order to reduce its conductivity, many efforts have been dedicated to study the electronic properties of graphene, for instance because creating a gap could allow the use of graphene in field effect transistors. Many mechanisms have been proposed with that purpose: e.g. by quantum confinement of electrons and holes in graphene nanoribbons [17] or quantum dots. [18] These patterning techniques are unfortunately affected by the edge roughness problem, [19] namely: the edges are extensively damaged and the resulting lattice disorder can even suppress the efficient charge transport. The sensitivity to the edge structure has been demonstrated through explicit calculations of the electronic states in ribbons [20]. More recently, it has been shown experimentally that a band gap as large as 0.45 eV can be opened if a graphene sheet is placed on an Ir(111) substrate and exposed to patterned hydrogen adsorption [21].

Non linear elastic features

Too conductive for transistors

The graphane is the fully hydrogenated graphene

Therefore, graphene-like carbon compound that acts as an insulator could be produced. The simplest and most straightforward candidate to do this is hydrogen. Exposing graphene to an atomic hydrogen atmosphere produces a material called graphane, which is described as a two-dimensional crystal mapped onto the graphene scaffold, and covalently bonded hydrocarbon with one to one C:H ratio. Graphane was theoretically predicted by Sofo *et al.* [22], further investigated by Boukhvalov *et al.* [23] and eventually was first synthesized by Elias *et al.* [24] in the 2009.

An additional attractive feature of graphane is that by variously decorating the graphene atomic scaffold with hydrogen atoms (still preserving periodicity) it is in fact possible to generate a set of two dimensional materials with new physico-chemical properties. These systems are all characterized by a sp^3 orbital hybridization instead the sp^2 hybridization of graphene. Because of in graphane the π -electrons are strongly bound to hydrogen atoms, the π -bands are absent altogether. Thus, a band gap is created, separating the highest occupied band from the lowest unoccupied band as in insulators. For instance, it has been calculated [22, 23] that graphane has got an energy gap as large as ~ 6 eV [25], while in case the hydrogenated sample is disordered, the resulting electronic and phonon properties are yet again different [24]. This simple change in hybridization may open up a whole new world of graphene-based chemistry, leading to novel two-dimensional crystals with predefined properties, and an ability to tune the electronic, optical, and other properties. Hydrogenation likely affects the elastic properties as well. Topsakal *et al.* [26] indeed calculated that the in-plane stiffness and Poisson ratio of graphane are smaller than those of graphene. In addition, the value of the yield strain is predicted to vary upon temperature and stoichiometry.

Elastic properties of graphane

Among many possible conformers of hydrogenated graphene, as discussed in detail in Chapter 6, we focus our study to three structures referred to as chair-, boat-, or washboard- graphane. By first principles calculations we determine their structural and phonon properties, as well as we establish their relative stability. Through continuum elasticity we measure by a computer experiment their linear and nonlinear elastic moduli, so that we can compare them with the elastic behavior of graphene. We argue that all graphane conformers respond to any arbitrarily-oriented extension with a much smaller lateral contraction than the one calculated for graphene. Furthermore, we provide evidence that boat-graphane has a small and negative Poisson ratio along the armchair and zigzag principal directions of the carbon honeycomb lattice (i.e. axially auxetic elastic behavior). Moreover, we

show that chair-graphane admits both softening and hardening hyperelasticity, depending on the direction of applied load.

Besides, an alternative technique to open a gap in the electronic structure of graphene involves the application of mechanical stress. For instance, an electronic band gap has been obtained by growing graphene sheets on an appropriately chosen substrate, inducing a reversible strain field controllable by temperature [27, 28, 29], and it has been experimentally shown that by using flexible substrates a reversible and controlled strain up to $\sim 18\%$ [29] can be generated with measurable variations in the optical, phonon and electronic properties of graphene [30].

Strain affects the band structure

This interesting result suggests that gap opening could be engineered by strain, rather than by patterning. The idea has been validated within linear elasticity theory and a tight-binding approach by Pereira and Castro Neto [31] showing that strain can generate a spectral gap. However this gap is critical, requiring threshold deformations in excess of 23%, approaching the graphene failure strain ($\epsilon_f = 25\%$) [12], and only along preferred directions with respect to the underlying lattice. The same authors propose an alternative origami technique [13] aimed at generating local strain profiles by means of appropriate geometrical patterns in the substrate, rather than by applying strain directly to the graphene sheet.

Shear deformation could open a gap

In Chapter 7 we exploit this concept of strain-induced band structure engineering in graphene through the calculation of its electronic properties under several deformations, by using linear elasticity theory and a semi-empirical tight-binding approach. We show that by combining shear deformations to uniaxial strains it is possible modulate the graphene energy gap value from zero up to 0.9 eV. Interestingly enough, the use of a shear component allows for a gap opening at moderate absolute deformation, safely smaller than the graphene failure strain, i.e. in a range of reversible and more easily accessible deformations, ranging in between 12% and 17%.

Among the many studies of graphene, a substantial portion have been devoted to the physics of graphene edges, whose structure in narrow graphene ribbons is predicted to have a major impact on their electronic properties [32]. Recent theoretical studies show that transport effects such as Coulomb blockade [18] or a mobility gap induced by edge disorder may affect the accuracy of bandgaps measured under transport conditions [33]. On the other hand, the free edges of graphene are amenable to edge instabilities, because of edges are under compressive stress rendering a mechanical edge rippling and warping instability [34, 35]. Rippling of graphene has been also observed with mesoscopic amplitude and wavelength, both for suspended monolayers [36] and sheets deposited on substrates such as silicon dioxide [37].

Rippling, warping and other bending issues

Besides, any bending phenomena, i.e. out-of-plane displacements, are critical in attaining the structural stability and morphology for both suspended and supported graphene sheets, and directly affect their electronic properties [38]. Moreover, the bending properties play a central role in the design of graphene-based devices, like e.g. mechanical resonators [39, 40]. The bending features of functionalized graphene sheets have been probed by atomic force microscopy, observing that the folding behavior is dominated by defects and functional groups [41]. Finally, bending ultimately governs the carbon nanotubes unzipping process, recently used to produce narrow ribbons for nanoelectronics [42]. With the same technique, a new class of carbon-based nanostructures, which combine nanoribbons and nanotubes, has been introduced in order to obtain magnetoresistive devices [43].

Within this scenario, in Chapter 8 we face the problem of the fundamental understanding of the bending properties of a two-dimensional carbon ribbon, and its interplay with the edge effects. The main goal is twofold: to draw a thorough theoretical picture on bending of two-dimensional structures, fully exploiting the elasticity theory and providing an atomistic quantitative estimation of the corresponding bending rigidity; to prove that the bending process of a carbon nanoribbon is always associated with the emergence of a (small) stretching, particularly close to the edges. These results have been obtained by combining continuum elasticity theory and tight-binding atomistic simulations too.

OUTLINE

The Thesis is organized as follows

- Part I

A brief outline of the theoretical framework is shown as follows

CHAPTER 2 We report the main concepts and formalism of the tight-binding theory, in particular addressed to the semi-empirical approach

CHAPTER 3 The density functional theory and its perturbative version are briefly discussed

CHAPTER 4 We show the continuum mechanics, in particular the main concepts of the two-dimensional nonlinear elasticity, and some reference to the atomistic treatment of the elastic continuum theory

- Part II

We discuss in detail the some meaningful results regard the elastic behavior of graphene

CHAPTER 5 We deal with the constitutive nonlinear stress-strain relation for graphene stretching elasticity, and with all the corresponding nonlinear elastic moduli

CHAPTER 6 We discuss about the linear and nonlinear elastic behavior of the hydrogenated conformers of graphene, namely graphane.

CHAPTER 7 We exploit the concept of strain-induced band gap engineering in graphene

CHAPTER 8 Some fundamental concepts about the bending properties of a two-dimensional ribbons of graphene have been discussed

Part I

THEORETICAL BACKGROUND

THE TIGHT-BINDING SEMI-EMPIRICAL SCHEME

“Everything should be made as simple as possible, but no simpler.”
 Albert Einstein, ‘Einstein’s razor’ (1934).

Contents

2.1	The Tight-Binding method	13
2.2	The Tight-Binding representation of carbon-base systems	21

In Chapter 3, we’ll briefly review the Density Functional Theory. This *ab-initio* theory offers accuracy, transferability, and reliability. These are undoubtedly three key features to achieve predictive investigation of materials properties, but it is just as certain that the corresponding computational workload can become quite heavy and sometimes overwhelming.

The Tight Binding (TB) method is an intermediate solution between a cheaper, from the computational point of view, totally empirical potential model and a much more expensive *ab-initio* calculation. Tight binding joins the advantage of the accuracy needed to describe complex systems and of a reduced computational workload.

2.1 THE TIGHT-BINDING METHOD

TB is based on the basic formalism of linear combination of atomic orbitals (LCAO) and Bloch sums. The Hamiltonian for a solid system is given by

$$\hat{H} = \hat{T}_n + \hat{T}_e + \hat{U}_{en} + \hat{U}_{ee} + \hat{U}_{nn}. \quad (2.1)$$

Here,

$$\begin{aligned} \hat{T}_n &= - \sum_{il} \frac{\hbar^2}{2M_i} \nabla^2(\mathbf{R}_{il}), \text{ kinetic energy operators for each ion} \\ \hat{T}_e &= - \sum_i \frac{\hbar^2}{2m_e} \nabla^2(\mathbf{r}_i), \text{ kinetic energy operators for each electron} \\ \hat{U}_{en} &= - \sum_{i,l,j} \frac{Z_i e^2}{|\mathbf{R}_{il} - \mathbf{r}_j|}, \text{ electron-nucleus potential energy} \end{aligned}$$

$$\begin{aligned}\hat{U}_{ee} &= \sum_{i,j>i} \frac{e^2}{|\mathbf{r}_i - \mathbf{r}_j|}, \text{ electron-electron potential energy} \\ \hat{U}_{nn} &= \sum_{l,l',j'>j} \frac{Z_j Z_{j'} e^2}{|\mathbf{R}_{jl} - \mathbf{R}_{j'l'}|}, \text{ nucleus-nucleus potential energy}\end{aligned}\tag{2.2}$$

where the i, j indices count the particles inside the unit cell, the l index runs over the Bravais lattice sites, and the atomic positions are $\mathbf{R}_{jl} = \mathbf{d}_j + \mathbf{R}_l$, with the generic translational lattice vector \mathbf{R}_l and \mathbf{d}_j labels the basis vector for the nuclei in the unit cell. The Coulomb potential, depending on difference vectors, is invariant as well. Under the assumption of the frozen-core picture for the electronic system and the Born-Oppenheimer or adiabatic approximation, the corresponding single-electron Hamiltonian is

$$\hat{\mathbf{h}}_{el} = \hat{\mathbf{T}}_e + \hat{U}_{en} + \hat{U}_{ee} + \hat{U}_{nn}.\tag{2.3}$$

describing the energy of the valence electrons in the electrostatic field of the ions, which are assumed as the nucleus and core-electrons together, where the nuclei are assumed to be stationary with respect to an inertial frame.

The adiabatic theorem: "A physical system remains in its instantaneous eigenstate if a given perturbation is acting on it slowly enough and if there is a gap between the eigenvalue and the rest of the Hamiltonian's spectrum."

Assuming the approximation of non-interacting (Hartree-like) electrons and the mean-field approximation, the i^{th} -electron has been described as particle moving in the ground-state of a effective periodic potential \mathcal{U}_{ave} due to the other valence electrons and to the ions

$$\hat{\mathbf{h}}(\mathbf{r}_i) = -\frac{\hbar^2}{2m_e} \nabla^2(\mathbf{r}_i) + \mathcal{U}_{ave},\tag{2.4}$$

invariant by lattice translation $\hat{\mathbf{h}}(\mathbf{r}_i) = \hat{\mathbf{h}}(\mathbf{r}_i + \mathbf{R}_l)$.

The wave functions $\psi_{n\mathbf{k}}(\mathbf{r})$, provided by the Schrödinger equation $\hat{\mathbf{h}}(\mathbf{r})\psi_{n\mathbf{k}}(\mathbf{r}) = \epsilon_n(\mathbf{k})\psi_{n\mathbf{k}}(\mathbf{r})$, must satisfy the Bloch condition as well; thus:

$$\psi_{n\mathbf{k}}(\mathbf{r} + \mathbf{R}_l) = \psi_{n\mathbf{k}}(\mathbf{r}) \exp(i\mathbf{k} \cdot \mathbf{R}_l)\tag{2.5}$$

where \mathbf{k} is the electron Bloch wavevector, n is the band index, $\epsilon_n(\mathbf{k})$ is the one-electron band energy and crystalline periodic symmetry is assumed. By means of a linear combination of atomic orbitals (LCAO), the electronic wave function $\psi_{n\mathbf{k}}(\mathbf{r})$ can be expanded as Bloch sum

Bloch sum

$$\begin{aligned}
 \Psi_{\mathbf{n}\mathbf{k}}(\mathbf{r}) &= \sum_{\alpha j} \tilde{B}_{n\alpha j} \phi_{\alpha j\mathbf{k}}(\mathbf{r}) \\
 &= \sum_{\alpha j\mathbf{l}} \exp(i\mathbf{k} \cdot \mathbf{R}_{\mathbf{l}}) \tilde{B}_{n\alpha j} \phi_{\alpha}(\mathbf{r} - \mathbf{R}_{\mathbf{l}} - \mathbf{d}_j) \\
 &= \sum_{\alpha j\mathbf{l}} B_{n\alpha(j\mathbf{l})}(\mathbf{k}) \phi_{\alpha j\mathbf{l}}(\mathbf{r})
 \end{aligned} \tag{2.6}$$

Here, the label α indicates the full set of atomic quantum numbers defining the orbital, and we assume that the wave function are normalized in the volume of crystal. The Bloch sum is defined as

$$\phi_{\alpha j\mathbf{k}}(\mathbf{r}) = \sum_{\mathbf{l}} \exp(i\mathbf{k} \cdot \mathbf{R}_{\mathbf{l}}) \phi_{\alpha}(\mathbf{r} - \mathbf{R}_{\mathbf{l}} - \mathbf{d}_j) \tag{2.7}$$

Despite the simplicity of this formalism, referred to as *tight-binding method*, it is very hard to carry out, mainly due to the difficulty in the computation of the overlap integrals between atomic functions centred on different lattice points. In fact, because of the basis orbitals $\phi_{\alpha j\mathbf{l}}(\mathbf{r})$ located at different atoms are generally not orthogonal, their calculation is numerically inconvenient, and the computational workload increase as well. These overlap integrals, defined by

$$\begin{aligned}
 \mathbf{S}_{\alpha'(j'\mathbf{l}'),\alpha(j\mathbf{l})} &= \int d\mathbf{r} \phi_{\alpha'(j'\mathbf{l}')}(\mathbf{r})^* \phi_{\alpha(j\mathbf{l})}(\mathbf{r}) - \delta_{\alpha\alpha'} \delta_{(j\mathbf{l})(j'\mathbf{l}')}, \\
 &\text{with } \mathbf{S}_{\alpha(j\mathbf{l}),\alpha(j\mathbf{l})} = 0
 \end{aligned} \tag{2.8}$$

are often small compared to unity, but, even if they have almost been neglected, overlap effects are often of essential importance for crystal properties. By joining the normalization condition, $\mathbf{B}_{\mathbf{n}}^{\dagger}(\mathbf{k})(\mathbb{1} + \mathbf{S})\mathbf{B}_{\mathbf{n}}(\mathbf{k}) = 1$, with the orthogonality theorem, consequence of the hermitian character of \mathbf{h} and \mathbf{S} , the Schrödinger equation can be written in the matrix formalism as

$$\hat{\mathbf{h}}\mathbf{B}_{\mathbf{n}}(\mathbf{k}) = \epsilon_{\mathbf{n}}(\mathbf{k})(\mathbb{1} + \mathbf{S})\mathbf{B}_{\mathbf{n}}(\mathbf{k}) \tag{2.9}$$

By introducing the substitution

$$\begin{aligned}
 \mathbf{B}_{\mathbf{n}}(\mathbf{k}) &= (\mathbb{1} + \mathbf{S})^{-1/2} \mathbf{C}_{\mathbf{n}}(\mathbf{k}) \\
 \text{where, } (\mathbb{1} + \mathbf{S})^{-1/2} &= \mathbb{1} - \frac{1}{2}\mathbf{S} + \frac{3}{8}\mathbf{S}^2 - \frac{5}{16}\mathbf{S}^3 + \dots
 \end{aligned} \tag{2.10}$$

the Eq. (2.9) becomes $\hat{\mathbf{h}}_{\mathcal{L}}\mathbf{C}_{\mathbf{n}\mathbf{k}}(\mathbf{r}) = \epsilon_{\mathbf{n}}(\mathbf{k})\mathbf{C}_{\mathbf{n}\mathbf{k}}(\mathbf{r})$. Here, the $\hat{\mathbf{h}}_{\mathcal{L}} = (\mathbb{1} + \mathbf{S})^{-1/2}\hat{\mathbf{h}}(\mathbb{1} + \mathbf{S})^{-1/2}$ is the Löwdin transformation [44] that leads to a new orthogonal set of atomic orbitals $\{\psi_{\alpha'(j'\mathbf{l}')}\}$

$$\psi_{\alpha'(j'\mathbf{l}')}\mathbf{r}) = \sum_{\alpha j\mathbf{l}} (\mathbb{1} + \mathbf{S})_{\alpha'(j'\mathbf{l}'),\alpha(j\mathbf{l})}^{-1/2} \phi_{\alpha}(\mathbf{r} - \mathbf{R}_{\mathbf{l}} - \mathbf{d}_j) \tag{2.11}$$

Löwdin theorem:
 "The problem of solving the secular equations including the overlap integrals \mathbf{S} can be reduced to the same form as it has in simplified theory, \mathbf{S} neglected, if the Hamiltonian \mathbf{h} is replaced by the $\mathbf{h}_{\mathcal{L}}$ "

These Löwdin orbitals have the same symmetry properties as the original non-orthogonal atomic wave functions [45].

The wave functions defined in Eq. (2.12) can be re-written as

$$\psi_{n\mathbf{k}}(\mathbf{r}) = \sum_{\alpha j l} C_{n\alpha(jl)}(\mathbf{k}) \psi_{\alpha j l}(\mathbf{r}) \quad (2.12)$$

The two center approximation as constants to fit

Therefore the one-electron energies can be obtained through the secular equation:

$$\sum_{\alpha j l} [\hbar_{\alpha'(j'l'),\alpha(jl)} - \epsilon_n(\mathbf{k}) \delta_{\alpha'\alpha} \delta_{(j'l')(jl)}] C_{n\alpha(jl)}(\mathbf{r}) = 0 \quad (2.13)$$

By using the the basis set of Löwdin orbitals, here the Hamiltonian matrix elements are given by

$$\hbar_{\alpha'(j'l'),\alpha(jl)} = \langle \psi_{\alpha'j'l'}(\mathbf{r}) | \hat{\mathbf{h}}(\mathbf{r}) | \psi_{\alpha j l}(\mathbf{r}) \rangle \quad (2.14)$$

and the $\{C_{n\alpha(jl)}\}$ are the expansion coefficients in the Eq. (2.10).

The average potential \mathcal{U}_{ave} energy term in Eq. (2.4) can be treated as being the sum of spherical potentials located at the various atoms, then it can be written as follows

$$\begin{aligned} \hat{\mathbf{h}}(\mathbf{r}) &= \frac{\mathbf{p}^2}{2m_e} \\ &+ \mathcal{U}_{j l}(\mathbf{r}) \quad \text{intra-atomic potential} \\ &+ \sum_{(j'l') \neq (j l)} \mathcal{U}_{j'l'}(\mathbf{r}) \quad \text{two-body potential} \\ &+ \sum_{(j''l'') \neq (j'l') \neq (j l)} \mathcal{U}_{j''l''}(\mathbf{r}) \quad \text{three-body potential,} \end{aligned} \quad (2.15)$$

where $\mathcal{U}_{j l}(\mathbf{r})$ is the spherical potential due to the ion located at position $\mathbf{R}_l + \mathbf{d}_j$. Accordingly, Eq.(2.14) can be separated into three qualitatively different contributions

$$\begin{aligned} \hbar_{\alpha'(j'l'),\alpha(jl)} &= \langle \psi_{\alpha'j'l'}(\mathbf{r}) | \left(\frac{\mathbf{p}^2}{2m_e} + \mathcal{U}_{j l}(\mathbf{r}) \right) | \psi_{\alpha j l}(\mathbf{r}) \rangle \\ &+ \langle \psi_{\alpha'j'l'}(\mathbf{r}) | \sum_{(j'l') \neq (j l)} \mathcal{U}_{j'l'}(\mathbf{r}) | \psi_{\alpha j l}(\mathbf{r}) \rangle \\ &+ \langle \psi_{\alpha'j'l'}(\mathbf{r}) | \sum_{(j''l'') \neq (j'l') \neq (j l)} \mathcal{U}_{j''l''}(\mathbf{r}) | \psi_{\alpha j l}(\mathbf{r}) \rangle \end{aligned} \quad (2.16)$$

where the first *intra-atomic* term is easily computed thanks to orthogonality. The remaining two contributions are called, respectively, *two-center* and *three-center* energy integrals. Noting that this problem is almost impossible to carry out with full rigor on account of the computation of three-center integrals. A simplified tight binding method has been introduced by Slater and Koster

[46]. Basically, they suggest to cut the expansion of spherical potential in Eq. (2.15) up to the second term, and instead the explicit computation of the first and second integrals in Eq. (2.16), they consider the two-center hopping integrals as disposable constants fitted from available experimental measures or from results of more accurate techniques, which are available only at a restricted set of symmetric points of Brillouin zone.

The first approximation is the so-called *two center approximation* for energy integrals.

These two-center hopping integrals can be expressed as products of a radial wave function and a spherical harmonic $Y_{lm}(\theta, \vartheta)$ with the atom chosen as the origin. We will denote the vector going from the first atom A, at \mathbf{R}_{j1} , to the second atom B, at $\mathbf{R}_{j'1'}$, as $\mathbf{t} = (\mathbf{R}_{j1} - \mathbf{R}_{j'1'})$. For both orbitals $\psi_{\alpha j1}$ and $\psi_{\alpha' j'1'}$, we will choose the coordinate axes such that the z -axes are parallel to \mathbf{t} and the azimuthal angles ϑ are the same. In these coordinate systems the spherical harmonic wave functions of the two atoms A and B are $Y_{lm}(\theta, \vartheta)$ and $Y_{l'm'}(\theta', \vartheta)$, respectively. The Hamiltonian \hat{h} has cylindrical symmetry with respect to \mathbf{t} and therefore cannot depend on ϑ . Thus the matrix element $h_{\alpha'(j'1'), \alpha(j1)}$ is proportional to the integral of the azimuthal wave functions $\exp(i(m' - m)\vartheta)$. This integral vanishes except when $m = m'$. symmetry. The concept of bonding and antibonding orbitals for molecules can be easily extended to crystals if one assumes that the orbitals of each atom in the crystal overlap with those of its nearest neighbors only. This is a reasonable approximation for most solids. The interaction between two atomic orbitals produces one symmetric orbital, with respect to the interchange of the two atoms, which is known as the bonding orbital, and one antisymmetric orbital, which is known as the antibonding orbital. The results of orbital overlap in a solid is that the bonding and antibonding orbitals are broadened into bands. Those occupied by electrons form valence bands while the empty ones form conduction bands. The hopping integrals are usually labeled σ , π , and δ for ($l = 2$ wave functions), depending on whether $m = 0, 1$, or 2 (in analogy with the s , p , and d atomic wave functions). In the case of p orbitals there are two ways for them to overlap. When they overlap along the direction of the p orbitals, they are said to form σ bonds. When they overlap in a direction perpendicular to the p orbitals they are said to form π bonds. These hopping integrals have a simple physical interpretation as representing interactions between electrons on adjacent atoms. The fitting procedure is carried out on the basis of some approximations. First of all, only interactions into close neighbor shell are taken into account. Therefore only atoms within a certain cut-off distance interact with each other. This approximation is validated by the localized character of the atomic orbitals. Second approximation

*Close neighbor
interaction
approximation*

Minimal basis set

Two-center Integrals	
$\langle \psi_{s,i} \hat{\mathbf{h}}(\mathbf{t}) \psi_{s,i} \rangle =$	\mathbf{E}_s
$\langle \psi_{p,i} \hat{\mathbf{h}}(\mathbf{t}) \psi_{p,i} \rangle =$	\mathbf{E}_p
$\langle \psi_{s,i} \hat{\mathbf{h}}(\mathbf{t}) \psi_{s,j} \rangle =$	$\mathbf{V}_{ss\sigma}$
$\langle \psi_{s,i} \hat{\mathbf{h}}(\mathbf{t}) \psi_{p_x,j} \rangle =$	$\hat{\mathbf{I}}(\mathbf{V}_{sp\sigma})$
$\langle \psi_{p_x,i} \hat{\mathbf{h}}(\mathbf{t}) \psi_{p_x,j} \rangle =$	$\hat{\mathbf{I}}^2(\mathbf{V}_{pp\sigma}) + (1 - \hat{\mathbf{I}}^2)(\mathbf{V}_{pp\pi})$
$\langle \psi_{p_x,i} \hat{\mathbf{h}}(\mathbf{t}) \psi_{p_y,j} \rangle =$	$\hat{\mathbf{I}}\hat{\mathbf{m}}(\mathbf{V}_{pp\sigma}) - \hat{\mathbf{I}}\hat{\mathbf{m}}(\mathbf{V}_{pp\pi})$
$\langle \psi_{p_x,i} \hat{\mathbf{h}}(\mathbf{t}) \psi_{p_z,j} \rangle =$	$\hat{\mathbf{I}}\hat{\mathbf{n}}(\mathbf{V}_{pp\sigma}) - \hat{\mathbf{I}}\hat{\mathbf{n}}(\mathbf{V}_{pp\pi})$

Table 2.1: Two-center hopping integrals up to the p-orbital [46]. Here the vector $\mathbf{t} = (\hat{\mathbf{l}}, \hat{\mathbf{m}}, \hat{\mathbf{n}})\mathbf{t}$ is written through its director cosines.

is the choice of a minimal basis set for the LCAO expansion, including only those Löwdin atomic orbitals whose energy is close to the energy of the electronic states we are interested in. This choice minimizes the size of the TB matrix to be diagonalized and, therefore, affects directly the computational workload associated to the TB method.

Rewriting the Löwdin wave functions $\psi_{\alpha j l}(\mathbf{r})$ of the Eq. (2.12) in form of Bloch functions

$$\psi_{\alpha j \mathbf{k}}(\mathbf{r}) = \sum_{\mathbf{l}} \exp(i\mathbf{k} \cdot \mathbf{R}_{\mathbf{l}}) \psi_{\alpha j l}(\mathbf{r}), \quad (2.17)$$

the matrix elements defined in the Eq. (2.14) is now in the form

$$\begin{aligned} h_{\alpha' j', \alpha j}(\mathbf{k}) &= \langle \psi_{\alpha' j' \mathbf{k}}(\mathbf{r}) | \hat{\mathbf{h}}(\mathbf{r}) | \psi_{\alpha j \mathbf{k}}(\mathbf{r}) \rangle \\ &= \sum_{\mathbf{l} \mathbf{l}'} \exp(i\mathbf{k} \cdot (\mathbf{R}_{\mathbf{l}} - \mathbf{R}_{\mathbf{l}'})) \langle \psi_{\alpha' j' \mathbf{l}'}(\mathbf{r}) | \hat{\mathbf{h}}(\mathbf{r}) | \psi_{\alpha j \mathbf{l}}(\mathbf{r}) \rangle \end{aligned} \quad (2.18)$$

where the matrix elements are basically the same hopping integrals defined in Eq. (2.14), which can also be expressed in terms of the overlap parameters shown in Table 2.1, and the phase factors are the geometrical factors containing the \mathbf{k} -dependence. Instead of summing over all the unit cells in the crystal, we sum over the nearest neighbors only. If needed, one can easily include second neighbor or even further interactions, applying symmetry arguments allows the number of nonzero and linearly independent matrix elements to be greatly reduced.

Starting from the previously described TB semi-empirical, two-center, short-ranged and orthogonal scheme, we now introduce the tight-binding molecular dynamics, (TBMD), namely the application of the above described tight binding TB model to the calculation of the forces for a molecular dynamics MD scheme.

The tight-binding molecular dynamics TBMD ionic trajectories are generated by the TBMD Hamiltonian

$$\mathcal{H} = \sum_j \frac{\mathbf{P}_j^2}{2M_j} + E_{bs} + U_{rep}(\mathbf{R}_1, \mathbf{R}_2, \dots, \mathbf{R}_N), \quad (2.19)$$

where \mathbf{P}_j and M_j represent atomic momenta and masses and ϵ_n is the one-electron energy and n the band index.

Because of it is not possible to directly compute the Hartree energy U_{el-el} , within the semi-empirical TB scheme, since the electron density $\rho(\mathbf{r})$ is unknown, the total energy E_{tot} of the (ions+electrons) system is re-written as

$$E_{tot} = U_{ion-ion} + U_{el-ion} + U_{el-el} = E_{bs} + U_{rep}. \quad (2.20)$$

Here, the $E_{bs} = U_{el-ion} + 2U_{el-el}$ is the so-called *band-structure energy*, which is calculated by solving the Eq. (2.13)

$$E_{bs} = 2 \sum_n^{\text{occup}} \epsilon_n, \quad (2.21)$$

and it can be written as the Fermi-Dirac function

$$E_{bs} = 2 \sum_{\mathbf{k}, n} f_{FD}[\epsilon_n(\mathbf{k}), T] \epsilon_n(\mathbf{k}),$$

at the temperature $T = 0$ evaluated at a single \mathbf{k} point in the Brillouin zone, and the $U_{rep} = U_{ion-ion} - U_{el-el}$ is an effective repulsive potential assumed to be short-ranged. Because of the hopping integrals have been fitted on the equilibrium properties that is with the ions at the equilibrium lattice positions, the so-called Harrison rule [47] is introduced. If $h_{\alpha'j', \alpha j}^{(0)}$ is the matrix elements referred to the equilibrium interatomic distance $\mathbf{R}_{jj'}^{(0)}$, the variation of the matrix element $h_{\alpha'j', \alpha j}(\mathbf{R}_{jj'})$ upon the actual distance $\mathbf{R}_{jj'}$ is given by

$$h_{\alpha'j', \alpha j}(\mathbf{R}_{jj'}) = h_{\alpha'j', \alpha j}^{(0)} \left(\frac{\mathbf{R}_{jj'}^{(0)}}{\mathbf{R}_{jj'}} \right)^n \quad (2.22)$$

Similarly, the repulsive energy $U_{rep} = \sum_{j \neq j'} u(\mathbf{R}_{jj'})$ obeys the Harrison-like rule

$$u(\mathbf{R}_{jj'}) = u^{(0)} \left(\frac{\mathbf{R}_{jj'}^{(0)}}{\mathbf{R}_{jj'}} \right)^m \quad (2.23)$$

where the two-body potential $u^{(0)}$ regards a couple of ions at their equilibrium distance. The parameters n and m have to be determined by fitting.

The effective repulsive potential

The universal Tight Binding method: Harrison rule

Calculation of the forces

These assumptions imply that the force \mathbf{F}_k acting on the k^{th} ion is given by

$$\begin{aligned}\mathbf{F}_k &= -\frac{\partial \mathcal{H}}{\partial \mathbf{R}_k} = -\frac{\partial}{\partial \mathbf{R}_k} [E_{\text{bs}} + U_{\text{rep}}(\mathbf{R}_1, \mathbf{R}_2, \dots, \mathbf{R}_N)] \\ &= \left[\mathbf{F}_k^{\text{A}} + \mathbf{F}_k^{\text{R}} \right] \quad (2.24)\end{aligned}$$

where the force \mathbf{F}_k is separated in an *attractive* contribution \mathbf{F}_k^{A} and in a *repulsive* term \mathbf{F}_k^{R} . The \mathbf{F}_k^{A} depends only on the actual tight binding model, while the \mathbf{F}_k^{R} depends just on the empirical repulsive potential and they require dissimilar numeric treatment. The repulsive term \mathbf{F}_k^{R} is straightforwardly calculated from $U_{\text{rep}}(\mathbf{R}_1, \mathbf{R}_2, \dots, \mathbf{R}_N)$, which is known as an analytic function of interatomic distances.

The attractive term \mathbf{F}_k^{A} is given by

$$\begin{aligned}\mathbf{F}_k^{\text{A}} &= -2 \frac{\partial}{\partial \mathbf{R}_k} \sum_n^{(\text{occup})} \epsilon_n \\ &= -2 \frac{\partial}{\partial \mathbf{R}_k} \sum_n^{(\text{occup})} \sum_{\alpha'j'} C_{n\alpha'j'}^* C_{n\alpha j} h_{\alpha'j',\alpha j} \quad (2.25)\end{aligned}$$

The derivative with respect to the ionic position has been developed as follow

$$\begin{aligned}\mathbf{F}_k^{\text{A}} &= -2 \sum_n^{(\text{occup})} \left[\sum_{\alpha'j'} \sum_{\alpha j} \frac{\partial C_{n\alpha'j'}^*}{\partial \mathbf{R}_k} C_{n\alpha j} h_{\alpha'j',\alpha j} \right. \\ &\quad + \sum_{\alpha'j'} \sum_{\alpha j} C_{n\alpha'j'}^* \frac{\partial C_{n\alpha j}}{\partial \mathbf{R}_k} h_{\alpha'j',\alpha j} + \\ &\quad \left. + \sum_{\alpha'j'} \sum_{\alpha j} C_{n\alpha'j'}^* C_{n\alpha j} \frac{\partial h_{\alpha'j',\alpha j}}{\partial \mathbf{R}_k} \right] \\ &= -2 \sum_n^{(\text{occup})} \left[\sum_{\alpha'j'} \frac{\partial C_{n\alpha'j'}^*}{\partial \mathbf{R}_k} \sum_{\alpha j} C_{n\alpha j} h_{\alpha'j',\alpha j} \right. \\ &\quad + \sum_{\alpha j} \frac{\partial C_{n\alpha j}}{\partial \mathbf{R}_k} \sum_{\alpha'j'} C_{n\alpha'j'}^* h_{\alpha'j',\alpha j} + \\ &\quad \left. + \sum_{\alpha'j'} \sum_{\alpha j} C_{n\alpha'j'}^* C_{n\alpha j} \frac{\partial h_{\alpha'j',\alpha j}}{\partial \mathbf{R}_k} \right] \quad (2.26)\end{aligned}$$

and imposing the orthogonality conditions

$$\sum_{\alpha j} h_{\alpha'j',\alpha j} C_{n\alpha j} = \epsilon_n C_{n\alpha'j'} \quad \text{and} \quad \sum_{\alpha'j'} C_{n\alpha'j'}^* h_{\alpha'j',\alpha j} = \epsilon_n C_{n\alpha j}^* \quad (2.27)$$

the Eq. (2.26) can be written into

$$\mathbf{F}_k^A = -2 \sum_n^{(\text{occup})} \left[\epsilon_n \frac{\partial}{\partial \mathbf{R}_k} \left(\sum_{\alpha_j} C_{n\alpha_j}^* C_{n\alpha_j} \right) + \sum_{\alpha'j'} \sum_{\alpha_j} C_{n\alpha'j'}^* C_{n\alpha_j} \frac{\partial h_{\alpha'j',\alpha_j}}{\partial \mathbf{R}_k} \right] \quad (2.28)$$

by assuming completeness of the basis set used for LCAO expansion, $\sum_{\alpha_j} C_{n\alpha_j}^* C_{n\alpha_j} = 1$, again

$$\mathbf{F}_k^A = -2 \sum_n^{(\text{occup})} \sum_{\alpha'j'} \sum_{\alpha_j} C_{n\alpha'j'}^* C_{n\alpha_j} \frac{\partial h_{\alpha'j',\alpha_j}}{\partial \mathbf{R}_k} \quad (2.29)$$

The Eq. (2.29) represents the final expression for the attractive contribution to the net force on the k^{th} atom and the simple derivation presented above is a special implementation of the Hellmann-Feynman theorem. Formally the derivative in Eq. (2.29) can be re-write as follows

$$\mathbf{F}_k^A = -2 \sum_n^{(\text{occup})} \left[\sum_{\alpha'j'} \sum_{\alpha_j} C_{n\alpha'j'}^* C_{n\alpha_j} \langle \psi_{\alpha'j'} | \frac{\partial \hat{h}}{\partial \mathbf{R}_k} | \psi_{\alpha_j} \rangle + \sum_{\alpha'j'} \sum_{\alpha_j} C_{n\alpha'j'}^* C_{n\alpha_j} \left(\langle \frac{\partial \psi_{\alpha'j'}}{\partial \mathbf{R}_k} | \hat{h} | \psi_{\alpha_j} \rangle + \langle \psi_{\alpha'j'} | \hat{h} | \frac{\partial \psi_{\alpha_j}}{\partial \mathbf{R}_k} \rangle \right) \right] \quad (2.30)$$

This form shows that the attractive force \mathbf{F}_k^A includes both the Hellmann-Feynman [48] and Pulay [49] contributions, as the first and second term of the right-hand side of Eq. (2.30). The Pulay force term must be added to the standard Hellmann-Feynman one, because of the basis set functions depends on the ionic coordinates. Let's come now to introduce the specific tight binding TB Hamiltonian we use for the carbon and hydro-carbon systems.

2.2 THE TIGHT-BINDING REPRESENTATION OF CARBON-BASE SYSTEMS

In this section we refer to the work of Xu *et al.* [50], where an interatomic potential for carbon is developed in the framework of the empirical TB approach.

The TB interatomic potential is developed adopting the scaling form given by Goodwin *et al.* [51] for the dependence of the TB hopping parameters and of the pairwise potential on the interatomic separation. In this model the total energy is written, as previously discussed (see Eq. (2.20)) as

$$E_{\text{tot}} = E_{\text{bs}} + U_{\text{rep}},$$

where E_{b_s} is twice the sum of electronic eigenvalues over all occupied electronic states and U_{rep} is a short-ranged repulsive term. The electronic eigenvalues are obtained by diagonalizing the TB Hamiltonian. Its off-diagonal elements are described by a set of orthogonal sp^3 two-center hopping parameters ($V_{ss\sigma}$, $V_{sp\sigma}$, $V_{pp\sigma}$ and $V_{ss\pi}$) scaled with interatomic separation $r_{ij} = |\mathbf{R}_i - \mathbf{R}_j|$ by means of a function $s(r)$; the onsite elements are the atomic orbital energies of the corresponding atom. The repulsive term U_{rep} is modelled as

$$U_{rep} = \sum_i f\left(\sum_j \phi(r_{ij})\right), \quad (2.31)$$

where $\phi(r_{ij})$ is a pairwise model potential between atoms i and j , and f is a functional expressed as a 4th-order polynomial with argument $\sum_j \phi(r_{ij})$. For the scaling function $s(r)$ and pairwise potential $\phi(r_{ij})$ we adopt the following functional forms:

$$s(r) = \left(\frac{r_0}{r}\right)^n e^{n\left[-\left(\frac{r}{r_c}\right)^{n_c} + \left(\frac{r_0}{r_c}\right)^{n_c}\right]} \quad (2.32)$$

$$\phi(r) = \phi_0 \left(\frac{d_0}{r}\right)^m e^{m\left[-\left(\frac{r}{d_c}\right)^{m_c} + \left(\frac{d_0}{d_c}\right)^{m_c}\right]} \quad (2.33)$$

where r_0 is the nearest neighbor atomic separation in *diamond* and n , n_c , r_c , ϕ_0 , m , d_c and m_c are parameters to be determined. It would be nice if the functions $s(r)$ and $\phi(r)$ vanished smoothly at some designed cut-off distances, r_c and d_c respectively. For the used carbon TBMD parameterization, this cut-off value is set to $r_c = d_c = 2.6 \text{ \AA}$, which is between the nearest-neighbor and the next-nearest-neighbor distances of carbon atoms in the equilibrium diamond structure. In fact the scaled TB matrix elements are truncated discontinuously to 0 at r_c , and the force is made change from a finite value to 0 abruptly. These small energy jumps creates no significant problem to the simulations. It is important to observe this TBMD cut-off is smaller than the interlayer distance in graphite, this choice strong affecting our work, as explained in the following chapters. The value of this model parameters are chosen by fitting first-principles LDA results of energy versus nearest-neighbor distance for different carbon allotropies (diamond, graphite, linear chain, simple and face-centered cubic). The resulting sp^3 TB parameters expressed in units of eV are shown in Table 5.1.

As shown by Xu *et al.* [50], these parameters reproduce excellently the energy curves of the diamond and graphite structures (see figure 1 and 2 in [50]). The parameters for $s(r)$, $\phi(r)$ and the coefficients for the polynomial function $f(x) = \sum_{n=0}^4 c_n x^n$ with $x = \sum_j \phi(r_{ij})$ are listed in Table 2.3. The presented TB approach gives an accurate description of atomic interactions in carbon system, it is able to reproduce the energy-volume curves of accurate LDA calculations with excellent transferability among

Two-center Integral	Xu <i>et al.</i> [50]
E_s	-2.99
E_p	+3.71
$V_{ss\sigma}$	-5.0
$V_{sp\sigma}$	+4.7
$V_{pp\sigma}$	+5.5
$V_{pp\pi}$	-1.55

Table 2.2: The sp^3 tight-binding parameters expressed in units of eV at the reference interatomic separation $r_0 = 1.536 \text{ \AA}$ of diamond nearest neighbors.

graphite and diamond structures, giving a good description of the dynamical and elastic properties of such structures.

Parameter	
n	2.0
n_c	6.5
r_c	2.18 Å
r_0	1.536329 Å
r_1	2.45 Å
ϕ_0	8.18555(eV)
m	3.30304
m_c	8.6655
d_c	2.1052 Å
d_0	1.64 Å
d_1	2.57 Å
c_0	-2.5909765118191
c_1	0.5721151498619
c_2	$-1.7896349903396 \cdot 10^{-3}$
c_3	$2.3539221516757 \cdot 10^{-5}$
c_4	$-1.24251169551587 \cdot 10^{-7}$

Table 2.3: The parameters defining $s(r)$, $\phi(r)$, and the coefficients for the polynomial function $f(x) = \sum_{n=0}^4 c_n x^n$.

DENSITY FUNCTIONAL THEORY

“ It doesn't matter how beautiful your theory is, it doesn't matter how smart you are. If it doesn't agree with experiment, it's wrong.”
Richard P. Feynman (1918 - 1988)

Contents

3.1	Density functional theory	25
3.1.1	Exchange and correlation energy approximations	28
3.1.2	Plane waves and Pseudopotentials	31
3.2	Density Functional Perturbation Theory	33

3.1 DENSITY FUNCTIONAL THEORY

Density functional theory (DFT) [52, 53] solves the electronic Schrödinger equation

$$\hat{H}\psi = E\psi \quad (3.1)$$

by reducing the quantum mechanical problem for a many-body interacting system to an equivalent problem for non-interacting particles. This is achieved by using as fundamental variable the electronic density instead of the many-body electronic wavefunction.

The theoretical base of DFT is the *Hohenberg and Kohn lemma* [54, 55] which considers an electronic system subject to an external potential. This theorem states that *any ground state density* $n(\mathbf{r})$ *of a many-electron system determines uniquely the external potential* $V^{\text{ext}}(\mathbf{r})$, *modulo an uninteresting additive constant*. This lemma is mathematically rigorous. Since $n(\mathbf{r})$ determines both the number of electrons N and $V^{\text{ext}}(\mathbf{r})$, it gives the full Hamiltonian for the electronic system, and it determines implicitly all physical properties derivable from H through the solutions of the Schrödinger equation (time-dependent or not).

Therefore according to this lemma, considering a set of Hamiltonians that have the same kinetic energy T_e and electron-electron operator U_{ee} but different external potentials, their ground state will have different densities, or rather two different potentials acting on the same electronic system cannot give rise to the same ground-state electronic charge density. The external potential is thus a functional of the ground-state density. Therefore once the external potential V^{ext} is fixed, the total energy will also be a functional $E_V[n(\mathbf{r})]$ of the electronic charge density $n(\mathbf{r})$.

Hohenberg and Kohn lemma

Applying the standard Rayleigh-Ritz variational principle of quantum mechanics, the electronic charge density of the ground state, corresponding to the external potential V^{ext} , minimizes the functional $E_V[n(\mathbf{r})]$, under the constraint that the integral of $n(\mathbf{r})$ equals the total number of electrons N . The ground state energy coincides with the minimum of the *constrained energy minimum* $E_V[\tilde{n}(\mathbf{r})] = \min (\tilde{\Psi}, \hat{H}\tilde{\Psi})$, where the trial function $\tilde{\Psi}$ corresponds to a fixed trial density \tilde{n}

$$\tilde{n}(\mathbf{r}) = N \int d^3r_2 \int d^3r_3 \cdots \int d^3r_N \tilde{\Psi}^*(\mathbf{r}, \mathbf{r}_2, \dots, \mathbf{r}_N) \tilde{\Psi}(\mathbf{r}, \mathbf{r}_2, \dots, \mathbf{r}_N) \quad (3.2)$$

The expression for the ground state energy of the electronic system is then

$$E_V = \min_{\tilde{n}} E_V[\tilde{n}] = \min_{\tilde{n}} \left(F[\tilde{n}] + \int d\mathbf{r} \tilde{n}(\mathbf{r}) V^{\text{ext}}(\mathbf{r}) \right) \quad (3.3)$$

where $F[n]$ is an *universal* functional of the density $n(\mathbf{r})$ that does not require explicit knowledge of $V^{\text{ext}}(\mathbf{r})$. It is defined by the kinetic energy T_e and by the electron-electron interaction U_{ee} as

$$F[\tilde{n}(\mathbf{r})] = \min (\tilde{\Psi}^*, (T_e + U_{ee})\tilde{\Psi}) \quad (3.4)$$

The functional $F[n]$ is not easy to calculate and represents most of the total energy E_V . Moreover there is no analytic expression for $F[n]$. Nevertheless, significant formal progress has been made, the problem of ground-state densities and energies has been well-formulated entirely in terms of the density \tilde{n} and of a well-defined, but explicitly unknown, functional of the density $F[\tilde{n}]$. In the work of Kohn and Sham [55] an approximate expression for $F[n]$ was proposed by considering an equivalent problem of non interacting electrons. The core of the Kohn and Sham assumption was that, for every system of interacting electrons, a corresponding system of non-interacting particles, described by single particle orbitals, exists subject to an external potential with the same ground state density as the interacting system.

The Kohn-Sham functional can be written as [55]

$$F[\tilde{n}] = T_e[\tilde{n}] + \frac{1}{2} \int d\mathbf{r} d\mathbf{r}' \frac{\tilde{n}(\mathbf{r})\tilde{n}(\mathbf{r}')}{|\mathbf{r} - \mathbf{r}'|} + E_{xc}[\tilde{n}] \quad (3.5)$$

Here and in the follows, any physical constant are assumed equal to the unit. $T_e[\tilde{n}]$ is the kinetic energy of the ground-state of *non-interacting* electrons with density $\tilde{n}(\mathbf{r})$, and $E_{xc}[\tilde{n}]$ is the so-called exchange and correlation energy. The last two terms of Eq. (3.5) derive from the decomposition of the U_{ee} operator, whose quantum mechanical effects are contained in $E_{xc}[n]$. A consequence of the Hohenberg and Kohn lemma is that the Eq.

(3.3) is variational with respect to the charge density, under the condition that the number of electrons is conserved. The solution of the corresponding variational equation leads to the equation

$$\delta E_V[\tilde{n}(\mathbf{r})] = \int \delta \tilde{n}(\mathbf{r}) \left\{ \left. \frac{\delta T_e[\tilde{n}]}{\delta \tilde{n}(\mathbf{r})} \right|_{\tilde{n}=n} + V_{KS} - \lambda \right\} d\mathbf{r} = 0 \quad (3.6)$$

where

$$V_{KS} = V^{ext} + \frac{1}{2} \int d\mathbf{r}' \frac{\tilde{n}(\mathbf{r}')}{|\mathbf{r} - \mathbf{r}'|} + v_{xc}(\mathbf{r}). \quad (3.7)$$

and λ is a Lagrange multiplier constraining the density to be normalized to the total number of the electrons. In Eq. (3.6), the local exchange-correlation potential $v_{xc}(\mathbf{r})$ is the functional derivative of exchange and correlation energy

$$v_{xc}(\mathbf{r}) = \left. \frac{\delta E_{xc}[\tilde{n}]}{\delta \tilde{n}(\mathbf{r})} \right|_{\tilde{n}=n} \quad (3.8)$$

depending functionally on the density $\tilde{n}(\mathbf{r})$.

Now the Hohenberg-Kohn variational problem for interacting systems becomes formally identically to a corresponding equation for a system of non-interacting electrons subject to an effective external potential V_{eff} instead V^{ext} , so the ground state of this system is obtained by solving the single particle equations

$$\left(-\frac{1}{2} \nabla^2 + V_{eff} - \varepsilon_j \right) \psi_j(\mathbf{r}) = 0 \quad (3.9)$$

where $\psi_j(\mathbf{r})$ are orthonormalized single particle orbitals, and the minimizing density $n(\mathbf{r})$ is given by

$$n(\mathbf{r}) = \sum_j |\psi_j(\mathbf{r})|^2 \quad (3.10)$$

It is possible to demonstrate that the two Eqs. (3.6) and (3.9) fulfill the same minimum conditions leading to the same density if the Kohn-Sham potential V_{KS} is equal to the V_{eff} . Therefore, assuming that the exchange-correlation energy functional is known, it is possible to treat the many-body problem as an independent particle problem. The self-consistent Eqs. (3.9) are the so-called the Kohn-Sham (KS) equations. The ground-state energy is now given by

$$E = \sum_j \varepsilon_j + E_{xc}[n] - \int d\mathbf{r} n(\mathbf{r}) v_{xc}(\mathbf{r}) - \frac{1}{2} \int d\mathbf{r} d\mathbf{r}' \frac{n(\mathbf{r})n(\mathbf{r}')}{|\mathbf{r} - \mathbf{r}'|} \quad (3.11)$$

reducible to the Hartree equations neglecting E_{xc} and v_{xc} . The KS theory may be regarded as the formal improvement of the Hartree theory, indeed with the exact E_{xc} and v_{xc} all many body

effects are in principle included. Unfortunately, the practical usefulness of the ground-state DFT depends entirely on whether approximations for the functional $E_{xc}[\tilde{n}]$ could be found, that at the same time has to be sufficiently simple and sufficiently accurate. The next section regards briefly the development and the current status of such approximations.

3.1.1 Exchange and correlation energy approximations

Dealing with the exchange and correlation energy $E_{xc}[n]$ is the most difficult task in the solutions of the Kohn-Sham equations. The exchange energy derives from Pauli exclusion principle, which imposes the antisymmetry of the many-electron wavefunction. This antisymmetrization produces a spatial separation between electrons with the same spin and thus reduces the Coulomb energy of the electronic system. This energy reduction is called the *exchange energy*. The *Hartree-Fock* method exactly describes exchange energy; the difference between the energy of an electronic system and the Hartree-Fock energy is called the *correlation energy*. It is extremely difficult to calculate the correlation energy of a complex system, although some attempts have been made by using quantum Monte Carlo simulations. The most important approximation for $E_{xc}[n]$ can be written in a quasi-local form

$$E_{xc}[n(\mathbf{r})] = \int d\mathbf{r} n(\mathbf{r}) \varepsilon_{xc}(\mathbf{r}; [n(\mathbf{r}')]) \quad (3.12)$$

where the exchange-correlation energy per particle ε_{xc} at the point \mathbf{r} which depending functionally on the density charge $n(\mathbf{r}')$ at the point \mathbf{r}' near \mathbf{r} , where "near" means at a distance such as the local Fermi wavelength $|\mathbf{r} - \mathbf{r}'| \simeq \lambda_F(\mathbf{r}) = (3\pi^2 n(\mathbf{r}'))^{-1/3}$. The most popular implementations of this quasi-local approach for the exchange and correlation energy are the *Local Density Approximation* (LDA) and the *Generalized Gradient Approximation* (GGA).

*Local Density
Approximation*

LDA was proposed in their original paper by Kohn and Sham [55] as the simplest method to describe the exchange-correlation energy $E_{xc}[n]$. They assume that the non-local exchange-correlation energy $\varepsilon_{xc}(\mathbf{r}; [n(\mathbf{r}')])$ in Eq. (3.16) can be equal to the local exchange-correlation energy per particle $\varepsilon_{xc}[n(\mathbf{r})]$ of a homogeneous electron gas, which has the same density as the electron gas at point $\mathbf{r} \in (\mathbf{r}, -\mathbf{F}(\mathbf{r}))$, if this volume is little enough that the charge density could be assume constant therein. In this assumption, the Eq. (3.16) becomes

$$E_{xc}^{LDA}[n] = \int d\mathbf{r} n(\mathbf{r}) \varepsilon_{xc}^{\text{hom}}[n(\mathbf{r})] \quad (3.13)$$

and the potential in Eq. (3.8)

$$v_{xc}^{\text{LDA}}[n(\mathbf{r})] = \left(\varepsilon_{xc}^{\text{hom}}[n] + n \frac{d\varepsilon_{xc}^{\text{hom}}[n]}{dn} \right)_{n=n(\mathbf{r})} \quad (3.14)$$

The LDA assumes that the exchange correlation energy functional is purely local, ignoring the corrections to the exchange correlation energy at a point \mathbf{r} due to the nearby inhomogeneities in the electron density, but it is exact in the limit of high density or of a slowly varying charge density. Moreover, the exchange-correlation energy $E_{xc}[n]$ can be separated in two terms

$$E_{xc}^{\text{LDA}}[n(\mathbf{r})] = E_x^{\text{LDA}}[n(\mathbf{r})] + E_c^{\text{LDA}}[n(\mathbf{r})] \quad (3.15)$$

The exchange term $E_x[n]$ is simply the Fermi-Thomas-Dirac exchange energy

$$E_x^{\text{LDA}}[n(\mathbf{r})] = -\frac{3}{4} \left(\frac{3}{\pi} \right)^{1/3} \int n(\mathbf{r})^{4/3} d\mathbf{r} \quad (3.16)$$

that comparing with Eq. (3.13) leads to an elementary form of the exchange part, given by, in atomic units

$$\varepsilon_x^{\text{hom}}[n(\mathbf{r})] \approx -\frac{0.4582}{r_s} \quad (3.17)$$

where r_s is the radius of a sphere containing an electron, namely radius of Sietz, and given by $(4\pi/3)r_s^3 = n^{-1}$. The correlation part was estimated by E.P. Wigner [56]

$$\varepsilon_c^{\text{hom}}[n(\mathbf{r})] \approx -\frac{0.44}{r_s + 7.8} \quad (3.18)$$

and using Monte Carlo methods it was calculated with higher precision for uniform electron gas by D.M. Ceperly and B.J. Alder [57, 58]

$$\begin{aligned} \varepsilon_c^{\text{hom}}[n(\mathbf{r})] &= \lambda (1 + \beta\sqrt{r_s} + \beta r_s)^{-1}, \quad r_s \geq 1 \\ \varepsilon_c^{\text{hom}}[n(\mathbf{r})] &= (A \ln r_s + B + C r_s \ln r_s + D r_s), \quad r_s < 1 \end{aligned} \quad (3.19)$$

which has been parametrized by J.P. Perdew and A. Zunger [59].

Another useful approximation is the so-called Generalized Gradient Approximation GGA. The basic concept is the average xc hole distribution around a given point \mathbf{r}

$$\begin{aligned} n_{xc}(\mathbf{r}, \mathbf{r}') &= g(\mathbf{r}, \mathbf{r}') - n(\mathbf{r}') \\ \int n_{xc}(\mathbf{r}, \mathbf{r}') d\mathbf{r}' &= -1 \end{aligned} \quad (3.20)$$

with the conditional density $g(\mathbf{r}, \mathbf{r}')$ at \mathbf{r}' due to an electron at \mathbf{r} . It describes the hole dug into the average density $n(\mathbf{r}')$ by

*Generalized
Gradient
Approximation*

the electron at \mathbf{r} , and it reflects the screening of the the electron at \mathbf{r} due to the Pauli effect and the electron-electron interaction. Introducing a parameter λ , ($0 \leq \lambda \leq 1$), the λ -average xc hole density $\bar{n}_{xc}(\mathbf{r}, \mathbf{r}')$ is then defined as

$$\bar{n}_{xc}(\mathbf{r}, \mathbf{r}') = \int n_{xc}(\mathbf{r}, \mathbf{r}'; \lambda) d\lambda \quad (3.21)$$

the very physical formally exact espretion of the exchange-correlation energy $\varepsilon_{xc}(\mathbf{r}; [n(\mathbf{r}')])$ in Eq. (3.16) is given by

$$\varepsilon_{xc}(\mathbf{r}; [n(\mathbf{r}')]) = -\frac{1}{2} R_{xc}^{-1}(\mathbf{r}; [n(\mathbf{r}')]) \quad (3.22)$$

where $R_{xc}^{-1}(\mathbf{r}; [n(\mathbf{r}')])$ is

$$R_{xc}^{-1}(\mathbf{r}; [n(\mathbf{r}')]) = \int \frac{-\bar{n}_{xc}(\mathbf{r}, \mathbf{r}')}{|\mathbf{r} - \mathbf{r}'|} d\mathbf{r}' \quad (3.23)$$

Since R_{xc}^{-1} is a functional of $n(\mathbf{r}')$, we can formally use the expansion of the electron density $n(\mathbf{r}')$ around the point \mathbf{r}

$$n(\mathbf{r}') = n(\mathbf{r}) + (\mathbf{r} - \mathbf{r}')[\nabla n(\mathbf{r}')]_{\mathbf{r}'=\mathbf{r}} + \frac{1}{2}(\mathbf{r} - \mathbf{r}')^2[\nabla^2 n(\mathbf{r}')]_{\mathbf{r}'=\mathbf{r}} + \dots \quad (3.24)$$

and we obtain

$$R_{xc}^{-1}(\mathbf{r}) = F_0(n(\mathbf{r})) + F_{21}(n(\mathbf{r}))\nabla^2 n(\mathbf{r}) + \dots \quad (3.25)$$

This leads to the gradient expression for E_{xc}

$$\begin{aligned} E_{xc} &= E_{xc}^{LDA} + \int G_2(n(\mathbf{r}))(\nabla n(\mathbf{r}))^2 d\mathbf{r} + \dots \\ &= \int n(\mathbf{r})\varepsilon_{xc}^{LDA}[n(\mathbf{r})] d\mathbf{r} + \int n(\mathbf{r})\varepsilon_{xc}^{GGA}[n(\mathbf{r}), |\nabla n(\mathbf{r})|] d\mathbf{r} + \dots \end{aligned} \quad (3.26)$$

where G_2 is an universal functional of $n(\mathbf{r})$. Generally the GGA method stops the expansion at the first derivative, and the exchange-correlation function is expressed as function of the two variables $n(\mathbf{r})$ e $|\nabla n(\mathbf{r})|$

$$E_{xc}^{GGA}[n] = \int n(\mathbf{r})\varepsilon_{xc}^{GGA}(n(\mathbf{r}), \nabla n(\mathbf{r})) d\mathbf{r} \quad (3.27)$$

An important point regard the parametrization of the ε_{xc}^{GGA} . Analytical form was proposed by Perdew-Wang [60, 61, 62], and Becke [63], namely (PW91), using the local spin density (LSD) approximation for the exchange-correlation energy, Eq. (3.27), which it can be separated in two terms

$$E_{xc}^{PW91}[n] = E_x^{PW91}[n] + E_c^{PW91}[n] \quad (3.28)$$

The exchange term is given by, using atomic units

$$\begin{aligned} E_x^{\text{PW91}}[n] &= \int n(\mathbf{r}) \varepsilon_x^{\text{PW91}}(\mathbf{r}_s, \sigma)_{\sigma=0} F_X^{\text{PW91}}(s) d\mathbf{r} \\ \varepsilon_x^{\text{GGA}}(\mathbf{r}_s, 0) &= -\frac{3k_F}{4\pi} \end{aligned} \quad (3.29)$$

$$(3.30)$$

Here, $\varepsilon_x^{\text{PW91}}(\mathbf{r}_s, \sigma)$ is the exchange-correlation energy per particle for a uniform electron gas, with \mathbf{r}_s is the local Seitz radius and $\sigma = (n_{\text{up}} - n_{\text{down}})/n$ is the local spin polarization,

$$k_F = (3\pi^2 n(\mathbf{r}))^{1/3} \quad (3.31)$$

is the local Fermi wave vector, and

$$s(\mathbf{r}) = \frac{|\nabla n(\mathbf{r})|}{2k_F n(\mathbf{r})}, \quad (3.32)$$

is a scaled density gradient. The function $F_X^{\text{PW91}}(s)$ is written as [60]

$$F_X^{\text{PW91}}(s(\mathbf{r})) = \frac{1 + s(\mathbf{r}) A \sinh^{-1}(s(\mathbf{r}) B) + (C - D e^{-100s^2(\mathbf{r})})s^2(\mathbf{r})}{1 + s(\mathbf{r}) A \sinh^{-1}(s(\mathbf{r}) B) + s^4(\mathbf{r}) E}, \quad (3.33)$$

The correlation part of Eq. (3.28) is

$$E_c^{\text{PW91}}[n] = \int n(\mathbf{r}) [\varepsilon_c(r_s, \zeta) + H(t, r_s, \zeta)] d\mathbf{r}, \quad (3.34)$$

where $\varepsilon_c(\mathbf{r}_s, \zeta)$ is the correlation energy per particle of an uniform electron gas [60], and t is another scaled density gradient

$$t = \frac{|\nabla n(\mathbf{r})|}{2g k_s n(\mathbf{r})}, \quad (3.35)$$

here, $k_s = (4k_F/\pi)^{1/2}$ is the local screening wave vector, and $g = [(1 + \zeta)^{2/3} + (1 - \zeta)^{2/3}]/2$. Analytic representations both for $\varepsilon_c(\mathbf{r}_s, \zeta)$ and for the function $H(t, r_s, \zeta)$ are available in Ref. [62]. Popular GGA implementations include Perdew-Burke-Ernzerhof (PBE) [64], and Becke-Lee-Yang-Parr (BLYP) [63, 65].

3.1.2 Plane waves and Pseudopotentials

As shown previously, DFT reduces a many-body interacting particle problem to an independent particle problem. However solving single particle equations also presents technical difficulties. In particular, if a plane-waves basis set is chosen to expand the wavefunctions, an extremely large number of plane waves is needed for expanding the core electron wavefunctions (strongly

localized in the region near the nucleus) and for reproducing the rapid oscillations of the valence electron wavefunctions in the core region. For this reason a calculation including all the electrons using a plane wave basis set requires a huge computational cost.

The pseudopotential approximation is an effective method to eliminate the core electrons in the calculations of the electronic structure. It is known that the core electrons are chemical inert and that most molecular properties can be calculated with acceptable precision assuming that the core electrons do not modify their state in different chemical configurations (free atom, molecule, solid): this is known as the *frozen core approximation*. Therefore in the solution of the Schrödinger equation it is possible to distinguish: *i*) The core region mainly constituted of electrons deeply bonded and almost non interacting with those of other atoms; *ii*) the remaining volume, where there are valence electrons that are involved in bonds with the neighbor atoms.

Although the potential in the core region is strongly attractive, the orthogonality condition between the valence and core electron wavefunctions results in oscillations of the valence electron wavefunctions, which correspond to a kinetic energy that almost balances the attractive potential. In the pseudopotential method this kinetic effect is simulated by a repulsive potential that balances the strong attractive potential in the core region. This results in the separation of the electron-electron interaction term U_{ee} into a term corresponding to the valence electrons and a term corresponding to the core electrons that screen the attraction of the nuclear potential onto the valence electrons. Therefore the pseudopotential (PP) is

$$U_{PP} = U_{eN} + U_{sc} + U_{val} \quad (3.36)$$

where U_{eN} represents the electron-nuclei interaction, U_{sc} represents the screening due to the core electrons and U_{val} represent the interaction between valence electrons. The pseudopotential is identical to the real potential at distance greater than the core radius r_c , while for $r \leq r_c$, it is built so as to simulate the combined action of the ionic and screening terms on the valence electrons. The eigenfunctions of the corresponding Schrödinger equation are therefore pseudo-eigenfunctions, which coincide with the real eigenfunctions only in the region for $r > r_c$. In the core region, the pseudo-eigenfunctions are continuous and node less. They allow a rapid convergence in the plane wave expansion.

The main advantages achieved by using the pseudopotential method are: the number of the electrons to deal with is reduced for a given system; the computational cost is lower due to the smaller number of plane waves necessary for the calculations. Technical aspects of the implementation of the KS equations in

plane wave pseudopotential (PW-PP) framework have been found in Ref. [66].

3.2 DENSITY FUNCTIONAL PERTUBATION THEORY: FROM ELECTRONIC STRUCTURE TO LATTICE DYNAMICS

Lattice dynamical properties of a system are determined by the solution of the Schrödinger equation for the ionic part, by using the adiabatic approximation of Born-Oppenheimer

$$\left(-\sum \frac{\hbar^2}{2M_i} \frac{\partial^2}{\partial \mathbf{R}_i^2} + E(\mathbf{R}) \right) \phi(\mathbf{R}) = \mathcal{E} \phi(\mathbf{R}) \quad (3.37)$$

where \mathbf{R}_i and M_i are the coordinate of the i^{th} -ion, and its mass, respectively, and $E(\mathbf{R})$ is the ground-state energy of the electronic system moving in the field of fixed ions. The equilibrium condition is achieved when the forces acting in the electronic ground-state on each ion vanish

$$\mathbf{F}_i = -\frac{\partial E(\mathbf{R})}{\partial \mathbf{R}_i} = \left\langle \psi(\mathbf{R}) \left| \frac{\partial \hat{H}_{el}}{\partial \mathbf{R}_i} \right| \psi(\mathbf{R}) \right\rangle = 0 \quad (3.38)$$

Here, the Hellmann-Feynman theorem has been applied in the framework of the Born-Oppenheimer approximation, the $\psi(\mathbf{R})$ is the electronic ground-state wave function, and the ion coordinates act as parameters in the electronic Hamiltonian \hat{H}_{el} .

The vibrational frequencies ω are determined by the eigenvalues of the Hessian of $E(\mathbf{R})$, namely the matrix of the *interatomic force constants*

$$\det \left| (M_i M_j)^{-1/2} \frac{\partial^2 E(\mathbf{R})}{\partial \mathbf{R}_i \partial \mathbf{R}_j} - \omega^2 \right| = 0 \quad (3.39)$$

interatomic force constants

The calculation of the equilibrium configuration and of the vibrational properties of the system need to compute the first and the second derivative [67], respectively, of the Born-Oppenheimer energy surface $E(\mathbf{R})$.

$$\frac{\partial E(\mathbf{R})}{\partial \mathbf{R}_i} = \int \frac{\partial V_{\mathbf{R}}(\mathbf{r})}{\partial \mathbf{R}_i} n_{\mathbf{R}}(\mathbf{r}) d\mathbf{r}, \quad (3.40)$$

$$\frac{\partial^2 E(\mathbf{R})}{\partial \mathbf{R}_i \partial \mathbf{R}_j} = \int \frac{\partial^2 V_{\mathbf{R}}(\mathbf{r})}{\partial \mathbf{R}_i \partial \mathbf{R}_j} n_{\mathbf{R}}(\mathbf{r}) d\mathbf{r} + \int \frac{\partial V_{\mathbf{R}}(\mathbf{r})}{\partial \mathbf{R}_i} \frac{\partial n_{\mathbf{R}}(\mathbf{r})}{\partial \mathbf{R}_j} d\mathbf{r} \quad (3.41)$$

linear response
 $\frac{\partial n_{\mathbf{R}}(\mathbf{r})}{\partial \mathbf{R}_j}$

where the derivative of the ion-ion electrostatic interaction is assumed constant. The calculation of the matrix interatomic force constants, Eq. (3.39), the calculation of the ground-state electronic charge density $n_{\mathbf{R}}(\mathbf{r})$ and its *linear response* to a distortion of the ion configuration, $\frac{\partial n_{\mathbf{R}}(\mathbf{r})}{\partial \mathbf{R}_j}$. The linear response can be computed within the perturbative version of the density functional

theory (DFT), usually referred as *density functional perturbation theory* (DFPT) [68, 69]. Through the linearization of the Kohn-Sham Eqs. (3.9), (3.10), and (3.7) with respect to wave function, density, and potential variations. Linearization of the charge density $n(\mathbf{r})$ leads to

$$\nabla_{\mathbf{R}}n(\mathbf{r}) = 2\text{Re} \sum_n \psi_n^*(\mathbf{r}) \nabla_{\mathbf{R}}\psi_n(\mathbf{r}) \quad (3.42)$$

By using the standard first-order perturbation theory, the variation of the Kohn-Sham unperturbed orbitals $\psi_n(\mathbf{r})$ is given by

$$\left(-\frac{1}{2}\nabla^2 + V_{\text{KS}} - \varepsilon_n\right) \nabla_{\mathbf{R}}\psi_n(\mathbf{r}) = -(\nabla_{\mathbf{R}}V_{\text{KS}} - \nabla_{\mathbf{R}}\varepsilon_n) \psi_n(\mathbf{r}) \quad (3.43)$$

Here,

$$\nabla_{\mathbf{R}}V_{\text{KS}}(\mathbf{r}) = \nabla_{\mathbf{R}}V^{\text{ext}}(\mathbf{r}) + \frac{1}{2} \int d\mathbf{r}' \frac{\nabla_{\mathbf{R}}n(\mathbf{r}')}{|\mathbf{r} - \mathbf{r}'|} + \left. \frac{dv_{\text{xc}}(n)}{dn} \right|_{n=n(\mathbf{r})} \nabla_{\mathbf{R}}n(\mathbf{r}) \quad (3.44)$$

is the first-order correction to the Kohn-Sham potential, and

$$\nabla_{\mathbf{R}}\varepsilon_n = \langle \psi_n | \nabla_{\mathbf{R}}V_{\text{KS}}(\mathbf{r}) | \psi_n \rangle \quad (3.45)$$

is the first-order variation of the Kohn-Sham eigenvalues. The knowledge of the first-order derivative of the wave functions is, hence, enough to compute the second-order derivative of the energy. This is a special case of the $(2n + 1)$ theorem [70], which states that the knowledge of the n^{th} -order derivative of the wave functions allows the calculation of derivative of the energy up to the $(2n + 1)^{\text{th}}$ -order. The set of self-consistent Eqs. (3.42), (3.44), and (3.45) for the perturbed system are analogous to the Kohn-Sham equation for the unperturbed case, Eqs. (3.9), (3.10), and (3.7).

CONTINUUM MECHANICS AND NONLINEAR
ELASTICITY

“ I try not to break the rules but merely to test their elasticity.”
Bill Veeck (American Baseball Player, 1914-1986)

Contents

4.1	Lagrangian versus Eulerian formalism	35
4.2	Finite Strain Theory	38
4.3	Stress Theory	41
4.4	The Continuity equation	46
4.5	Balance equations	46
4.5.1	The Euler description	46
4.5.2	The Lagrange description	48
4.6	Nonlinear constitutive equations	50
4.7	The small-strain approximation	53
4.8	The Stiffness tensor and the Elastic moduli in two-dimensional systems.	60
4.9	The virial stress tensor	66
4.9.1	Physical meaning of the virial stress	70
4.9.2	The atomistic nonlinear Cauchy stress	71
4.9.3	Atomic stress for two-body interac- tions	72

In this Chapter we introduce the basic formalism of the continuum theory of elasticity, summarizing its foundation and key concepts. We also discuss some general features regarding the elastic theory in two dimensional systems.

4.1 LAGRANGIAN VERSUS EULERIAN FORMALISM

The motion of a body is typically referred to a reference configuration $\Omega_0 \subset \mathbb{R}^3$, which is often chosen to be the undeformed configuration. After the deformation the body occupies the current configuration $\Omega_t \subset \mathbb{R}^3$. Thus, the current coordinates ($\mathbf{x} \in \Omega_t$) are expressed in terms of the reference coordinates ($\mathbf{X} \in \Omega_0$):

$$\mathbf{X} \mapsto \mathbf{x} = \mathcal{F}_t(\mathbf{X}) \quad (4.1)$$

where \mathcal{F}_t is the transformation function at any time t (see Fig. 4.1). More explicitly, it means that

$$\begin{aligned} x_1 &= x_1(X_1, X_2, X_3, t) \\ x_2 &= x_2(X_1, X_2, X_3, t) \\ x_3 &= x_3(X_1, X_2, X_3, t) \end{aligned} \quad (4.2)$$

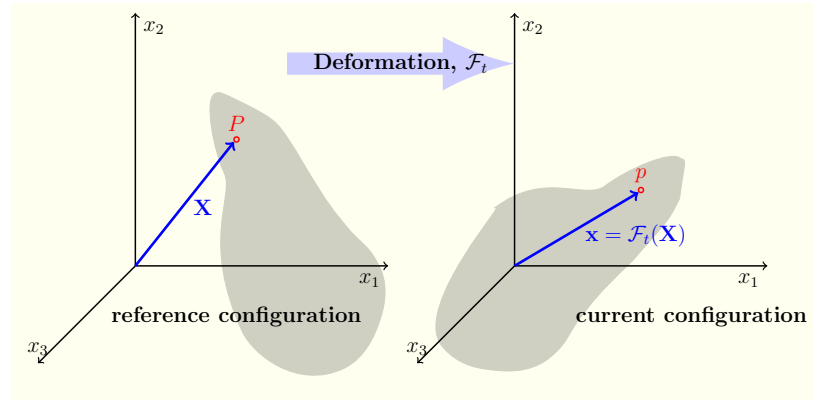


Figure 4.1: Reference configuration and current configuration after a deformation.

We call the set $(\mathbf{X}$ and t) Lagrangian coordinates, named after Joseph Louis Lagrange [1736-1813], or material coordinates, or reference coordinates. The application of these coordinates is called Lagrangian description or reference description. We can obtain also the inverse function of Eq. (4.1) in the form

Lagrangian reference coordinates

$$\mathbf{x} \mapsto \mathbf{X} = \mathcal{F}_t^{-1}(\mathbf{x}) \tag{4.3}$$

or, in components

$$\begin{aligned} X_1 &= X_1(x_1, x_2, x_3, t) \\ X_2 &= X_2(x_1, x_2, x_3, t) \\ X_3 &= X_3(x_1, x_2, x_3, t) \end{aligned} \tag{4.4}$$

Eulerian space coordinate

The set $\{\mathbf{x}, t\}$ is called Eulerian coordinates, named after Leonhard Euler [1707-1783], or space coordinates, and their application is said Eulerian description or spatial description. The Lagrangian coordinates were introduced by Euler in 1762, while Jean le Rond D’Alembert [1717-1783] was the first to use the Eulerian coordinates in 1752. In general Continuum Mechanics Lagrangian coordinates and the reference description are the most common. The same holds true in solid Mechanics. However, in Fluid Mechanics, due to large displacements and complex deformations, it is usually necessary and most practical to use Eulerian coordinates and spatial description. One of the key quantities in deformation analysis is the deformation gradient of Ω_t relative to the reference configuration Ω_0 , denoted $\hat{\mathbf{F}}$, which gives the relationship of a material line $d\mathbf{X}$ before deformation to the line $d\mathbf{x}$ (consisting of the same material as $d\mathbf{X}$) after deformation. It is defined as

Deformation gradient

$$\mathbf{x} = \mathcal{F}_t(\mathbf{X}) : \hat{\mathbf{F}}(\mathbf{X}, t) = \nabla_{\mathbf{X}} \mathcal{F}_t(\mathbf{X}) \Rightarrow d\mathbf{x} = \hat{\mathbf{F}}(\mathbf{X}, t) d\mathbf{X} \tag{4.5}$$

Its components are given by

$$F_{iK} = \frac{\partial x_i}{\partial X_K}, \quad \forall (i, K) \in \{1, 2, 3\}^2 \quad (4.6)$$

As before, we can define a deformation gradient \hat{G} of the inverse function relating Ω_0 to the current configuration Ω_t

$$\mathbf{X} = \mathcal{F}_t^{-1}(\mathbf{x}) : \hat{G}(\mathbf{x}, t) = \nabla_{\mathbf{x}} \mathcal{F}_t^{-1}(\mathbf{x}) \Rightarrow d\mathbf{X} = \hat{G}(\mathbf{x}, t) d\mathbf{x} \quad (4.7)$$

In components, it assumes the form

$$G_{Ki} = \frac{\partial X_K}{\partial x_i}, \quad \forall (i, K) \in \{1, 2, 3\}^2 \quad (4.8)$$

The tensors \hat{F} and \hat{G} are related by the relationships

$$\hat{G}(\mathcal{F}_t(\mathbf{X}), t) = \hat{F}^{-1}(\mathbf{X}, t) \quad (4.9)$$

$$\hat{F}(\mathcal{F}_t^{-1}(\mathbf{x}), t) = \hat{G}^{-1}(\mathbf{x}, t) \quad (4.10)$$

Here, \hat{F} is a Lagrangian tensor while \hat{G} is an Eulerian tensor. The velocity and acceleration fields, related to the trajectory of the particle starting at \mathbf{X} (Lagrangian description) are given by

*Velocity and
acceleration fields*

$$\mathbf{v}(\mathbf{X}, t) = \frac{\partial \mathbf{x}}{\partial t}(\mathbf{X}, t) \quad (4.11)$$

$$\mathbf{a}(\mathbf{X}, t) = \frac{\partial^2 \mathbf{x}}{\partial t^2}(\mathbf{X}, t) \quad (4.12)$$

On the other hand, the velocity and acceleration fields in the Euler description are given by

$$\mathbf{v}(\mathbf{x}, t) = \frac{\partial \mathbf{x}}{\partial t}(\mathcal{F}_t^{-1}(\mathbf{x}), t) \quad (4.13)$$

$$\mathbf{a}(\mathbf{x}, t) = \frac{\partial^2 \mathbf{x}}{\partial t^2}(\mathcal{F}_t^{-1}(\mathbf{x}), t) \quad (4.14)$$

Any time-dependent scalar, vector, or tensor field can be regarded as a function of (\mathbf{X}, t) (Lagrangian or material variables) or (\mathbf{x}, t) (Eulerian or spatial variables) whenever the motion $\mathbf{x} = \mathcal{F}_t(\mathbf{X})$ is given. For example, for a scalar field we can write $\phi(\mathbf{x}, t) = \Phi(\mathbf{X}, t)$ where

$$\Phi(\mathbf{X}, t) = \phi(\mathcal{F}_t(\mathbf{X}), t) \quad (4.15)$$

The time derivative of the field $\Phi(\mathbf{X}, t)$ can be calculated as

$$\frac{\partial \Phi}{\partial t} = \frac{\partial \phi}{\partial t} + \frac{\partial \phi}{\partial \mathbf{x}} \cdot \frac{\partial \mathbf{x}}{\partial t} = \frac{\partial \phi}{\partial t} + \frac{\partial \phi}{\partial \mathbf{x}} \cdot \mathbf{v} \quad (4.16)$$

Instead of using different symbols for the quantities (i.e. ϕ and Φ) in the Lagrangian and Eulerian descriptions, we can use the dot for the Lagrangian or material derivative ($\dot{\phi}$) and the partial

differentiation symbol ($\frac{\partial \phi}{\partial t}$) for the Eulerian or spatial derivative. Therefore, Eq. (4.16) assumes the simpler form

$$\dot{\phi} = \frac{\partial \phi}{\partial t} + \frac{\partial \phi}{\partial \mathbf{x}} \cdot \mathbf{v} \quad (4.17)$$

The Eulerian tensor

$$\hat{\mathbf{L}} = \frac{\partial \mathbf{v}}{\partial \mathbf{x}} \quad (4.18)$$

with components

$$L_{ij} = \frac{\partial v_i}{\partial x_j} \quad (4.19)$$

satisfies the important relation

$$\dot{\hat{\mathbf{F}}} = \hat{\mathbf{L}}\hat{\mathbf{F}} \quad (4.20)$$

It can be proved as follows

$$\dot{\hat{\mathbf{F}}} = \frac{\partial}{\partial t} \frac{\partial}{\partial \mathbf{X}} \mathcal{F}_t(\mathbf{X}) = \frac{\partial}{\partial \mathbf{X}} \frac{\partial}{\partial t} \mathcal{F}_t(\mathbf{X}) = \frac{\partial \mathbf{v}}{\partial \mathbf{X}} = \frac{\partial \mathbf{v}}{\partial \mathbf{x}} \frac{\partial \mathbf{x}}{\partial \mathbf{X}} = \hat{\mathbf{L}}\hat{\mathbf{F}} \quad (4.21)$$

It is also important an inverse relation given by

$$\dot{\hat{\mathbf{F}}}^{-1} = -\hat{\mathbf{G}}\hat{\mathbf{L}} \quad (4.22)$$

Since $\frac{d}{dt}(\hat{\mathbf{F}}^{-1}\hat{\mathbf{F}}) = 0$ we have $\dot{\hat{\mathbf{F}}}^{-1} = -\hat{\mathbf{F}}^{-1}\dot{\hat{\mathbf{F}}}\hat{\mathbf{F}}^{-1}$ (where $\dot{\hat{\mathbf{F}}}^{-1}$ represents the Lagrangian time derivative of the inverse of $\hat{\mathbf{F}}$) and, therefore, we obtain the proof of Eq. (4.22)

$$\dot{\hat{\mathbf{F}}}^{-1} = -\hat{\mathbf{F}}^{-1}\dot{\hat{\mathbf{F}}}\hat{\mathbf{F}}^{-1} = -\hat{\mathbf{F}}^{-1}\hat{\mathbf{L}}\hat{\mathbf{F}}\hat{\mathbf{F}}^{-1} = -\hat{\mathbf{F}}^{-1}\hat{\mathbf{L}} = -\hat{\mathbf{G}}\hat{\mathbf{L}} \quad (4.23)$$

4.2 FINITE STRAIN THEORY

The measure of the deformation between the reference and the current configuration is an important topic in continuum mechanics and it can be performed in several ways. The starting quantity is the deformation gradient $\hat{\mathbf{F}}(\mathbf{X})$ (in the Lagrangian formalism) or its inverse $\hat{\mathbf{G}}(\mathbf{x})$ (in the Eulerian formalism). We consider two infinitesimal vectors $d\mathbf{X}$ and $d\mathbf{Y}$ in Ω_0 and their deformed versions $d\mathbf{x}$ and $d\mathbf{y}$ in Ω_t (see Fig. 4.2 for the deformation of $d\mathbf{X}$). The changes of lengths and angles are controlled by the scalar product of the vectors and, therefore, we define the right and the left Cauchy tensors $\hat{\mathbf{C}}$ and $\hat{\mathbf{B}}$ in order to obtain $d\mathbf{x} \cdot d\mathbf{y} = d\mathbf{X} \cdot \hat{\mathbf{C}}d\mathbf{Y}$ or $d\mathbf{X} \cdot d\mathbf{Y} = d\mathbf{x} \cdot \hat{\mathbf{B}}^{-1}d\mathbf{y}$ (see Table 4.1). The variations of the scalar product (moving from the reference to the current configuration) are described by the Green-Lagrange strain tensor $\hat{\eta}$ and by the Almansi-Eulero strain tensor $\hat{\epsilon}$ as summarized in Table 4.1.

Moreover, the gradients of the displacements field $\mathbf{u}(\mathbf{X})$ and $\mathbf{u}(\mathbf{x})$ are defined by $\hat{\mathbf{J}}_L = \frac{\partial \mathbf{u}}{\partial \mathbf{X}}$ and $\hat{\mathbf{J}}_E = \frac{\partial \mathbf{u}}{\partial \mathbf{x}}$ in the Lagrangian

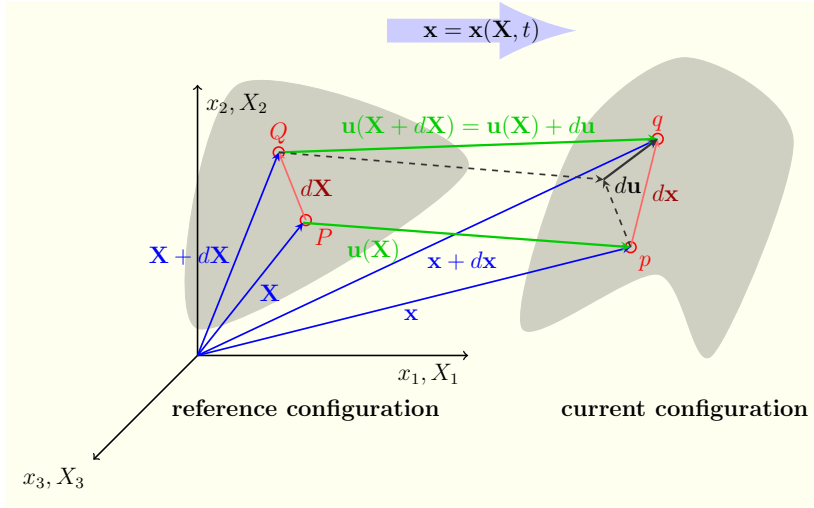


Figure 4.2: Infinitesimal vector $d\mathbf{X}$ in Ω_0 and its deformed version $d\mathbf{x}$ in Ω_t .

and Eulerian vision, respectively. In Table 4.2 we can find: *i*) the effective variation of length for the vector $d\mathbf{X} = \mathbf{N}\|d\mathbf{X}\|$ deformed into $d\mathbf{x} = \mathbf{n}\|d\mathbf{x}\|$; *ii*) the variation of the right angle between the unit vectors \mathbf{N} and \mathbf{T} ($\mathbf{N} \cdot \mathbf{T} = 0$ in Ω_0) deformed into \mathbf{n} and \mathbf{t} (in Ω_t): $\theta_{\mathbf{n}\mathbf{t}}$ is the angle in Ω_t and, therefore, $\gamma_{\mathbf{N}\mathbf{T}} = \frac{\pi}{2} - \theta_{\mathbf{n}\mathbf{t}}$ is the angle variation (with opposite sign); *iii*) the variation of the right angle between the unit vectors \mathbf{n} and \mathbf{t} ($\mathbf{n} \cdot \mathbf{t} = 0$ in Ω_t) originally placed at \mathbf{N} and \mathbf{T} (in Ω_0): $\theta_{\mathbf{N}\mathbf{T}}$ is the angle in Ω_0 and, therefore, $\gamma_{\mathbf{n}\mathbf{t}} = \theta_{\mathbf{N}\mathbf{T}} - \frac{\pi}{2}$ is the angle variation (with opposite sign); *iv*) the variations of volume and surface measures.

Any non singular tensor (describing a deformation) can be decomposed in two different ways

$$\hat{\mathbf{F}} = \hat{\mathbf{R}} \hat{\mathbf{U}} = \hat{\mathbf{V}} \hat{\mathbf{R}} \tag{4.24}$$

where $\hat{\mathbf{R}}$ is a rotation matrix ($\hat{\mathbf{R}}\hat{\mathbf{R}}^T = \hat{\mathbf{R}}^T\hat{\mathbf{R}} = \hat{\mathbf{I}}$) while $\hat{\mathbf{U}}$ and $\hat{\mathbf{V}}$ are symmetric and positive definite tensors. In order to prove this polar decomposition theorem due to Cauchy, we use the right Cauchy tensor $\hat{\mathbf{C}} = \hat{\mathbf{F}}^T\hat{\mathbf{F}}$: it is symmetric since $(\hat{\mathbf{F}}^T\hat{\mathbf{F}})^T = \hat{\mathbf{F}}^T\hat{\mathbf{F}}^{TT} = \hat{\mathbf{F}}^T\hat{\mathbf{F}}$ and it is positive definite as proved by the following relation

$$\mathbf{w}^T \hat{\mathbf{F}}^T \hat{\mathbf{F}} \mathbf{w} = (\hat{\mathbf{F}}\mathbf{w})^T (\hat{\mathbf{F}}\mathbf{w}) = \|\hat{\mathbf{F}}\mathbf{w}\| \geq 0 \quad \forall \mathbf{w} \tag{4.25}$$

If $\hat{\mathbf{F}}^T\hat{\mathbf{F}}$ is symmetric and positive definite then it can be diagonalized in the field of real numbers. Therefore, we can write $\hat{\mathbf{F}}^T\hat{\mathbf{F}} = \hat{\mathbf{Q}}^{-1}\hat{\Delta}\hat{\mathbf{Q}}$ where $\hat{\mathbf{Q}}$ is non singular and $\hat{\Delta}$ is diagonal. We define

$$\hat{\mathbf{U}} = \sqrt{\hat{\mathbf{F}}^T\hat{\mathbf{F}}} = \sqrt{\hat{\mathbf{C}}} \tag{4.26}$$

*Polar decomposition
Cauchy theorem*

Table 4.1: Strains definitions and properties in Lagrangian and Eulerian formalisms.

Lagrangian vision	Eulerian vision
Right Cauchy tensor	Left Cauchy tensor
$\hat{C} = \hat{F}^T \hat{F}$	$\hat{B} = \hat{F} \hat{F}^T$
$\hat{C}^{-1} = \hat{G} \hat{G}^T$	$\hat{B}^{-1} = \hat{G}^T \hat{G}$
$d\mathbf{x} \cdot d\mathbf{y} = d\mathbf{X} \cdot \hat{C} d\mathbf{Y}$	$d\mathbf{X} \cdot d\mathbf{Y} = d\mathbf{x} \cdot \hat{B}^{-1} d\mathbf{y}$
Green-Lagrange tensor	Almansi-Eulero tensor
$\hat{\eta} = \frac{1}{2} (\hat{C} - \hat{I})$	$\hat{e} = \frac{1}{2} (\hat{I} - \hat{B}^{-1})$
$d\mathbf{x} \cdot d\mathbf{y} - d\mathbf{X} \cdot d\mathbf{Y} = 2d\mathbf{X} \cdot \hat{\eta} d\mathbf{Y}$	$d\mathbf{x} \cdot d\mathbf{y} - d\mathbf{X} \cdot d\mathbf{Y} = 2d\mathbf{x} \cdot \hat{e} d\mathbf{y}$
Lagrange displacement gradient	Eulero displacement gradient
$\hat{J}_L = \frac{\partial \mathbf{u}}{\partial \mathbf{X}}$	$\hat{J}_E = \frac{\partial \mathbf{u}}{\partial \mathbf{x}}$
$\hat{F} = \hat{I} + \hat{J}_L$	$\hat{F}^{-1} = \hat{I} - \hat{J}_E$
$\hat{C} = \hat{I} + \hat{J}_L + \hat{J}_L^T + \hat{J}_L^T \hat{J}_L$	$\hat{B}^{-1} = \hat{I} - \hat{J}_E - \hat{J}_E^T + \hat{J}_E^T \hat{J}_E$
$\hat{\eta} = \frac{1}{2} (\hat{J}_L + \hat{J}_L^T + \hat{J}_L^T \hat{J}_L)$	$\hat{e} = \frac{1}{2} (\hat{J}_E + \hat{J}_E^T - \hat{J}_E^T \hat{J}_E)$

The square root of the tensor can be defined (and calculated) as follows

$$\hat{U} = \sqrt{\hat{F}^T \hat{F}} = \sqrt{\hat{Q}^{-1} \hat{\Delta} \hat{Q}} = \hat{Q}^{-1} \sqrt{\hat{\Delta}} \hat{Q} \quad (4.27)$$

in fact

$$\begin{aligned} \left(\hat{Q}^{-1} \sqrt{\hat{\Delta}} \hat{Q} \right)^2 &= \hat{Q}^{-1} \sqrt{\hat{\Delta}} \hat{Q} \hat{Q}^{-1} \sqrt{\hat{\Delta}} \hat{Q} \\ &= \hat{Q}^{-1} \sqrt{\hat{\Delta}} \sqrt{\hat{\Delta}} \hat{Q} = \hat{Q}^{-1} \hat{\Delta} \hat{Q} \end{aligned} \quad (4.28)$$

where $\sqrt{\hat{\Delta}} = \text{diag}(\sqrt{\lambda_i})$ if $\hat{\Delta} = \text{diag}(\lambda_i)$ (the symbol diag explicitly indicates the entries of a diagonal matrix). Finally, we define $\hat{R} = \hat{F} \hat{U}^{-1}$ and we verify its orthogonality

$$\hat{R}^T \hat{R} = (\hat{U}^{-1})^T \hat{F}^T \hat{F} \hat{U}^{-1} = (\hat{U}^{-1})^T \hat{U}^2 \hat{U}^{-1} = \hat{U}^{-1} \hat{U} \hat{U} \hat{U}^{-1} = \hat{I} \quad (4.29)$$

This concludes the proof of the first polar decomposition. We have to prove the unicity of the right decomposition $\hat{F} = \hat{R} \hat{U}$. We can suppose the two different decompositions $\hat{F} = \hat{R} \hat{U} = \hat{R}^* \hat{U}^*$ exist. It follows that $\hat{F}^T \hat{F} = \hat{U}^2 = \hat{U}^{*2}$ from which $\hat{U} = \hat{U}^*$ and, therefore, $\hat{R} = \hat{R}^*$. It proves the unicity of the right decomposition. Similarly we can obtain the left decomposition by defining $\hat{V} =$

Table 4.2: Variations measure in Lagrangian and Eulerian formalisms.

Lagrangian vision	Eulerian vision
Lagrangian length variation	Eulerian length variation
$\mathbf{N} = \frac{d\mathbf{X}}{\ d\mathbf{X}\ }$ $\epsilon_{NN} = \frac{\ dx\ - \ d\mathbf{X}\ }{\ d\mathbf{X}\ } = \sqrt{\mathbf{N} \cdot \hat{\mathbf{C}} \mathbf{N}} - 1$ $\epsilon_{NN} + \frac{1}{2} \epsilon_{NN}^2 = \mathbf{N} \cdot \hat{\eta} \mathbf{N}$	$\mathbf{n} = \frac{dx}{\ dx\ }$ $\epsilon_{nn} = \frac{\ dx\ - \ d\mathbf{X}\ }{\ dx\ } = 1 - \sqrt{\mathbf{n} \cdot \hat{\mathbf{B}}^{-1} \mathbf{n}}$ $\epsilon_{nn} - \frac{1}{2} \epsilon_{nn}^2 = \mathbf{n} \cdot \hat{\epsilon} \mathbf{n}$
Lagrangian angle variation	Eulerian angle variation
$\mathbf{N} \cdot \mathbf{T} = 0$ $\gamma_{NT} = \frac{\pi}{2} - \theta_{nt}$ $\sin(\gamma_{NT}) = \frac{2\mathbf{N} \cdot \hat{\eta} \mathbf{T}}{\sqrt{\mathbf{N} \cdot \hat{\mathbf{C}} \mathbf{N}} \sqrt{\mathbf{T} \cdot \hat{\mathbf{C}} \mathbf{T}}}$	$\mathbf{n} \cdot \mathbf{t} = 0$ $\gamma_{nt} = \theta_{NT} - \frac{\pi}{2}$ $\sin(\gamma_{nt}) = \frac{2\mathbf{n} \cdot \hat{\epsilon} \mathbf{t}}{\sqrt{\mathbf{n} \cdot \hat{\mathbf{B}}^{-1} \mathbf{n}} \sqrt{\mathbf{t} \cdot \hat{\mathbf{B}}^{-1} \mathbf{t}}}$
Lagrangian volume variation	Eulerian volume variation
$J = \det(\hat{\mathbf{F}})$ $\Theta_V = \frac{dv - dV}{dV} = J - 1$	$J^{-1} = \det(\hat{\mathbf{G}})$ $\Theta_v = \frac{dv - dV}{dv} = 1 - \frac{1}{J}$
Lagrangian surface variation	Eulerian surface variation
$\mathbf{N} dS = J^{-1} \hat{\mathbf{F}}^T \mathbf{n} ds$ $\Theta_N = \frac{\ \mathbf{n} ds\ - \ \mathbf{N} dS\ }{\ \mathbf{N} dS\ }$ $\Theta_N = J \sqrt{\mathbf{N} \cdot \hat{\mathbf{C}}^{-1} \mathbf{N}} - 1$	$\mathbf{n} ds = J \hat{\mathbf{F}}^{-T} \mathbf{N} dS$ $\Theta_n = \frac{\ \mathbf{n} ds\ - \ \mathbf{N} dS\ }{\ \mathbf{n} ds\ }$ $\Theta_n = 1 - J^{-1} \sqrt{\mathbf{n} \cdot \hat{\mathbf{B}} \mathbf{n}}$

$\sqrt{\hat{\mathbf{F}} \hat{\mathbf{F}}^T} = \sqrt{\hat{\mathbf{B}}}$: it is possible to prove that it is symmetric and positive definite and we define $\hat{\mathbf{R}}' = \hat{\mathbf{V}}^{-1} \hat{\mathbf{F}}$, which is orthogonal.

To conclude we must verify that $\hat{\mathbf{R}}' = \hat{\mathbf{R}}$. Since $\hat{\mathbf{R}}' (\hat{\mathbf{R}}')^T = \hat{\mathbf{I}}$ we have $\hat{\mathbf{F}} = \hat{\mathbf{V}} \hat{\mathbf{R}}' = \hat{\mathbf{R}}' (\hat{\mathbf{R}}')^T \hat{\mathbf{V}} \hat{\mathbf{R}}'$. The unicity of the right decomposition ($\hat{\mathbf{F}} = \hat{\mathbf{R}} \hat{\mathbf{U}}$) allows us to affirm that $\hat{\mathbf{R}}' = \hat{\mathbf{R}}$ and that $\hat{\mathbf{U}} = \hat{\mathbf{R}}^T \hat{\mathbf{V}} \hat{\mathbf{R}}$. This completes the proof of the polar decomposition Cauchy theorem.

This decomposition implies that the deformation of a line element $d\mathbf{X}$ in the undeformed configuration onto dx in the deformed configuration, i.e. $dx = \hat{\mathbf{F}} d\mathbf{X}$ may be obtained either by first stretching the element by $\hat{\mathbf{U}}$ i.e. $dx' = \hat{\mathbf{U}} d\mathbf{X}$, followed by a rotation $\hat{\mathbf{R}}$, i.e. $dx = \hat{\mathbf{R}} dx'$ or, equivalently, by applying a rigid rotation $\hat{\mathbf{R}}$ first, i.e. $dx'' = \hat{\mathbf{R}} d\mathbf{X}$ followed later by a stretching $\hat{\mathbf{V}}$, i.e. $dx = \hat{\mathbf{V}} dx''$ (see Fig. 4.3).

4.3 STRESS THEORY

In continuum mechanics we must consider two systems of forces acting on a given region of a material body. They are dependent on the external fields acting on the elastic body and

The body forces

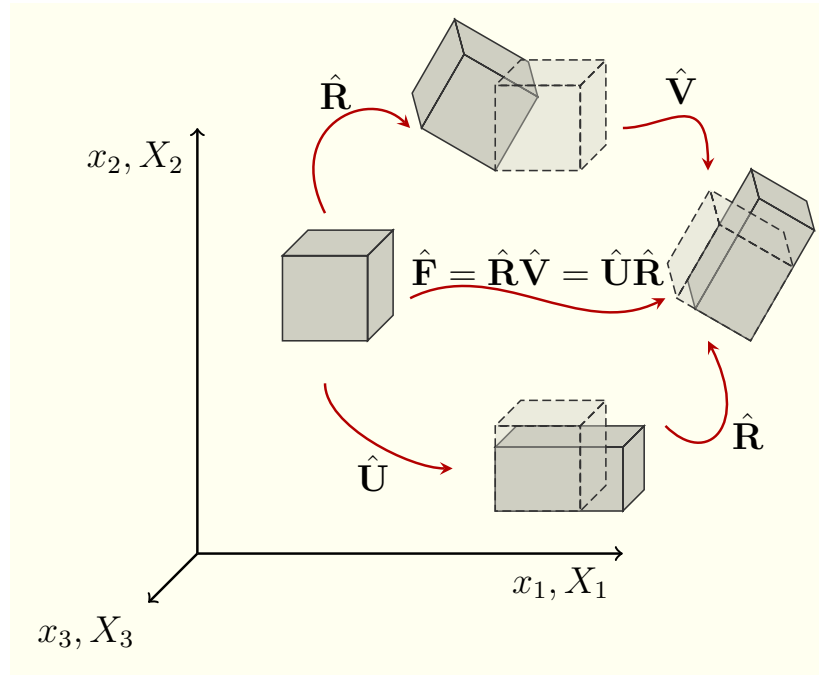


Figure 4.3: Polar decomposition applied to a given deformation.

they are described by the vector field $\mathbf{b}(\mathbf{x})$ representing their density on the volume in the current configuration. The physical meaning of such a density of forces can be summed up stating that the total force $d\mathbf{F}_v$ applied to a small volume dx centered on the point \mathbf{x} is given by $d\mathbf{F}_v = \mathbf{b}(\mathbf{x})dx$. A typical example is given by the gravitational forces proportional to the mass of the region under consideration. In this case we can write $d\mathbf{F}_v = \mathbf{g}dm$ where \mathbf{g} is the gravitational acceleration and dm is the mass of the volume dx . If we define $\rho = \frac{dm}{dx}$ as the density of the body, we simply obtain $\mathbf{b}(\mathbf{x}) = \rho\mathbf{g}$. In continuum mechanics we are additionally concerned with the interaction between neighboring portions of the interiors of deformable bodies. In reality such an interaction consists of complex interatomic forces, but we make the simplifying assumption that the effect of all such forces across any given surface may be adequately represented by a single vector field defined over the surface. It is important to observe that the nature of the forces exerted between two bodies in contact is identical to the nature of the actions applied between two portions of the same body, separated by an ideal surface.

In order to begin the mathematical descriptions of the forces, it is useful to introduce the following notation for the surface force $d\mathbf{F}_s$ applied to the area element ds (with unit normal vector \mathbf{n}) of the deformed configuration

$$d\mathbf{F}_s = \mathbf{f}(\mathbf{x}, \mathbf{n}, t) ds \quad (4.30)$$

The surface forces

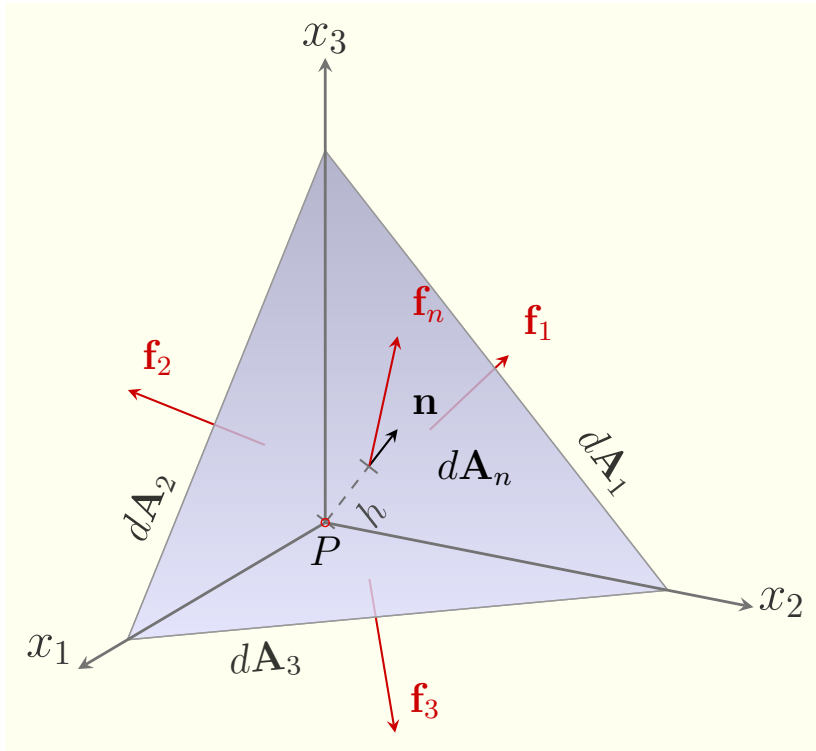


Figure 4.4: Cauchy tetrahedron on a generic point P.

where \mathbf{f} assumes the meaning of a density of forces distributed over the surface. By definition, the force $d\mathbf{F}_s$ is applied by the region where the unit vector \mathbf{n} is directed to the other region beyond the ideal surface (or interface). We can now recall the Cauchy theorem on the existence of the stress tensor describing the distribution of the surface forces in a given elastic body. More precisely, we can say that a tensor $\hat{\mathbf{T}}$ exists such that

The Cauchy theorem

$$\mathbf{f}(\mathbf{x}, \mathbf{n}, t) = \hat{\mathbf{T}}(\mathbf{x}, t)\mathbf{n} \tag{4.31}$$

where \mathbf{n} is the external normal unit vector to the surface delimiting the portion of body subjected to the force field \mathbf{f} . The quantity $\hat{\mathbf{T}}$ has been called Cauchy stress tensor or simply stress tensor. This very important result has been firstly published by Cauchy in 1827 in the text "Exercices de mathématique". The forces applied to the area element can be therefore written in the following form

Cauchy stress tensor

$$d\mathbf{F}_s = \hat{\mathbf{T}}(\mathbf{x})\mathbf{n}ds \tag{4.32}$$

or, considering the different components, $\frac{dF_{s,i}}{ds} = T_{ij}n_j$. The proof of the Cauchy theorem can be performed as follows.

We consider a generic point P in the deformed configuration and a small tetrahedron as described in Fig. 4.4. The oblique plane is defined by a unit vector \mathbf{n} and by the distance dh from P.

The faces of the tetrahedron have areas dA_1 , dA_2 , dA_3 and dA_n and the outgoing normal unit vectors are $-\mathbf{E}_1$, $-\mathbf{E}_2$, $-\mathbf{E}_3$ and \mathbf{n} (where the vectors \mathbf{E}_i belong to the reference base). We define \mathbf{f}_1 , \mathbf{f}_2 , \mathbf{f}_3 and \mathbf{f}_n as the surface forces acting on each face and \mathbf{b} as the body force distributed over the volume. The motion equation is

$$\mathbf{f}_n dA_n + \mathbf{f}_1 dA_1 + \mathbf{f}_2 dA_2 + \mathbf{f}_3 dA_3 + \mathbf{b} dv = \rho \mathbf{a} dv \quad (4.33)$$

where \mathbf{a} is the acceleration of the tetrahedron with mass ρdv . From Eq. (4.30) we can identify $\mathbf{f}_n = \mathbf{f}(\mathbf{n}, \mathbf{x}, t)$ and $\mathbf{f}_k = \mathbf{f}(-\mathbf{E}_k, \mathbf{x}, t)$, $\forall k = 1, 2, 3$. Moreover, $dA_i = n_i dA_n$, $\forall i = 1, 2, 3$ and $dv = \frac{1}{3} dA_n dh$, so we can write Eq. (4.33) as follows (sum over j)

$$\mathbf{f}(\mathbf{n}, \mathbf{x}, t) + \mathbf{f}(-\mathbf{E}_j, \mathbf{x}, t) n_j + \frac{1}{3} \mathbf{b} dh = \frac{1}{3} \rho \mathbf{a} dh \quad (4.34)$$

In the limit of $dh \rightarrow 0$ we obtain (sum over j)

$$\mathbf{f}(\mathbf{n}, \mathbf{x}, t) = -\mathbf{f}(-\mathbf{E}_j, \mathbf{x}, t) n_j \quad (4.35)$$

We can now use the previous result with $\mathbf{n} = \mathbf{E}_i$ (for any $i = 1, 2, 3$), by obtaining

$$\mathbf{f}(\mathbf{E}_i, \mathbf{x}, t) = -\mathbf{f}(-\mathbf{E}_i, \mathbf{x}, t) \quad (4.36)$$

This is a sort of third law of the dynamics written in term of surface forces. Now, Eq. (4.35) can be simply rewritten as (sum over j)

$$\mathbf{f}(\mathbf{n}, \mathbf{x}, t) = \mathbf{f}(\mathbf{E}_j, \mathbf{x}, t) n_j \quad (4.37)$$

This result shows that the surface force \mathbf{f} on a given plane is determined by the three surface forces on the three coordinate planes; in components

$$f_i(\mathbf{n}, \mathbf{x}, t) = \mathbf{f}(\mathbf{n}, \mathbf{x}, t) \cdot \mathbf{E}_i = \mathbf{f}(\mathbf{E}_j, \mathbf{x}, t) \cdot \mathbf{E}_i n_j = T_{ij} n_j \quad (4.38)$$

where the Cauchy stress $\hat{\mathbf{T}}$ is represented by $T_{ij} = \mathbf{f}(\mathbf{E}_j, \mathbf{x}, t) \cdot \mathbf{E}_i$. To better understand the physical meaning of the stress tensor we consider the cubic element of volume shown in Fig. 4.5, corresponding to an infinitesimal portion $dV = (dl)^3$ taken in an arbitrary solid body. The six faces of the cube have been numbered as shown in Fig. 4.5. We suppose that a stress $\hat{\mathbf{T}}$ is applied to that region: the T_{ij} component represents the pressure applied on the j^{th} face along the i^{th} direction.

The Cauchy stress tensor is the most natural and physical measure of the state of stress at a point in the deformed configuration and measured per unit area of the deformed configuration. It is the quantity most commonly used in spatial or Eulerian description of problems in continuum mechanics. Some other stress

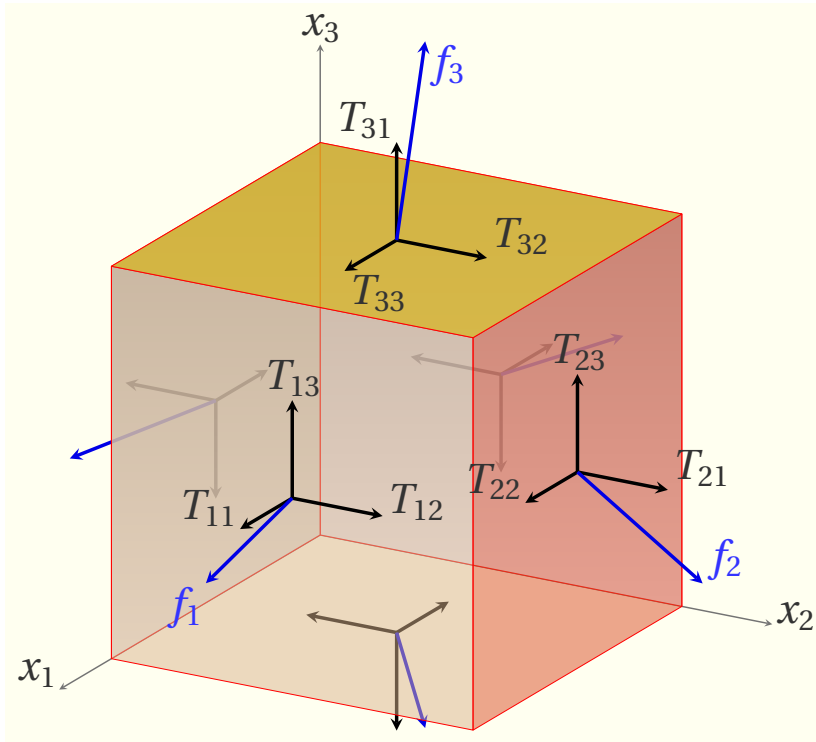


Figure 4.5: Geometrical representation of the stress tensor \hat{T} : the T_{ij} component represents the pressure applied on the j^{th} face of the cubic volume along the i^{th} direction.

measures must be introduced in order to describe continuum mechanics in the Lagrangian formalism. From Cauchy formula, we have $d\mathbf{F}_s = \hat{T}\mathbf{n}ds$, where \hat{T} is the Cauchy stress tensor. In a similar fashion, we introduce a stress tensor $\hat{T}^{1\mathcal{PK}}$, called the first Piola-Kirchhoff stress tensor, such that $d\mathbf{F}_s = \hat{T}^{1\mathcal{PK}}\mathbf{N}dS$. By using the Nanson formula $\mathbf{n}ds = \mathbf{J}\hat{\mathbf{F}}^{-T}\mathbf{N}dS$ we obtain

1st Piola-Kirchhoff stress tensor

$$d\mathbf{F}_s = \hat{T}\mathbf{J}\hat{\mathbf{F}}^{-T}\mathbf{N}dS = \hat{T}^{1\mathcal{PK}}\mathbf{N}dS \tag{4.39}$$

and therefore

$$\hat{T}^{1\mathcal{PK}} = \mathbf{J}\hat{\mathbf{T}}\hat{\mathbf{F}}^{-T} \tag{4.40}$$

Sometimes it is useful to introduce another state of stress $\hat{T}^{2\mathcal{PK}}$, called the second Piola-Kirchhoff stress tensor, defined as $\hat{\mathbf{F}}^{-1}d\mathbf{F}_s = \hat{T}^{2\mathcal{PK}}\mathbf{N}dS$. We simply obtain

2nd Piola-Kirchhoff stress tensor

$$\hat{\mathbf{F}}^{-1}d\mathbf{F}_s = \hat{\mathbf{F}}^{-1}\hat{\mathbf{T}}\mathbf{J}\hat{\mathbf{F}}^{-T}\mathbf{N}dS = \hat{T}^{2\mathcal{PK}}\mathbf{N}dS \tag{4.41}$$

and therefore

$$\hat{T}^{2\mathcal{PK}} = \mathbf{J}\hat{\mathbf{F}}^{-1}\hat{\mathbf{T}}\hat{\mathbf{F}}^{-T} = \hat{\mathbf{F}}^{-1}\hat{T}^{1\mathcal{PK}} \tag{4.42}$$

The stress tensors $\hat{T}^{1\mathcal{PK}}$ and $\hat{T}^{2\mathcal{PK}}$ will be very useful for the finite elasticity theory described within the Lagrangian formalism.

4.4 THE CONTINUITY EQUATION

*Balance equation of
the mass distribution*

The first balance equation of the continuum mechanics concerns the mass distribution. We define the mass density: we will use $\rho_0(\mathbf{X})$ in the Lagrangian formalism and $\rho(\mathbf{x}, t)$ in the Eulerian description. The total mass of the region \mathcal{P}_t is given by

$$m(\mathcal{P}_t) = \int_{\mathcal{P}_t} \rho(\mathbf{x}, t) d\mathbf{x} \quad (4.43)$$

The conservation of the mass gives

$$\int_{\mathcal{P}_t} \rho(\mathbf{x}, t) d\mathbf{x} = \int_{\mathcal{P}_0} \rho_0(\mathbf{X}) d\mathbf{X}, \quad \text{or} \quad \frac{d}{dt} \int_{\mathcal{P}_t} \rho(\mathbf{x}, t) d\mathbf{x} = 0 \quad (4.44)$$

The first equality in Eq. (4.44) can be also written

$$\int_{\mathcal{P}_0} \rho J d\mathbf{X} = \int_{\mathcal{P}_0} \rho_0 d\mathbf{X}, \quad (4.45)$$

and we simply obtain

$$\rho J = \rho_0 \quad (4.46)$$

On the other hand, from the second equality in Eq. (4.44) we have

$$\int_{\mathcal{P}_t} (\dot{\rho} + \rho \nabla_{\mathbf{x}} \cdot \mathbf{v}) d\mathbf{x} = \int_{\mathcal{P}_t} \left[\frac{\partial \rho}{\partial t} + \nabla_{\mathbf{x}} \cdot (\rho \mathbf{v}) \right] d\mathbf{x} = 0 \quad (4.47)$$

and therefore we obtain two forms of the continuity equation

$$\dot{\rho} + \rho \nabla_{\mathbf{x}} \cdot \mathbf{v} = 0 \quad (4.48)$$

$$\frac{\partial \rho}{\partial t} + \nabla_{\mathbf{x}} \cdot (\rho \mathbf{v}) = 0 \quad (4.49)$$

It is important for the following applications to evaluate expressions of this kind: $\frac{d}{dt} \int_{\mathcal{P}_t} \rho(\mathbf{x}, t) \Psi(\mathbf{x}, t) d\mathbf{x}$; to this aim we use the Reynolds theorem with $\phi = \rho \Psi$

$$\frac{d}{dt} \int_{\mathcal{P}_t} \rho \Psi d\mathbf{x} = \int_{\mathcal{P}_t} (\dot{\rho} \Psi + \rho \dot{\Psi} + \rho \Psi \nabla_{\mathbf{x}} \cdot \mathbf{v}) d\mathbf{x} = \int_{\mathcal{P}_t} \rho \dot{\Psi} d\mathbf{x} \quad (4.50)$$

It means that, when there is the density in the integrand, the time derivative must be applied directly to the function Ψ .

4.5 BALANCE EQUATIONS

4.5.1 *The Euler description*

The other two important balance equations can be derived by the principles of linear and angular momentum. When dealing with a system of particles, we can deduce from Newton's laws of

motion that the resultant of the external forces is equal to the rate of change of the total linear momentum of the system. By taking moments about a fixed point, we can also show that the resultant moment of the external forces is equal to the rate of change of the total moment of momentum. Here we define the linear and angular momentum density for a continuum and we introduce balance laws for these quantities. We consider a portion \mathcal{P}_t in a material body and we define \mathbf{P} as its linear momentum, \mathbf{F} as the resultant of the applied forces, \mathbf{L} as the total angular momentum and, finally, \mathbf{M} as the resultant moment of the applied forces. The standard principles for a system of particles can be written as follows

$$\frac{d\mathbf{P}}{dt} = \mathbf{F}, \quad \frac{d\mathbf{L}}{dt} = \mathbf{M} \quad (4.51)$$

We start with the first principle, applied to the portion of body contained to the region \mathcal{P}_t , limited by the closed surface $\partial\mathcal{P}_t$

$$\frac{d}{dt} \int_{\mathcal{P}_t} \rho \mathbf{v} dx = \int_{\partial\mathcal{P}_t} \hat{\mathbf{T}} \mathbf{n} ds + \int_{\mathcal{P}_t} \mathbf{b} dx \quad (4.52)$$

where we have utilized the decomposition of the forces (body forces and surface forces) as described in the previous section. The previous equation can be simplified by means of Eq. (4.50) and the divergence theorem, by obtaining

$$\int_{\mathcal{P}_t} \rho \dot{\mathbf{v}} dx = \int_{\mathcal{P}_t} \nabla_x \cdot \hat{\mathbf{T}} dx + \int_{\mathcal{P}_t} \mathbf{b} dx \quad (4.53)$$

Since the volume \mathcal{P}_t is arbitrary, we easily obtain the first balance equation for the elasticity theory (Eulerian description)

$$\nabla_x \cdot \hat{\mathbf{T}} + \mathbf{b} = \rho \dot{\mathbf{v}} \quad (4.54)$$

1st Eulerian balance equation for the elasticity theory

This is the basic linear momentum equation of continuum mechanics. We remark that the divergence of a tensor is applied on the second index; in fact, in components, we simply obtain

$$\frac{\partial T_{ji}}{\partial x_i} + b_j = \rho \dot{v}_j \quad (4.55)$$

Further, we observe that

$$\dot{\mathbf{v}} = \frac{\partial \mathbf{v}}{\partial t} + \frac{\partial \mathbf{v}}{\partial \mathbf{x}} \cdot \mathbf{v} = \frac{\partial \mathbf{v}}{\partial t} + \frac{1}{2} \nabla_x (\mathbf{v} \cdot \mathbf{v}) + (\nabla_x \wedge \mathbf{v}) \wedge \mathbf{v} \quad (4.56)$$

and, therefore Eq. (4.54) is equivalent to

$$\nabla_x \cdot \hat{\mathbf{T}} + \mathbf{b} = \rho \left[\frac{\partial \mathbf{v}}{\partial t} + \frac{\partial \mathbf{v}}{\partial \mathbf{x}} \cdot \mathbf{v} \right] \quad (4.57)$$

or

$$\nabla_x \cdot \hat{\mathbf{T}} + \mathbf{b} = \rho \left[\frac{\partial \mathbf{v}}{\partial t} + \frac{1}{2} \nabla_x (\mathbf{v} \cdot \mathbf{v}) + (\nabla_x \wedge \mathbf{v}) \wedge \mathbf{v} \right] \quad (4.58)$$

Now, we consider the principle of the angular momentum. For the region \mathcal{P}_t such a balance equation can be written in the following form

$$\frac{d}{dt} \int_{\mathcal{P}_t} \mathbf{x} \wedge \rho \mathbf{v} d\mathbf{x} = \int_{\partial \mathcal{P}_t} \mathbf{x} \wedge (\hat{\mathbf{T}} \mathbf{n}) ds + \int_{\mathcal{P}_t} \mathbf{x} \wedge \mathbf{b} d\mathbf{x} \quad (4.59)$$

As before, the surface integral can be simplified with the application of the divergence theorem, by obtaining, after some straightforward calculations

$$\int_{\partial \mathcal{P}_t} \mathbf{x} \times (\hat{\mathbf{T}} \mathbf{n}) ds = \int_{\mathcal{P}_t} \left[T_{kh} + x_h \frac{\partial T_{kp}}{\partial x_p} \right] \eta_{hkj} \mathbf{e}_j d\mathbf{x} \quad (4.60)$$

2nd Eulerian
balance equation

So, the second balance equation assumes the form

$$\int_{\mathcal{P}_t} \left\{ x_h \left[\rho \dot{v}_k - \frac{\partial T_{kp}}{\partial x_p} - b_k \right] - T_{kh} \right\} \eta_{hkj} \mathbf{e}_j d\mathbf{x} = 0 \quad (4.61)$$

The term in bracket is zero because of the first balance equation. Therefore, we obtain $\int_{\mathcal{P}_t} T_{kh} \eta_{hkj} \mathbf{e}_j d\mathbf{x} = 0$ or, equivalently, $T_{kh} \eta_{hkj} = 0$. Finally, the second principle leads to

$$T_{ij} = T_{ji} \quad (4.62)$$

In other words, we may state that the principle of the angular momentum assures the symmetry of the Cauchy stress tensor.

4.5.2 The Lagrange description

In finite elasticity theory the Lagrangian description is the most important point of view since it allows to determine the exact transformation $\mathbf{x} = \mathcal{F}_t(\mathbf{X})$ between the reference and the actual configurations. In the case of finite deformations (arbitrarily large), the Piola-Kirchhoff stress tensors above defined are used to express the stress relative to the reference configuration. This is in contrast to the Cauchy stress tensor which expresses the stress relative to the current configuration. In order to obtain the Lagrangian equations of motion it is useful to introduce the so-called Piola transformation $\mathbf{W}(\mathbf{X}, t)$ (which is a Lagrangian vector field) of a given Eulerian vector field $\mathbf{w}(\mathbf{x}, t)$

Piola transformation

$$\mathbf{w}(\mathbf{x}, t) \Rightarrow \mathbf{W}(\mathbf{X}, t) = J \hat{\mathbf{F}}^{-1} \mathbf{w}(\mathcal{F}_t(\mathbf{X}), t) \quad (4.63)$$

An important relation gives the relationship between the divergence of the two fields: of course, the divergence of $\mathbf{W}(\mathbf{X}, t)$ is calculated with respect to the Lagrangian variables \mathbf{X} while that of $\mathbf{w}(\mathbf{x}, t)$ is calculated with respect to the Eulerian variables \mathbf{x}

$$\begin{aligned} \nabla_{\mathbf{X}} \cdot \mathbf{W}(\mathbf{X}, t) &= \frac{\partial W_i}{\partial X_i} = \frac{\partial}{\partial X_i} \left(J \frac{\partial X_i}{\partial x_s} w_s \right) \\ &= \frac{\partial}{\partial X_i} \left(J \frac{\partial X_i}{\partial x_s} \right) w_s + J \frac{\partial X_i}{\partial x_s} \frac{\partial w_s}{\partial X_i} \end{aligned} \quad (4.64)$$

The first term is zero for the Piola identity given in Eq. (A.21), and therefore

$$\nabla_{\mathbf{X}} \cdot \mathbf{W}(\mathbf{X}, t) = J \frac{\partial X_i}{\partial x_s} \frac{\partial w_s}{\partial X_i} = J \frac{\partial w_s}{\partial x_s} \quad (4.65)$$

It means that we have obtained the important relation

$$\nabla_{\mathbf{X}} \cdot \mathbf{W}(\mathbf{X}, t) = J \nabla_{\mathbf{x}} \cdot \mathbf{w}(\mathbf{x}, t) \quad (4.66)$$

We can also make a Piola transformation on a given index of a tensor. For example, if T_{ji} the Cauchy stress tensor, we may use the above transformation on the last index. We apply this procedure to transform the motion equation from the Eulerian to the Lagrangian coordinates

$$\frac{\partial T_{ji}}{\partial x_i} + b_j = \rho v_j \Rightarrow \frac{1}{J} \frac{\partial}{\partial X_i} \left(J \frac{\partial X_i}{\partial x_s} T_{js} \right) + b_j = \rho v_j \quad (4.67)$$

or, identifying the deformation gradient

$$\frac{\partial}{\partial X_i} [J(\hat{\mathbf{F}}^{-1})_{is} T_{js}] + J b_j = \rho J v_j \quad (4.68)$$

By using the relation $\rho_0 = J\rho$ we obtain

$$\frac{\partial}{\partial X_i} [J T_{js} (\hat{\mathbf{F}}^{-T})_{si}] + \frac{\rho_0}{\rho} b_j = \rho_0 v_j \quad (4.69)$$

Since we have defined the first Piola-Kirchhoff stress tensor as $\hat{\mathbf{T}}^{1\mathcal{PK}} = J\hat{\mathbf{T}}\hat{\mathbf{F}}^{-T}$ we obtain

$$\nabla_{\mathbf{X}} \cdot \hat{\mathbf{T}}^{1\mathcal{PK}} + \frac{\rho_0}{\rho} \mathbf{b} = \rho_0 \dot{\mathbf{v}} \quad (4.70)$$

Now, we consider the principle of the angular momentum: since $\hat{\mathbf{T}} = \frac{1}{J} \hat{\mathbf{T}}^{1\mathcal{PK}} \hat{\mathbf{F}}^T$ and $\hat{\mathbf{T}} = \hat{\mathbf{T}}^T$ we obtain

$$\hat{\mathbf{T}}^{1\mathcal{PK}} \hat{\mathbf{F}}^T = (\hat{\mathbf{F}}) \hat{\mathbf{T}}^{1\mathcal{PK}T} \quad (4.71)$$

These two important results can be also expressed in terms of the second Piola-Kirchhoff stress tensor $\hat{\mathbf{T}}^{2\mathcal{PK}} = \hat{\mathbf{F}}^{-1} \hat{\mathbf{T}}^{1\mathcal{PK}}$. We simply obtain the linear momentum balance

$$\nabla_{\mathbf{X}} \cdot (\hat{\mathbf{F}} \hat{\mathbf{T}}^{2\mathcal{PK}}) + \frac{\rho_0}{\rho} \mathbf{b} = \rho_0 \dot{\mathbf{v}} \quad (4.72)$$

and the angular momentum balance

$$\hat{\mathbf{T}}^{2\mathcal{PK}} = (\hat{\mathbf{T}}^{2\mathcal{PK}})^T \quad (4.73)$$

Of course, Eqs. (4.72) and (4.73) must be completed by the constitutive equations and by the boundary conditions.

4.6 NONLINEAR CONSTITUTIVE EQUATIONS

The constitutive equations represent the relation between the stress and the strain and, therefore, they depend on the material under consideration. Here we prove that there is a strong conceptual connection between the constitutive equations and the energy balance for a continuum body. We start from the motion equation in the Eulerian formalism and we multiply both sides to the velocity component v_j

$$v_j \frac{\partial T_{ji}}{\partial x_i} + v_j b_j = \rho v_j \dot{v}_j \quad (4.74)$$

This expression can also be written as

$$\frac{\partial (v_j T_{ji})}{\partial x_i} - T_{ji} \frac{\partial v_j}{\partial x_i} + v_j b_j = \rho v_j \dot{v}_j \quad (4.75)$$

The Eulerian velocity gradient $L_{ji} = \frac{\partial v_j}{\partial x_i}$ can be decomposed in the symmetric and skew-symmetric parts

$$L_{ji} = \frac{\partial v_j}{\partial x_i} = \underbrace{\frac{1}{2} \left(\frac{\partial v_j}{\partial x_i} + \frac{\partial v_i}{\partial x_j} \right)}_{\text{symmetric}} + \underbrace{\frac{1}{2} \left(\frac{\partial v_j}{\partial x_i} - \frac{\partial v_i}{\partial x_j} \right)}_{\text{skew-symmetric}} = D_{ji} + W_{ji} \quad (4.76)$$

where \hat{D} is the rate of deformation tensor and \hat{W} is the spin tensor. Therefore, the energy balance equation assumes the local form

The local form of the Energy Balance Equation

$$\frac{\partial (v_j T_{ji})}{\partial x_i} - T_{ji} D_{ji} + v_j b_j = \rho v_j \dot{v}_j \quad (4.77)$$

By using the property in Eq. (4.50) we also obtain the global version on the region \mathcal{P}_t

$$\frac{d}{dt} \int_{\mathcal{P}_t} \frac{1}{2} \rho v_j v_j dx + \int_{\mathcal{P}_t} T_{ji} D_{ji} dx = \int_{\partial \mathcal{P}_t} T_{ji} n_i v_j dx + \int_{\mathcal{P}_t} v_j b_j dx \quad (4.78)$$

The second side of this balance represents the power input (product between force and velocity) consisting of the rate of work done by external surface tractions $T_{ji} n_i$ per unit area and body forces b_j per unit volume of the region \mathcal{P}_t bounded by $\partial \mathcal{P}_t$. Since the time-rate of change of the total energy is equal to the the rate of work done by the external forces (first principle of thermodynamics without thermal effects), we identify the first side as $d\mathcal{E}/dt$, where \mathcal{E} is the total energy contained in \mathcal{P}_t . Moreover, the total energy can be written as $\mathcal{E} = \mathcal{K} + \mathcal{U}$ where \mathcal{K} is the kinetic energy and \mathcal{U} is the potential energy. Since $\mathcal{K} = \int_{\mathcal{P}_t} \frac{1}{2} \rho v_j v_j dx$ is the standard kinetic energy, we identify

$$\frac{d\mathcal{U}}{dt} = \int_{\mathcal{P}_t} T_{ji} D_{ji} dx \quad (4.79)$$

We define the energy density U per unit volume in the reference configuration and therefore $\frac{\rho}{\rho_0}U$ is the energy density per unit volume in the current configuration. We obtain

The strain energy density function U

$$u = \int_{\mathcal{P}_t} \frac{\rho}{\rho_0} U dx \quad (4.80)$$

By drawing a comparison between Eqs. (4.79) and (4.80) we obtain

$$\int_{\mathcal{P}_t} T_{ji} D_{ji} dx = \frac{d}{dt} \int_{\mathcal{P}_t} \frac{\rho}{\rho_0} U dx \quad (4.81)$$

By using the property in Eq. (4.50) we obtain

$$\frac{\rho}{\rho_0} \dot{U} = T_{ji} D_{ji} \quad (4.82)$$

We introduce now a general statement affirming that the strain energy function U depends upon the deformation gradient \hat{F} : therefore, we have $U = U(\hat{F})$. This relation can be simplified by means of the principle of material objectivity (or material frame indifference), which says that the energy (and the stress) in the body should be the same regardless of the reference frame from which it is measured. If we consider a motion $\mathbf{x} = \mathcal{F}_t(\mathbf{X})$ we obtain a corresponding deformation gradient \hat{F} ; on the other hand, if we consider a roto-translated motion $\mathbf{x} = \hat{Q}(t)\mathcal{F}_t(\mathbf{X}) + \mathbf{c}(t)$ (where $\hat{Q}(t)$ is an orthogonal matrix and $\mathbf{c}(t)$ is an arbitrary vector), then the deformation gradient is $\hat{Q}\hat{F}$. In both cases we must have the same energy and therefore

$$U(\hat{F}) = U(\hat{Q}\hat{F}), \quad \forall \hat{Q}: \hat{Q}\hat{Q}^T = \hat{I} \quad (4.83)$$

Now, the deformation gradient \hat{F} can be decomposed through $\hat{F} = \hat{R}\hat{U}$ by obtaining

$$U(\hat{F}) = U(\hat{Q}\hat{R}\hat{U}), \quad \forall \hat{Q}: \hat{Q}\hat{Q}^T = \hat{I} \quad (4.84)$$

By imposing $\hat{Q} = \hat{R}^T$ we have $U(\hat{F}) = U(\hat{U})$ and, since $\hat{U}^2 = \hat{C}$, we finally obtain the dependence

$$U(\hat{F}) = U(\hat{C}) \quad (4.85)$$

where \hat{C} is the right Cauchy tensor. The choice of \hat{C} as an independent variable is convenient because, from its definition, $\hat{C} = \hat{F}^T \hat{F}$ is a rational function of the deformation gradient \hat{F} . Now we can calculate \dot{U} as follows

$$\dot{U} = \frac{\partial U}{\partial C_{ij}} \dot{C}_{ij} = \frac{\partial U}{\partial C_{ij}} (F_{ki} \dot{F}_{kj} + \dot{F}_{ki} F_{kj}) \quad (4.86)$$

We remember that $\dot{F}_{kj} = L_{ks} F_{sj}$ (see Eq. (4.20)) and we obtain

$$\begin{aligned} \dot{U} &= \frac{\partial U}{\partial C_{ij}} (F_{ki} L_{ks} F_{sj} + L_{ks} F_{si} F_{kj}) \\ &= \text{tr} \left[\frac{\partial U}{\partial \hat{C}} \hat{F}^T \hat{L} \hat{F} + \frac{\partial U}{\partial \hat{C}} \hat{F}^T \hat{L}^T \hat{F} \right] = \text{tr} \left[2 \frac{\partial U}{\partial \hat{C}} \hat{F}^T \hat{D} \hat{F} \right] \end{aligned} \quad (4.87)$$

where $\hat{\mathbf{D}}$ is the rate of deformation tensor defined as the symmetric part of the velocity gradient $\hat{\mathbf{L}}$. Through the comparison of Eqs. (4.82) and (4.87) we obtain

$$\operatorname{tr} \left[\frac{\rho_0}{\rho} \hat{\mathbf{T}} \hat{\mathbf{D}} \right] = \operatorname{tr} \left[2 \frac{\partial \mathbf{U}}{\partial \hat{\mathbf{C}}} \hat{\mathbf{F}}^T \hat{\mathbf{D}} \hat{\mathbf{F}} \right] \quad (4.88)$$

Further, from the commutation rule $\operatorname{tr}(\hat{\mathbf{A}}\hat{\mathbf{B}}) = \operatorname{tr}(\hat{\mathbf{B}}\hat{\mathbf{A}})$ of the trace operation we arrive at the following relationships, which must be satisfied for any possible $\hat{\mathbf{D}}$

$$\operatorname{tr} \left[\frac{\rho_0}{\rho} \hat{\mathbf{T}} \hat{\mathbf{D}} \right] = \operatorname{tr} \left[2 \hat{\mathbf{F}} \frac{\partial \mathbf{U}}{\partial \hat{\mathbf{C}}} \hat{\mathbf{F}}^T \hat{\mathbf{D}} \right] \quad (4.89)$$

Therefore, we obtain the formal connection between the constitutive equation (giving the Cauchy stress tensor) and the strain energy function in the form

$$\hat{\mathbf{T}} = 2 \frac{\rho}{\rho_0} \hat{\mathbf{F}} \frac{\partial \mathbf{U}}{\partial \hat{\mathbf{C}}} \hat{\mathbf{F}}^T \quad (4.90)$$

Similarly for the first Piola-Kirchhoff stress tensor we obtain

$$\hat{\mathbf{T}}^{1\mathcal{PK}} = \mathbf{J} \hat{\mathbf{T}} \hat{\mathbf{F}}^{-T} = 2 \hat{\mathbf{F}} \frac{\partial \mathbf{U}}{\partial \hat{\mathbf{C}}} \quad (4.91)$$

and finally for the second Piola-Kirchhoff stress tensor

$$\hat{\mathbf{T}}^{2\mathcal{PK}} = \hat{\mathbf{F}}^{-1} \hat{\mathbf{T}}^{1\mathcal{PK}} = 2 \frac{\partial \mathbf{U}}{\partial \hat{\mathbf{C}}} \quad (4.92)$$

We have proved that an arbitrarily nonlinear constitutive equation can be always written by means of derivations of the strain energy function: it means that the strain energy function contains the complete information about the nonlinear elastic response of a given material. For the particular case of nonlinear isotropic material the strain energy function \mathbf{U} must depend only upon the invariants of the right Cauchy tensor $\hat{\mathbf{C}}$. We observe that they are defined as

$$\text{I}_{\mathbf{C}} = \operatorname{tr} [\hat{\mathbf{C}}] \quad (4.93)$$

$$\text{II}_{\mathbf{C}} = \frac{1}{2} \left[(\operatorname{tr} \hat{\mathbf{C}})^2 - \operatorname{tr} (\hat{\mathbf{C}}^2) \right] \quad (4.94)$$

$$\text{III}_{\mathbf{C}} = \det \hat{\mathbf{C}} \quad (4.95)$$

and therefore we have $\mathbf{U} = \mathbf{U}(\text{I}_{\mathbf{C}}, \text{II}_{\mathbf{C}}, \text{III}_{\mathbf{C}})$. We remember that the three invariants define the characteristic polynomial of the tensor $\hat{\mathbf{C}}$

$$\det (\hat{\mathbf{C}} - \lambda \hat{\mathbf{I}}) = -\lambda^3 + \lambda^2 \text{I}_{\mathbf{C}} - \lambda \text{II}_{\mathbf{C}} + \text{III}_{\mathbf{C}} \quad (4.96)$$

and satisfy the so-called Cayley-Hamilton theorem

$$\hat{\mathbf{O}} = -\hat{\mathbf{C}}^3 + \text{I}_{\mathbf{C}} \hat{\mathbf{C}}^2 - \text{II}_{\mathbf{C}} \hat{\mathbf{C}} + \text{III}_{\mathbf{C}} \hat{\mathbf{I}} \quad (4.97)$$

Nonlinear isotropic material: the Cauchy invariants

Cayley-Hamilton theorem

It is possible to prove that

$$\frac{\partial I_C}{\partial \hat{C}} = \hat{I}; \quad \frac{\partial II_C}{\partial \hat{C}} = I_C \hat{I} - \hat{C}; \quad \frac{\partial III_C}{\partial \hat{C}} = III_C \hat{C}^{-1}; \quad (4.98)$$

and therefore we obtain

$$\begin{aligned} \frac{\partial U(I_C, II_C, III_C)}{\partial \hat{C}} &= \frac{\partial U}{\partial I_C} \frac{\partial I_C}{\partial \hat{C}} + \frac{\partial U}{\partial II_C} \frac{\partial II_C}{\partial \hat{C}} + \frac{\partial U}{\partial III_C} \frac{\partial III_C}{\partial \hat{C}} \\ &= \frac{\partial U}{\partial I_C} \hat{I} + \frac{\partial U}{\partial II_C} (I_C \hat{I} - \hat{C}) + \frac{\partial U}{\partial III_C} III_C \hat{C}^{-1} \end{aligned} \quad (4.99)$$

This expression can be used in the Cauchy and Piola-Kirchhoff tensors given in Eqs. (4.90), (4.91) and (4.92) in order to obtain their final form in terms of the invariants of the right Cauchy tensor \hat{C} . Sometime the stress tensors can also be expressed in term of the Green-Lagrange strain tensor $\hat{\eta} = \frac{1}{2} (\hat{C} - \hat{I})$; since $2d\hat{\eta} = d\hat{C}$, we have

$$\hat{T} = \frac{\rho}{\rho_0} \hat{F} \frac{\partial U}{\partial \hat{\eta}} \hat{F}^T; \quad \hat{T}^{1\mathcal{PK}} = \hat{F} \frac{\partial U}{\partial \hat{\eta}}; \quad \hat{T}^{2\mathcal{PK}} = \frac{\partial U}{\partial \hat{\eta}} \quad (4.100)$$

In this case the strain energy function U (for unit volume of the reference configuration) may be developed in power series with respect to the components of $\hat{\eta}$. This leads to the expression

$$U(\hat{\eta}) = \frac{1}{2} \mathcal{C}_{ijkh}^{\mathcal{L}} \eta_{ij} \eta_{kh} + \frac{1}{6} \mathcal{C}_{ijkhnm}^{\mathcal{L}} \eta_{ij} \eta_{kh} \eta_{nm} + \dots \quad (4.101)$$

Here the $\mathcal{C}_{ijkh}^{\mathcal{L}}$ and the $\mathcal{C}_{ijkhnm}^{\mathcal{L}}$ denote the second order elastic constants (SEOC) and the third order elastic constants (TOEC), respectively (within the Lagrangian formalism).

4.7 THE SMALL-STRAIN APPROXIMATION

In the infinitesimal elasticity theory the extent of the deformations is assumed small. While this notion is rather intuitive, it can be formalized by imposing that for small deformations \hat{F} is very similar to \hat{I} or, equivalently, that \hat{G} is similar to \hat{I} as well. It means that both \hat{J}_L and \hat{J}_E are very small. Therefore, we adopt as an operative definition of *small deformation* the relations

$$\text{Tr}(\hat{J}_L \hat{J}_L^T) \ll 1 \quad \text{and} \quad \text{Tr}(\hat{J}_E \hat{J}_E^T) \ll 1 \quad (4.102)$$

i.e., a deformation will be hereafter regarded to as *small* provided that the trace of the product $\hat{J}_L \hat{J}_L^T$ or $\hat{J}_E \hat{J}_E^T$ is negligible. It means that we can assume $\hat{J}_L = \hat{J}_E = \hat{J}$ and that we can interchange the Eulerian and the Lagrangian variables without problems. Here, we write all the equations with the Eulerian variables \mathbf{x} . We observe that the displacement gradient \hat{J} can be written as the

Small deformation: a deformation will be hereafter regarded to as small provided that the trace of the product $\hat{J}_L \hat{J}_L^T$ or $\hat{J}_E \hat{J}_E^T$ is negligible.

sum of a symmetric and a skew-symmetric (antisymmetric) part as follows

$$J_{ij} = \underbrace{\frac{1}{2} \left(\frac{\partial u_i}{\partial x_j} + \frac{\partial u_j}{\partial x_i} \right)}_{\text{symmetric}} + \underbrace{\frac{1}{2} \left(\frac{\partial u_i}{\partial x_j} - \frac{\partial u_j}{\partial x_i} \right)}_{\text{skew-symmetric}} = \epsilon_{ij} + \Omega_{ij} \quad (4.103)$$

The meaning of the displacement gradient can be found in Fig. 4.6 for a two-dimensional configuration. Accordingly, we define the (symmetric) *infinitesimal strain tensor* (or *small strain tensor*) as

The small strain tensor

$$\epsilon_{ij} = \frac{1}{2} \left(\frac{\partial u_i}{\partial x_j} + \frac{\partial u_j}{\partial x_i} \right) \quad (4.104)$$

and the (antisymmetric) *local rotation tensor* as

$$\Omega_{ij} = \frac{1}{2} \left(\frac{\partial u_i}{\partial x_j} - \frac{\partial u_j}{\partial x_i} \right) \quad (4.105)$$

Such a decomposition is useful to obtain three very important properties of the small strain tensor, which is the key quantity to determine the state of deformation of an elastic body.

Small strain tensor must not affect by pure local rotations, but only by the changes of shape and size of the given element of volume.

First, for a pure local rotation (a volume element is rotated, but not changed in shape and size) we have $\hat{J} = \hat{\Omega}$ and therefore $\hat{\epsilon} = 0$. This means that the small strain tensor does not take into account any local rotation, but only the changes of shape and size (dilatation or compression) of that element of volume.

Let us clarify this fundamental result. We consider a point \mathbf{x} inside a volume element which is transformed to $\mathbf{x} + \mathbf{u}(\mathbf{x})$ in the current configuration. Under a pure local rotation we have: $\mathbf{x} + \mathbf{u}(\mathbf{x}) = \hat{R}\mathbf{x}$, where \hat{R} is a given orthogonal rotation matrix (satisfying $\hat{R}\hat{R}^T = \hat{I}$). We simply obtain $\mathbf{u}(\mathbf{x}) = (\hat{R} - \hat{I})\mathbf{x}$ or, equivalently, $\hat{J} = \hat{R} - \hat{I}$. Since the applied deformation (i.e., the local rotation) is small by hypothesis, we observe that the difference $\hat{R} - \hat{I}$ is very small too. The product $\hat{J}\hat{J}^T$ will be therefore negligible, leading to the following expression

$$\begin{aligned} 0 &\cong \hat{J}\hat{J}^T = (\hat{R} - \hat{I})(\hat{R}^T - \hat{I}) = \hat{R}\hat{R}^T - \hat{R} - \hat{R}^T + \hat{I} \\ &= \hat{I} - \hat{R} - \hat{R}^T + \hat{I} = -\hat{J} - \hat{J}^T \end{aligned} \quad (4.106)$$

Therefore $\hat{J} = -\hat{J}^T$ or, equivalently, \hat{J} is a skew-symmetric tensor. It follows that $\hat{J} = \hat{\Omega}$ and $\hat{\epsilon} = 0$. We have verified that a pure rotation corresponds to zero strain. In addition, we remark that the local rotation of a volume element within a body cannot be correlated with any arbitrary force exerted in that region (the forces are correlated with $\hat{\epsilon}$ and not with $\hat{\Omega}$): for this reason the infinitesimal strain tensor is the only relevant object for the analysis of the deformation due to applied loads in elasticity theory.

Small strain tensor determines the length variation of any vector from the reference to the current configuration.

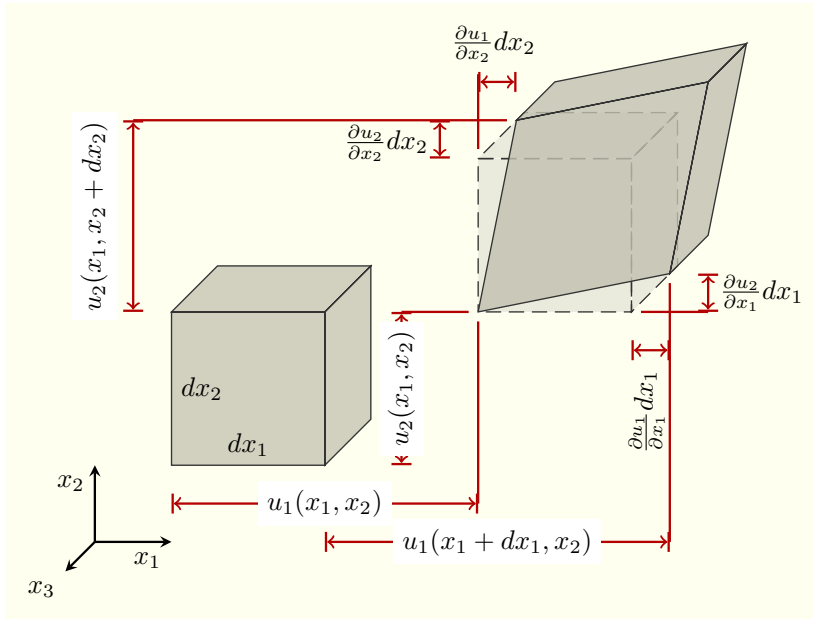


Figure 4.6: Two-dimensional geometric deformation of an infinitesimal material element.

Second, the infinitesimal strain tensor allows for the determination of the length variation of any vector from the reference to the current configuration. By defining ϵ_{nn} as the relative length variation in direction \mathbf{n} , we have from Table 4.2

$$\epsilon_{nn} = \mathbf{n} \cdot \hat{\epsilon} \mathbf{n} \tag{4.107}$$

If \mathbf{n} is actually any unit vector of the reference frame, it is straightforward to attribute a geometrical meaning to the components ϵ_{11} , ϵ_{22} , ϵ_{33} of the strain tensor. Since $\epsilon_{nn} = \mathbf{e}_i \cdot (\hat{\epsilon} \mathbf{e}_i) = \epsilon_{ii}$, they describe the relative length variations along the three axes of the reference frame. Third, the infinitesimal strain tensor allows for the determination of the angle variation between any two vectors from the reference to the current configuration. The variation of the angle defined by the two orthogonal directions \mathbf{n} and \mathbf{t} can be obtained from Table 4.2

$$\gamma_{nt} = 2\mathbf{n} \cdot \hat{\epsilon} \mathbf{t} \tag{4.108}$$

Small strain tensor determines the angle variation between any pair of vectors from the reference to the current configuration.

The present result is also useful for giving a direct geometrical interpretation of the components ϵ_{12} , ϵ_{23} and ϵ_{13} of the infinitesimal strain tensor. As an example, we take into consideration the component ϵ_{12} and we assume that $\mathbf{n} = \mathbf{e}_1$ and $\mathbf{t} = \mathbf{e}_2$. The quantity γ_{nt} represents the variation of a right angle lying on the plane (x_1, x_2) . Since $\epsilon_{12} = \mathbf{e}_1 \cdot (\hat{\epsilon} \mathbf{e}_2)$, we easily obtain the relationship $\gamma_{nt} = 2\epsilon_{12} = \frac{\partial u_1}{\partial x_2} + \frac{\partial u_2}{\partial x_1}$. In other words, ϵ_{12} is half the variation of the right angle formed by the axis x_1 and x_2 . Of

Table 4.3: The small strain approximation.

Lagrangian vision	Eulerian vision
$\hat{\mathbf{J}}_L = \hat{\mathbf{J}}$	$\hat{\mathbf{J}}_E = \hat{\mathbf{J}}$
$\hat{\mathbf{F}} = \hat{\mathbf{G}}^{-1} = \hat{\mathbf{I}} + \hat{\mathbf{J}}$	$\hat{\mathbf{F}}^{-1} = \hat{\mathbf{G}} = \hat{\mathbf{I}} - \hat{\mathbf{J}}$
$\hat{\boldsymbol{\eta}} = \hat{\boldsymbol{\epsilon}}$	$\hat{\boldsymbol{\epsilon}} = \hat{\boldsymbol{\epsilon}}$
$\hat{\mathbf{C}} = \hat{\mathbf{B}} = \hat{\mathbf{I}} + 2\hat{\boldsymbol{\epsilon}}$	$\hat{\mathbf{C}}^{-1} = \hat{\mathbf{B}}^{-1} = \hat{\mathbf{I}} - 2\hat{\boldsymbol{\epsilon}}$
$\hat{\mathbf{U}} = \hat{\mathbf{V}} = \hat{\mathbf{I}} + \hat{\boldsymbol{\epsilon}}$	$\hat{\mathbf{U}}^{-1} = \hat{\mathbf{V}}^{-1} = \hat{\mathbf{I}} - \hat{\boldsymbol{\epsilon}}$
$\hat{\mathbf{R}} = \hat{\mathbf{I}} + \hat{\boldsymbol{\Omega}}$	$\hat{\mathbf{R}}^{-1} = \hat{\mathbf{I}} - \hat{\boldsymbol{\Omega}}$
$\hat{\mathbf{T}}^{1\mathcal{PK}} = \hat{\mathbf{T}}^{2\mathcal{PK}} = \frac{\partial \mathbf{U}}{\partial \hat{\boldsymbol{\epsilon}}}$	$\hat{\mathbf{T}} = \frac{\partial \mathbf{U}}{\partial \hat{\boldsymbol{\epsilon}}}$

course, the same interpretation is valid for the other components ϵ_{23} and ϵ_{13} .

The result of the application of the small strain approximation on the main quantities of the continuum mechanics is summarized in Table 4.3.

Knowing the $\hat{\boldsymbol{\epsilon}}$ tensor field within a strained (i.e., deformed) elastic body allows us to calculate the volume change ΔV of a given region. Reminding that the Lagrangian volume variation (ΔV) during a finite deformation is given by $\Delta V = \int_V (\mathbf{J} - 1) d\mathbf{x}$, where in the case of infinitesimal deformations, the displacement gradient can be written as

$$\det \mathbf{F} = \det(\mathbf{1} + \nabla \mathbf{u}) = 1 + \text{Tr} \nabla \mathbf{u} + \mathcal{O}(\epsilon^2) = 1 + \nabla \cdot \mathbf{u} + \mathcal{O}(\epsilon^2) \quad (4.109)$$

Here, the quantity $\nabla \cdot \mathbf{u} = \text{Tr}(\hat{\boldsymbol{\epsilon}})$ is the dilatation. We get $\Delta V = \int_V \text{Tr}(\hat{\boldsymbol{\epsilon}}) d\mathbf{x}$, where V is the reference volume of the unstrained region.

The above discussion states that, given a displacement field $\mathbf{u}(\mathbf{x})$, the components of the infinitesimal strain tensor are easily calculated by direct differentiation. The inverse problem is much more complicated. Given an arbitrary infinitesimal strain tensor $\hat{\boldsymbol{\epsilon}}(\mathbf{x})$ we could search for that displacement field $\mathbf{u}(\mathbf{x})$ generating the imposed deformation. In general, such a displacement field may not exist. There are, however, suitable conditions under which the solution of this inverse problem is actually found. These conditions are written in the very compact form

$$\eta_{qki} \eta_{phj} \frac{\partial^2 \epsilon_{ij}}{\partial x_k \partial x_h} = 0 \quad (4.110)$$

where η 's are the Levi-Civita permutation symbols. Eqs. (4.110) are known as infinitesimal strain compatibility equations or Beltrami Saint-Venant equations.

The balance equations assume the standard form

$$\frac{\partial T_{ji}}{\partial x_i} + b_j = \rho \frac{\partial^2 u_j}{\partial t^2} \quad (4.111)$$

$$T_{ij} = T_{ji} \quad (4.112)$$

The principles of linear and angular momentum, the definition of strain and its compatibility conditions need to be supplemented by a further set of equations, known as constitutive equations, which characterize the constitution of the elastic solid body. In the case of small deformation we can write

Constitutive equations

$$\hat{T} = \hat{T}^{1\mathcal{PK}} = \hat{T}^{2\mathcal{PK}} = \frac{\partial U}{\partial \hat{\epsilon}} \quad (4.113)$$

where the strain energy function is expressed as $U = U(\hat{\epsilon})$. Such a strain energy function U may be developed in power series with respect to the components of $\hat{\epsilon}$. This leads to the expression

$$U(\hat{\epsilon}) = \frac{1}{2} \mathcal{C}_{ijkh} \epsilon_{ij} \epsilon_{kh} + \frac{1}{6} \mathcal{C}_{ijkhnm} \epsilon_{ij} \epsilon_{kh} \epsilon_{nm} + \dots \quad (4.114)$$

Here the \mathcal{C}_{ijkh} and the \mathcal{C}_{ijkhnm} denote the second order elastic constant (SEOC) and the third order elastic constant (TOEC), respectively, with reference to the small strain tensor. We can determine the relations with the elastic constants defined in Eq. (4.101): to this aim, we consider an homogeneous deformation with $\hat{F} = \hat{I} + \hat{\epsilon}$ (i.e. with $\Omega = 0$ or $\hat{J} = \hat{\epsilon}$) and we obtain $\hat{\eta} = \hat{\epsilon} + \frac{1}{2} \hat{\epsilon}^2$; so, by imposing $U(\hat{\epsilon}) = U(\hat{\eta})$ we eventually obtain

$$\begin{aligned} \mathcal{C}_{ijkh} &= \mathcal{C}_{ijkh}^{\mathcal{L}} \\ \mathcal{C}_{ijkhnm} &= \mathcal{C}_{ijkhnm}^{\mathcal{L}} + \frac{3}{2} \mathcal{C}_{imkh}^{\mathcal{L}} \delta_{jn} + \frac{3}{2} \mathcal{C}_{ijkm}^{\mathcal{L}} \delta_{hn} \end{aligned} \quad (4.115)$$

The linear law for the relation between stress and strain is called the generalized Hooke's law. The general form of writing Hooke's law is as follows

The generalized Hooke's law

$$T_{ij} = \mathcal{C}_{ijkh} \epsilon_{kh} \quad (4.116)$$

where \mathcal{C}_{ijkh} are constants (for homogeneous materials). Equation (4.116) is of general validity, including all the possible crystalline symmetry or, in other words, any kind of anisotropy.

The tensor of the elastic constants, which is called also stiffness tensor, must satisfy the following symmetry rules. Since $T_{ij} = T_{ji}$ we have symmetry in the first pair of indices $\mathcal{C}_{ijkh} = \mathcal{C}_{jikh}$, this reduces the number independent components of \mathcal{C}_{ijkh} from 81 (think of a 9×9 matrix because the stresses and strains have nine components each) to 54 (6 components for the ij term and 3 each for the k, l terms). Similarly, using the symmetry of the

The stiffness tensor symmetries

strain tensor $\epsilon_{kh} = \epsilon_{hk}$, we obtain a symmetry in the last pair of indices $\mathcal{C}_{ijkh} = \mathcal{C}_{ijhk}$. These are called the minor symmetries of the elasticity tensor and we are then left with only 36 independent components. Since the strain energy function should not change when we interchange ij and kl in the quadratic form, it leads to a symmetry between the first pair and the last pair of indices $\mathcal{C}_{ijkh} = \mathcal{C}_{k hij}$. These are known as the major symmetries of the stiffness tensor. At the end \mathcal{C}_{ijkh} has at most 21 (think of a symmetric 6×6 matrix) independent components rather than the $3^4 = 81$ which, as a general fourth-rank tensor, it might have had. The inverse relation between the strain and the stress can be determined by taking the inverse of stress-strain relation to get

$$\epsilon_{ij} = \mathcal{S}_{ijkh} T_{kh} \quad (4.117)$$

The compliance tensor

where \hat{S} is defined as the compliance tensor. The compliance tensor has 21 components and the same symmetries as well as the stiffness tensor.

In the case of a linear and isotropic material we have

$$\hat{T} = \frac{E}{1+\nu} \hat{\epsilon} + \frac{\nu E}{(1+\nu)(1-2\nu)} \hat{T} \text{Tr}(\hat{\epsilon}) \quad (4.118)$$

where E and ν are the Young modulus and the Poisson ratio, respectively. We can also introduce the Lamé coefficients μ and λ as follows

$$\mu = \frac{E}{2(1+\nu)} \quad \lambda = \frac{\nu E}{(1+\nu)(1-2\nu)} \quad (4.119)$$

Therefore, Eq. (4.118) assumes the standard form

$$\hat{T} = 2\mu \hat{\epsilon} + \lambda \hat{T} \text{Tr}(\hat{\epsilon}) \quad (4.120)$$

or, in index notation,

$$T_{ij} = 2\mu \epsilon_{ij} + \lambda \epsilon_{kk} \delta_{ij} \quad (4.121)$$

The number of independent elastic moduli can be also derived from the Eq. (4.116) and the algebraic properties of the forth-rank stiffness tensor, \mathcal{C}_{ijkh} . Since the general form of an isotropic forth-rank tensor is

$$\mathcal{C}_{ijkh} = \lambda \delta_{ij} \delta_{kh} + \zeta \delta_{ik} \delta_{jh} + \xi \delta_{ih} \delta_{jk} \quad (4.122)$$

where λ , ζ , and ξ are constants which do not depend on the choosing coordinate system. Given the symmetry of the strain tensor, the Eq. (4.116) can be rewritten as

$$\begin{aligned} T_{ij} &= (\lambda \delta_{ij} \delta_{kh} + \zeta \delta_{ik} \delta_{jh} + \xi \delta_{ih} \delta_{jk}) \epsilon_{kh} \\ &= \lambda \delta_{ij} \epsilon_{kk} + \zeta \epsilon_{ij} + \xi \epsilon_{ji} \\ &= \lambda \delta_{ij} \epsilon_{kk} + (\zeta + \xi) \epsilon_{ij} \\ &= \lambda \delta_{ij} \epsilon_{kk} + 2\mu \epsilon_{ij} \end{aligned}$$

here we have set $2\mu = (\zeta + \xi)$, hence there are only two independent constants in the constitutive equation for isotropic systems.

The inverse relationship can be derived from Eq. (4.120) by calculating its trace $\text{Tr}(\hat{\mathbf{T}}) = 2\mu\text{Tr}(\hat{\boldsymbol{\epsilon}}) + 3\lambda\text{Tr}(\hat{\boldsymbol{\epsilon}})$, so that

$$\hat{\boldsymbol{\epsilon}} = \frac{1}{2\mu} \hat{\mathbf{T}} - \frac{\lambda}{2\mu(2\mu + 3\lambda)} \hat{\mathbf{T}} \text{Tr}(\hat{\mathbf{T}}) \quad (4.123)$$

or, in index notation,

$$\epsilon_{ij} = \frac{1}{2\mu} T_{ij} - \frac{\lambda}{2\mu(2\mu + 3\lambda)} T_{kk} \delta_{ij} \quad (4.124)$$

When we are dealing with a linear, isotropic and homogeneous material the governing equations of the elasticity theory can be summed up as follows

The Navier equation

$$(\lambda + \mu) \nabla (\nabla \cdot \mathbf{u}) + \mu \nabla^2 \mathbf{u} + \mathbf{b} = \rho \frac{\partial^2 \mathbf{u}}{\partial t^2} \quad (4.125)$$

This is an equation of motion where the displacement field is the single unknown, which have been called Lamé or Navier equation. Such a motion equation for a isotropic elastic body can be also written in a different form by utilizing the general property $\nabla \times (\nabla \times \mathbf{u}) = \nabla (\nabla \cdot \mathbf{u}) - \nabla^2 \mathbf{u}$, which holds for the differential operators. The result is

$$(\lambda + \mu) \nabla \times (\nabla \times \mathbf{u}) + (\lambda + 2\mu) \nabla^2 \mathbf{u} + \mathbf{b} = \rho \frac{\partial^2 \mathbf{u}}{\partial t^2} \quad (4.126)$$

Both Eq. (4.125) and Eq. (4.126) are linear partial differential equations of the second order with a vector field $\mathbf{u}(\mathbf{r})$ as unknown. In order to find a solution of Eq. (4.125) or Eq. (4.126) we must impose some boundary conditions depending on the physical problem under consideration. If we consider a body with an external surface S , a first type of boundary condition fixes the values of the displacement field on this surface at any time. It means that $\mathbf{u} = \mathbf{u}(\mathbf{x}, t)$ for any $\mathbf{x} \in S$ and for any t in a given interval. When the entire external surface is described by these conditions we say that we are solving an elastic problem of the first kind (Dirichlet). A second kind of boundary conditions fixes the stress applied on the external surface. It means that $T_{ij} n_j = f_i(\mathbf{x}, t)$ for any $\mathbf{x} \in S$ and for any t in a given interval. When the entire external surface is described by these conditions we say that we are solving an elastic problem of the second kind (Neumann). Finally, a third case can be defined by dividing the surface S in two parts and by applying the Dirichlet conditions to the first part and the Neumann conditions to the second part. In this case we say that we are solving an elastic problem of the third kind, subjected to mixed boundary conditions.

*The first kind
(Dirichlet) elastic
problem*

*The second kind
(Neumann) elastic
problem*

*The third kind elastic
problem*

4.8 THE STIFFNESS TENSOR AND THE ELASTIC MODULI IN TWO-DIMENSIONAL SYSTEMS.

Voigt notation

To express the general stress-strain relation for a linear elastic material in terms of matrix elements, we can use the Voigt notation. We have seen that both stress and strain tensors involve six components identifiable by a double subscript notation. Both the second-rank tensors are symmetric with respect to an interchange of the subscripts, $T_{ij} = T_{ji}$, or with the Janh symbols $[V^2]$. So it is convenient to abbreviate the notation by using single subscript, running from 1 to 6, $11 \rightarrow 1$, $22 \rightarrow 2$, $33 \rightarrow 3$, $23 \rightarrow 4$, $13 \rightarrow 5$, and $12 \rightarrow 6$. In this notation, the stress and strain are expressed as 6×1 column vectors. The Voigt notation can be adopted also for higher-rank tensor with different internal symmetries, as in the case of the fourth-rank stiffness and compliance tensors, which are symmetric with respect to the first and second pair of indices and also with respect to their permutation, or differently with respect the $[[V^2]^2]$ internal symmetry, and for the sixth-rank tensor build with the third-order derivate of energy strain $C_{ijklmn} = \frac{\partial^3 U}{\partial \epsilon_{ij} \partial \epsilon_{kl} \partial \epsilon_{mn}}$ in Eq. (4.114) with respect the $[[[V^2]]^3]$ internal symmetry.

The elasticity tensor can be expressed as a symmetric 6×6 matrix, and the Eq. 4.116 can be written as

$$T_\lambda = C_{\lambda\mu} \epsilon_\mu, \quad \text{with } (ij) \leftrightarrow \lambda, \quad (kh) \leftrightarrow \mu, \quad (4.127)$$

or equivalently in term of matrix as

$$\begin{pmatrix} T_{11} \\ T_{22} \\ T_{33} \\ T_{23} \\ T_{31} \\ T_{12} \end{pmatrix} = \begin{pmatrix} C_{1111} & C_{1122} & C_{1133} & C_{1123} & C_{1131} & C_{1112} \\ C_{2211} & C_{2222} & C_{2233} & C_{2223} & C_{2231} & C_{2212} \\ C_{3311} & C_{3322} & C_{3333} & C_{3323} & C_{3331} & C_{3312} \\ C_{2311} & C_{2322} & C_{2333} & C_{2323} & C_{2331} & C_{2312} \\ C_{3111} & C_{3122} & C_{3133} & C_{3123} & C_{3131} & C_{3112} \\ C_{1211} & C_{1222} & C_{1233} & C_{1223} & C_{1231} & C_{1212} \end{pmatrix} \begin{pmatrix} \epsilon_{11} \\ \epsilon_{22} \\ \epsilon_{33} \\ \epsilon_{23} \\ \epsilon_{31} \\ \epsilon_{12} \end{pmatrix}$$

$$\Rightarrow \begin{pmatrix} T_1 \\ T_2 \\ T_3 \\ T_4 \\ T_5 \\ T_6 \end{pmatrix} = \begin{pmatrix} C_{11} & C_{12} & C_{13} & C_{14} & C_{15} & C_{16} \\ C_{21} & C_{22} & C_{23} & C_{24} & C_{25} & C_{26} \\ C_{31} & C_{32} & C_{33} & C_{34} & C_{35} & C_{36} \\ C_{41} & C_{42} & C_{43} & C_{44} & C_{45} & C_{46} \\ C_{51} & C_{52} & C_{53} & C_{54} & C_{55} & C_{56} \\ C_{61} & C_{62} & C_{63} & C_{64} & C_{65} & C_{66} \end{pmatrix} \begin{pmatrix} \epsilon_1 \\ \epsilon_2 \\ \epsilon_3 \\ \epsilon_4 \\ \epsilon_5 \\ \epsilon_6 \end{pmatrix} \quad (4.128)$$

The inverse relation, defined in Eq. (4.117), is more complicated. Again from the Eq. (4.104) the indices of the compliance tensor can be written according to the following rules

$$S_{\lambda\mu} = \begin{cases} S_{ijkl}, & \text{if } \forall \lambda, \mu = 1, 2, 3, \\ 2S_{ijkl}, & \text{if } \lambda = 1, 2, 3, \mu = 4, 5, 6, \\ 4S_{ijkl}, & \text{if } \lambda = 4, 5, 6, \mu = 4, 5, 6, \end{cases} \quad (4.129)$$

where each indices λ , or μ greater than 3 leads to doubling the corresponding matrix element, in order to take in account of the permutations.

The number of independent stiffness coefficients in Eq. (4.128) can be further reduced by imposing the symmetry operators of the respective crystal classes. In all of them, but the triclinic one, the effects of crystal symmetries are revealed by the presence of null and repeated elements among the matrix components. For more detail see the Appendix A.4.

As an example of these effects, we show the stiffness tensor of an isotropic material. In this case only two components are independent, because of its symmetry group contains all orthogonal transformations. In Voigt notation the stiffness tensor of an isotropic materials can be written as

Isotropic materials

$$\begin{pmatrix} C_{11} & C_{12} & C_{12} & 0 & 0 & 0 \\ C_{12} & C_{11} & C_{12} & 0 & 0 & 0 \\ C_{12} & C_{12} & C_{11} & 0 & 0 & 0 \\ 0 & 0 & 0 & (C_{11} - C_{12}) & 0 & 0 \\ 0 & 0 & 0 & 0 & (C_{11} - C_{12}) & 0 \\ 0 & 0 & 0 & 0 & 0 & (C_{11} - C_{12}) \end{pmatrix} \quad (4.130)$$

Combining the Eq. (4.116) with the Eq. (4.121)

$$C_{ijkl}\epsilon_{kl} = 2\mu\epsilon_{ij} + \lambda\delta_{ij}\epsilon_{kk} \quad (4.131)$$

and because of $\epsilon_{kk} = \delta_{kl}\epsilon_{kl}$, and $\epsilon_{ij} = \delta_{ik}\delta_{jl}\epsilon_{kl}$

$$C_{ijkl}\epsilon_{kl} = 2\mu\delta_{ik}\delta_{jl}\epsilon_{kl} + \lambda\delta_{ij}\delta_{kl}\epsilon_{kl} \quad (4.132)$$

So the stiffness coefficients for an isotropic crystal can be expressed in term of elastic moduli as

$$C_{ijkl} = 2\mu\delta_{ik}\delta_{jl} + \lambda\delta_{ij}\delta_{kl} \quad (4.133)$$

Table 4.4: Relations between different couples of elastic moduli. Here (λ, μ) are the Lamè coefficients, E , ν , and K are the Young modulus, the Poisson ratio, and the Bulk modulus, respectively.

	(λ, μ)	(K, μ)	(μ, ν)	(E, ν)	(E, μ)
λ		$K - \frac{2}{3}\mu$	$\frac{2\mu\nu}{1-2\nu}$	$\frac{\nu E}{(1+\nu)(1-2\nu)}$	$\frac{\mu(E-2\mu)}{3\mu-E}$
μ				$\frac{E}{2(1+\nu)}$	
K	$\frac{3\lambda+2\mu}{3}$		$\frac{2\mu(1+\nu)}{3(1-2\nu)}$	$\frac{E}{3(1-2\nu)}$	$\frac{E\mu}{3(3\mu-E)}$
E	$\frac{\mu(3\lambda+2\mu)}{\lambda+\mu}$	$\frac{9K\mu}{3K+\mu}$	$2(1+\nu)\mu$		
ν	$\frac{\lambda}{2(\lambda+\mu)}$	$\frac{3K-\mu}{2(3K+\mu)}$			$\frac{E-2\mu}{2\mu}$

or, in more explicit way

$$\begin{pmatrix} 2\mu + \lambda & \lambda & \lambda & 0 & 0 & 0 \\ \lambda & 2\mu + \lambda & \lambda & 0 & 0 & 0 \\ \lambda & \lambda & 2\mu + \lambda & 0 & 0 & 0 \\ 0 & 0 & 0 & 2\mu & 0 & 0 \\ 0 & 0 & 0 & 0 & 2\mu & 0 \\ 0 & 0 & 0 & 0 & 0 & 2\mu \end{pmatrix} \quad (4.134)$$

which gives us the direct connection between stiffness coefficients and elastic moduli.

Another peculiar example regards the transversely isotropic materials. A transversely isotropic material is symmetric about an axis that is normal to a plane of isotropy. This transverse plane has infinite planes of symmetry and thus, within this plane, the material properties are same in all directions. With this type of material symmetry, the number of independent constants in the elasticity tensor are reduced to 5 from a total of 21 independent constants in case of fully anisotropic solid. The stiffness tensor has the following form

*Transversely
isotropic materials*

$$\begin{pmatrix} \mathcal{C}_{11} & \mathcal{C}_{12} & \mathcal{C}_{13} & 0 & 0 & 0 \\ \mathcal{C}_{12} & \mathcal{C}_{11} & \mathcal{C}_{13} & 0 & 0 & 0 \\ \mathcal{C}_{13} & \mathcal{C}_{13} & \mathcal{C}_{33} & 0 & 0 & 0 \\ 0 & 0 & 0 & \mathcal{C}_{44} & 0 & 0 \\ 0 & 0 & 0 & 0 & \mathcal{C}_{44} & 0 \\ 0 & 0 & 0 & 0 & 0 & (\mathcal{C}_{11} - \mathcal{C}_{12}) \end{pmatrix} \quad (4.135)$$

Starting from the constitutive equation (4.116)

$$\hat{\mathbf{T}} = 2\mu\hat{\mathbf{e}} + \lambda\text{Tr}(\hat{\mathbf{e}})\mathbf{I}_3 \quad (4.136)$$

where all the matrices are in rank 3, we can obtain the physical meaning of the Lamè moduli, λ and μ . By setting $\lambda = 0$ and considering the out-of-diagonal strain elements ϵ_{ij} with $i \neq j$, we can rewrite the constitutive equation as

$$\tau_{ij} = 2\mu\epsilon_{ij}, \quad \text{with } i \neq j, \quad (4.137)$$

$$= \mu \left(\frac{\partial u_i}{\partial x_j} + \frac{\partial u_j}{\partial x_i} \right) \quad (4.138)$$

where μ is the coefficient that relates stress to a change in shape, as discuss in Eq. (4.108), therefore it is a measure of the rigidity. If μ vanishes and we consider only $i = j$, the Eq. (4.116) becomes

$$\lim_{\mu \rightarrow 0^+} \tau_{ij} = \lambda \epsilon_{kk} \delta_{ij}, \quad \text{with } i = j, \quad (4.139)$$

$$= \lambda \text{Tr}(\hat{\epsilon}) = \lambda \frac{\Delta V}{V} \quad (4.140)$$

where $\Delta V/V$ is the dilatation as defined in Eq. (4.109), so the Lamè modulus λ is related to the compressibility κ . Since we have considered an hydrostatic deformation, namely $\epsilon_{11} = \epsilon_{22} = \epsilon_{33}$, and since in the hydrostatic case the trace of stress is related to the negative hydrostatic pressure, namely $\text{Tr}(\hat{\mathbf{T}}) = -3P$, the trace of the Eq. (4.116) may be written as

$$\text{Tr}(\hat{\mathbf{T}}) = 2\mu \text{Tr}(\hat{\epsilon}) + 3\lambda \text{Tr}(\hat{\epsilon}) \quad (4.141)$$

$$-P = \left(\frac{2}{3}\mu + \lambda \right) \frac{\Delta V}{V} \quad \text{with } i = j, \quad (4.142)$$

Because of the compressibility κ is defined as

$$\kappa = -\frac{1}{P} \frac{\Delta V}{V} \quad (4.143)$$

Solving for λ , we obtain

$$\lambda = \frac{1}{\kappa} - \frac{2}{3}\mu \quad (4.144)$$

Hence, the Lamè modulus λ combines the compressibility and the rigidity. The reciprocal of the compressibility is defined as the Bulk modulus of a material K (see also Table 4.4)

$$K = \lambda + \frac{2}{3}\mu \quad (4.145)$$

We focus now our attention in the case of in plane strain condition, where the infinitesimal displacement $\mathbf{u} = (u_1, u_2, 0)$ has only two-dimensional components, namely $u_1, u_2 = f(x_1, x_2)$. So, the strain tensor $\hat{\epsilon} = \frac{1}{2}(\nabla \mathbf{u} + \nabla \mathbf{u}^T)$ takes the form

$$\hat{\epsilon} = \begin{pmatrix} \epsilon_{11} & \epsilon_{12} & 0 \\ \epsilon_{12} & \epsilon_{22} & 0 \\ 0 & 0 & 0 \end{pmatrix} \quad (4.146)$$

The physical meaning of the Lamè moduli

*Plane strain
condition: 3D vs 2D
notation*

It is easy now to introduce a two dimensional notation, where the Eq. (4.116) is rewritten with only matrix in rank 2

$$\begin{pmatrix} T_{11} & T_{12} \\ T_{12} & T_{22} \end{pmatrix} = 2\mu \begin{pmatrix} \epsilon_{11} & \epsilon_{12} \\ \epsilon_{12} & \epsilon_{22} \end{pmatrix} + \lambda(\epsilon_{11} + \epsilon_{22})\mathbf{I}_2 \quad (4.147)$$

Now, we have obtained the constitutive relation for two-dimensional (2D) systems

$$\hat{\mathbf{T}} = 2\mu_{2D}\hat{\epsilon} + \lambda_{2D}\text{Tr}(\hat{\epsilon})\mathbf{I}_2 \quad (4.148)$$

With the same arguments discussed before for the three-dimensional case, instead the Eq. (4.145), the two-dimensional Bulk modulus is

$$K_{2D} = \lambda_{2D} + \mu_{2D} \quad (4.149)$$

Note that this is a very important issue to study the two-dimensional elastic properties of a given two-dimensional system. The relations between different two-dimensional elastic moduli is shown in Table 4.5.

Using the two-dimensional version of the Eq. (4.116), we can define the relations between elastic moduli and the stiffness coefficients (see also Table 4.5)

$$\begin{aligned} \begin{pmatrix} T_{11} \\ T_{22} \\ T_{12} \end{pmatrix} &= \begin{pmatrix} \mathcal{C}_{11} & \mathcal{C}_{12} & 0 \\ \mathcal{C}_{12} & \mathcal{C}_{11} & 0 \\ 0 & 0 & (\mathcal{C}_{11} - \mathcal{C}_{12}) \end{pmatrix} \begin{pmatrix} \epsilon_{11} \\ \epsilon_{22} \\ \epsilon_{12} \end{pmatrix} = \\ &= \begin{pmatrix} 2\mu_{2D} + \lambda_{2D} & \lambda_{2D} & 0 \\ \lambda_{2D} & 2\mu_{2D} + \lambda_{2D} & 0 \\ 0 & 0 & 2\mu_{2D} \end{pmatrix} \begin{pmatrix} \epsilon_{11} \\ \epsilon_{22} \\ \epsilon_{12} \end{pmatrix} \end{aligned} \quad (4.150)$$

*Plane stress
condition: 3D vs 2D
notation*

Imposing the plane stress boundary condition instead the plane strain one, the out-of-plane components of the stress tensor have to null, namely $\hat{\mathbf{T}}\mathbf{n} = 0$, where \mathbf{n} is the normal versor parallel to the x_3 -axis. Hence the stress tensor is in the following form

$$\hat{\mathbf{T}} = \begin{pmatrix} T_{11} & T_{12} & 0 \\ T_{12} & T_{22} & 0 \\ 0 & 0 & 0 \end{pmatrix} \quad (4.151)$$

Therefore, instead the Eq. (4.123) which is reported below

$$\hat{\epsilon} = \frac{1}{2\mu}\hat{\mathbf{T}} - \frac{\lambda}{2\mu(2\mu + 3\lambda)}\hat{\mathbf{I}}_3\text{Tr}(\hat{\sigma}), \quad (4.152)$$

we derive the two-dimensional inverse constitutive equation from the Eq. (4.148)

$$\hat{\epsilon} = \frac{1}{2\mu_{2D}}\hat{\mathbf{T}} - \frac{\lambda_{2D}}{4\mu_{2D}(\mu_{2D} + \lambda_{2D})}\hat{\mathbf{I}}_2\text{Tr}(\hat{\mathbf{T}}) \quad (4.153)$$

where all the matrices are in rank 2.

Table 4.5: Relations between different couples of two-dimensional elastic moduli. Here (λ_{2D}, μ_{2D}) are the Lamè coefficients, E_{2D} , μ_{2D} , and K_{2D} are the two-dimensional Young modulus, the two-dimensional Poisson ratio, and the two-dimensional Bulk modulus, respectively. Moreover, we show the relation between elastic moduli and stiffness coefficients $C_{\lambda\mu}$.

	(λ_{2D}, μ_{2D})	(K_{2D}, μ_{2D})	(μ_{2D}, ν_{2D})	(E_{2D}, ν_{2D})	(E_{2D}, μ_{2D})	$C_{\lambda\mu}$
λ_{2D}		$K_{2D} - \mu_{2D}$	$\frac{2\mu_{2D}\nu_{2D}}{1-\nu_{2D}}$	$\frac{\nu_{2D}E_{2D}}{(1+\nu_{2D})(1-\nu_{2D})}$	$\frac{2\mu_{2D}(E_{2D}-2\mu_{2D})}{4\mu_{2D}-E}$	C_{12}
μ_{2D}				$\frac{E_{2D}}{2(1+\nu_{2D})}$		$\frac{C_{11}-C_{12}}{2}$
K_{2D}	$\lambda_{2D} + \mu_{2D}$		$\frac{\mu_{2D}(1+\nu_{2D})}{(1-\nu_{2D})}$	$\frac{E_{2D}}{2(1-\nu_{2D})}$	$\frac{E_{2D}\mu_{2D}}{(4\mu_{2D}-E_{2D})}$	$\frac{C_{11}+C_{12}}{2}$
E_{2D}	$\frac{4\mu_{2D}(\lambda_{2D} + \mu_{2D})}{\lambda_{2D} + 2\mu_{2D}}$	$\frac{4K_{2D}\mu_{2D}}{K_{2D} + \mu_{2D}}$	$2(1+\nu_{2D})\mu_{2D}$			$\frac{C_{11}^2 - C_{12}^2}{C_{11}}$
ν_{2D}	$\frac{\lambda_{2D}}{\lambda_{2D} + 2\mu_{2D}}$	$\frac{K_{2D} - \mu_{2D}}{K_{2D} + \mu_{2D}}$			$\frac{E_{2D} - 2\mu_{2D}}{2\mu_{2D}}$	$\frac{C_{12}}{C_{11}}$

4.9 THE VIRIAL STRESS TENSOR

*The continuum
stress interpretation
of atomic force fields*

The continuum stress interpretation of atomic force fields is important because it allows the intensity and nature of internal interactions in materials to be measured. In order to obtain the atomic-molecular counterpart of the Cauchy stress tensor defined in Eq. (4.31), we consider a small volume V , with surface S , of a given elastic body. We suppose that in this region there are N atoms, described by positions \mathbf{x}_i for $i = 1 \dots N$. The number of the atoms is large enough to allow the definition of the macroscopic elastic fields (stress and strain) in that region, but it is also small enough to identify the effective stress with its average on the volume. The components of the position vector \mathbf{x}_i will be denoted with $(x_{i,1}, x_{i,2}, x_{i,3})$. In order to obtain the continuum-molecular equivalence it is useful to introduce the so-called virial form $\sum_{i=1}^N \mathbf{x}_i \otimes \mathbf{F}_i$ where the symbol \otimes represents the tensor product of vectors. The quantity \mathbf{F}_i is the total force acting on the i^{th} atom and, therefore, the equation of motion $\mathbf{F}_i = m_i \mathbf{a}_i$ leads to the balance

$$\sum_{i=1}^N \mathbf{x}_i \otimes \mathbf{F}_i = \sum_{i=1}^N m_i \mathbf{x}_i \otimes \mathbf{a}_i \quad (4.154)$$

where m_i is the mass of the i^{th} atom. The total force \mathbf{F}_i can be written as the sum of two contributes: the internal force $\mathbf{F}_i^{\text{int}}$, which is defined as the force on the i^{th} atom exerted by the other atoms contained in the volume V , and the external force $\mathbf{F}_i^{\text{est}}$, i.e. the force on the i^{th} atom exerted by the atoms outside the volume V and by any external action. Therefore the balance equation (4.154) becomes

$$\sum_{i=1}^N \mathbf{x}_i \otimes \mathbf{F}_i^{\text{int}} + \sum_{i=1}^N \mathbf{x}_i \otimes \mathbf{F}_i^{\text{est}} = \sum_{i=1}^N m_i \mathbf{x}_i \otimes \mathbf{a}_i \quad (4.155)$$

Moreover, because of the external force $\mathbf{F}_i^{\text{est}}$ is made by the surface force $\mathbf{F}_i^{\text{est}}(S)$, that is the force on the i^{th} atom exerted by the atoms outside the volume V , and by the body force $\mathbf{F}_i^{\text{est}}(V)$, i.e. the force on the i^{th} atom exerted by any external action (e.g. gravity), again we write the Eq. (4.154) as follows

$$\begin{aligned} \sum_{i=1}^N \mathbf{x}_i \otimes \mathbf{F}_i^{\text{int}} + \sum_{i=1}^N \mathbf{x}_i \otimes \mathbf{F}_i^{\text{est}}(V) + \sum_{i=1}^N \mathbf{x}_i \otimes \mathbf{F}_i^{\text{est}}(S) \\ = \sum_{i=1}^N m_i \mathbf{x}_i \otimes \frac{d\mathbf{v}_i}{dt} \end{aligned} \quad (4.156)$$

where \mathbf{v}_i is the velocity of the i^{th} atom, and the contribute $\mathbf{F}_i^{\text{est}}(S)$ can be different from zero only for atoms very close to the surface S , i.e. interacting with the atoms outside the volume

V. We observe that the velocity \mathbf{v}_i of each atom is composed by a term corresponding to an effective macroscopic drift $\mathbf{v}_i^{(0)}$ and a statistical (thermal) fluctuation $\delta\mathbf{v}_i$. Therefore, we substitute $\mathbf{v}_i = (\mathbf{v}_i^{(0)} + \delta\mathbf{v}_i)$ into Eq. (4.156)

$$\begin{aligned} \sum_{i=1}^N \mathbf{x}_i \otimes \mathbf{F}_i^{\text{int}} + \sum_{i=1}^N \mathbf{x}_i \otimes \mathbf{F}_i^{\text{est}}(\mathbf{V}) + \sum_{i=1}^N \mathbf{x}_i \otimes \mathbf{F}_i^{\text{est}}(\mathbf{S}) \\ = \sum_{i=1}^N m_i \mathbf{x}_i \otimes \frac{d\mathbf{v}_i^{(0)}}{dt} + \sum_{i=1}^N m_i \mathbf{x}_i \otimes \frac{d\delta\mathbf{v}_i}{dt} \end{aligned} \quad (4.157)$$

If we introduce the time average $\langle \cdot \rangle_\tau = \lim_{\tau \rightarrow \infty} \frac{1}{\tau} \int_0^\tau (\cdot) dt$ and we can develop the average value of the last term of the right hand side of Eq. (4.157) as follows

$$\begin{aligned} \left\langle \sum_{i=1}^N m_i \mathbf{x}_i \otimes \frac{d\delta\mathbf{v}_i}{dt} \right\rangle_\tau &= \left\langle \sum_{i=1}^N m_i \left[\frac{d}{dt} (\mathbf{x}_i \otimes \delta\mathbf{v}_i) - \mathbf{v}_i \otimes \delta\mathbf{v}_i \right] \right\rangle_\tau \\ &= \lim_{\tau \rightarrow \infty} \frac{1}{\tau} \int_0^\tau \sum_{i=1}^N m_i \frac{d}{dt} (\mathbf{x}_i \otimes \delta\mathbf{v}_i) dt - \left\langle \sum_{i=1}^N m_i \mathbf{v}_i \otimes \delta\mathbf{v}_i \right\rangle_\tau \\ &= \lim_{\tau \rightarrow \infty} \frac{1}{\tau} \sum_{i=1}^N m_i \mathbf{x}_i \otimes \delta\mathbf{v}_i \Big|_{t=0}^{t=\tau} - \left\langle \sum_{i=1}^N m_i \mathbf{v}_i \otimes \delta\mathbf{v}_i \right\rangle_\tau \end{aligned} \quad (4.158)$$

The virial theorem

We are dealing with an elastic solid body which is a stable bound system, i.e. a system that hold together. In other words, coordinates and velocities for all particles remain finite. In this case, the quantity $G(t) = \sum_{i=1}^N m_i \mathbf{x}_i \otimes \delta\mathbf{v}_i$ is a limited function with extremes, G_{min} and G_{max} , and its average goes to zero in the limit of very long times τ

$$\begin{aligned} \lim_{\tau \rightarrow \infty} \frac{1}{\tau} \sum_{i=1}^N m_i \mathbf{x}_i \otimes \delta\mathbf{v}_i \Big|_{t=0}^{t=\tau} \\ = \lim_{\tau \rightarrow \infty} \frac{G(\tau) - G(0)}{\tau} \leq \lim_{\tau \rightarrow \infty} \frac{G_{\text{max}} - G_{\text{min}}}{\tau} = 0 \end{aligned} \quad (4.159)$$

Moreover, the last term in Eq. (4.158) can be developed by recalling the decomposition of the velocity $\mathbf{v}_i = (\mathbf{v}_i^{(0)} + \delta\mathbf{v}_i)$, and by using the statistical independence of $\mathbf{v}_i^{(0)}$ and $\delta\mathbf{v}_i$ as follows

$$\left\langle \sum_{i=1}^N m_i \mathbf{v}_i \otimes \delta\mathbf{v}_i \right\rangle_\tau = \left\langle \sum_{i=1}^N m_i \mathbf{v}_i^{(0)} \otimes \delta\mathbf{v}_i \right\rangle_\tau + \left\langle \sum_{i=1}^N m_i \delta\mathbf{v}_i \otimes \delta\mathbf{v}_i \right\rangle_\tau \quad (4.160)$$

The first average value in the right hand side is zero, because the average value of the velocity fluctuation $\delta\mathbf{v}_i$ is null. Conversely,

the second average value is a quadratic term in the fluctuation $\delta \mathbf{v}_i$ and therefore it is not negligible. Hence, this important equality has been obtained from Eq. (4.158)

$$\left\langle \sum_{i=1}^N m_i \mathbf{x}_i \otimes \frac{d\delta \mathbf{v}_i}{dt} \right\rangle_{\tau} = - \left\langle \sum_{i=1}^N m_i \delta \mathbf{v}_i \otimes \delta \mathbf{v}_i \right\rangle_{\tau} \quad (4.161)$$

Summing up, the virial balance in Eq. (4.157) can be written as

$$\begin{aligned} & \left\langle \sum_{i=1}^N \mathbf{x}_i \otimes \mathbf{F}_i^{\text{int}} \right\rangle_{\tau} + \left\langle \sum_{i=1}^N \mathbf{x}_i \otimes \mathbf{F}_i^{\text{est}}(V) \right\rangle_{\tau} + \left\langle \sum_{i=1}^N \mathbf{x}_i \otimes \mathbf{F}_i^{\text{est}}(S) \right\rangle_{\tau} \\ & = \left\langle \sum_{i=1}^N m_i \mathbf{x}_i \otimes \frac{d\mathbf{v}_i^{(0)}}{dt} \right\rangle_{\tau} - \left\langle \sum_{i=1}^N m_i \delta \mathbf{v}_i \otimes \delta \mathbf{v}_i \right\rangle_{\tau} \end{aligned} \quad (4.162)$$

Here, the term with the body force $\mathbf{F}_i^{\text{est}}(V)$ corresponds to a volume integral, the term with the surface force $\mathbf{F}_i^{\text{est}}(S)$ corresponds to a surface integral and the first sum in the right hand side can be converted to a volume integral by observing that $d\mathbf{v}_i^{(0)}/dt$ is the macroscopic acceleration field \mathbf{a} . By identifying these atomic terms with their continuum counterparts, we can rewrite

$$\begin{aligned} & \left\langle \sum_{i=1}^N \mathbf{x}_i \otimes \mathbf{F}_i^{\text{int}} \right\rangle_{\tau} + \left\langle \int_V \mathbf{x} \otimes \mathbf{F}^{\text{est}}(V) d\mathbf{x} \right\rangle_{\tau} + \left\langle \int_S \mathbf{x} \otimes \mathbf{F}^{\text{est}}(S) dS \right\rangle_{\tau} \\ & = \left\langle \int_V \rho \mathbf{x} \otimes \mathbf{a} d\mathbf{x} \right\rangle_{\tau} - \left\langle \sum_{i=1}^N m_i \delta \mathbf{v}_i \otimes \delta \mathbf{v}_i \right\rangle_{\tau} \end{aligned} \quad (4.163)$$

As described in Section 4.3, the body and the surface forces can be identified as $\mathbf{F}^{\text{est}}(V) = \mathbf{b}$, and $\mathbf{F}^{\text{est}}(S) = \hat{\mathbf{T}}\mathbf{n}$, where $\hat{\mathbf{T}}$ is the stress tensor and \mathbf{n} is the unit vector normal to S . Therefore, the balance equation assumes the form

$$\begin{aligned} & \left\langle \sum_{i=1}^N \mathbf{x}_i \otimes \mathbf{F}_i^{\text{int}} \right\rangle_{\tau} + \left\langle \int_V \mathbf{x} \otimes \mathbf{b} d\mathbf{x} \right\rangle_{\tau} + \left\langle \int_S \mathbf{x} \otimes (\hat{\mathbf{T}}\mathbf{n}) dS \right\rangle_{\tau} \\ & = \left\langle \int_V \rho \mathbf{x} \otimes \mathbf{a} d\mathbf{x} \right\rangle_{\tau} - \left\langle \sum_{i=1}^N m_i \delta \mathbf{v}_i \otimes \delta \mathbf{v}_i \right\rangle_{\tau}, \end{aligned} \quad (4.164)$$

or equivalently through its components

$$\begin{aligned} & \left\langle \sum_{i=1}^N x_{i,k} F_{i,h}^{\text{int}} \right\rangle_{\tau} + \left\langle \int_V x_k b_h d\mathbf{x} \right\rangle_{\tau} + \left\langle \int_S x_k T_{hp} n_p dS \right\rangle_{\tau} \\ & = \left\langle \int_V \rho x_k a_h d\mathbf{x} \right\rangle_{\tau} - \left\langle \sum_{i=1}^N m_i \delta v_{i,k} \delta v_{i,h} \right\rangle_{\tau} \end{aligned} \quad (4.165)$$

Applying the divergence theorem (see Appendix A.2) the surface integral can be converted into a volume integral as follows

$$\begin{aligned} \left\langle \sum_{i=1}^N x_{i,k} F_{i,h}^{\text{int}} \right\rangle_{\tau} + \left\langle \int_V x_k b_h \mathbf{dx} \right\rangle_{\tau} + \left\langle \int_V \frac{\partial}{\partial x_p} (x_k T_{hp}) \mathbf{dx} \right\rangle_{\tau} \\ = \left\langle \int_V \rho x_k a_h \mathbf{dx} \right\rangle_{\tau} - \left\langle \sum_{i=1}^N m_i \delta v_{i,k} \delta v_{i,h} \right\rangle_{\tau} \end{aligned} \quad (4.166)$$

The derivative can be developed by obtaining

$$\begin{aligned} \left\langle \sum_{i=1}^N x_{i,k} F_{i,h}^{\text{int}} \right\rangle_{\tau} + \left\langle \int_V x_k b_h \mathbf{dx} \right\rangle_{\tau} + \left\langle \int_V \left(\delta_{kp} T_{hp} + x_k \frac{\partial T_{hp}}{\partial x_p} \right) \mathbf{dx} \right\rangle_{\tau} \\ = \left\langle \int_V \rho x_k a_h \mathbf{dx} \right\rangle_{\tau} - \left\langle \sum_{i=1}^N m_i \delta v_{i,k} \delta v_{i,h} \right\rangle_{\tau} \end{aligned} \quad (4.167)$$

Therefore, we can collect the terms as shown in the following relation

$$\begin{aligned} \left\langle \sum_{i=1}^N x_{i,k} F_{i,h}^{\text{int}} \right\rangle_{\tau} + \left\langle \int_V T_{hk} \mathbf{dx} \right\rangle_{\tau} + \left\langle \sum_{i=1}^N m_i \delta v_{i,k} \delta v_{i,h} \right\rangle_{\tau} \\ + \left\langle \int_V x_k \left(\frac{\partial T_{hp}}{\partial x_p} + b_h - \rho a_h \right) \mathbf{dx} \right\rangle_{\tau} = 0 \end{aligned} \quad (4.168)$$

The quantity in brackets is zero because of the Equation (4.54), $\frac{\partial T_{ji}}{\partial x_i} + b_j - \rho a_j = 0$, which describes the motion of any elastic body. Moreover, we can define the average value of the stress tensor over the volume V , namely $\bar{T}_{hk} = \frac{1}{V} \int_V T_{hk} \mathbf{dx}$. It follows that the balance equation for the virial sum leads to the following definition of stress, based on atomic quantities

The virial stress tensor

$$\langle \bar{T}_{hk} \rangle_{\tau} = -\frac{1}{V} \left\langle \sum_{i=1}^N m_i \delta v_{i,k} \delta v_{i,h} \right\rangle_{\tau} - \frac{1}{V} \left\langle \sum_{i=1}^N x_{i,k} F_{i,h}^{\text{int}} \right\rangle_{\tau} \quad (4.169)$$

This very important relation, called virial stress tensor, links among microscopic atomic quantities and macroscopic observables and it can be written in tensor form, as follows

$$\langle \bar{\hat{T}} \rangle_{\tau} = -\frac{1}{V} \left\langle \sum_{i=1}^N m_i \delta \mathbf{v}_i \otimes \delta \mathbf{v}_i \right\rangle_{\tau} - \frac{1}{V} \left\langle \sum_{i=1}^N \mathbf{x}_i \otimes \mathbf{F}_i^{\text{int}} \right\rangle_{\tau} \quad (4.170)$$

This result has innumerable applications in the field of the molecular dynamic simulations of mechanical structures. In fact, it enables us to evaluate the macroscopic Cauchy stress in an elastic solid system defined at the atomic or molecular level. It is

important to observe that the first kinetic term considers the fluctuations of the velocities and not the absolute velocities: it is very important for analyzing thermoelasticity with molecular dynamic simulations [71]. To conclude, we have obtained the atomic-molecular counterpart of the Cauchy stress tensor, as given in Eq. (4.170): we point out that this result is exactly correct (at any time) for systems undergoing arbitrary time-dependent deformations.

4.9.1 Physical meaning of the virial stress

We add some comments on other quantities defined for a system of particles similar to that above derived. This discussion is useful to avoid some errors and misunderstandings often encountered in the development of these concepts. The *pressure stress* $\langle \hat{\Pi} \rangle_\tau$ is the most commonly used definition of stress-like quantity in discrete particle systems

The pressure tensor

$$\langle \hat{\Pi} \rangle_\tau = -\frac{1}{V} \left\langle \sum_{i=1}^N m_i \frac{d\mathbf{x}_i}{dt} \otimes \frac{d\mathbf{x}_i}{dt} \right\rangle_\tau - \frac{1}{V} \left\langle \sum_{i=1}^N \mathbf{x}_i \otimes \mathbf{F}_i^{\text{int}} \right\rangle_\tau \quad (4.171)$$

This quantity includes two terms [72, 73]. The first part depends on the mass and on the absolute velocity of atomic particles, reflecting the assertion that mass transfer causes pressure to be applied on stationary spatial surfaces external to an atomic-particle system. The second part depends on interatomic forces and atomic positions, providing a continuum measure for the internal mechanical interactions between particles. Historic derivations of the *pressure stress* include generalization from the virial theorem of Clausius or Maxwell for gas pressure and solution of the spatial equation of balance of momentum [74, 75]. However, the *pressure stress* is not a measure for the Cauchy mechanical stress in an elastic body [76]. We have proved, in the previous Section 4.9, that the absolute velocities $\mathbf{v}_i = d\mathbf{x}_i/dt$ in Eq. (4.171) must be substituted with their fluctuations $\delta\mathbf{v}_i$ for obtaining the Cauchy stress, as shown in Eq. (4.170).

We also remark that the virial approach or virial theorem (Clausius 1870), as applied to gas systems for the evaluation of external pressure strictly in the statistical average sense, correctly captures this effect. The key is that the pressure represents external forces between an atomic system and a container, where the pressure is generated by the collisions of the atoms on the container. In contrast, stress represents internal forces between particles inside a body, and it is not generated by collisions against a wall. Indeed, Eq. (4.171) correctly describes the macroscopic pressure of a gas system under the three following conditions: *i*) the system is in statistical equilibrium, *ii*) the pressure must be interpreted in a time and volume averaged sense, i.e. fluctuations at the molecular

level are assumed to average out over time and space, and *iii*) the pressure must be recognized as the average force per unit area on the wall of a physical container holding the gas system. The *pressure stress* given in Eq. (4.171) can be correctly applied in molecular dynamic simulations when one is analyzing the pressure (or pressure tensor) of a gas or a fluid at thermodynamic equilibrium.

Furthermore, we remark that Eq. (4.170) represents the atomic counterpart of the Cauchy stress when it is considered in an Eulerian (spatial) reference frame. Andia et al. (see Refs.[77, 78]), have taken a Lagrangian (material) frame of reference to show that the stress in the atomic system does not contain velocity term at all, by obtaining the further relation

$$\langle \hat{\mathbf{T}}_{\mathcal{E}} \rangle_{\tau} = -\frac{1}{V} \left\langle \sum_{i=1}^N \mathbf{x}_i \otimes \mathbf{F}_i^{\text{int}} \right\rangle_{\tau} \quad (4.172)$$

For example, Gao and Weiner (see Ref.[79]) clearly show that the dynamic term is included only in an Eulerian (spatial) reference frame and not in a Lagrangian frame of reference. They also show the equivalence between the Eulerian (spatial) and the Lagrangian (material) definitions of virial stress [79]. Anyway, in molecular dynamic simulations the Eulerian point of view must be always considered in order to draw coherent comparisons among numerical and continuum results [71].

4.9.2 The atomistic nonlinear Cauchy stress

The virial stress defined as in Eq. (4.170) corresponds to the Cauchy stress only in the framework of the linear approximation. To achieve also the nonlinear elastic behavior of the system, we need to derive a different form of the atomistic stress. A relation between the atomic stress and the Cauchy stress tensor can be straightforwardly derived by the strain energy function, as in Eq. (4.113).

In a given system, the strain energy function $\mathcal{U}(\hat{\epsilon})$ can be identified with the thermodynamic potential of the corresponding statistical ensemble (i.e. the internal energy for an isolated system, the Helmholtz free energy for a system in equilibrium with a thermal bath, etc...). By considering the basic case of an isolated system at $T = 0$ K, the internal energy corresponds to the interatomic potential energy \mathcal{U} which is a function of the atomic positions \mathbf{x}_i $i = 1, \dots, N$, namely: $\mathcal{U} = \mathcal{U}(\{\mathbf{x}_i\})$. In absence of any external load, the system lies in the minimum energy configuration $\{\mathbf{x}_i^0\}$. If a uniform strain field $\hat{\epsilon}$ is applied, the new atomic positions can be expressed as $\mathbf{x}_i = (\hat{\mathbf{I}} + \hat{\epsilon})\mathbf{x}_i^0$ and the correspond-

*Thermodynamical
identification of the
strain energy*

ing internal energy is given by $\mathcal{U}(\{(\hat{\mathbb{I}} + \hat{\epsilon})\mathbf{x}_i^0\})$. Thus, the strain energy density can be written as

$$\mathcal{U}(\hat{\epsilon}) = \frac{1}{V} \mathcal{U}(\{(\hat{\mathbb{I}} + \hat{\epsilon})\mathbf{x}_i^0\}) \quad (4.173)$$

where V is the volume of the system. According to Eq. (4.113), the stress tensor is given by

The nonlinear form of the Cauchy stress

$$\begin{aligned} \hat{\mathbb{T}} &= \frac{\partial \mathcal{U}(\hat{\epsilon})}{\partial \hat{\epsilon}} = \frac{1}{V} \sum_i^N \frac{\partial \mathcal{U}}{\partial \mathbf{x}_i} \frac{\partial \mathbf{x}_i}{\partial \hat{\epsilon}} \\ &= \frac{1}{V} \sum_i^N \frac{\partial \mathcal{U}}{\partial \mathbf{x}_i} \frac{\partial}{\partial \hat{\epsilon}} (\hat{\mathbb{I}} + \hat{\epsilon}) \mathbf{x}_i^0 \\ &= \frac{1}{V} \sum_i^N \frac{\partial \mathcal{U}}{\partial \mathbf{x}_i} \otimes \mathbf{x}_i^0 \\ &= -\frac{1}{V} \sum_i^N \mathbf{x}_i^0 \otimes \mathbf{F}_i^{\text{int}} \end{aligned} \quad (4.174)$$

This expression corresponds to that in Eq. (4.170) but the positions \mathbf{x}_i in the deformed configuration are replaced by the positions \mathbf{x}_i^0 of the system in the minimum energy state. Note that Eq. (4.170) is coincident with the first-order expansion in $\hat{\epsilon}$ of Eq. (4.174). Therefore we can obtain that to take in account nonlinear effect of stress up to the second order in the strain, we need to evaluate the following version of the virial stress tensor instead the Eq. (4.170)

$$\frac{1}{V} \sum_i^N \frac{\partial \mathcal{U}}{\partial \mathbf{x}_i} \otimes \mathbf{x}_i^0 = \frac{1}{V} \sum_i^N \frac{\partial \mathcal{U}}{\partial \mathbf{x}_i} \otimes \mathbf{x}_i + o(\epsilon^2) \quad (4.175)$$

$$\mathbf{x}_i^0 = \mathbf{x}_i + o(\epsilon), \text{ and } \frac{\partial V}{\partial \mathbf{x}_i} = o(\epsilon) \quad (4.176)$$

4.9.3 Atomic stress for two-body interactions

In this Section we specialize the general result given in Eq. (4.170) to the case of two-body interactions among the atoms of the solid elastic body. We remember that the internal force $\mathbf{F}_i^{\text{int}}$ on the i^{th} atom is given by all the forces exerted by other atoms contained into the volume V . Therefore, the quantity $\mathbf{F}_i^{\text{int}}$ can be written as the sum $\sum_{j \neq i}^N \mathbf{f}_{ij}$ where \mathbf{f}_{ij} is the force applied on the i^{th} atom by the j^{th} atom. It follows that Eq. (4.170) can be converted to

$$\langle \hat{\mathbb{T}} \rangle_{\tau} = -\frac{1}{V} \left\langle \sum_{i=1}^N m_i \delta \mathbf{v}_i \otimes \delta \mathbf{v}_i \right\rangle_{\tau} - \frac{1}{V} \left\langle \sum_{i=1}^N \mathbf{x}_i \otimes \sum_{j \neq i}^N \mathbf{f}_{ij} \right\rangle_{\tau} \quad (4.177)$$

The last term can be split in two identical terms as follows

$$\begin{aligned} \langle \hat{\mathbb{T}} \rangle_{\tau} &= -\frac{1}{V} \left\langle \sum_{i=1}^N m_i \delta \mathbf{v}_i \otimes \delta \mathbf{v}_i \right\rangle_{\tau} \\ &\quad - \frac{1}{2V} \left\langle \sum_{i=1}^N \mathbf{x}_i \otimes \sum_{j \neq i}^N \mathbf{f}_{ij} \right\rangle_{\tau} + \frac{1}{2V} \left\langle \sum_{i=1}^N \mathbf{x}_i \otimes \sum_{j \neq i}^N \mathbf{f}_{ji} \right\rangle_{\tau} \end{aligned} \quad (4.178)$$

where we have utilized the Newton's third law $\mathbf{f}_{ji} = -\mathbf{f}_{ij}$. In the last double sum we can exchange the names of the summed indices, by obtaining

$$\langle \hat{\mathbb{T}} \rangle_{\tau} = -\frac{1}{V} \left\langle \sum_{i=1}^N m_i \delta \mathbf{v}_i \otimes \delta \mathbf{v}_i \right\rangle_{\tau} + \frac{1}{2V} \left\langle \sum_{i=1}^N (\mathbf{x}_j - \mathbf{x}_i) \otimes \sum_{j \neq i}^N \mathbf{f}_{ij} \right\rangle_{\tau} \quad (4.179)$$

Moreover, we define the vector from the i^{th} atom to the j^{th} atom with $\mathbf{x}_{ij} = (\mathbf{x}_j - \mathbf{x}_i)$. It follows that

$$\langle \hat{\mathbb{T}} \rangle_{\tau} = -\frac{1}{V} \left\langle \sum_{i=1}^N m_i \delta \mathbf{v}_i \otimes \delta \mathbf{v}_i \right\rangle_{\tau} + \frac{1}{2V} \left\langle \sum_{i=1}^N \sum_{j \neq i}^N \mathbf{x}_{ij} \otimes \mathbf{f}_{ij} \right\rangle_{\tau} \quad (4.180)$$

This form is particularly useful for the applications to the molecular dynamic simulations since the force term \mathbf{f}_{ij} is directly linked with the interaction potential energy $U^{2B}(r)$ between two atoms

$$\mathbf{f}_{ij} = \frac{dU^{2B}(r)}{dr} \Big|_{r=|\mathbf{x}_{ij}|} \frac{\mathbf{x}_{ij}}{|\mathbf{x}_{ij}|} \quad (4.181)$$

By substituting Eq. (4.181) into Eq. (4.180) we obtain the final relation

$$\begin{aligned} \langle \hat{\mathbb{T}} \rangle_{\tau} &= -\frac{1}{V} \left\langle \sum_{i=1}^N m_i \delta \mathbf{v}_i \otimes \delta \mathbf{v}_i \right\rangle_{\tau} \\ &\quad + \frac{1}{2V} \left\langle \sum_{i=1}^N \sum_{j \neq i}^N \mathbf{x}_{ij} \otimes \mathbf{x}_{ij} \left(\frac{1}{r} \frac{dU^{2B}(r)}{dr} \right) \Big|_{r=|\mathbf{x}_{ij}|} \right\rangle_{\tau} \end{aligned} \quad (4.182)$$

This form is useful since it considers only quantities available in standard molecular dynamic procedures and it is perfectly suited for being used under the typical assumption of periodic boundary conditions. In fact, when the periodic boundary conditions are applied, the system interacts with the copies of the unit cell which are called images. When a molecule passes through one face of the unit cell, it reappears on the opposite face with the

same velocity and, therefore, the definition of internal forces and external ones is not applicable. Nevertheless, the stress expression given in Eq. (4.182) solves the problem, being written in terms of \mathcal{U}^{2B} . However, it is important to consider the correct periodicity in the definition of the vectors $\mathbf{x}_{ij} = (\mathbf{x}_j - \mathbf{x}_i)$ by applying the standard minimum-image convention [80].

Part II

ELASTIC BEHAVIOR OF GRAPHENE

“The most exciting phrase to hear in science, the one that heralds new discoveries, is not ‘Eureka!’ but ‘That’s funny...’”

Isaac Asimov (1920-1992)

Contents

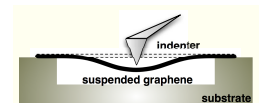
5.1	Elastic properties of graphene	78
5.2	The computational approach	83
5.3	The stress-strain approach	86

The elastic properties of graphene have been recently determined by atomic force microscope nanoindentation [12, 81], measuring the deformation of a free-standing monolayer. In particular, in Ref. [12] the experimental force-deformation relation has been expressed as a phenomenological nonlinear scalar relation between the applied stress (σ) and the observed strain (ϵ)

$$\sigma = E\epsilon + D\epsilon^2 \quad (5.1)$$

where E and D are, respectively, the Young modulus and an effective nonlinear (third-order) elastic modulus of the two dimensional carbon sheet. The reported experimental values are: $E = 340 \pm 40 \text{ Nm}^{-1}$ and $D = -690 \pm 120 \text{ Nm}^{-1}$. While the first result is consistent with previous existing data [82, 14, 83, 15], the above value for D represents so far the only available information about the nonlinear elasticity of a one-atom thick carbon sheet. Although nonlinear features are summarized in Eq. (5.1) by one effective parameter D , continuum elasticity theory predicts the existence of three independent third-order parameters C_{ijk} for graphene, as reported below. In other words, while Eq. (5.1) represents a valuable effective relation for the interpretation of a complex experiment [12], it must be worked out a more rigorous theoretical picture in order to properly define all the nonlinear elastic constants of graphene and to understand the physical meaning of D .

This corresponds to the content of the present Chapter where we investigate the constitutive nonlinear stress-strain relation of graphene for graphene stretching elasticity and we calculate all the corresponding nonlinear elastic moduli, by combining continuum elasticity and tight-binding atomistic simulation (TB-AS) [84]. Present results represent a robust picture on elastic behavior and provide the proper interpretation of recent experiments. In



Scheme of the indentation of a suspended monolayer graphene.

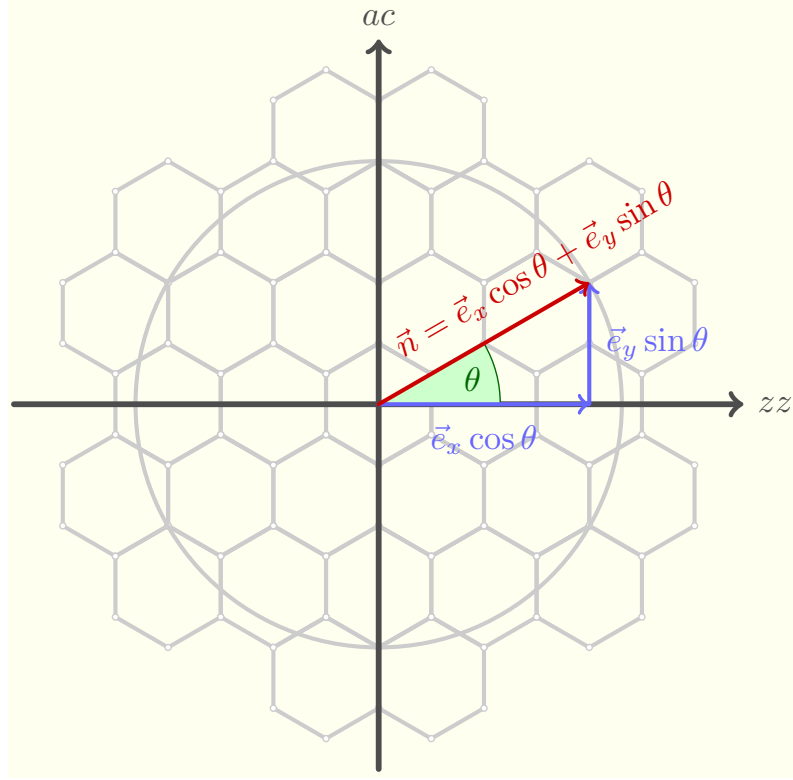


Figure 5.1: By applying an axial tension σ along the arbitrary direction \vec{n} ($\theta = \vec{z}\vec{z} \angle \vec{n}$), the Cauchy stress tensor $\hat{T} = \partial U / \partial \hat{\epsilon}$ is $\hat{T} = \sigma \vec{n} \otimes \vec{n}$, where the in-plane stress components are defined, respectively, as $T_{xx} = \sigma \cos^2 \theta$, $T_{xy} = \sigma \cos \theta \sin \theta$, and $T_{yy} = \sigma \sin^2 \theta$.

particular, we discuss the physical meaning of the effective nonlinear elastic modulus there introduced and we predict its value in good agreement with available data. Finally, a hyperelastic softening behavior is observed and discussed, so determining the failure properties of graphene.

5.1 ELASTIC PROPERTIES OF GRAPHENE

To obtain the nonlinear stress-strain relation of an elastic membrane, we need at first to elaborate an expression for the corresponding strain energy function U (per unit area), which was defined in Eq. (4.114) as follows

$$U(\hat{\epsilon}) = \frac{1}{2} \mathcal{C}_{ijkh} \epsilon_{ij} \epsilon_{kh} + \frac{1}{6} \mathcal{C}_{ijkhnm} \epsilon_{ij} \epsilon_{kh} \epsilon_{nm} \quad (5.2)$$

Reminding that the \mathcal{C}_{ijkh} and the \mathcal{C}_{ijkhnm} denote the second order elastic constant (SEOC) and the third order elastic constant (TOEC), respectively

$$\mathcal{C}_{ijkh} = \frac{\partial^2 U}{\partial \epsilon_{ij} \partial \epsilon_{kh}}; \quad \mathcal{C}_{ijkhnm} = \frac{\partial^3 U}{\partial \epsilon_{ij} \partial \epsilon_{kh} \partial \epsilon_{nm}} \quad (5.3)$$

Since, as illustrated in Figure 5.1, the graphene lattice is hexagonal, it is useful to consider the coordinate set $\alpha = (x + iy)$ and $\beta = (x - iy)$ [85], where the x and y directions are respectively identified with the zig-zag (zz) and the armchair (ac) directions. We introduce the corresponding form for the strain energy function U as follows

$$2U = \lambda_{ijkh} \epsilon_{ij} \epsilon_{kh} + \Lambda_{ijkhnm} \epsilon_{ij} \epsilon_{kh} \epsilon_{nm} \quad (5.4)$$

where λ_{ijkh} and Λ_{ijkhnm} are parameters analogous to the C_{ijkh} and the C_{ijkhnm} in the Eq. (5.2). Because of the six-fold symmetry of hexagonal lattices, the strain energy function U have to be invariant under a rotation of $\pi/3$ about the z -axis (normal to the graphene plane).

$$\begin{aligned} \alpha &= (x + iy) \longrightarrow \alpha e^{\frac{2\pi i}{6}} \\ \beta &= (x - iy) \longrightarrow \beta e^{-\frac{2\pi i}{6}} \end{aligned} \quad (5.5)$$

Since $(e^{\pm \frac{2\pi i}{6}})^6 = 1$ and $e^{\frac{2\pi i}{6}} e^{-\frac{2\pi i}{6}} = 1$, the parameters λ_{ijkh} and Λ_{ijkhnm} must have among their indices 6-times α or β , or an equal number of them to be invariant under these transformations. We get the follows complete set of elastic moduli for an hexagonal symmetry which is composed by a couple of linear moduli λ_1 and λ_2 and by three nonlinear independent elastic coefficients, namely Λ_i , $i = 1, 2, 3$, all expressed in units of force/length as follows

$$\begin{aligned} \lambda_1 &= \lambda_{\alpha\alpha\beta\beta}; \quad \lambda_2 = \lambda_{\alpha\beta\alpha\beta}; \\ \Lambda_1 &= \Lambda_{\alpha\alpha\alpha\alpha\alpha\alpha} \equiv \Lambda_{\beta\beta\beta\beta\beta\beta}; \\ \Lambda_2 &= \Lambda_{\alpha\alpha\beta\beta\alpha\beta}; \quad \Lambda_3 = \Lambda_{\alpha\beta\alpha\beta\alpha\beta} \end{aligned} \quad (5.6)$$

Hence the strain energy function U can be written considering separately the quadratic terms and the cubic terms, $U = U^{(2)} + U^{(3)}$, the Eq. (5.4) is given by

$$\begin{aligned} 2U^{(2)} &= +\lambda_1 \epsilon_{\alpha\alpha} \epsilon_{\beta\beta} + \lambda_2 \epsilon_{\alpha\beta}^2 \\ 6U^{(3)} &= +\Lambda_1 (\epsilon_{\alpha\alpha}^3 + \epsilon_{\beta\beta}^3) + \Lambda_2 \epsilon_{\alpha\alpha} \epsilon_{\beta\beta} \epsilon_{\alpha\beta} + \Lambda_3 \epsilon_{\alpha\beta}^3, \end{aligned} \quad (5.7)$$

In order to further proceed we must better focus the strain definition which in elasticity theory is twofold: we can introduce the so-called small strain tensor $\hat{\epsilon} = \frac{1}{2}(\vec{\nabla}\vec{u} + \vec{\nabla}\vec{u}^T)$, being \vec{u} the displacement field, or the Lagrangian strain $\hat{\eta} = \frac{1}{2}(\vec{\nabla}\vec{u} + \vec{\nabla}\vec{u}^T + \vec{\nabla}\vec{u}^T \vec{\nabla}\vec{u})$. While $\hat{\epsilon}$ takes into account only the physical nonlinearity features (i.e. a nonlinear stress-strain dependence observed in regime of small deformation), $\hat{\eta}$ describes any possible source of nonlinearity, including both physical and geometrical (large deformation)

ones. To turn back in Cartesian coordinates, x, y , we can derive the strain elements from their definition

$$\begin{aligned}\epsilon_{\alpha\beta} &= \frac{1}{2} \left(\frac{\partial u_\alpha}{\partial \beta} + \frac{\partial u_\beta}{\partial \alpha} \right) = \epsilon_{xx} + \epsilon_{yy} \\ \epsilon_{\alpha\alpha} &= \frac{1}{2} \left(\frac{\partial u_\alpha}{\partial \alpha} + \frac{\partial u_\alpha}{\partial \alpha} \right) = \epsilon_{xx} - \epsilon_{yy} + 2i\epsilon_{xy} \\ \epsilon_{\beta\beta} &= \frac{1}{2} \left(\frac{\partial u_\beta}{\partial \beta} + \frac{\partial u_\beta}{\partial \beta} \right) = \epsilon_{xx} - \epsilon_{yy} - 2i\epsilon_{xy}\end{aligned}\quad (5.8)$$

Combining the Eq. (5.7) with the Eq. (5.8) we have a complete relationship for density of energy in a non linear form

$$\begin{aligned}2\mathbf{U}^{(2)} &= + \epsilon_{xx}^2 (\lambda_1 + \lambda_2) + \epsilon_{yy}^2 (\lambda_1 + \lambda_2) \\ &\quad + 2\epsilon_{xx}\epsilon_{yy}(-\lambda_1 + \lambda_2) + 4\epsilon_{xy}^2 \lambda_1 \\ 6\mathbf{U}^{(3)} &= + \epsilon_{xx}^3 (2\Lambda_1 + \Lambda_2 + \Lambda_3) \\ &\quad + \epsilon_{yy}^3 (-2\Lambda_1 + \Lambda_2 + \Lambda_3) \\ &\quad + \epsilon_{xx}^2 \epsilon_{yy} (-6\Lambda_1 - \Lambda_2 + 3\Lambda_3) \\ &\quad + \epsilon_{xx} \epsilon_{yy}^2 (6\Lambda_1 - \Lambda_2 + 3\Lambda_3) \\ &\quad + \epsilon_{xy}^2 \epsilon_{xx} (-24\Lambda_1 + 4\Lambda_2) \\ &\quad + \epsilon_{xy}^2 \epsilon_{yy} (24\Lambda_1 + 4\Lambda_2)\end{aligned}\quad (5.9)$$

Otherwise we can write it also in terms of stiffness tensor coefficients by the complete expansion of the Eq. (5.2)

$$\begin{aligned}2\mathbf{U}^{(2)} &= \mathcal{C}_{11}\epsilon_{xx}^2 + \mathcal{C}_{22}\epsilon_{yy}^2 + 2\mathcal{C}_{12}\epsilon_{xx}\epsilon_{yy} + 4\mathcal{C}_{66}\epsilon_{xy}^2 \\ &\quad + 2\mathcal{C}_{16}\epsilon_{xx}\epsilon_{xy} + 2\mathcal{C}_{26}\epsilon_{yy}\epsilon_{xy} \\ 6\mathbf{U}^{(3)} &= +\mathcal{C}_{111}\epsilon_{xx}^3 + \mathcal{C}_{222}\epsilon_{yy}^3 \\ &\quad + 3\mathcal{C}_{112}\epsilon_{xx}^2\epsilon_{yy} + 3\mathcal{C}_{122}\epsilon_{xx}\epsilon_{yy}^2 \\ &\quad + 12\mathcal{C}_{166}\epsilon_{xx}\epsilon_{xy}^2 + 12\mathcal{C}_{266}\epsilon_{yy}\epsilon_{xy}^2 \\ &\quad + 6\mathcal{C}_{116}\epsilon_{xx}^2\epsilon_{xy} + 6\mathcal{C}_{226}\epsilon_{yy}^2\epsilon_{xy} \\ &\quad + 12\mathcal{C}_{126}\epsilon_{xx}\epsilon_{yy}\epsilon_{xy} + 8\mathcal{C}_{666}\epsilon_{xy}^3\end{aligned}\quad (5.10)$$

By comparing term by term the Eq. (5.9) and the Eq. (5.10), we get the relationships between the linear elastic coefficients λ_1, λ_2 and the nonlinear elastic coefficients Λ_1, Λ_2 and Λ_3 with the second order elastic constants and the third order elastic constants, respectively Thus we obtain that

$$\lambda_1 = \frac{1}{2}(\mathcal{C}_{11} - \mathcal{C}_{12}), \quad \lambda_2 = \frac{1}{2}(\mathcal{C}_{11} + \mathcal{C}_{12}) \quad (5.12)$$

$$\begin{aligned}\Lambda_1 &= \frac{1}{12}(\mathcal{C}_{111} - \mathcal{C}_{222}), \quad \Lambda_2 = \frac{1}{4}(\mathcal{C}_{222} - \mathcal{C}_{112}), \\ \Lambda_3 &= \frac{1}{12}(2\mathcal{C}_{111} - \mathcal{C}_{222} + 3\mathcal{C}_{112}).\end{aligned}\quad (5.13)$$

Furthermore, we obtain that the hexagonal symmetry dictates 2-independent \mathcal{C}_{ijkl} ($\mathcal{C}_{11}, \mathcal{C}_{12}$) as well as we aspect for an isotropic

material, and 3-independent \mathcal{C}_{ijklmn} ($\mathcal{C}_{1111}, \mathcal{C}_{2222}, \mathcal{C}_{112}$). There are some linear terms null, $\mathcal{C}_{16} = \mathcal{C}_{26} = 0$, and some non-linear terms, $\mathcal{C}_{116} = \mathcal{C}_{226} = \mathcal{C}_{126} = \mathcal{C}_{666} = 0$ as well. For the same symmetry reasons the follows relations between stiffness coefficients have been derived: $\mathcal{C}_{11} = \mathcal{C}_{22}$, $2\mathcal{C}_{66} = \mathcal{C}_{11} - \mathcal{C}_{12}$, $\mathcal{C}_{122} = \mathcal{C}_{111} - \mathcal{C}_{222} + \mathcal{C}_{112}$, $\mathcal{C}_{166} = -2\mathcal{C}_{111} + 3\mathcal{C}_{222} - \mathcal{C}_{112}$, and $\mathcal{C}_{222} = 2\mathcal{C}_{111} - \mathcal{C}_{222} - \mathcal{C}_{112}$.

The quadratic terms of the density energy $\mathcal{U}^{(2)}$ in Eq. (5.9) have been derived also as follows

$$\begin{aligned} 2\mathcal{U}^{(2)} &= \lambda_1 \epsilon_{\alpha\alpha} \epsilon_{\beta\beta} + \lambda_2 \epsilon_{\alpha\beta}^2 \\ &= \lambda_1 (2\text{Tr}(\hat{\epsilon}^2) - (\text{Tr}(\hat{\epsilon}))^2) + \lambda_2 (\text{Tr}(\hat{\epsilon}))^2 \\ &= 2\lambda_1 \text{Tr}(\hat{\epsilon}^2) + (\lambda_2 - \lambda_1) (\text{Tr}(\hat{\epsilon}))^2 \end{aligned} \quad (5.14)$$

where we have used the follows relations, which have been derived from the Eq. (5.8)

$$\begin{aligned} \epsilon_{\alpha\alpha} \epsilon_{\beta\beta} &= (\epsilon_{xx} - \epsilon_{yy})^2 + 4\epsilon_{xy}^2 \\ \epsilon_{\alpha\beta}^2 &= (\epsilon_{xx} + \epsilon_{yy})^2 \\ (\text{Tr}(\hat{\epsilon}))^2 &= (\epsilon_{xx} + \epsilon_{yy})^2 \\ \text{Tr}(\hat{\epsilon}^2) &= \epsilon_{xx}^2 + \epsilon_{yy}^2 + 2\epsilon_{xy}^2 \end{aligned} \quad (5.15)$$

Hence, starting from the Eq. (5.2) and using the tensor stress formulations, $T_{ij} = \mathcal{C}_{ijkh} \epsilon_{kh}$ and $\hat{T} = 2\mu\hat{\epsilon} + (K - \mu)\text{Tr}(\hat{\epsilon})\mathbf{I}_2$ (see Eq. (4.116) and Eq. (4.148) respectively), the density energy $\mathcal{U}^{(2)}$ can be written as

$$\begin{aligned} \mathcal{U}^{(2)} &= \frac{1}{2} \mathcal{C}_{ijkl} \epsilon_{ij} \epsilon_{kl} \\ &= \frac{1}{2} T_{ij} \epsilon_{ij} = \frac{1}{2} \text{Tr}(\hat{T}\hat{\epsilon}) \\ &= \frac{1}{2} [2\mu\text{Tr}(\hat{\epsilon}^2) + (K - \mu)\text{Tr}(\hat{\epsilon})^2] \end{aligned} \quad (5.16)$$

Finally, comparing the Eq. (5.16) with the Eq. (5.14), we have obtained that the two elastic constant λ_1, λ_2 are directly related to the Lamè modulus μ and the Bulk modulus K (see also Table 4.5), respectively

$$\begin{aligned} \lambda_1 &\equiv \mu = \frac{\mathcal{C}_{11} - \mathcal{C}_{12}}{2} \\ \lambda_2 &\equiv K = \mu + \lambda = \frac{\mathcal{C}_{11} + \mathcal{C}_{12}}{2} \end{aligned} \quad (5.17)$$

The strain energy function is finally obtained as

$$\begin{aligned} 2\mathcal{U} &= 2\mu\text{Tr}(\hat{\epsilon}^2) + \lambda (\text{Tr}\hat{\epsilon})^2 \\ &+ \frac{1}{3} \mathcal{C}_{111} \epsilon_{xx}^3 + \frac{1}{3} \mathcal{C}_{222} \epsilon_{yy}^3 + \mathcal{C}_{112} \epsilon_{xx}^2 \epsilon_{yy} \\ &+ (\mathcal{C}_{111} - \mathcal{C}_{222} + \mathcal{C}_{112}) \epsilon_{xx} \epsilon_{yy}^2 \\ &+ (3\mathcal{C}_{222} - 2\mathcal{C}_{111} - \mathcal{C}_{112}) \epsilon_{xx} \epsilon_{xy}^2 \\ &+ (2\mathcal{C}_{111} - \mathcal{C}_{222} - \mathcal{C}_{112}) \epsilon_{yy} \epsilon_{xy}^2 \end{aligned} \quad (5.18)$$

*Uniform uniaxial
stress in plane stress
boundary condition:
the stress-strain
nonlinear
constitutive equation*

where we set $\epsilon_{\alpha\alpha}\epsilon_{\beta\beta} = \text{Tr}(\hat{\epsilon}^2)$ and $\epsilon_{\alpha\beta}^2 = (\text{Tr}\hat{\epsilon})^2$.

The analysis of the experimental data provided in Ref. [12] through Eq. (5.1) is assuming an applied uniaxial stress in plane stress boundary condition. Since the stress-strain nonlinear constitutive equation for in-plane stretching is straightforwardly obtained by $\hat{T} = \partial U / \partial \hat{\epsilon}$, where \hat{T} is the Cauchy stress tensor defined in Section 4.3, we can write its components as function of the strain tensor elements

$$\begin{cases} T_{xx} = \frac{\partial U}{\partial \epsilon_{xx}} = f_1(\epsilon_{xx}, \epsilon_{yy}, \epsilon_{xy}) = f_1(\epsilon_{xx}, \epsilon_{yy}, 0) \\ T_{yy} = \frac{\partial U}{\partial \epsilon_{yy}} = f_2(\epsilon_{xx}, \epsilon_{yy}, \epsilon_{xy}) = f_2(\epsilon_{xx}, \epsilon_{yy}, 0) \\ T_{xy} = \frac{\partial U}{\partial \epsilon_{xy}} = f_3(\epsilon_{xx}, \epsilon_{yy}, \epsilon_{xy}) = 0 \end{cases} \quad (5.19)$$

Here to achieve the uniaxial stress condition we have to impose that $T_{xy} = 0$ and consequently $\epsilon_{xy} = 0$. We now suppose to apply a uniaxial tension $\sigma_{\vec{n}}$ along the arbitrary direction $\vec{n} = \cos \theta \vec{e}_x + \sin \theta \vec{e}_y$, where \vec{e}_x and \vec{e}_y are the unit vectors along the zig-zag and the armchair directions, respectively (see Figure 5.1). Under this assumption we get: $\hat{T} = \sigma_{\vec{n}} \vec{n} \otimes \vec{n}$, with in-plane components defined as $T_{xx} = \sigma_{\vec{n}} \cos^2 \theta$, $T_{xy} = \sigma_{\vec{n}} \cos \theta \sin \theta$, and $T_{yy} = \sigma_{\vec{n}} \sin^2 \theta$. Similarly, by inverting the nonlinear constitutive equation we find the corresponding strain tensor and the relative variation of length $\epsilon_{\vec{n}} = \vec{n} \cdot \hat{\epsilon} \vec{n}$ along the direction \vec{n} . By combining these results, we obtain the stress-strain relation $\sigma_{\vec{n}} = E \epsilon_{\vec{n}} + D_{\vec{n}} \epsilon_{\vec{n}}^2$ along the arbitrary direction \vec{n} (see Figure 1, bottom), where $D_{\vec{n}}$ is given by

*The nonlinear
effective elastic
modulus*

$$D_{\vec{n}} = \frac{3}{2} (1 - \nu)^3 \Lambda_3 + \frac{3}{2} (1 - \nu) (1 + \nu)^2 \Lambda_2 + 3 (2 \cos^2 \theta - 1) (16 \cos^4 \theta - 16 \cos^2 \theta + 1) (1 + \nu)^3 \Lambda_1 \quad (5.20)$$

If we set $\vec{n} = \vec{e}_x$ (i.e. $\theta = 0$), we get the nonlinear modulus $D^{(zz)}$ for stretching along the zig-zag direction

$$D^{(zz)} = D_{\vec{e}_x} = 3 (1 + \nu)^3 \Lambda_1 + \frac{3}{2} (1 - \nu) (1 + \nu)^2 \Lambda_2 + \frac{3}{2} (1 - \nu)^3 \Lambda_3 \quad (5.21)$$

Similarly, by setting $\vec{n} = \vec{e}_y$ (i.e. $\theta = \pi/2$), we obtain the nonlinear modulus $D^{(ac)}$ for stretching along the armchair direction

$$D^{(ac)} = D_{\vec{e}_y} = -3 (1 + \nu)^3 \Lambda_1 + \frac{3}{2} (1 - \nu) (1 + \nu)^2 \Lambda_2 + \frac{3}{2} (1 - \nu)^3 \Lambda_3 \quad (5.22)$$

We observe that the above expression for $D^{(zz)}$ apply for all stretching directions defined by the angles $\theta = k\pi/3$ ($k \in \mathbb{Z}$), while $D^{(ac)}$ holds for the angles $\theta = \pi/6 + k\pi/3$. Since the

Table 5.1: Relationship among the energy expansion coefficients $U^{(2)}$ and $U^{(3)}$ of Eq. (5.24) and the elastic moduli of graphene for four in-plane deformations (see text).

deformation	$U^{(2)}$	$U^{(3)}$
$\epsilon_{ij}^{(zz)}$	$\frac{E}{1-\nu^2}$	\mathcal{C}_{111}
$\epsilon_{ij}^{(ac)}$	$\frac{E}{1-\nu^2}$	\mathcal{C}_{222}
$\epsilon_{ij}^{(p)}$	$\frac{2E}{1-\nu}$	$4\mathcal{C}_{111} - 2\mathcal{C}_{222} + 6\mathcal{C}_{112}$
$\epsilon_{ij}^{(s)}$	$\frac{2E}{1+\nu}$	0

nanindentation experiments generate a strain field with radial symmetry [12], as sketched in Figure 5.1, in order to get the unique *scalar* nonlinear elastic modulus appearing in Eq.(1) we need to average the expression of $D_{\vec{n}}$ over θ . This procedure leads to

$$\begin{aligned} \langle D_{\vec{n}} \rangle &= \frac{1}{2\pi} \int_0^{2\pi} D_{\vec{n}} d\theta = \frac{D^{(zz)} + D^{(ac)}}{2} \\ &= \frac{3}{2} (1-\nu) \left[(1+\nu)^2 \Lambda_2 + (1-\nu)^2 \Lambda_3 \right] \end{aligned} \quad (5.23)$$

proving that the experimentally determined nonlinear modulus actually corresponds to the average value of the moduli for the zig-zag and armchair directions.

We now repeat the above procedure by using the Lagrangian strain $\hat{\eta}$: even in this case we demonstrated that the strain energy function is given by the very same Eq. (5.18), where $\hat{\epsilon}$ is replaced by $\hat{\eta}$ and the \mathcal{C}_{ijk} by the Lagrangian third-order moduli $\mathcal{C}_{ijk}^{\mathcal{L}}$. By imposing the identity $U(\hat{\epsilon}) = U(\hat{\eta})$ (where the Lagrangian strain can be written in term of the small strain by $\hat{\eta} = \hat{\epsilon} + \frac{1}{2}\hat{\epsilon}^2$ [86, 87]) we obtain the conversion rules: $\mathcal{C}_{111}^{\mathcal{L}} = \mathcal{C}_{111} - \frac{3E}{1-\nu^2}$, $\mathcal{C}_{222}^{\mathcal{L}} = \mathcal{C}_{222} - \frac{3E}{1-\nu^2}$, $\mathcal{C}_{112}^{\mathcal{L}} = \mathcal{C}_{112} - \frac{E\nu}{1-\nu^2}$, $D_{\vec{n}}^{\mathcal{L}} = D_{\vec{n}} - \frac{3}{2}E$ (for any \vec{n}) and $\langle D_{\vec{n}}^{\mathcal{L}} \rangle = \langle D_{\vec{n}} \rangle - \frac{3}{2}E$. The constitutive equation can be finally derived in the form $\hat{T}^{\mathcal{PK}} = \partial U / \partial \hat{\eta}$, where $\hat{T}^{\mathcal{PK}}$ is the second Piola-Kirchhoff stress tensor. Hereafter we will refer to the small strain and Lagrangian scalar nonlinear modulus by $\langle D_{\vec{n}} \rangle$ and $\langle D_{\vec{n}}^{\mathcal{L}} \rangle$, respectively. They both will be compared with the experimental parameter D of Eq. (5.1). The analysis below will identify the actual theoretical counterpart of D .

*The nonlinear
Lagrangian
constitutive equation*

5.2 THE COMPUTATIONAL APPROACH

The important result summarized in Eq. (5.23) (as well as in its Lagrangian version) implies that the scalar nonlinear modulus can be obtained by the third-order elastic constants (as well as the linear ones). They can be computed through energy-vs-strain curves corresponding to suitable homogeneous in-plane

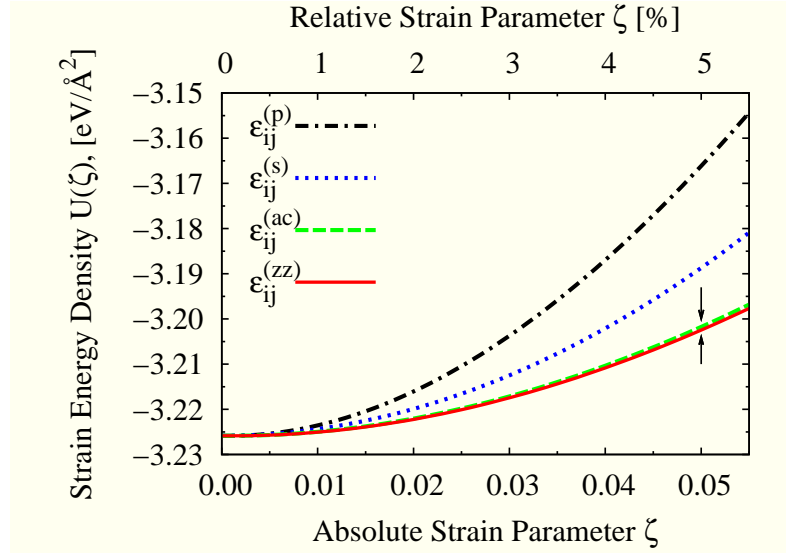


Figure 5.2: Strain energy density U , obtained by TB-AS, as function of the strain parameter ζ corresponding to the four homogeneous deformations summarized in Table 5.1.

The uniform deformation method

deformations, thus avoiding a technically complicated simulation of the nanoindentation experiment. Therefore, the following in-plane deformation have been applied: (i) an uniaxial deformation ζ along the zig-zag direction, corresponding to a strain tensor $\epsilon_{ij}^{(zz)} = \zeta \delta_{ix} \delta_{jx}$; (ii) an uniaxial deformation ζ along the armchair direction, corresponding to a strain tensor $\epsilon_{ij}^{(ac)} = \zeta \delta_{iy} \delta_{jy}$; (iii) an hydrostatic planar deformation ζ , corresponding to the strain tensor $\epsilon_{ij}^{(p)} = \zeta \delta_{ij}$; (iv) a shear deformation ζ , corresponding to an in-plain strain tensor $\epsilon_{ij}^{(s)} = \zeta (\delta_{ix} \delta_{jy} + \delta_{iy} \delta_{jx})$.

All the needed energy-vs-strain curves have been determined by TB-AS, making use of the tight-binding representation by Xu et al. [50]. A periodically repeated square cell containing 400 carbon atoms was deformed as above. For any given applied deformation, full relaxation of the internal degrees of freedom of the simulation cell was performed by zero temperature damped dynamics until interatomic forces resulted not larger than $0.5 \cdot 10^{-11} \text{ eV/\AA}$.

For the deformations $\epsilon_{ij}^{(zz)}$, $\epsilon_{ij}^{(ac)}$, $\epsilon_{ij}^{(p)}$ and $\epsilon_{ij}^{(s)}$ the elastic energy of strained graphene can be written in terms of just the single deformation parameter ζ

Polynomial fitting method

$$U(\zeta) = U_0 + \frac{1}{2} U^{(2)} \zeta^2 + \frac{1}{6} U^{(3)} \zeta^3 + O(\zeta^4) \quad (5.24)$$

where U_0 is the energy of the unstrained configuration. Since the expansion coefficients $U^{(2)}$ and $U^{(3)}$ are related to elastic moduli as summarized in Table 5.1, a straightforward fit of Eq. (5.24) has provided the full set of linear moduli and third order elastic constants, while the shear deformation was used to confirm the

isotropy of the lattice in the linear approximation. Each energy-vs-strain curve, shown in Figure 5.2, has been computed by TB-AS as above described, by increasing the magnitude of ζ in steps of 0.005 up to a maximum strain $|\zeta_{\max}| = 0.055$. Arrows in Figure 5.16 indicate the different nonlinear behavior along the zz and ac directions.

The outputs of the fitting procedure are reported in Table 5.2 where the full set of third order elastic constants of monolayer graphene is shown. We remark that \mathcal{C}_{111} is different than \mathcal{C}_{222} , i.e. a monolayer graphene is isotropic in the linear elasticity approximation, while it is anisotropic when nonlinear features are taken into account. By inserting the elastic constants \mathcal{C}_{ijk} of Table 5.2 into Eqs. (5.12), (5.21) and (5.22), we also obtained the nonlinear moduli for both the zz and ac directions.

In Table 5.3 we report the values of the calculated elastic moduli, together with the available experimental and theoretical data. The present TB-AS value for E is in reasonable agreement with literature [12, 88, 83, 89], while the value of ν is larger than most of the ab-initio results [83, 89, 90, 91] (but for the result in Ref. [76]). While this disagreement is clearly due to the empirical character of the adopted TB model (where, however, no elastic data were inserted in the fitting data base), we remark that the values of $\langle D_{\bar{n}} \rangle$ and $\langle D_{\bar{n}}^{\mathcal{L}} \rangle$ predicted by means of Eq. (5.23) are affected by only 10% if we vary ν in the range of values shown in Table 5.3.

Table 5.3 shows that the predicted $\langle D_{\bar{n}} \rangle$ is much closer to the experimental value D than its Lagrangian counterpart $\langle D_{\bar{n}}^{\mathcal{L}} \rangle$. This seems to suggest that measurements in Ref. [12] were performed in the physical nonlinearity regime (small strain formalism), rather than in the geometrical nonlinearity one (Lagrangian formalism), as also confirmed by the excellent agreement shown in Figure 5.3 commented below. Since $\mathcal{C}_{ijk} < 0$ (and $D < 0$), graphene is an hyperelastic softening system. Therefore, the present model plays a crucial role in determining the failure behavior of the graphene membrane [92, 93].

*Nonlinear
anisotropy of
graphene*

*Hyperelastic
softening behavior of
graphene*

Table 5.2: Small strain and Lagrangian nonlinear elastic moduli of graphene in units of Nm^{-1} .

Small strain		Lagrangian	
\mathcal{C}_{111}	-1689.2	$\mathcal{C}_{111}^{\mathcal{L}}$	-2724.7
\mathcal{C}_{222}	-1487.7	$\mathcal{C}_{222}^{\mathcal{L}}$	-2523.2
\mathcal{C}_{112}	-484.1	$\mathcal{C}_{112}^{\mathcal{L}}$	-591.1
$D^{(zz)}$	-696.2	$D^{\mathcal{L}(zz)}$	-1163.7
$D^{(ac)}$	-469.6	$D^{\mathcal{L}(ac)}$	-937.9

Table 5.3: Linear and nonlinear elastic moduli of graphene in units of Nm^{-1} (ν is dimensionless).

	E	ν	D	$\langle D_{\bar{\pi}} \rangle$	$\langle D_{\bar{\pi}}^{\mathcal{L}} \rangle$
Present	312	0.31	-	-582.9	-1050.9
Ref. [12] ^a	340 ± 40	-	-690 ± 120	-	-
Ref. [82, 14] ^b	235	0.413	-	-	-
Ref. [88] ^c	384	0.227	-	-	-
Ref. [83] ^d	345	0.149	-	-	-
Ref. [90] ^d	-	0.173	-	-	-
Ref. [89] ^d	350	0.186	-	-	-
Ref. [76] ^d	-	0.32	-	-	-
Ref. [91] ^d	-	0.12-0.19	-	-	-

^a Experimental, ^b Tersoff-Brenner, ^c Empirical force-constant calculations, ^d Ab-initio

In order to substantiate the above statement, we show in Figure 5.3 the graphene stress-strain curve, as defined in Eq. (5.1). Both the theoretical and experimental curves have been obtained by using the Young modulus and the scalar nonlinear coefficient as reported in Table 5.3. We remark that in Figure 5.3 the small strain $\langle D_{\bar{\pi}} \rangle$ value was used. The agreement between the experimental curve and the theoretical (small strain) one is remarkable. In addition, by means of Figure 5.3 we can determine the failure stress (maximum of the stress-strain curve) $\sigma_f = -E^2/4\langle D_{\bar{\pi}} \rangle$, corresponding to a predicted failure stress as high as 42.4 Nm^{-1} . This result is in excellent agreement with the experimental value $42 \pm 4 \text{ Nm}^{-1}$, reported in Ref. [12]. These values correspond to the failure strength of a two-dimensional system. In order to draw a comparison with bulk materials, we define an effective three-dimensional failure stress $\sigma_f^{3D} = \sigma_f/d$, where d is taken as the interlayer spacing in graphite. By considering $d = 0.335 \text{ nm}$ [94], we obtain $\sigma_f^{3D} \cong 130 \text{ GPa}$. This very high value, exceeding that of most materials (even including multi-walled nanotubes [95]), motivates the use of one-atom thick carbon layers as possible reinforcement in advanced composites.

Failure stress

5.3 THE STRESS-STRAIN APPROACH

The same quantities derived and discussed previously have been computed by using the fitting method applied to a set of stress-strain curves instead the energy-strain approach. The previous results are confirmed and in Fig. 5.4 we show the stress-strain curves calculated by TB-AS through the implementation of the atomic stress tensor version defined in Eq. (4.180). Using the

The stress-strain approach

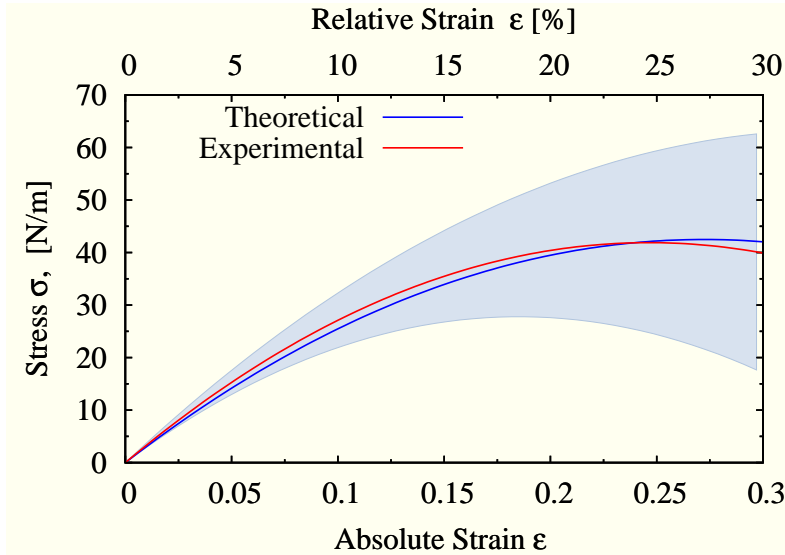


Figure 5.3: Experimental (see Ref. [12]) and present theoretical stress-strain curves, as defined in Eq. (5.1). Shaded area represents the experimental error.

Cauchy stress tensor definition (see Eq. (4.113) and the Eq. (4.114), we can derive an expression for the stress tensor in terms of the stiffness coefficients. Thus we can solve the follows derivative

$$\begin{aligned}
 T_{ij} &= \frac{\partial U}{\partial \varepsilon_{ij}} = \frac{\partial}{\partial \varepsilon_{ij}} \left(\frac{1}{2} C_{ijkl} \varepsilon_{ij} \varepsilon_{kl} + \frac{1}{6} C_{ijklmn} \varepsilon_{ij} \varepsilon_{kl} \varepsilon_{mn} \right) \\
 &+ \frac{1}{2} C_{ijkl} \left(\frac{\partial \varepsilon_{ij}}{\partial \varepsilon_{ij}} \varepsilon_{kl} + \frac{\partial \varepsilon_{kl}}{\partial \varepsilon_{ij}} \varepsilon_{ij} \right) \\
 &+ \frac{1}{6} C_{ijklmn} \left(\frac{\partial \varepsilon_{ij}}{\partial \varepsilon_{ij}} \varepsilon_{kl} \varepsilon_{mn} + \varepsilon_{ij} \frac{\partial \varepsilon_{kl}}{\partial \varepsilon_{ij}} \varepsilon_{mn} + \varepsilon_{ij} \varepsilon_{kl} \frac{\partial \varepsilon_{mn}}{\partial \varepsilon_{ij}} \right) \\
 &= \frac{1}{2} C_{ijkl} \left(\varepsilon_{kl} + \frac{1}{2} (\delta_{ki} \delta_{lj} + \delta_{kj} \delta_{li}) \varepsilon_{ij} \right) \\
 &+ \frac{1}{6} C_{ijklmn} \left(\varepsilon_{kl} \varepsilon_{mn} + \varepsilon_{ij} \frac{1}{2} (\delta_{ki} \delta_{lj} + \delta_{kj} \delta_{li}) \varepsilon_{mn} \right. \\
 &\quad \left. + \varepsilon_{ij} \varepsilon_{kl} \frac{1}{2} (\delta_{mi} \delta_{nj} + \delta_{mj} \delta_{ni}) \right) \\
 &= \frac{1}{2} C_{ijkl} \left(\varepsilon_{kl} + \frac{1}{2} (\varepsilon_{kl} + \varepsilon_{lk}) \right) \\
 &+ \frac{1}{6} C_{ijklmn} \left(\varepsilon_{kl} \varepsilon_{mn} + \frac{1}{2} (\varepsilon_{kl} \varepsilon_{mn} + \varepsilon_{lk} \varepsilon_{mn} + \varepsilon_{nm} \varepsilon_{kl}) \right) \\
 &= C_{ijkl} \varepsilon_{kl} + \frac{1}{2} C_{ijklmn} \varepsilon_{kl} \varepsilon_{mn}
 \end{aligned} \tag{5.25}$$

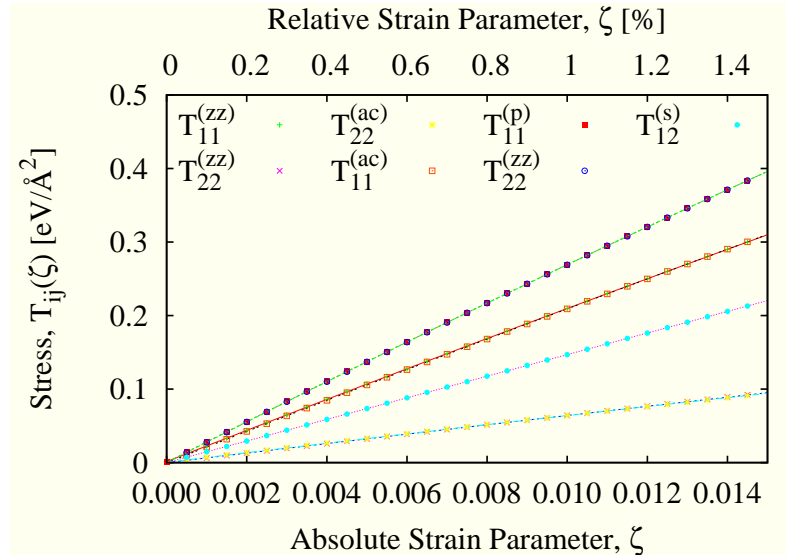


Figure 5.4: Stress tensor components T_{ij} , obtained by TB-AS, as function of the strain parameter ζ corresponding to the four homogeneous deformations summarized in Table 5.1. Note that couples of curves overlap perfectly as imposed by symmetry.

or, in more explicit way, we can write

$$\begin{aligned}
 T_{11} &= C_{11}\varepsilon_{11} + C_{12}\varepsilon_{22} + \frac{1}{2}(+C_{111}\varepsilon_{11}^2 + 4C_{166}\varepsilon_{12}^2 \\
 &\quad + 2C_{112}\varepsilon_{11}\varepsilon_{22} + C_{122}\varepsilon_{22}^2) \\
 T_{22} &= C_{11}\varepsilon_{22} + C_{12}\varepsilon_{11} + \frac{1}{2}(+C_{222}\varepsilon_{22}^2 + 4C_{266}\varepsilon_{12}^2 \\
 &\quad + 2C_{122}\varepsilon_{11}\varepsilon_{22} + C_{112}\varepsilon_{11}^2) \\
 T_{12} &= +2C_{66}\varepsilon_{12} + \frac{1}{2}(+8C_{166}\varepsilon_{11}\varepsilon_{12} + 8C_{266}\varepsilon_{12}\varepsilon_{22})
 \end{aligned}$$

Note that from the computational point of view, the stress-strain approach is more advantageous than the energy-strain method, because of the number of experiments needed to achieve the same informations is smaller. In fact, each deformation leads to a set of three equations, i.e. three curves to fit.

ELASTIC PROPERTIES OF GRAPHANE

*“On a piece of paper, a picture’s drawn. It floats on down the street,
till the wind is gone. The memory now is like the picture was then;
When the paper’s crumpled up, it can’t be perfect again.”*
Linkin Park ‘Hybrid Theory’

Contents

6.1	Graphane	89
6.2	Methods and computational setup	92
6.3	Structure and stability of graphane conformers	94
6.4	Linear elasticity	96
6.5	Nonlinear elasticity	103

There exist three conformers of hydrogenated graphene, referred to as chair-, boat-, or washboard-graphane. These systems have a perfect two-dimensional periodicity mapped onto the graphene scaffold, but they are characterized by a sp^3 orbital hybridization, have different crystal symmetry, and otherwise behave upon loading. By first principles calculations we determine their structural and phonon properties, as well as we establish their relative stability. Through continuum elasticity we define a simulation protocol addressed to measure by a computer experiment their linear and nonlinear elastic moduli and we actually compute them by first principles. We argue that all graphane conformers respond to any arbitrarily-oriented extension with a much smaller lateral contraction than the one calculated for graphene. Furthermore, we provide evidence that boat-graphane has a small and negative Poisson ratio along the armchair and zigzag principal directions of the carbon honeycomb lattice (axially auxetic elastic behavior). Moreover, we show that chair-graphane admits both softening and hardening hyperelasticity, depending on the direction of applied load.

The graphane is the fully hydrogenated graphene

6.1 GRAPHANE

The hydrogenated form of graphene is referred to as graphane. It is described as a two-dimensional, periodic, and covalently bonded hydrocarbon with a C:H ratio of 1. Hydrogen atoms decorate the carbon honeycomb lattice on both the top and bottom side (see Fig. 6.1). Graphane was theoretically predicted by Sofu *et al.*, [22] further investigated by Boukhvalov *et al.* [23]

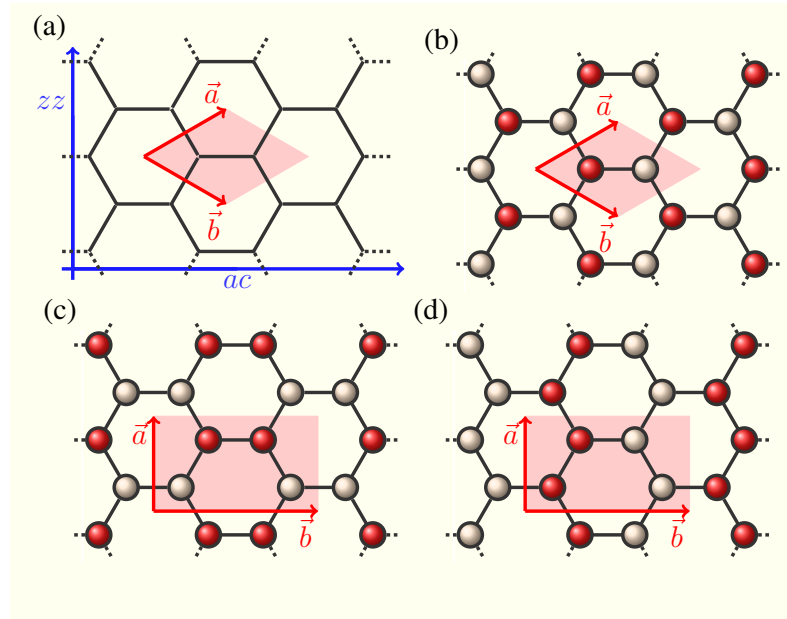


Figure 6.1: Pictorial representations of the graphane conformers, obtained by different hydrogen decorations (the actual atomic positions are reported in Fig. 6.2). Top hydrogen atoms are indicated by red (dark) circles, while bottom ones by gray (light) circles. Shaded areas represent the unit cell and the corresponding lattice vectors are indicated by \vec{a} and \vec{b} . Panel a: graphene scaffold (full lines) with zigzag (zz) and armchair (ac) directions. Panel b, c, and d: chair-, boat-, and washboard-graphane, respectively.

and eventually grown by Elias *et al.* [24] The investigation of graphane properties was originally motivated by the search for novel materials with possibly large impact in nanotechnology.

The attractive feature of graphane is that by variously decorating the graphene atomic scaffold with hydrogen atoms (still preserving periodicity) it is in fact possible to generate a set of two dimensional materials with new physico-chemical properties. This is obviously due to change in the orbital hybridization which, because of hydrogenation, is now sp^3 -like. For instance, it has been calculated [22, 23] that graphane is an insulator, with an energy gap as large as ~ 6 eV [96], while graphene is a highly conductive semi-metal. In case the hydrogenated sample is disordered, the resulting electronic and phonon properties are yet again different [24]. Hydrogenation likely affects the elastic properties as well. Topsakal *et al.* [26] indeed calculated that the in-plane stiffness and Poisson ratio of graphane are smaller than those of graphene. In addition, the value of the yield strain is predicted to vary upon temperature and stoichiometry.

As far as the mechanical properties of graphane are concerned, the sp^2 -to- sp^3 change in orbital hybridization causes a major

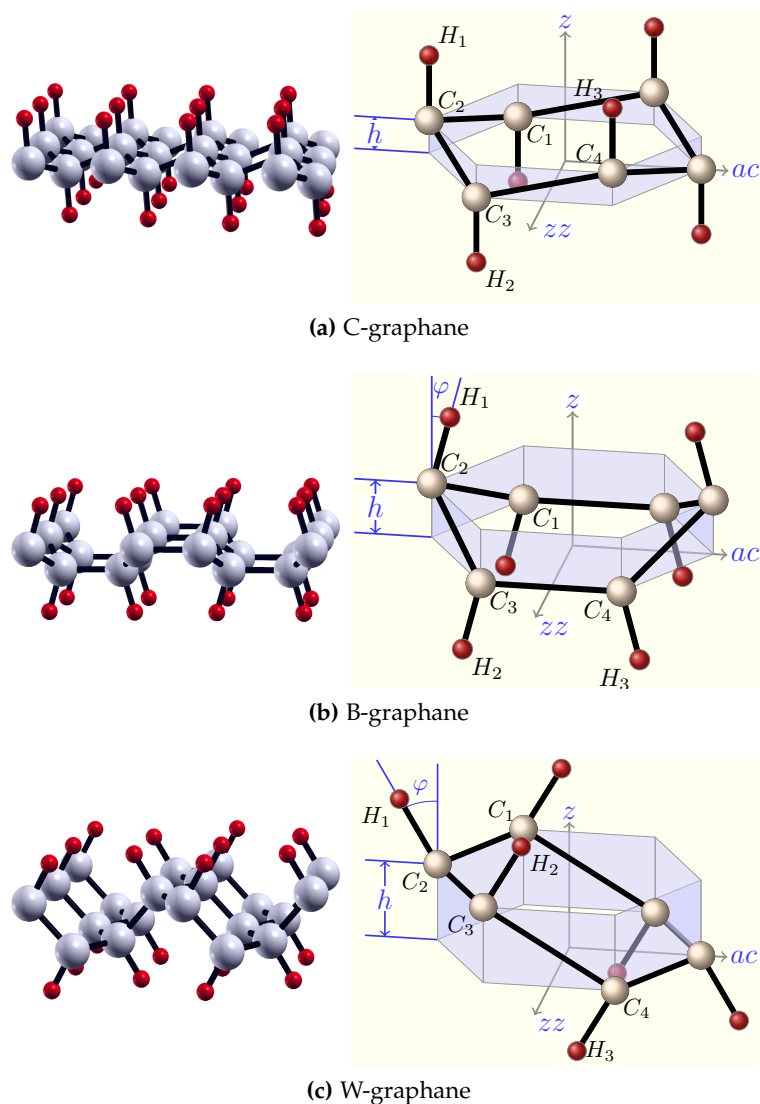


Figure 6.2: Perspective representations of fully relaxed graphane conformers. Gray (light gray) and red (dark gray) spheres represent carbon and hydrogen atoms, respectively. Labels C_n and H_n (with $n = 1, 2, 3$ and 4) provide the atom identifications used in Table 6.1. Right panels show the orientation with respect to the armchair (ac) and zigzag (zz) direction, as well as the structural parameters h and φ reported in Table 6.1.

*There exist
anisotropic graphane
conformers*

difference with respect to graphene. There in fact exist graphane conformers which are not isotropic, at variance with graphene which is so (in linear approximation as shown in Chapter 5). This feature stimulates an intriguing change of perspective, namely: hydrogenation could not only affect the actual value of some linear elastic moduli [26]; it could even dramatically change the overall mechanical behavior of the system by introducing an anisotropic dependence of its response to an external load. This is in fact what we predict in this work by first principles total energy calculations, combined to continuum elasticity: we show that there is a graphane conformer (i.e., boat graphane as detailed below) showing a vanishingly small (possibly negative) Poisson ratio upon loading along given directions. In other words, we provide evidence that upon suitable hydrogenation a graphene sheet behaves as an axially auxetic material [97], namely: it does not shrink, but actually slightly elongates perpendicularly to an applied traction force. Nonlinear elastic features show an interesting anisotropic behavior as well.

This Chapter is organized as follows. In Sec. 6.2, the methods and the general computational setup adopted in our calculations are outlined. In Sec. 6.3 we provide a full structural characterization of three graphane conformers and we discuss their stability. In Sec. 6.4 and Sec. 6.5 we describe their linear and nonlinear elastic properties, respectively, and we compute all the relevant elastic moduli.

6.2 METHODS AND COMPUTATIONAL SETUP

All calculations have been performed by Density Functional Theory (DFT) (Chapter 3) as implemented in the QUANTUM ESPRESSO package [98]. The exchange correlation potential was evaluated through the generalized gradient approximation (GGA), using the Vanderbilt ultrasoft pseudopotential PW91 [99]. A plane wave basis set with kinetic energy cutoff as high as 50 Ry was used and in most calculations the Brillouin zone (BZ) has been sampled by means of a (18x18x3) Monkhorst-Pack grid. The atomic positions of the investigated samples have been optimized by using the quasi-Newton algorithm and periodically-repeated simulation cells. Accordingly, the interactions between adjacent atomic sheets in the supercell geometry was hindered by a large spacing greater than 10 Å.

The elastic moduli of the structures under consideration have been obtained from the energy-vs-strain curves, corresponding to suitable sets of deformations applied to a single unit cell sample. As discussed in more detail in Sec. 6.4 and Sec. 6.5, for any deformation the magnitude of the strain is represented by a single parameter ζ . The curves have been carefully generated by

Table 6.1: Space groups and structural parameters for each graphane conformers. The cell parameters a and b are defined in Fig. 6.1 while the other quantities are reported in Fig. 6.2. Note that the B-graphane shows two types of C-C bonds while W-graphane exhibits a large buckling parameter, h .

	C-graphane	B-graphane	W-graphane
Space Group	P-3m1 (164)	Pmmn (59)	Pmna (53)
a	2.54 Å	2.53 Å	2.55 Å
b	-	4.31 Å	3.82 Å
$C_1 - C_2$	1.54 Å	1.54 Å	1.54 Å
$C_3 - C_4$	1.54 Å	1.57 Å	1.54 Å
$C - H$	1.11 Å	1.11 Å	1.11 Å
h	0.46 Å	0.65 Å	1.14 Å
φ	0.0°	16.7°	30.1°
$\widehat{C_1 C_2 C_3}$	111.5°	110.7°	111.2°
$\widehat{C_2 C_3 C_4}$	111.5°	112.3°	112.3°
$\widehat{H_1 C_2 C_3}$	107.4°	107.2°	106.5°
$\widehat{H_1 C_2 C_3 H_2}$	180.0°	180.0°	51.2°
$\widehat{H_2 C_3 C_4 H_3}$	180.0°	0.0°	0.0°

increasing the magnitude of ζ in steps of 0.001 up to a maximum strain $|\zeta_{\max}| = 0.05$. All results have been confirmed by checking the stability of the estimated elastic moduli over several fitting ranges. The reliability of the above computational set up is proved by the estimated values for the Young modulus and the Poisson ratio of graphene, respectively 344 Nm^{-1} and 0.169, which are in excellent agreement with recent literature [83, 90, 89]. Similarly, our results for the same moduli in C-graphane (respectively, 246 Nm^{-1} and 0.08) agree very well with data reported in Ref. [26].

The stability of the three graphane conformers has been established by calculating the corresponding phonon dispersions. Phonon dispersions, have been obtained by means of Density-Functional Perturbation Theory (DFPT) [69], based on the $(2n + 1)$ theorem (Sec. 3.2). In this case, during the self-consistent field calculation, the BZ has been sampled by a $(16 \times 16 \times 3)$ Monkhorst-Pack grid. The accuracy of the phonon dispersion evaluations has been tested on a graphene sample.

6.3 STRUCTURE AND STABILITY OF GRAPHANE CONFORMERS

*structure of trigonal
and orthorhombic
graphane*

By hydrogenating a honeycomb graphene lattice, three ordered graphane structures can be generated, namely: the chair (C-graphane), boat (B-graphane) and washboard (W-graphane) conformers [22, 100] shown in Fig. 6.2.

Each conformer is characterized by a specific hydrogen sublattice and by a different buckling of the carbon sublattice. In particular: in C-graphane the hydrogen atoms alternate on both sides of the carbon sheet; in B-graphane pairs of H-atoms alternate along the armchair direction of the carbon sheet; finally, in W-graphane double rows of hydrogen atoms, aligned along the zigzag direction of the carbon sublattice, alternate on both sides of the carbon sheet. A perspective view of the conformers is shown in Fig. 6.2 and the corresponding structural data are given in Table 6.1. In C-graphane and W-graphane the calculated C-C bond length of 1.54 Å is similar to the sp^3 bond length in diamond and much larger than in graphene. Moreover, we note that the B-graphane shows two types of C-C bonds, namely: those connecting two carbon atoms bonded to hydrogen atoms either lying on opposite sides (bond length 1.57 Å) or lying on the same side of honeycomb scaffold (bond length 1.54 Å). Finally, the C-H bond length of 1.1 Å is similar in all conformers and it is typical of any hydrocarbon.

*Ab-initio phonon
dispersion
calculations*

The stability of the three graphane conformers has been established by calculating the phonon dispersion curves reported in Fig. 6.3. Graphene phonon spectrum is reported as well for comparison. No soft modes (with negative frequency) corresponding to possible instabilities were found along any high-symmetry direction of the Brillouin zone. Furthermore, as expected [101], the zone-center longitudinal (LA) and transverse (TA) acoustic branches show a linear dependence upon the wavevector, while the acoustic mode ZA (with displacement patterns along the z-direction shown in Fig. 6.2) shows a quadratic dependence. We observe that in C-graphane, as well as in graphene, the speed of sound (i.e. the slope of the acoustic branches at Γ -point) is the same along the $\Gamma - M$ and $\Gamma - K$ directions. On the other hand, the B- and W-graphane conformers are characterized by different sound velocities along the $\Gamma - X$ and $\Gamma - Y$ directions. This is the fingerprint of an unlike elastic behavior: as extensively discussed in Sec. 6.4, C-graphane is elastically isotropic while neither B- nor W-graphane are so.

Finally, according to the present first principles total energy calculations we identified C-graphane as the most energetically favorable conformer. W- and B-graphane have higher ground-state energy of 0.05 and 0.10 eV (per C-H unit), respectively. These small differences in energy demonstrate that all three conform-

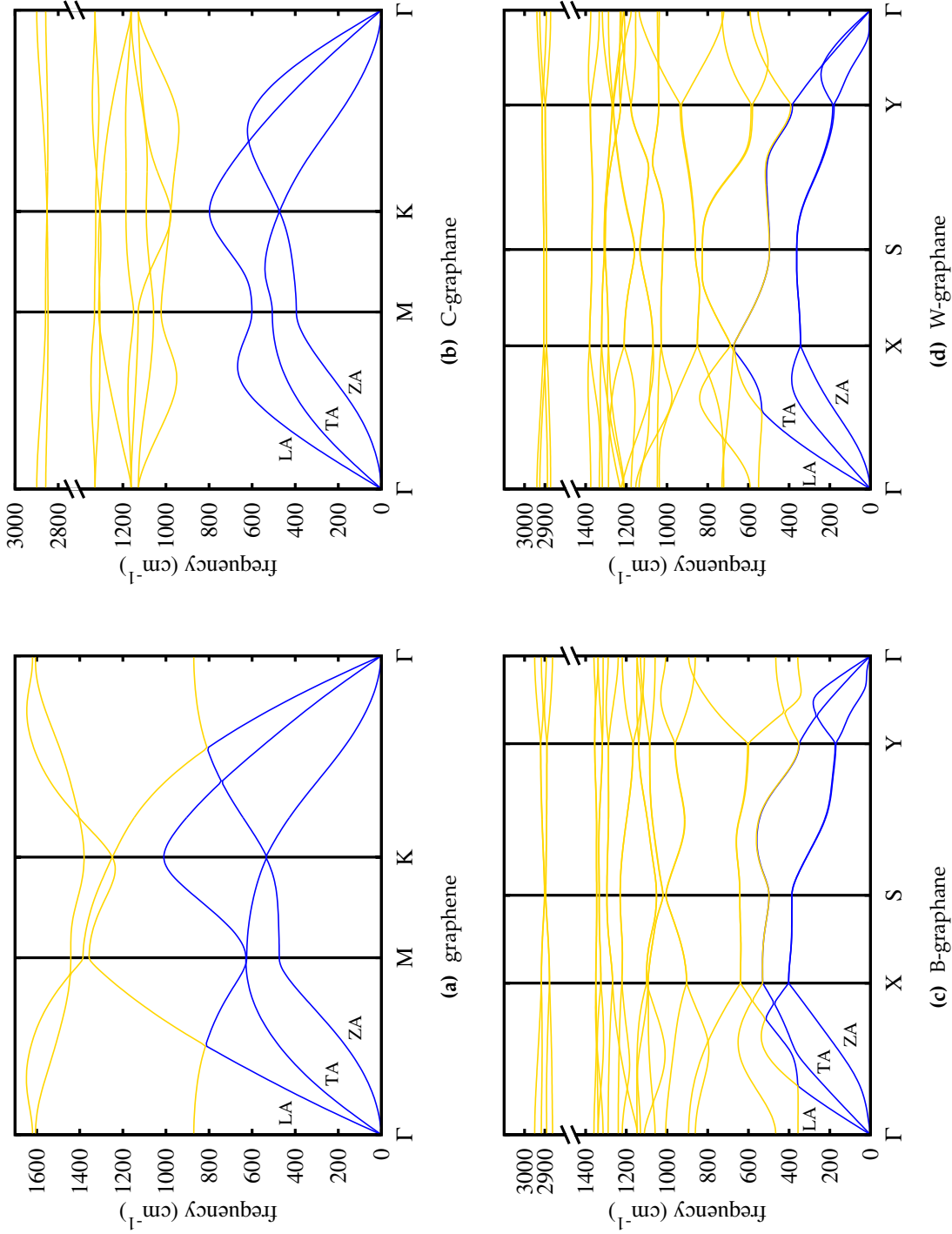


Figure 6.3: Phonon dispersion relations of graphene (panel a), C- (panel b), B- (panel c) and W- (panel d) graphane. Acoustic and optical modes correspond, respectively, to blue (dark gray) and yellow (light gray) dispersions. Longitudinal and transverse acoustic branches are indicated as LA and TA, respectively. The acoustic branch with displacement patterns along the z-direction of Fig. 6.2 is marked as ZA.

ers are thermodynamically accessible, as indeed experimentally guessed [100].

6.4 LINEAR ELASTICITY

While C-graphane has trigonal symmetry (and, therefore, is elastically isotropic as hexagonal graphene), the remaining B- and W-conformers show an orthorhombic symmetry, which causes an anisotropic linear elastic behavior. Accordingly, the elastic energy density (per unit of area) accumulated upon strain can be expressed as [102]

Elastic energy density for trigonal and orthorhombic symmetries

$$U_{\text{trigo}} = \frac{1}{2} \mathcal{C}_{11} (\epsilon_{xx}^2 + \epsilon_{yy}^2 + 2\epsilon_{xy}^2) + \mathcal{C}_{12} (\epsilon_{xx}\epsilon_{yy} - \epsilon_{xy}^2) \quad (6.1)$$

for the isotropic structures and as

$$U_{\text{ortho}} = \frac{1}{2} \mathcal{C}_{11} \epsilon_{xx}^2 + \frac{1}{2} \mathcal{C}_{22} \epsilon_{yy}^2 + \mathcal{C}_{12} \epsilon_{xx}\epsilon_{yy} + 2\mathcal{C}_{44} \epsilon_{xy}^2 \quad (6.2)$$

for the anisotropic ones. In Eqs.(6.1) and (6.2) we have explicitly made use of the elastic linear constants \mathcal{C}_{11} , \mathcal{C}_{22} , \mathcal{C}_{12} and \mathcal{C}_{44} . Furthermore, the infinitesimal strain tensor $\hat{\epsilon} = \frac{1}{2}(\vec{\nabla}\vec{u} + \vec{\nabla}\vec{u}^T)$ is represented by a symmetric matrix with elements $\epsilon_{xx} = \frac{\partial u_x}{\partial x}$, $\epsilon_{yy} = \frac{\partial u_y}{\partial y}$ and $\epsilon_{xy} = \frac{1}{2} \left(\frac{\partial u_x}{\partial y} + \frac{\partial u_y}{\partial x} \right)$, where the functions $u_x(x, y)$ and $u_y(x, y)$ correspond to the planar displacement $\vec{u} = (u_x, u_y)$. It is important to remark that U_{trigo} can be obtained from the U_{ortho} by simply imposing the isotropy condition $\mathcal{C}_{11} = \mathcal{C}_{22}$ and the Cauchy relation $2\mathcal{C}_{44} = \mathcal{C}_{11} - \mathcal{C}_{12}$, holding for both the hexagonal and trigonal symmetry. We will take profit of this by focussing just on the elastic behavior of a system described by Eq.(6.2); when needed, the general results so obtained will be applied to the isotropic structures by fully exploiting the above conditions. The constitutive in-plane stress-strain equations are straightforwardly derived from Eq.(6.2) through $\hat{T} = \partial U / \partial \hat{\epsilon}$, where \hat{T} is the Cauchy stress tensor [85]. They are: $T_{xx} = \mathcal{C}_{11}\epsilon_{xx} + \mathcal{C}_{12}\epsilon_{yy}$, $T_{yy} = \mathcal{C}_{22}\epsilon_{yy} + \mathcal{C}_{12}\epsilon_{xx}$ and $T_{xy} = 2\mathcal{C}_{44}\epsilon_{xy}$. We now suppose to apply an axial tension σ to any two dimensional hydrocarbon shown in Fig. 6.2 along the arbitrary direction $\vec{n} = \cos\theta\vec{e}_x + \sin\theta\vec{e}_y$, where \vec{e}_x and \vec{e}_y are, respectively, the unit vectors along the zigzag and the armchair directions of the underlying honeycomb lattice. In this notation, therefore, θ is the angle between \vec{n} and the zigzag direction. Under this assumption we get $\hat{T} = \sigma\vec{n} \otimes \vec{n}$, where the in-plane stress components are defined, respectively, as $T_{xx} = \sigma \cos^2 \theta$, $T_{xy} = \sigma \cos \theta \sin \theta$, and $T_{yy} = \sigma \sin^2 \theta$. By inverting the constitutive equation we find the corresponding strain tensor $\hat{\epsilon}$. In

The anisotropic elastic moduli

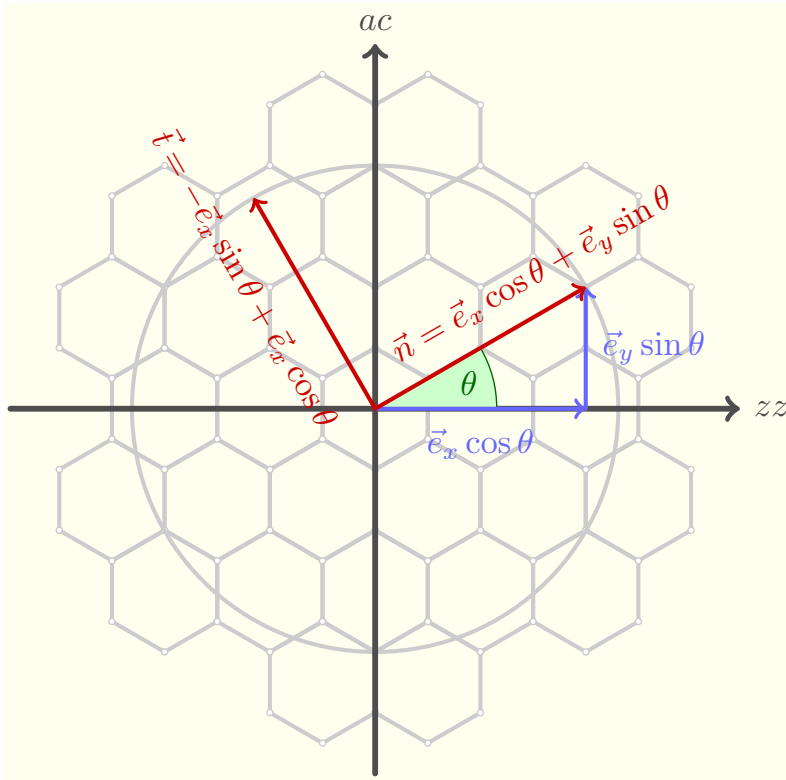


Figure 6.4: By applying an axial tension σ along the arbitrary direction \vec{n} ($\theta = \vec{z}\vec{z} \angle \vec{n}$), the Cauchy stress tensor $\hat{T} = \partial U / \partial \hat{\epsilon}$ is $\hat{T} = \sigma \vec{n} \otimes \vec{n}$. By inverting the constitutive equation $\hat{T} = \hat{C} : \hat{\epsilon} \implies \hat{\epsilon} = \hat{S} : \hat{T}$ we find the corresponding strain tensor $\hat{\epsilon}$. $\epsilon_l = \vec{n} \cdot \hat{\epsilon} \vec{n}$ longitudinal component; $\epsilon_t = \vec{t} \cdot \hat{\epsilon} \vec{t}$ transverse component (with $\vec{t} \cdot \vec{n} = 0$). In particular, we easily get its longitudinal component $\epsilon_l = \vec{n} \cdot \hat{\epsilon} \vec{n}$ along the direction \vec{n} as well as its transverse component $\epsilon_t = \vec{t} \cdot \hat{\epsilon} \vec{t}$ along the direction $\vec{t} = -\sin \theta \vec{e}_x + \cos \theta \vec{e}_y$.

particular, we easily get its longitudinal component $\epsilon_l = \vec{n} \cdot \hat{\epsilon} \vec{n}$ along the direction \vec{n}

$$\epsilon_l = \sigma \left[\frac{\mathcal{C}_{11}}{\Delta} s^4 + \frac{\mathcal{C}_{22}}{\Delta} c^4 + \left(\frac{1}{\mathcal{C}_{44}} - 2 \frac{\mathcal{C}_{12}}{\Delta} \right) c^2 s^2 \right] \quad (6.3)$$

as well as its transverse component $\epsilon_t = \vec{t} \cdot \hat{\epsilon} \vec{t}$ along the direction $\vec{t} = -\sin \theta \vec{e}_x + \cos \theta \vec{e}_y$ (with $\vec{t} \cdot \vec{n} = 0$)

$$\epsilon_t = \sigma \left[\left(\frac{\mathcal{C}_{11} + \mathcal{C}_{22}}{\Delta} - \frac{1}{\mathcal{C}_{44}} \right) c^2 s^2 - \frac{\mathcal{C}_{12}}{\Delta} (c^4 + s^4) \right] \quad (6.4)$$

*The \vec{n} -dependent
Young modulus*

where $\Delta = \mathcal{C}_{11}\mathcal{C}_{22} - \mathcal{C}_{12}^2$, $c = \cos \theta$, and $s = \sin \theta$. By means of Eqs.(6.3) and (6.4) we obtain, respectively, the \vec{n} -dependent Young modulus $E_{\vec{n}} = \sigma/\epsilon_l$ (i.e. the ratio between the applied traction and the longitudinal extension) as

$$E_{\vec{n}} = \frac{\Delta}{\mathcal{C}_{11}s^4 + \mathcal{C}_{22}c^4 + \left(\frac{\Delta}{\mathcal{C}_{44}} - 2\mathcal{C}_{12} \right) c^2s^2} \quad (6.5)$$

*The \vec{n} -dependent
Poisson ratio*

and the \vec{n} -dependent Poisson ratio $\nu_{\vec{n}} = -\epsilon_t/\epsilon_l$ (i.e. the ratio between the lateral contraction and the longitudinal extension) as

$$\nu_{\vec{n}} = - \frac{\left(\mathcal{C}_{11} + \mathcal{C}_{22} - \frac{\Delta}{\mathcal{C}_{44}} \right) c^2s^2 - \mathcal{C}_{12} (c^4 + s^4)}{\mathcal{C}_{11}s^4 + \mathcal{C}_{22}c^4 + \left(\frac{\Delta}{\mathcal{C}_{44}} - 2\mathcal{C}_{12} \right) c^2s^2} \quad (6.6)$$

Eqs.(6.5) and (6.6) are central to our investigation. More detail regard these derivations can be found in the Appendix A.6

First of all, we remark that they allow for the full linear elastic characterization of both the anisotropic graphane conformers and the trigonal one (as well as graphene), provided that in the latter case the isotropy and Cauchy conditions are duly exploited. In this case we in fact obtain the Young modulus $E = (\mathcal{C}_{11}^2 - \mathcal{C}_{12}^2)/\mathcal{C}_{11}$ and the Poisson ratio $\nu = \mathcal{C}_{12}/\mathcal{C}_{11}$, which are independent of the angle θ , confirming the planar isotropy.

*Homogeneous
in-plane deformation
method*

More importantly, however, Eqs.(6.5) and (6.6) imply that $E_{\vec{n}}$ and $\nu_{\vec{n}}$ can be directly obtained by the linear elastic constants \mathcal{C}_{ij} , in turn computed through energy-vs-strain curves corresponding to suitable homogeneous in-plane deformations. This implies that there is no actual need to mimic by a computer simulation a traction experiment along the arbitrary direction identified by \vec{n} or θ , indeed a technically complicated issue to accomplish. Rather, for the isotropic case (graphene and C-graphane) only two in-plane deformations should be applied in order to obtain all the relevant elastic constants, namely: (i) an axial deformation along the zigzag direction; and (ii) an hydrostatic planar deformation. For the anisotropic case (B- and W-graphane) two more in-plane deformations must be applied: (iii) an axial deformation

Table 6.2: Deformations and corresponding strain tensors applied to compute the elastic constants C_{ij} of graphene. The relation between such constants and the fitting term $U^{(2)}$ of Eq.(6.7) is reported as well. Deformations (i)-(ii) are applied to the C-conformer, while the full set (i)-(iv) of deformations is applied to the B- and W-conformers. ζ is the scalar strain parameter.

	strain tensor	$U^{(2)}$	$U^{(2)}$
		isotropic structures	anisotropic structures
(i) zigzag axial deformation	$\begin{pmatrix} \zeta & 0 \\ 0 & 0 \end{pmatrix}$	C_{11}	C_{11}
(ii) hydrostatic planar deformation	$\begin{pmatrix} \zeta & 0 \\ 0 & \zeta \end{pmatrix}$	$2(C_{11} + C_{12})$	$C_{11} + C_{22} + 2C_{12}$
(iii) armchair axial deformation	$\begin{pmatrix} 0 & 0 \\ 0 & \zeta \end{pmatrix}$		C_{22}
(iv) shear deformation	$\begin{pmatrix} 0 & \zeta \\ \zeta & 0 \end{pmatrix}$		$4C_{44}$

along the armchair direction; and (iv) a shear deformation. The strain tensors corresponding to deformations (i)-(iv) depend by a unique scalar strain parameter ζ as shown in Table 6.2. For all imposed deformations the elastic energy of strained structures can be written in terms of ζ as

$$U(\zeta) = U_0 + \frac{1}{2}U^{(2)}\zeta^2 + O(\zeta^3) \quad (6.7)$$

where U_0 is the energy of the unstrained configuration. Since the expansion coefficient $U^{(2)}$ is related to the elastic moduli as summarized in Table 6.2, a straightforward fit of Eq.(6.7) has provided the full set of linear moduli for all structures.

The synopsis of the calculated elastic constants for all graphane conformers, as well as graphene, is reported in Table 6.3, from which three qualitative information can be extracted. First, we observe that the difference between \mathcal{C}_{11} and \mathcal{C}_{22} is much smaller for the B-conformer than for W-graphane; therefore, this latter is by far the most elastically anisotropic conformer. Then, the value of \mathcal{C}_{44} , measuring the resistance to a shear deformation, decreases monotonically from graphene to W-graphane. Finally, we remark that the value of \mathcal{C}_{12} (or, similarly, of the Poisson ratio) is much smaller in any graphane structure than in pristine graphene. The change in hybridization has therefore largely reduced the property of lateral contraction upon extension. Interestingly enough, the B-conformer is characterized by a negative \mathcal{C}_{12} value, something unexpected and worthy of further investigation, as reported below.

Through Eqs.(6.5) and (6.6) and by using the elastic constants reported in Table 6.3, we can quantify the \vec{n} -dependence of E and ν for the anisotropic structures by using polar coordinates, as illustrated in Fig. 6.5 and Fig. 6.6, respectively. In such a representation, a fully isotropic elastic behavior is represented by a perfectly circular shape of the $E_{\vec{n}}$ and $\nu_{\vec{n}}$ plots. This is indeed the case, as expected, of graphene and C-graphane. On the other hand, Fig. 6.5 confirms that W-graphane is much more anisotropic than the B-conformer. Furthermore, as anticipated,

Table 6.3: Graphene and graphane independent elastic constants (units of Nm^{-1}). For graphene and C-graphane $\mathcal{C}_{11} = \mathcal{C}_{22}$ and $2\mathcal{C}_{44} = \mathcal{C}_{11} - \mathcal{C}_{12}$.

	graphene	C-graphane	B-graphane	W-graphane
\mathcal{C}_{11}	354	248	258	280
\mathcal{C}_{22}			225	121
\mathcal{C}_{12}	60	20	-1.7	14
\mathcal{C}_{44}			93	81

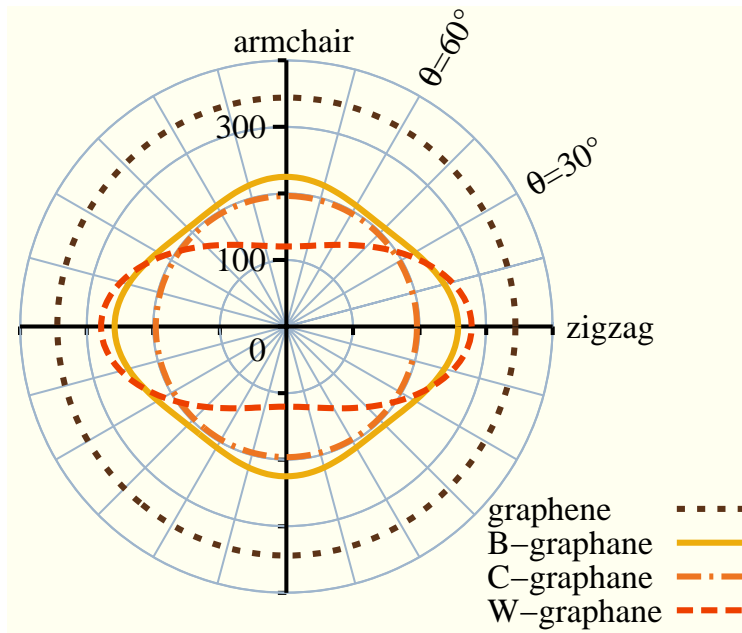


Figure 6.5: Polar diagram for the Young modulus E of graphene and graphane conformers. The angle θ identifies the extension direction with respect to the zigzag one. Isotropic (anisotropic) behavior is associated to a circular (non circular) shape of the $E_{\bar{n}}$ plot.

Fig. 6.6 provides evidence that the Poisson ratio in any graphane conformer is much smaller than in pristine graphene, since the corresponding $\nu_{\bar{n}}$ polar plots are contained within the graphene circle.

An intriguing unconventional behavior is observed in Fig. 6.6 for B-graphane, namely: for extensions along to the zigzag and armchair directions, the corresponding Poisson value is vanishingly small. This feature appears as a flower petal structure of the $\nu_{\bar{n}}$ plot for such a system. By considering Fig. 6.7, where a zoom of the previous plot nearby the origin has been reported, we can actually learn more information. It is evident that four small lobes appear along the zigzag and armchair directions (i.e. along the principal axis of the orthorhombic symmetry), corresponding to a Poisson ratio varying in the range $-0.0075 < \nu < -0.0065$. The limiting values are computed for extensions along the zigzag and armchair directions, respectively. It is truly remarkable that ν could be negative in B-graphane. While a negative Poisson ratio value is allowed by thermo-elasticity, this peculiar situation is only observed in special systems (i.e. foams, molecular networks or tailored engineering structures) or just rarely in ordinary bulk materials (i.e. SiO_2 , cubic metals, or polymer networks) [103].

Negative Poisson ratio

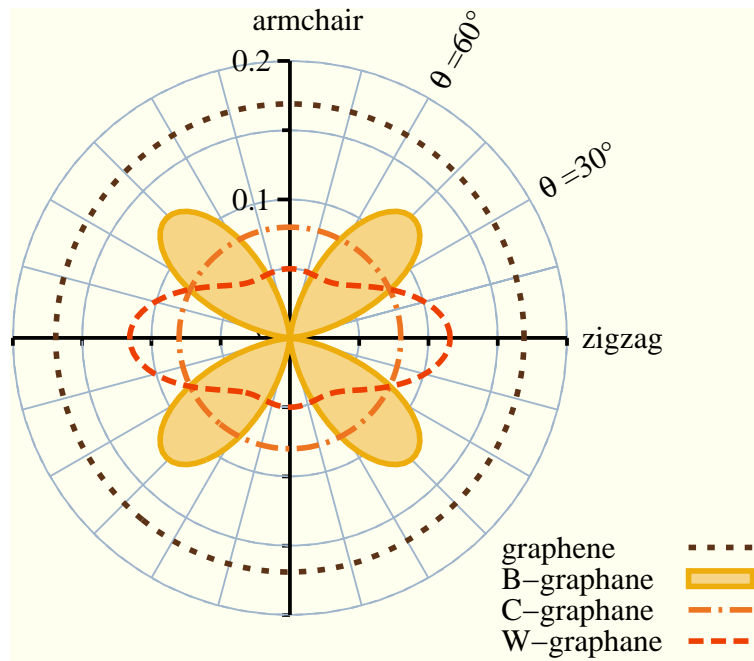


Figure 6.6: Polar diagram for the Poisson ratio ν of graphene and graphane conformers. The angle θ identifies the extension direction with respect to the zigzag one. Isotropic (anisotropic) behavior is associated to a circular (non circular) shape of the $\nu_{\vec{r}}$ plot. The special case of B-graphane is enlighten by shading (see text).

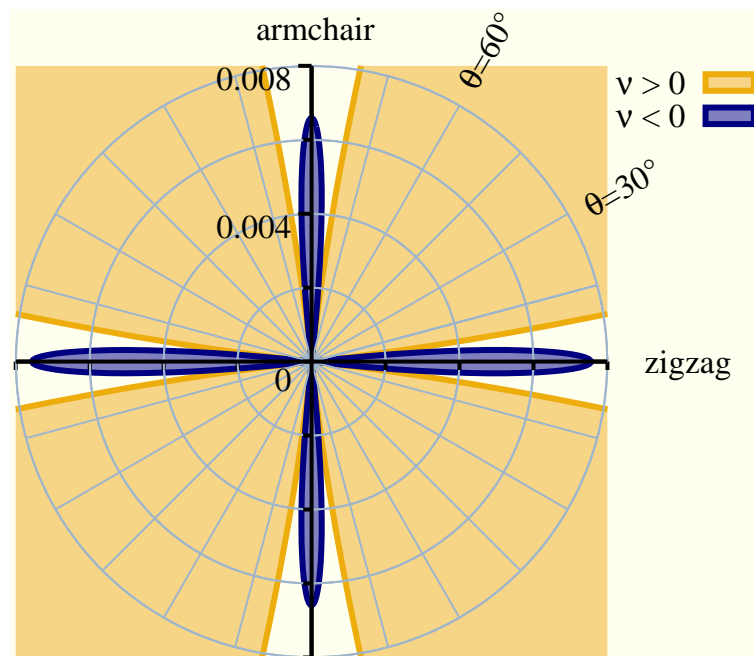


Figure 6.7: The same as Fig. 6.6 zoomed in the region nearby the origin. Positive and negative Poisson ratio values are differently shaded as indicated.

Table 6.4: Strain fields applied to compute the linear (\mathcal{C}_{ij}) and nonlinear (\mathcal{C}_{ijk}) elastic constants of the C-graphane. The relation between such constants and the fitting terms $\mathcal{U}^{(2)}$ and $\mathcal{U}^{(3)}$ of Eq.(6.11) is reported as well.

Strain tensor	$\mathcal{U}^{(2)}$	$\mathcal{U}^{(3)}$
$\begin{pmatrix} \zeta & 0 \\ 0 & 0 \end{pmatrix}$	\mathcal{C}_{11}	\mathcal{C}_{111}
$\begin{pmatrix} \zeta & 0 \\ 0 & \zeta \end{pmatrix}$	$2(\mathcal{C}_{11} + \mathcal{C}_{12})$	$2\mathcal{C}_{111} + 6\mathcal{C}_{112}$
$\begin{pmatrix} 0 & \zeta \\ \zeta & 0 \end{pmatrix}$	$2(\mathcal{C}_{11} - \mathcal{C}_{12})$	$8\mathcal{C}_{444}$
$\begin{pmatrix} \zeta & \zeta \\ \zeta & 0 \end{pmatrix}$	$3\mathcal{C}_{11} - 2\mathcal{C}_{12}$	$\mathcal{C}_{111} + 12\mathcal{C}_{144} + 6\mathcal{C}_{114} + 8\mathcal{C}_{444}$
$\begin{pmatrix} 0 & \zeta \\ \zeta & -\zeta \end{pmatrix}$	$3\mathcal{C}_{11} - 2\mathcal{C}_{12}$	$-\mathcal{C}_{111} - 12\mathcal{C}_{144} + 6\mathcal{C}_{114} + 8\mathcal{C}_{444}$
$\begin{pmatrix} \zeta & \zeta \\ \zeta & -\zeta \end{pmatrix}$	$4(\mathcal{C}_{11} - \mathcal{C}_{12})$	$12\mathcal{C}_{114} - 12\mathcal{C}_{124} + 8\mathcal{C}_{444}$

6.5 NONLINEAR ELASTICITY

In this Section we generalize the previous analysis in order to draw a comparison between the nonlinear elastic behavior of graphene, see Chapter 5, and the three conformers of graphane. The nonlinear strain energy function \mathcal{U}_{hex} for an hexagonal two dimensional lattice is (see Chapter 5)

$$\begin{aligned}
\mathcal{U}_{\text{hex}} = & \frac{1}{2}\mathcal{C}_{11} (\epsilon_{xx}^2 + \epsilon_{yy}^2 + 2\epsilon_{xy}^2) + \mathcal{C}_{12} (\epsilon_{xx}\epsilon_{yy} - \epsilon_{xy}^2) \\
& + \frac{1}{6}\mathcal{C}_{111}\epsilon_{xx}^3 + \frac{1}{6}\mathcal{C}_{222}\epsilon_{yy}^3 + \frac{1}{2}\mathcal{C}_{112}\epsilon_{xx}^2\epsilon_{yy} \\
& + \frac{1}{2}(\mathcal{C}_{111} - \mathcal{C}_{222} + \mathcal{C}_{112})\epsilon_{xx}\epsilon_{yy}^2 \\
& + \frac{1}{2}(3\mathcal{C}_{222} - 2\mathcal{C}_{111} - \mathcal{C}_{112})\epsilon_{xx}\epsilon_{xy}^2 \\
& + \frac{1}{2}(2\mathcal{C}_{111} - \mathcal{C}_{222} - \mathcal{C}_{112})\epsilon_{yy}\epsilon_{xy}^2 \quad (6.8)
\end{aligned}$$

Nonlinear strain energy function

where all the nonlinear features are described by the three independent moduli \mathcal{C}_{111} , \mathcal{C}_{222} and \mathcal{C}_{112} . Similarly, the strain energy function $\mathcal{U}_{\text{trigo}}$ for C-graphane depending on the linear (\mathcal{C}_{11} and \mathcal{C}_{12}) and nonlinear ($\mathcal{C}_{111}, \mathcal{C}_{112}, \mathcal{C}_{144}, \mathcal{C}_{114}, \mathcal{C}_{124}$ and \mathcal{C}_{444}) elastic constants is found to be

$$\begin{aligned}
\mathcal{U}_{\text{trigo}} = & \frac{1}{2}\mathcal{C}_{11} (\epsilon_{xx}^2 + \epsilon_{yy}^2 + 2\epsilon_{xy}^2) + \mathcal{C}_{12} (\epsilon_{xx}\epsilon_{yy} - \epsilon_{xy}^2) \\
& + \frac{1}{6}\mathcal{C}_{111} (\epsilon_{xx}^3 + \epsilon_{yy}^3) + \frac{1}{2}\mathcal{C}_{112} (\epsilon_{xx}^2\epsilon_{yy} + \epsilon_{xx}\epsilon_{yy}^2) \\
& + 2\mathcal{C}_{144} (\epsilon_{xx}\epsilon_{xy}^2 + \epsilon_{yy}\epsilon_{xy}^2) + \mathcal{C}_{114} (\epsilon_{xx}^2\epsilon_{xy} + \epsilon_{yy}^2\epsilon_{xy}) \\
& + 2\mathcal{C}_{124}\epsilon_{xx}\epsilon_{xy}\epsilon_{yy} + \frac{4}{3}\mathcal{C}_{444}\epsilon_{xy}^3 \quad (6.9)
\end{aligned}$$

Table 6.5: Strain fields applied to compute the linear (\mathcal{C}_{ij}) and nonlinear (\mathcal{C}_{ijk}) elastic constants of the B- and W-graphane. The relation between such constants and the fitting terms $U^{(2)}$ and $U^{(3)}$ of Eq.(6.11) is reported as well.

Strain tensor	$U^{(2)}$	$U^{(3)}$
$\begin{pmatrix} \zeta & 0 \\ 0 & 0 \end{pmatrix}$	\mathcal{C}_{11}	\mathcal{C}_{111}
$\begin{pmatrix} 0 & 0 \\ 0 & \zeta \end{pmatrix}$	\mathcal{C}_{22}	\mathcal{C}_{222}
$\begin{pmatrix} \zeta & 0 \\ 0 & \zeta \end{pmatrix}$	$\mathcal{C}_{11} + \mathcal{C}_{22} + 2\mathcal{C}_{12}$	$\mathcal{C}_{111} + \mathcal{C}_{222} + 3\mathcal{C}_{112} + 3\mathcal{C}_{122}$
$\begin{pmatrix} 0 & \zeta \\ \zeta & 0 \end{pmatrix}$	$4\mathcal{C}_{44}$	0
$\begin{pmatrix} \zeta & \zeta \\ \zeta & 0 \end{pmatrix}$	$\mathcal{C}_{11} + 4\mathcal{C}_{44}$	$\mathcal{C}_{111} + 12\mathcal{C}_{144}$
$\begin{pmatrix} 0 & \zeta \\ \zeta & \zeta \end{pmatrix}$	$\mathcal{C}_{22} + 4\mathcal{C}_{44}$	$\mathcal{C}_{222} + 12\mathcal{C}_{244}$
$\begin{pmatrix} \zeta & 0 \\ 0 & -\zeta \end{pmatrix}$	$\mathcal{C}_{11} + \mathcal{C}_{22} - 2\mathcal{C}_{12}$	$\mathcal{C}_{111} - \mathcal{C}_{222} - 3\mathcal{C}_{112} + 3\mathcal{C}_{122}$

For such a trigonal symmetry we have $\mathcal{C}_{111} = \mathcal{C}_{222}$, $\mathcal{C}_{112} = \mathcal{C}_{122}$ and $\mathcal{C}_{144} = \mathcal{C}_{244}$. Nevertheless, it is important to underline that the overall nonlinear elastic response is truly anisotropic since not all the relevant isotropic conditions are fulfilled.

Finally, the strain energy function U_{ortho} for the B- and W-graphane, expressed through the linear ($\mathcal{C}_{11}, \mathcal{C}_{22}, \mathcal{C}_{12}$ and \mathcal{C}_{44}) and nonlinear ($\mathcal{C}_{111}, \mathcal{C}_{222}, \mathcal{C}_{112}, \mathcal{C}_{122}, \mathcal{C}_{144}$ and \mathcal{C}_{244}) elastic constants, is given by

$$\begin{aligned}
U_{\text{ortho}} &= \frac{1}{2}\mathcal{C}_{11}\epsilon_{xx}^2 + \frac{1}{2}\mathcal{C}_{22}\epsilon_{yy}^2 + 2\mathcal{C}_{44}\epsilon_{xy}^2 + \mathcal{C}_{12}\epsilon_{xx}\epsilon_{yy} \\
&+ \frac{1}{6}\mathcal{C}_{111}\epsilon_{xx}^3 + \frac{1}{6}\mathcal{C}_{222}\epsilon_{yy}^3 + \frac{1}{2}\mathcal{C}_{112}\epsilon_{xx}^2\epsilon_{yy} \\
&+ \frac{1}{2}\mathcal{C}_{122}\epsilon_{xx}\epsilon_{yy}^2 + 2\mathcal{C}_{144}\epsilon_{xx}\epsilon_{xy}^2 + 2\mathcal{C}_{244}\epsilon_{yy}\epsilon_{xy}^2 \quad (6.10)
\end{aligned}$$

Eqs.(6.8), (6.9) and (6.10) can be obtained by using the standard tables of the tensor symmetries, found in many crystallography textbooks (see for instance Ref. [102]).

As above described, in any symmetry the strain energy function depends on the third-order elastic constants (as well as the linear ones). Once again, they can be computed through energy-vs-strain curves corresponding to suitable homogeneous in-plane deformations. For each deformation the elastic energy of strained graphene or graphane can be written in terms of just the single deformation parameter ζ

$$U(\zeta) = U_0 + \frac{1}{2}U^{(2)}\zeta^2 + \frac{1}{6}U^{(3)}\zeta^3 + O(\zeta^4) \quad (6.11)$$

Table 6.6: Graphene and graphane independent nonlinear elastic constants (units of Nm^{-1}).

	graphene	C-graphane	B-graphane	W-graphane
\mathcal{C}_{111}	-1910 ± 11	-1385 ± 18	-1609 ± 31	-1756 ± 33
\mathcal{C}_{222}	-1764 ± 3		-1827 ± 7	-487 ± 85
\mathcal{C}_{112}	-341 ± 35	-195 ± 41	-20 ± 14	-75 ± 54
\mathcal{C}_{122}			-55 ± 22	-296 ± 36
\mathcal{C}_{124}		-411 ± 17		
\mathcal{C}_{114}		530 ± 12		
\mathcal{C}_{144}		568 ± 7	-161 ± 4	-143 ± 17
\mathcal{C}_{244}			-159 ± 3	-287 ± 10
\mathcal{C}_{444}		0.0 ± 10^{-5}		

Since the expansion coefficients $U^{(2)}$ and $U^{(3)}$ are related to elastic constants, as summarized in Table 6.4 for the C-graphane and in Table 6.5 for the B- and W-graphane, a straightforward fit of Eq.(6.11) has provided the full set of third-order elastic constants.

The results have been reported in Table 6.6 where only the values of the independent elastic constants appearing in Eqs. (6.8), (6.9) and (6.10) are reported. We note that graphene and B-graphane are characterized by an inverted anisotropy: while $\mathcal{C}_{111} < \mathcal{C}_{222}$ for graphene, we found $\mathcal{C}_{222} > \mathcal{C}_{111}$ for B-graphane. On the contrary, W-graphane has the same anisotropy of graphene ($\mathcal{C}_{111} < \mathcal{C}_{222}$), but a larger $|\mathcal{C}_{111} - \mathcal{C}_{222}|$ difference. So, it is interesting to observe that the different distribution of hydrogen atoms can induce strong qualitative variations for the nonlinear elastic behavior of these structures.

We finally observe that necessarily $\mathcal{C}_{444} = 0$ for B- and W-graphane because of the orthorhombic symmetry. On the other hand, this nonlinear shear modulus could assume any value for the trigonal lattice. Interesting enough, we have verified that $\mathcal{C}_{444} = 0$ also for C-graphane. This is due to the additional (with respect to the trigonal symmetry) mirror symmetry of C-graphane.

As shown in Chapter 5, similarly to the case of graphene [12], a nonlinear stress-strain relation can be derived for the three graphane conformers:

$$\sigma_{\vec{n}} = E_{\vec{n}} \epsilon_{\vec{n}} + D_{\vec{n}} \epsilon_{\vec{n}}^2 \quad (6.12)$$

where $E_{\vec{n}}$ and $D_{\vec{n}}$ are, respectively, the Young modulus and an effective nonlinear (third-order) elastic modulus, along the arbitrary direction \vec{n} , as defined in Sec. 6.4. The nonlinear elastic

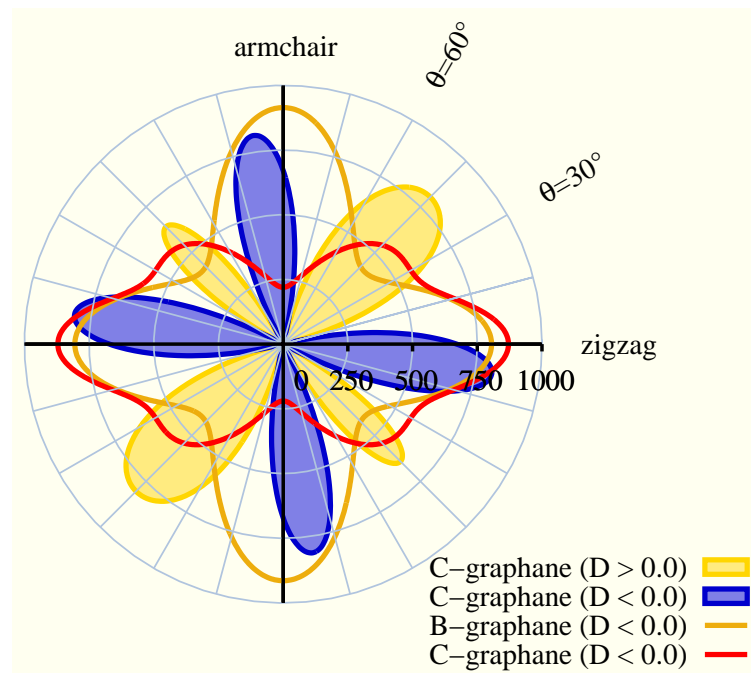


Figure 6.8: Polar representation of the nonlinear elastic moduli $D_{\vec{n}}$ of the three graphane conformers. In the B- and W-graphane cases, $D_{\vec{n}} \equiv D$ are everywhere negative (softening hyperelasticity), while in the C-graphane one the $D_{\vec{n}}$ alternates negative and positive values (hardening hyperelasticity).

modulus $D_{\vec{n}}^{(\text{trigo})}$ for the C-graphane (as well as for any trigonal 2D lattice) is given by

$$\begin{aligned} D_{\vec{n}}^{(\text{trigo})} = & \frac{1}{2} \left[\nu (1 - \nu) (\mathcal{C}_{111} - 3\mathcal{C}_{112}) \right. \\ & + (1 - \nu) (1 + \nu^2) \mathcal{C}_{111} \\ & + 6cs (1 + \nu) (1 + \nu^2) \mathcal{C}_{114} - 12cs (1 + \nu) \nu \mathcal{C}_{124} \\ & + 3c^2 s^2 (1 - \nu) (1 + \nu^2) (-\mathcal{C}_{111} + 4\mathcal{C}_{144} + \mathcal{C}_{112}) \\ & + 4c^3 s^3 (1 + \nu) (1 + \nu^2) (-3\mathcal{C}_{114} + 2\mathcal{C}_{444} + 3\mathcal{C}_{124}) \\ & \left. + 8c^3 s^3 (1 + \nu) \nu (-6\mathcal{C}_{114} + 5\mathcal{C}_{444} + 6\mathcal{C}_{124}) \right] \quad (6.13) \end{aligned}$$

while the corresponding modulus $D_{\vec{n}}^{(\text{ortho})}$ B- and W-graphene is

$$\begin{aligned} D_{\vec{n}}^{(\text{ortho})} = & \frac{1}{2\Delta^3 E_{\vec{n}}^3} \left[\mathcal{C}_{111} (\mathcal{C}_{22}c^2 - \mathcal{C}_{12}s^2)^3 \right. \\ & + \mathcal{C}_{222} (\mathcal{C}_{11}s^2 - \mathcal{C}_{12}c^2)^3 \\ & + 3\mathcal{C}_{112} (\mathcal{C}_{11}s^2 - \mathcal{C}_{12}c^2) (\mathcal{C}_{22}c^2 - \mathcal{C}_{12}s^2)^2 \\ & + 3\mathcal{C}_{122} (\mathcal{C}_{22}c^2 - \mathcal{C}_{12}c^2) (\mathcal{C}_{11}s^2 - \mathcal{C}_{12}c^2)^2 \\ & - 3\mathcal{C}_{166}c^2s^2 (\mathcal{C}_{22}c^2 - \mathcal{C}_{12}s^2) (\Delta/\mathcal{C}_{44})^2 \\ & \left. - 3\mathcal{C}_{266}c^2s^2 (\mathcal{C}_{11}s^2 - \mathcal{C}_{12}c^2) (\Delta/\mathcal{C}_{44})^2 \right] (6.14) \end{aligned}$$

where $\Delta = \mathcal{C}_{11}\mathcal{C}_{22} - \mathcal{C}_{12}^2$, $c = \cos \theta$, and $s = \sin \theta$. Since $\mathcal{C}_{ijk} < 0$, as shown in Tab.6.6, $D_{\vec{n}}^{(\text{ortho})}$ are negative for any direction (see Fig. 6.8), so both B- and W-graphane show an hyperelastic softening behavior. The trigonal C-graphane behaves in a very different way instead. Since the \mathcal{C}_{114} and \mathcal{C}_{144} are positive, the C-graphane can show an hyperelastic hardening behavior in the angular sectors $5/12\pi + k\pi < \theta < 1/12 + k\pi$ and $8/12\pi + k\pi < \theta < 10/12 + k\pi$ ($k \in \mathbb{Z}$).

In conclusion, present first principles calculations predict that the class of auxetic materials is larger than reported so far, including as well two dimensional hydrocarbons like B-graphane. More precisely, since a negative Poisson ratio is observed for extensions along the zigzag and armchair principal directions, B-graphane is better referred to as an axially auxetic atomic sheet. Moreover, we calculated that the other two conformers, namely the C- and W-graphane, exhibit a vanishingly small value of the Poisson ratio. The linear moduli values are in agreements with those recently reported in literature [25]. The nonlinear elastic behavior of graphane shows peculiar features as well. In particular, we have found that the C-graphane admits both softening and hardening hyperelasticity, depending on the direction of the applied strain. These features makes graphane a very intriguing material with potentially large technological impact in nanomechanics.

GAP OPENING IN GRAPHENE BY SHEAR STRAIN

“The Indians are finding the gaps like a pin in a haystack.”
Navjot Singh Sidhu

Contents

7.1	Introduction and motivation	109
7.2	The electronic structure of graphene	110
7.3	Some detail about the out-of-plane relaxation	117

In this Chapter we exploit the concept of strain-induced band structure engineering in graphene through the calculation of its electronic properties under uniaxial, shear, and combined uniaxial-shear deformations. We show that by combining shear deformations to uniaxial strains it is possible to modulate the graphene energy gap value from zero up to 0.9 eV. Interestingly enough, the use of a shear component allows for a gap opening at moderate absolute deformation, safely smaller than the graphene failure strain, i.e. in a range of reversible and more easily accessible deformations, ranging in between 12% and 17%. We also discuss the merging of Dirac points [104], which is involved in the gap opening process.

7.1 INTRODUCTION AND MOTIVATION

As reported in Chapter 1, graphene exhibits a number of exotic electronic properties, such as unconventional integer quantum Hall effect, ultrahigh electron mobility, electron-hole symmetry and ballistic transport even at room temperature [5, 38, 105]. Full account of these features is provided by the relativistic Dirac theory [7] suitably developed within the standard condensed matter formalism. A key feature of graphene is that its electronic density of states vanishes at the so-called Dirac points, where the valence and the conduction bands cross with a linear energy-momentum dispersion. Due to the hexagonal symmetry of graphene, the Dirac points are located at two high-symmetry points of its Brillouin zone.

While many other properties of graphene are very promising for nanoelectronics, its zero-gap semiconductor nature is detrimental, since it prevents the pinch off of charge current as requested in conventional electronic devices. Different attempts

Dirac points due to the hexagonal symmetry

have been therefore tried in order to induce a gap, for instance by quantum confinement of electrons and holes in graphene nanoribbons [17] or quantum dots [18]. These patterning techniques are unfortunately affected by the edge roughness problem [19], namely: the edges are extensively damaged and the resulting lattice disorder can even suppress the efficient charge transport. The sensitivity to the edge structure has been demonstrated through explicit calculations of the electronic states in ribbons [20]. More recently, it has been shown experimentally that a band gap as large as 0.45 eV can be opened if a graphene sheet is placed on an Ir(111) substrate and exposed to patterned hydrogen adsorption [21].

Alternatively, an electronic band gap can be obtained by growing graphene sheets on an appropriately chosen substrate, inducing a strain field controllable by temperature [27, 28, 29, 30]. Recently, it has been experimentally shown that by using flexible substrates a reversible and controlled strain up to $\sim 18\%$ [29] can be generated with measurable variations in the optical, phonon and electronic properties of graphene [30]. This interesting result suggests that gap opening could be engineered by strain, rather than by patterning. The idea has been theoretically validated by Pereira and Castro Neto [31] showing that a gap is indeed generated by applying an uniaxial strain as large as $\sim 23\%$, approaching the graphene failure strain $\epsilon_f = 25\%$ [12] (see Chapter 5). This large value stands for the high robustness of the gapless feature of graphene under deformation. The same authors propose an alternative origami technique [13] aimed at generating local strain profiles by means of appropriate geometrical patterns in the substrate, rather than by applying strain directly to the graphene sheet.

7.2 THE ELECTRONIC STRUCTURE OF GRAPHENE

The electronic structure of graphene by means of a semi-empirical sp^3 tight-binding (TB) model

The electronic structure of graphene has been computed for each deformed configuration by means of a semi-empirical sp^3 tight-binding (TB) model, making use of the two-center parameterization by Xu *et al.* [50], as discussed in Sec. 2.1. Despite its semi-empirical character, the present TB model correctly provides the occurrence of Dirac points in the band structure of graphene in its equilibrium geometry. Furthermore, the Xu *et al.* parametrization provides accurate scaling functions for the variation of the TB hopping integrals upon lattice distortions. This feature is instrumental for investigating gap opening in graphene by strain.

As discuss in Chapter 1, graphene is an hexagonal lattice with two carbon atoms per unit cell and a lattice basis defined by the vectors $(\mathbf{a}_1, \mathbf{a}_2)$, as shown in Fig. 7.1, with a nearest-neighbor

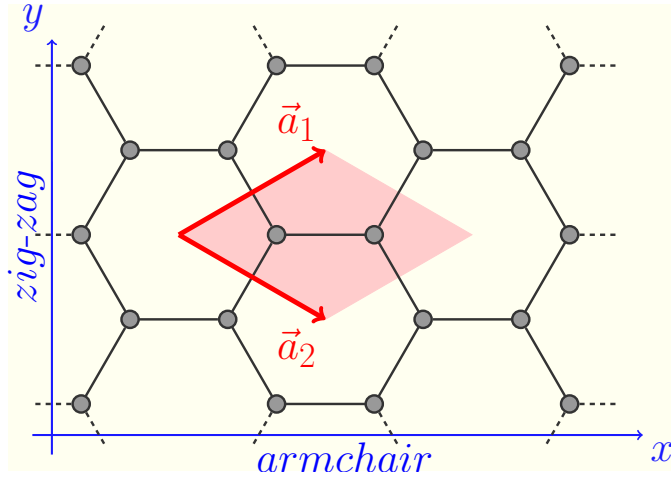


Figure 7.1: Top view of the hexagonal graphene lattice with its lattice vectors $\mathbf{a}_{1,2} = a_0 \left(\frac{3}{2}, \pm \frac{\sqrt{3}}{2} \right)$, where a_0 is the equilibrium C-C distance. Axis x and y corresponds to the armchair and zig-zag direction, respectively. Shaded area represents the unit cell.

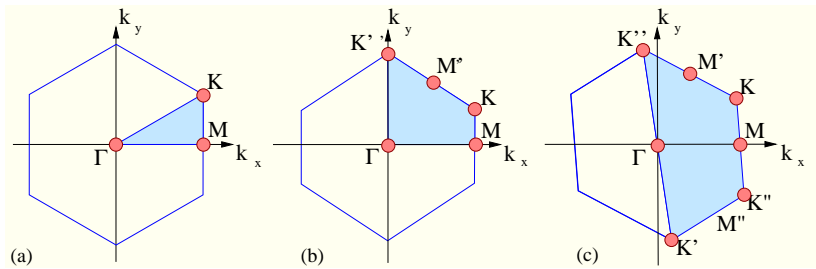
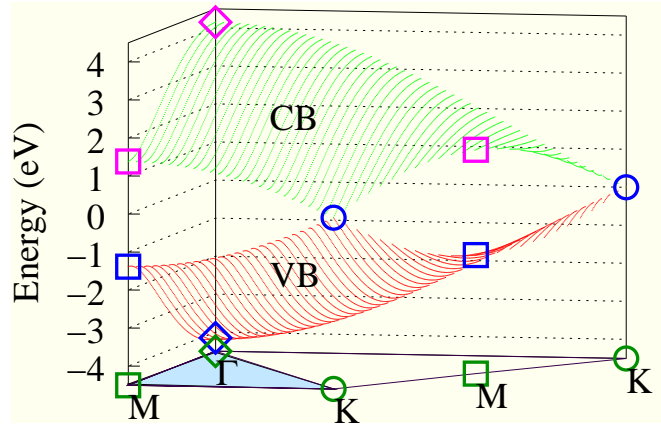


Figure 7.2: Brillouin zone of graphene under strain. The shaded areas are the corresponding irreducible part: Panel (a), undeformed BZ with $6/mmm$ hexagonal symmetries; Panel (b), BZ deformed by uniaxial strain with mmm rhombic symmetry; Panel (c), BZ deformed by shear strain with $2/m$ monoclinic symmetry.



(a) undeformed graphene

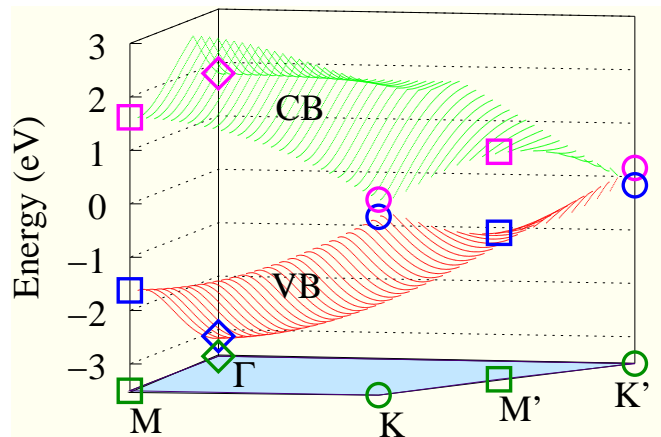
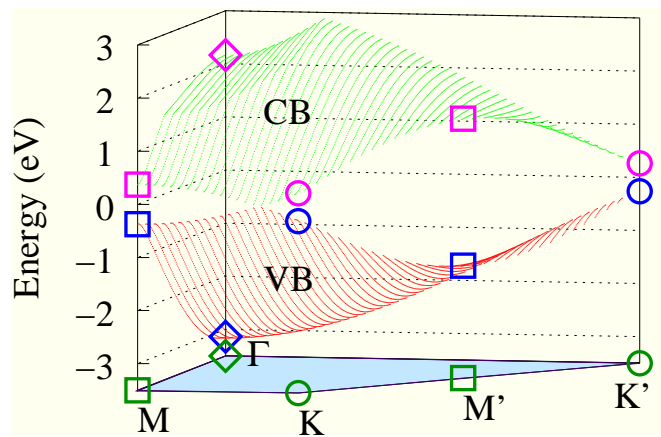
(b) uniaxial (armchair) strain with $\zeta = 15\%$ (c) uniaxial (zig-zag) strain with $\zeta = 15\%$

Figure 7.3: Top of the valence band (red, marked as VB) and bottom of the conduction band (green, marked as CB) of graphene under uniaxial strain. Panel (a): band structure of the undeformed lattice. Panel (b) and (c): band structure under uniaxial strain along the armchair and the zig-zag direction, respectively. Symbols connect the high-symmetry points of the BZ (bottom shaded area) to the energy of the corresponding electronic states.

carbon-carbon distance as small as $a_0 = 1.42 \text{ \AA}$. The in-plane elastic behavior of the honeycomb lattice is isotropic in the linear regime, but two inequivalent crystallographic directions can be nevertheless defined: the so-called armchair and zig-zag directions, shown in Fig. 7.1 as x and y axis, respectively. According to the Cauchy-Born rule, when straining a graphene sample its lattice vectors are affected accordingly, as well as the associated reciprocal vectors ($\mathbf{b}_1, \mathbf{b}_2$). The deformed metric tensor are given by $\mathbf{a}'_{i\alpha} = (\epsilon_{ik} + \delta_{ik}) \mathbf{a}_{k\alpha}$, here the vector indices $i = 1, 2$ and the Cartesian indices $\alpha = x, y$, and $\hat{\epsilon} = \{\epsilon_{ij}\}$ is the strain tensor describing the deformation and $i, j = x, y$. The condition $(\mathbf{b}'_1, \mathbf{b}'_2)^T = 2\pi (\mathbf{a}'_1, \mathbf{a}'_2)^{-1}$ allows us to obtain the deformed reciprocal lattice vectors.

The deformed reciprocal lattice vectors ($\mathbf{b}'_1, \mathbf{b}'_2$)

The following in-plane deformations have been applied to the equilibrium honeycomb lattice under plane-strain border conditions: *i*) an uniaxial deformation ζ along the armchair direction, corresponding to a strain tensor $\epsilon_{ij}^{(ac)} = \zeta \delta_{ix} \delta_{jx}$; *ii*) an uniaxial deformation ζ along the zig-zag direction, corresponding to a strain tensor $\epsilon_{ij}^{(zz)} = \zeta \delta_{iy} \delta_{jy}$; *iii*) an hydrostatic planar deformation ζ , corresponding to the strain tensor $\epsilon_{ij}^{(p)} = \zeta \delta_{ij}$; *iv*) a shear deformation ζ , corresponding to an in-plane strain tensor $\epsilon_{ij}^{(s)} = \zeta (\delta_{ix} \delta_{jy} + \delta_{iy} \delta_{jx})$. For any deformed configuration, we have computed the corresponding electronic band structure and density of states. The carbon atoms in graphene shown the sp^2 hybridization. Among the four valence orbitals, three ($2s, 2p_x, 2p_y$) are combined to form the in-plane σ (bonding or occupied) and σ^* (anti-bonding or unoccupied) orbitals, while the delocalized π (bonding) and π^* (anti-bonding) are due to the interaction with neighboring $2p_z$ (where \vec{z} are orthogonal to the graphene sheet). Because of the σ and σ^* bands are well separated in energy (10 eV at Γ), the π and π^* bands coincide with the valence and the conduction bands, respectively. Such that they are enough to describe the electronic properties of graphene in its equilibrium status and also up to an applied strain of 10% , when the σ, σ^* and π, π^* bands overlap at Γ . In the following we discuss the results simply in terms of valence and conduction bands.

The applied in-plane deformations to honeycomb lattice under plane-strain border conditions

In order to extend the reliability of the present model to electronic features under strain, our results about the effects of hydrostatic and uniaxial deformations on the band structure are at first compared with previous data available in literature. For graphene under in-plane hydrostatic deformation with $\zeta \leq 15\%$, both in compression and in traction, we have calculated the band electronic structure and the density of states. Since the hydrostatic strain does not change the $D_{6h}(6/mmm)$ symmetry of the hexagonal lattice (Fig. 7.2a), we only observe the variation of the pseudogaps at Γ and M points, while the location of the Dirac

In-plane hydrostatic deformation

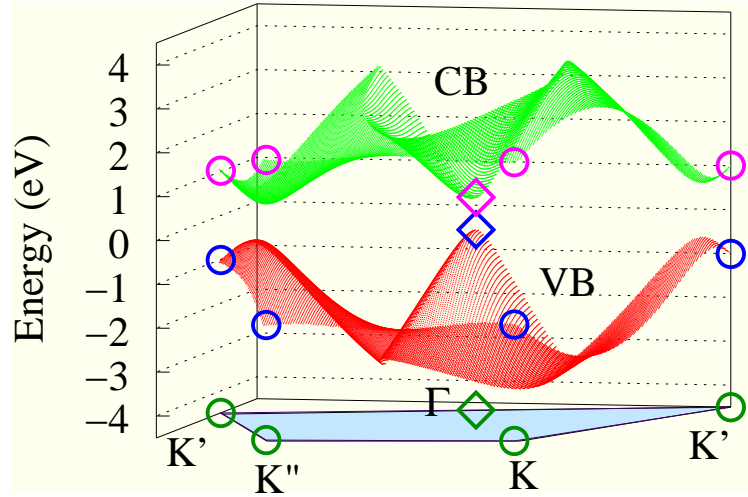


Figure 7.4: Top of the valence band (red, marked as VB) and bottom of the conduction band (green, marked as CB) of graphene under pure shear strain with $\zeta = 20\%$. Symbols connect the high-symmetry points of the BZ (bottom shaded area) to the energy of the corresponding electronic states.

points is clamped at the K point. In particular, the pseudogap at M decreases almost linearly from 6 eV (for $\zeta = -15\%$) to 1.8 eV (for $\zeta = +15\%$). We remind that its value for the unstrained configuration is 2.2 eV. These results are in quantitative good agreement with Ref. [90]. Any other non-hydrostatic deformation lowers the symmetry of the graphene lattice. When an uniaxial strain is applied, all the 6- and 3-fold rotational symmetries are lost: a transition from the hexagonal $D_{6h}(6/mmm)$ to the rhombic $D_{2h}(mmm)$ symmetry is observed (Fig. 7.2b). The irreducible part of the first Brillouin zone (BZ) is also affected by such deformations, since its original triangular shape (Fig. 7.2a) is varied to the polygonal form represented in Fig. 7.2b. The top of the valence band and the bottom of the conduction band are shown in Fig. 7.3 for the undeformed configuration (panel a), as well as under uniaxial deformation (panels b and c, corresponding to a strain $\zeta = 15\%$ along the armchair direction and in the zig-zag direction respectively). The main effect of strain is the opening of a pseudo-gap at K and K'. Accordingly, the Dirac points are no more located at such high-symmetry points; rather, they drift away within the BZ, either for deformations along armchair direction or along zig-zag one. Once again this important qualitative feature is in good agreement with Ref. [31].

Uniaxial strain

In-plane shear deformation

Let us now consider the case of an in-plane shear deformation, described by the following shear strain

$$\hat{\epsilon} = \begin{pmatrix} 0 & \zeta \\ \zeta & 0 \end{pmatrix} \quad (7.1)$$

where ζ is the strain parameter. Such a deformation modifies the original reciprocal lattice vectors \mathbf{b}_1 and \mathbf{b}_2 into

$$\begin{aligned}\mathbf{b}'_1 &= \frac{2\pi}{a_o} (1 - \zeta^2)^{-1} \left(\frac{1}{3} - \frac{\sqrt{3}}{3}\zeta, \frac{\sqrt{3}}{3} - \frac{1}{3}\zeta \right) \\ \mathbf{b}'_2 &= \frac{2\pi}{a_o} (1 - \zeta^2)^{-1} \left(+\frac{1}{3} + \frac{\sqrt{3}}{3}\zeta, -\frac{\sqrt{3}}{3} - \frac{1}{3}\zeta \right)\end{aligned}\quad (7.2)$$

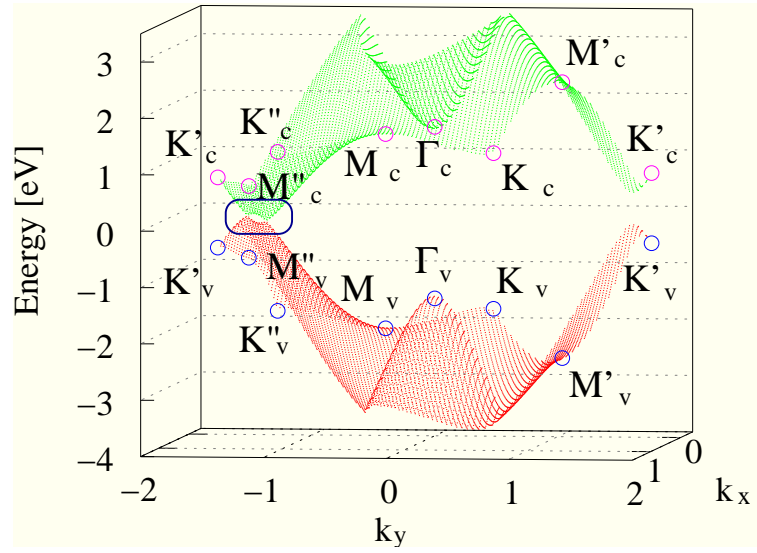
By applying the shear strain given in Eq. (7.1) to the graphene lattice, its symmetry class is further lowered to monoclinic. The corresponding symmetry group is $2/m$. Because of this change in symmetry, the irreducible part of the BZ is affected accordingly as shown in Fig. 7.2c, which has K' , K , K'' , K' as corners. In the undeformed lattice, a Dirac point is located at each of these corners. The scenario under shear strain is quite different from the case of uniaxial deformations: at the comparatively small strain $\zeta \simeq 16\%$, a gap is indeed opened. The rise of a gap in the electronic band structure under shear is due to a peculiar process that involves the merging of two Dirac points, namely D' and D'' , which move away from the corners K' and K'' and approach each other inside the BZ. By “merging” we mean the following: as shown in Fig. 7.5, at a critical strain $\zeta \simeq 15.95\%$ the Dirac points are so close that they annihilate in a single hybrid Dirac cone, which shows a peculiar energy-momentum dispersion: it is linear (quadratic) along (perpendicular) to the direction joining the two Dirac points. At $\zeta = 16.0\%$, a gap as small as 0.05 eV is eventually opened. More details about the motion of Dirac points in two-dimensional crystals under uniaxial stress are reported in Ref. [104, 106, 107].

Merging of Dirac cones

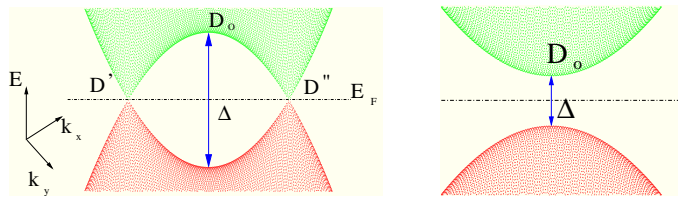
Is important to remark that the merging of the two inequivalent Dirac points and the opening of a gap, appear for a shear strain value $\zeta \simeq 16\%$ which is lower than in the case of zig-zag uniaxial deformation [31]. The gap increases up to a maximum value of 0.72 eV for shear strain parameter of $\zeta \simeq 20\%$, as shown in Fig. 7.4. Moreover, the same detail is shown in Fig. 7.5b-c: in panel b, at a strain $\zeta \simeq 15.9\%$ the couple of Dirac points are very close, but not yet annihilated and at their middle point D_o a pseudo-gap Δ can be observed; in panel c, the band structure shows a small gap already at $\zeta \simeq 16\%$. We conclude that shear strain seems a likely candidate to achieve gap opening in graphene for a deformation far enough from failure strain and, therefore, achievable with no danger for the overall mechanical stability of the two-dimensional sheet.

Gap opening is predicted by the present TB calculation to occur at an even smaller strain parameter ζ , provided that a combination of shear and uniaxial strain is considered. By adding an uniaxial component to shear we generate a strain tensor of the form

Combining uniaxial and shear deformations



(a) shear strain $\zeta = 15\%$



(b) $\zeta = 15.9\%$

(c) $\zeta = 16.0\%$

Figure 7.5: (a) Electronic band structure of purely sheared graphene (with the same value of strain parameter $\zeta = 15\%$) are shown in the corresponding irreducible zone. The Dirac cones (blue ellipse) are enlarged and shown in panels b-c: (b) with $\zeta = 15.9\%$ the couple of Dirac cones D' and D'' are just before merging and shown a pseudo-gap Δ at D_0 equal to 0.15eV ; (c) with $\zeta = 16.0\%$ the merging is occurred and the gap is equal to 0.05 eV .

$$\hat{\epsilon} = \begin{pmatrix} \zeta & \zeta \\ \zeta & 0 \end{pmatrix} \quad \text{or} \quad \hat{\epsilon} = \begin{pmatrix} 0 & \zeta \\ \zeta & \zeta \end{pmatrix} \quad (7.3)$$

for which the symmetry class of the lattice is not changed with respect to the pure shear case.

Nevertheless, uniaxial deformations along the armchair or zig-zag direction are found to dissimilarly affect the band structure of graphene. Only in the last case we have observed the merging of the Dirac points already at $\zeta \simeq 12\%$. The main features of the transition is the same as described before. The energy gap grows up to a maximum value of 0.95 eV (when the strain parameter achieves a value of $\zeta \simeq 17\%$), reducing again to zero at $\zeta \simeq 20\%$ due to the steady decrease of the direct gap at Γ .

In order to quantitatively describe the evolution of the gap opening as function of the applied strain, the density of states (DOS) has been calculated by a two-dimensional $75 \times 150 \times 1$ regular k-point mesh of the (deformed) BZ. As shown in Fig. 7.6, for a strain value less than 15% (panel a) or 11% (panel b), the DOS depends linearly on energy close to the Fermi level, showing a slope increasing with the strain. The two characteristic Van Hove singularities into the DOS move closer the Fermi energy and disappear into abrupt gap-edges as soon as the gap is open. After the annihilation of the Dirac points, the DOS shows a $\sim \sqrt{E}$ behavior.

We conclude by remarking that the two strain contributions (i.e. uniaxial and shear) could be combined in different ways so as to modulate the energy gap value. In Fig. 7.7, the electronic band structures of graphene under different combinations of shear and uniaxial strain are compared, keeping the same value of the strain parameter $\zeta = 15\%$. While the combination of shear with uniaxial armchair shows a sizable energy gap of about 0.6 eV, the combination of shear with uniaxial zig-zag is associated to a gapless band structure.

7.3 SOME DETAIL ABOUT THE OUT-OF-PLANE RELAXATION

We showed that by combining shear deformations to uniaxial strains it is possible to affect the gapless electronic structure of graphene by opening a gap as large as 0.9 eV. The use of a shear component allows for gap opening at a moderate absolute deformation, safely smaller than the graphene failure strain. This result was obtained in absence of out-of-plane deformations (as due, e.g., to bending or rippling), a situation corresponding to configurations where the graphene sheet is supported, i.e. deposited on a suitable substrate [27, 30, 29]. On the other hand out-of-plane atomic relaxations on a free standing graphene monolayer under shear strain can induced ripples. This is consistent with a well

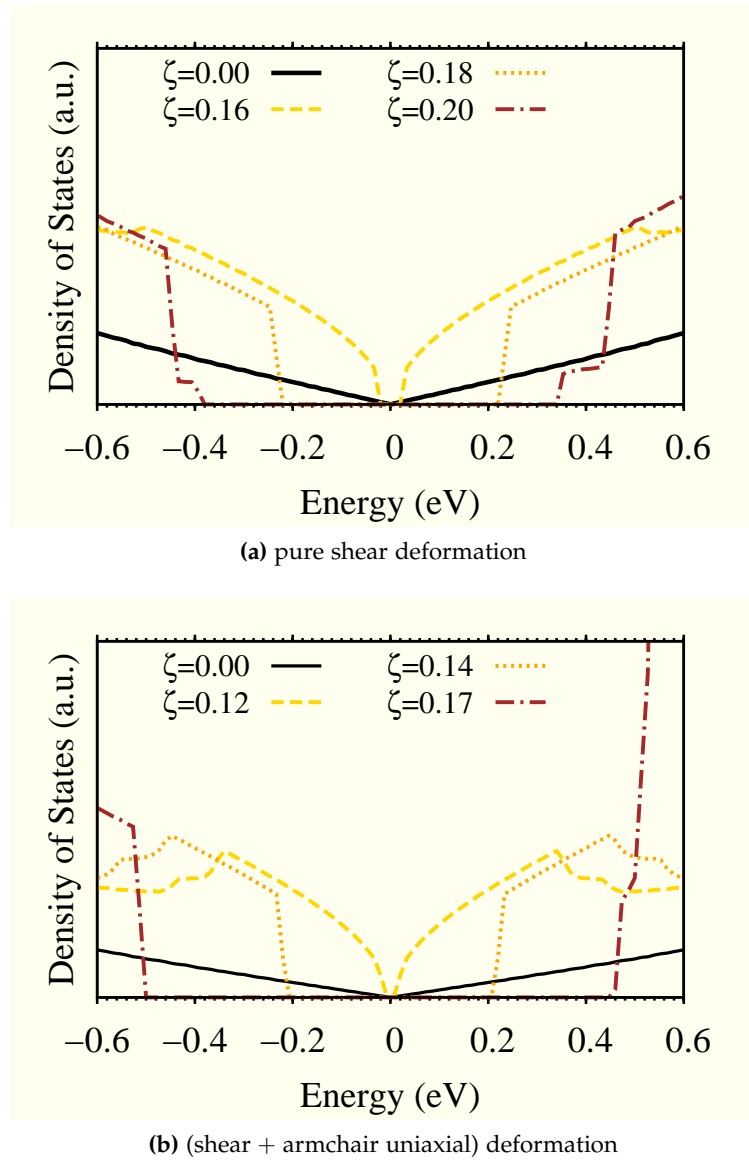


Figure 7.6: Density of states around the Fermi level (set conventionally at 0 eV) as function of the strain parameter ζ . Panel (a): graphene under pure shear deformation. Panel (b): graphene under combined shear and uniaxial deformation (along the armchair direction). The maximum value of the energy gap is observed for a strain parameter as large as $\zeta \simeq 20\%$ and $\zeta \simeq 17\%$ respectively.

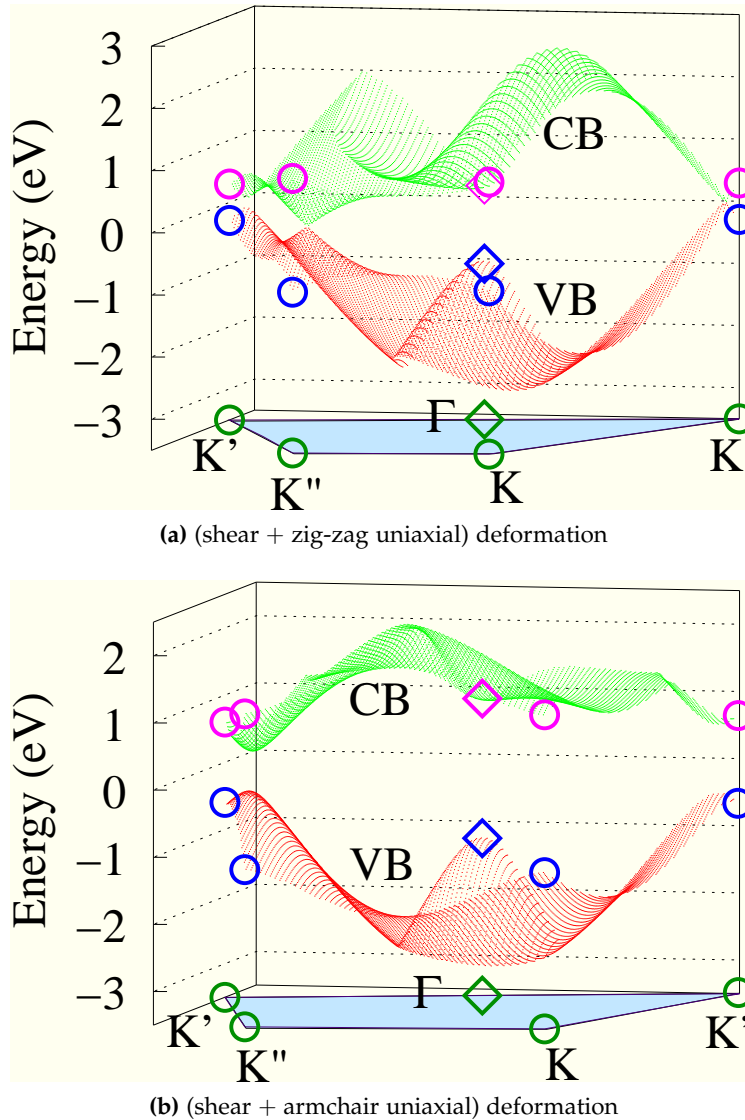


Figure 7.7: Top of the valence band (red, marked as VB) and bottom of the conduction band (green, marked as CB) of graphene under combined shear and uniaxial strain with $\zeta = 15\%$. The uniaxial component of the strain is applied along the zig-zag [panel (a)] and armchair [panel (b)] directions. Symbols connect the high-symmetry points of the BZ (bottom shaded area) to the energy of the corresponding electronic states.

known result of continuum mechanics: shear, as well as uniaxial, deformations come with reversible corrugations, whether applied to a free standing elastic membrane [108, 109]. Therefore the gap opening in graphene under shear deformation (or combined uniaxial and shear deformations) could be unlikely inhibited, since ripples should cancel the strain effects we found for a flat graphene sheet. While overall interesting, our results are addressed to a graphene sheet where out-of-plane relaxations are inhibited. The first and second configurations correspond, respectively, to a suspended and to a supported sample. In addition, we observe that the ripple geometry of a suspended sheet can be effectively altered via thermal manipulation, up to a complete suppression when temperature is raised to 450-600K, as experimentally found by Bao *al.* [110]. We believe that this result provides another example of ripple-free, but strained graphene membrane, making our investigation relevant and physically sound even for some suspended samples.

Interesting enough, in Ref. [110] it has been also reported that the measured wavelength of the ripples ranges from 370 to 5000 nm. Under this respect, once again we believe that our calculations are meaningful: the larger is the wavelength of the ripples, the better is the approximation of a ripple-free graphene sheet (which locally is basically flat). Moreover, Pereira *et al.* [13] explore the influence of local strain on the electronic structure of graphene. They suggest that the graphene electronics can be controlled by suitable engineering of local strain profiles, a perspective which is indeed in nice agreement with our conclusions.

“Notice that the stiffest tree is most easily cracked, while the bamboo or willow survives by bending with the wind.”

Bruce Lee (1940- 1973)

Contents

8.1	Bending in carbon nanoribbons	121
8.2	The bending rigidity theory	122
8.2.1	Continuum picture	122
8.2.2	Atomistic simulations	126
8.3	Simulation protocol and the calculated bending features	130

In present Chapter we discuss the bending properties of carbon nanoribbons by combining continuum elasticity theory and tight-binding atomistic simulations. First, we develop a complete analysis of a given bended configuration through continuum mechanics. Then, we provide by tight-binding calculations the value of the bending rigidity in good agreement with recent literature. We discuss the emergence of a stretching field induced by the full atomic-scale relaxation of the nanoribbon architecture. We further prove that such an in-plane strain field can be decomposed in a first contribution due to the actual bending of the sheet and a second one due to the edges effects induced by the finite size of the nanoribbon.

8.1 BENDING IN CARBON NANORIBBONS

Graphene [111] plays a unique role in materials science since it is the mother structure of most carbon sp^2 nanosystems of current interest. By stacking, folding or bending a graphene sheet it is indeed possible to generate, respectively, graphite-like systems, fullerene cages (pentagonal rings are here needed as well) or nanotubes. In particular, the bending properties are critical in attaining the structural stability and morphology for both suspended and supported graphene sheets, and directly affect their electronic properties [38]. Rippling of pure graphene has been also observed with mesoscopic amplitude and wavelength, both for suspended monolayers [36] and sheets deposited on substrates such as silicon dioxide [37]. Moreover, the bending properties play a central role in the design of graphene- or carbon

nanotube-based devices, like e.g. mechanical resonators [39, 40]. The bending features of functionalized graphene sheets have been probed by atomic force microscopy, observing that the folding behavior is dominated by defects and functional groups [41]. Finally, bending ultimately governs the carbon nanotubes unzipping process, recently used to produce narrow ribbons for nanoelectronics [42]. With the same technique, a new class of carbon-based nanostructures, which combine nanoribbons and nanotubes, has been introduced in order to obtain magnetoresistive devices [43].

Within this scenario we frame the present investigation, addressed to improve our fundamental understanding of the bending properties of a one-atom thick carbon sheet. The main goal is twofold: *i)* to draw a thorough theoretical picture on bending, fully exploiting the elasticity theory and providing an atomistic quantitative estimation of the corresponding bending rigidity; *ii)* to prove that the bending process of a carbon nanoribbon is always associated with the emergence of a (small) stretching, particularly close to the edges. These results have been obtained by combining continuum elasticity theory and tight-binding atomistic simulations (TB-AS).

The conceptual development and actual exploitation of our theoretical model proceeds through the following steps. At first, by means of continuum mechanics we have obtained the exact shape for a purely bended nanoribbon, by imposing suitable boundary conditions. The bending rigidity is then evaluated by TB-AS for several nanoribbons differing by length and width. As a second step, we observed that, under the above assumption of pure bending, the corresponding rigidity must be a constant independent of the actual shape of the sheet. Nevertheless by allowing full atomic-scale relaxation during bending, we rather found a geometry-dependent rigidity, a feature that we have attributed to the onset of stretching phenomena. Therefore, as final step, we have developed a procedure to discriminate between stretching and bending energy, so providing a complete picture about the mechanical behavior of graphene and also reconciling the atomistic data with the continuum theory results.

8.2 THE BENDING RIGIDITY THEORY

8.2.1 Continuum picture

The graphene strain energy density u [eVÅ⁻²] is defined as [112, 85]

$$u = \frac{1}{2} \frac{E}{1+\nu} \text{Tr}(\hat{\varepsilon}^2) + \frac{1}{2} \frac{E\nu}{1-\nu^2} [\text{Tr}(\hat{\varepsilon})]^2 + \frac{1}{2} \kappa (2\mathcal{H})^2 - \bar{\kappa} \mathcal{K} \quad (8.1)$$

where E [Nm^{-1}] and ν are the two dimensional Young modulus and the Poisson ratio, while κ [eV] and $\bar{\kappa}$ [eV] are the bending rigidity and the Gaussian rigidity, respectively. The in-plane deformation (stretching) energy [given by the first two terms in Eq. (8.1)] is described by the standard small strain tensor $\hat{\epsilon} = \frac{1}{2}(\vec{\nabla}\vec{u} + \vec{\nabla}\vec{u}^T)$, being \vec{u} the displacement field. On the other hand, the out of plane deformation (bending) energy [given by the last two terms in Eq. (8.1)] is described by the mean curvature $\mathcal{H} = \frac{k_1+k_2}{2}$ [m^{-1}] and by the Gaussian curvature $\mathcal{K} = k_1 k_2$ [m^{-2}], where k_1 and k_2 are the principal curvatures at a given point on the surface [113], as shown in Fig. 8.1a. They are straightforwardly given by $k_1 = 1/R_1$ and $k_2 = 1/R_2$ where R_1 and R_2 are the principal radii of curvature at that point. In the case of a continuum plate of thickness h made of an isotropic and homogeneous material, the classical Kirchhoff theory provides $\kappa = \frac{1}{12} \frac{Eh^2}{1-\nu^2}$ and $\bar{\kappa} = \frac{1}{12} \frac{Eh^2}{1+\nu}$ (note that $E = Yh$ where Y is the three-dimensional Young modulus) [85]. For an infinitesimally thin graphene monolayer such a theory does not apply, since the thickness h cannot be unambiguously defined and the bending moment has simply a different physical origin. While the bending moment for the Kirchhoff plate derives from a compression/extension of the different material layers forming the thickness h , in graphene it is due to the interactions among orbitals p_z which are affected by the bending process. Therefore, the determination of κ and $\bar{\kappa}$ for graphene is a well-posed (and, to a large extent, still open) problem, which is independent of the evaluation of E and ν [114].

To evaluate only the bending energy term, the ribbon has been bended without stretching (i.e. strain $\hat{\epsilon} = 0$) Thus the Eq. (8.1) is reduced to the only bending energy contribution \mathcal{U}_b [$\text{eV}\text{\AA}^{-2}$] of a given cylindrical surface

$$\begin{aligned} \mathcal{U}_s &= \frac{1}{2} \frac{E}{1+\nu} \text{Tr}(\hat{\epsilon}^2) + \frac{1}{2} \frac{E\nu}{1-\nu^2} [\text{Tr}(\hat{\epsilon})]^2 = 0 \\ \mathcal{U}_b &= \frac{1}{2} \kappa k_1^2 \end{aligned} \quad (8.2)$$

As sketched in Fig. 8.1b, our model system is a rectangular ribbon with length l and width L . The boundary conditions consist in fixing the positions of the two parallel edges (with length l) at a given distance a , while the attack angles θ is free to relax. This configuration involves only one curvature k_1 , leading to $\mathcal{H} = \frac{k_1}{2}$ and $\mathcal{K} = 0$, as shown in Fig. 8.1b. By considering different values of a in the range $(0, L)$, we obtained a set of differently bended configurations. The elastic problem consists in finding the sheet shape by minimizing the bending energy

$$\mathcal{U}_b = \iint_{\mathcal{A}} \mathcal{U} dA = \frac{1}{2} \kappa l \int_0^L k_1^2 ds \quad (8.3)$$

Bending rigidity and the Gaussian rigidity

Geometric feature of a surface

The classical Kirchhoff theory

The bending energy of a bended ribbon without stretching

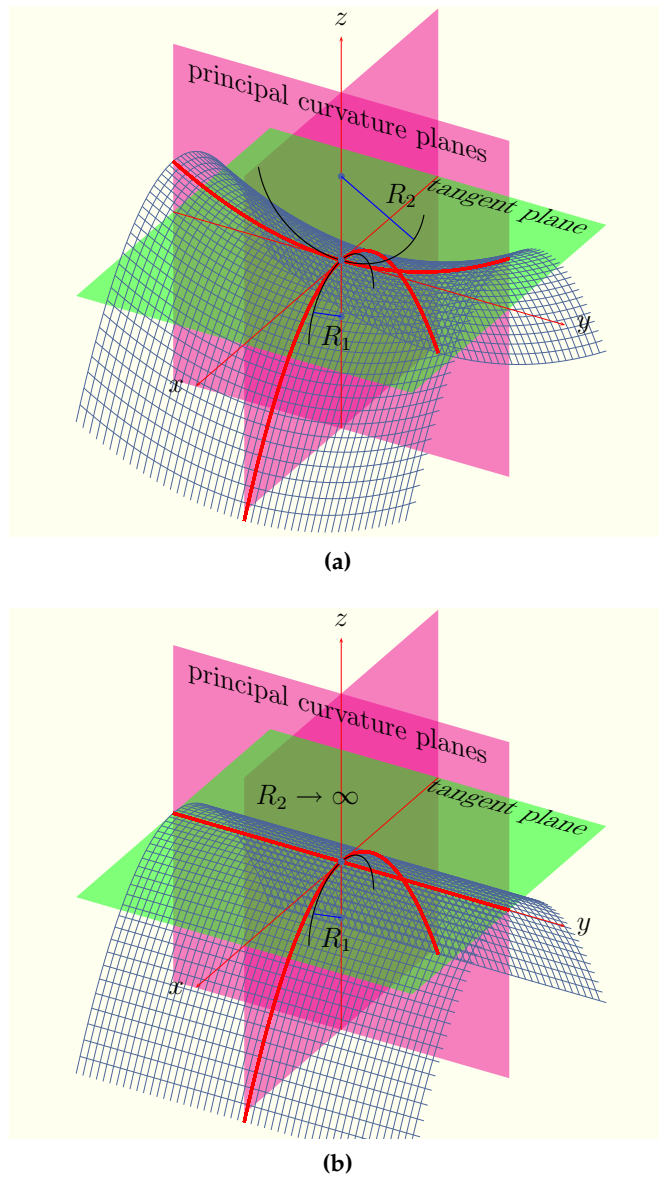


Figure 8.1: Panel (a) A sketch of the main geometrical features of a generic surface. At a given point on the surface the principal curvature planes and the corresponding principal radii R_1, R_2 are shown. The red lines on the surface represent the geodesics at the given point, i.e. the intersections between the surface and the principal planes. Panel (b) In cylindric surfaces one geodesic has to be a straight, here $R_2 \rightarrow \text{inf}$, so that the Gaussian curvature goes to zero.

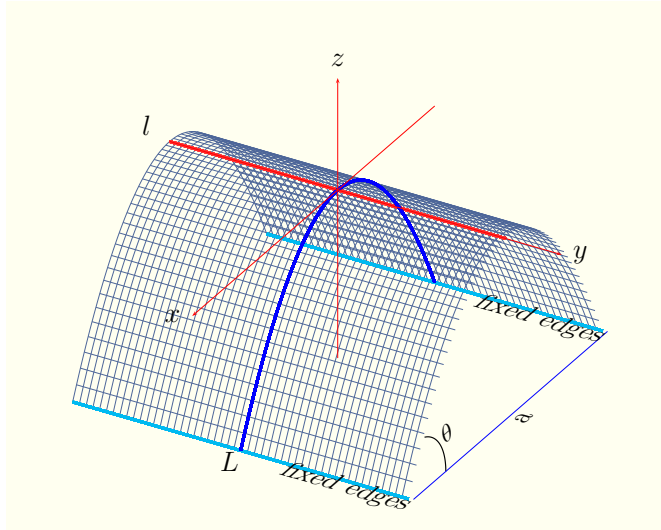


Figure 8.2: Bended ribbon with length l and width L (red dashed line). The parallel edges with length l are fixed at distance α , while the attack angles θ is free to relax.

where $A = Ll$ is the total area of the system, and s is the arc length ($0 < s < L$)

We have to minimize the surface integral $\mathcal{J} = \int_0^L k_1^2 ds$ by the calculus of the variations. A more detailed discussion can be found in Appendix A.8. Let's to consider the Eq. (8.3) as follows

$$\mathcal{J} = \int_0^L ds \sqrt{g} (2\mathcal{H}(P))^2 = \int_0^L ds \sqrt{g} (\text{tr}(W_P))^2 \quad (8.4)$$

where we got the metric, g , the Weingarten operator, $W_P(u) = -\frac{\partial \hat{n}}{\partial u}$, and the mean curvature at a given point on the surface, $\mathcal{H}(P) = \frac{1}{2} \text{tr}(W_P)$. If the configuration is described by the function $z = z(x)$, then we get $k_1 = \ddot{z} / (1 + \dot{z}^2)^{3/2}$, where $\dot{z} = dz/dx$ and $\ddot{z} = d^2z/dx^2$. On the other hand, $ds = \sqrt{g} dx$ where $\sqrt{g} = \sqrt{1 + \dot{z}^2}$. Therefore, Eq. (8.3) assumes the explicit form

$$U_b = \frac{1}{2} \kappa l \int_0^\alpha \frac{\ddot{z}^2}{(1 + \dot{z}^2)^{5/2}} dx \quad (8.5)$$

The problem consists in finding the curve $z = z(x)$ minimizing the energy functional in Eq. (8.5) by the method of Lagrange multipliers λ

$$\int_0^\alpha dx \left[\frac{\ddot{z}^2}{(1 + \dot{z}^2)^{5/2}} + \lambda \sqrt{1 + \dot{z}^2} \right], \quad (8.6)$$

under the follows boundary conditions

$$\begin{aligned} & \text{a constrained width, } L = \int_0^\alpha dx \sqrt{1 + \dot{z}^2}, \\ & \text{a fixed parallel edges, } z(0) = z(\alpha) = 0, \\ & \text{a free attack angle, } \theta = \text{arctg}\left(\frac{dz}{dx}\right), \quad \dot{z}(0) = \dot{z}(\alpha) = 0. \end{aligned} \quad (8.7)$$

A variational approach to find the minimum surface shape

The method of Lagrange multipliers λ

Eulero-Poisson
equation

enforcing the absence of any in-plane stretching. The above integral can be written in the general form $G(z) = \int_0^a dx \mathcal{F}(z, \dot{z}, \ddot{z}, x)$, which is the solution of the Euler-Poisson differential equation

$$\frac{\partial \mathcal{F}}{\partial z} - \frac{d}{dx} \frac{\partial \mathcal{F}}{\partial \dot{z}} + \frac{d^2}{dx^2} \frac{\partial \mathcal{F}}{\partial \ddot{z}} = 0 \quad (8.8)$$

The minimum
surface in parametric
representation
[$x(s), z(s)$]

By the application of the constrained variational calculus we eventually obtain the final geometry in parametric representation [$x(s), z(s)$]

$$\frac{x}{L} = \frac{E(q) - \mathcal{E}(\operatorname{am}\{\mathbf{K}(q)(1 - 2\frac{s}{L})\}, q)}{\mathbf{K}(q)} - \frac{s}{L} \quad (8.9)$$

$$\frac{z}{L} = \frac{q}{\mathbf{K}(q)} \operatorname{cn}\left\{\mathbf{K}(q)\left(1 - 2\frac{s}{L}\right)\right\} \quad (8.10)$$

where s is the arc length ($0 < s < L$), $q = \sin \frac{\theta}{2}$ is the elliptic modulus and θ is the attack angle given by

$$\frac{a}{L} = 2 \frac{E(q)}{\mathbf{K}(q)} - 1. \quad (8.11)$$

The complete elliptic
integrals

The quantities $E(q)$ and $\mathbf{K}(q)$ are the complete elliptic integrals, defined as [115, 116]

$$E(q) = \mathcal{F}\left(\frac{\pi}{2}, q\right), \quad \mathbf{K}(q) = \mathcal{E}\left(\frac{\pi}{2}, q\right) \quad (8.12)$$

where the functions $\mathcal{F}(v, q)$ and $\mathcal{E}(v, q)$ are incomplete elliptic integrals of the first and second kind, respectively [115, 116]

$$\begin{aligned} \mathcal{F}(v, q) &= \int_0^v \frac{d\alpha}{\sqrt{1 - q^2 \sin^2 \alpha}} \\ \mathcal{E}(v, q) &= \int_0^v \sqrt{1 - q^2 \sin^2 \alpha} d\alpha. \end{aligned} \quad (8.13)$$

Universal value of
the attack angle

Moreover, by considering $u = \mathcal{F}(v, q)$ we define the inverse relation (with fixed modulus q) $v = \operatorname{am}\{u\}$, which is called Jacobi amplitude function. Further, $\operatorname{cn}\{u\} = \cos v = \cos(\operatorname{am}\{u\})$ and $\operatorname{sn}\{u\} = \sin v = \sin(\operatorname{am}\{u\})$ are the Jacobi elliptic functions [116]. Interesting enough, one can prove that $\lim_{a/L \rightarrow 0} \theta = 130.709^\circ$, an universal value of the attack angle found whenever $a = 0$ or L is very large.

8.2.2 Atomistic simulations

The present TB-AS [84] have been performed making use of the sp^3 , orthogonal, and next-neighbors tight-binding representation by Xu et al. [50]. The present TB total energy model has been implemented within the scheme given by Goodwin *et al.* [117]

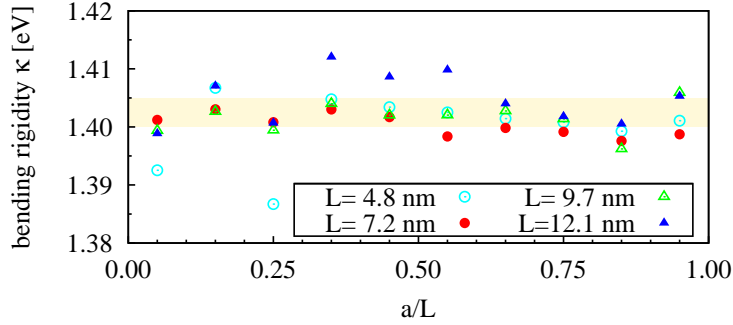


Figure 8.3: Bending rigidity κ obtained for purely ribbons with several widths L . The average value is given by $\kappa_{\text{ave}} = 1.4025 \pm 0.0025$ eV (yellow area shows the error bar)

for the dependence of the TB hopping integrals and the pairwise potential on the interatomic separation.

Applications to molecular-dynamics studies of liquid carbon and small carbon clusters indicate that this model correctly describes carbon systems over a wide range of environments [50]. This approach has been successfully used to show that the surface of nanodiamond particles reconstructs in a fullerene-like manner, generating carbon clusters called bucky diamonds [118]. Moreover, the growth of nanostructures (linear, ring, and fullerene-like objects) in a carbon plasma [119] and the formation of carbon clusters (onion-like and endohedral structures) from the condensation of liquid droplets [120] have been simulated by the present tight-binding model.

The previous continuum analysis is useful both to create the input configurations for atomistic calculations and to define the simulation protocol. The investigated system consists in a nanoribbon formed by a perfect hexagonal carbon lattice, having width L in the range 4–12 nm and length l imposed to obtain a simulation box containing a constant number of ~ 600 carbon atoms. In Figs. 8.2.2, 8.2.2 there are shown some examples of the atomistic samples under bending. Moreover, periodic boundary conditions are assumed along the direction of the length l . The length (width) is developed along the armchair (zig-zag) direction of the honeycomb lattice. Each nanoribbon is deformed as defined in Eqs. (8.9) and (8.10) in ten configurations corresponding to different values of a . In any bended configuration, all the interatomic distances are fixed at the equilibrium value for flat graphene (so that no bond stretching is for the moment allowed). The bending rigidity has been straightforwardly obtained as $\kappa = \frac{2}{l^3} U_b$ with U_b given by Eq. (8.3), where the integral $\mathcal{J} = \int_0^L k_1^2 ds$ is computed for the given configuration. It is important to remark that the obtained

*Simulative protocol:
Step 1.*

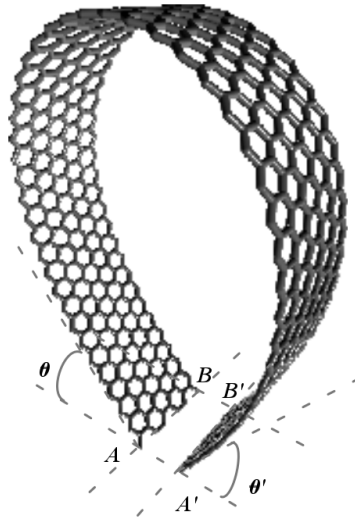


Figure 8.4: For instance we show a relaxed atomic configuration for a nanoribbon of graphene bended with parallel fixed edges and attach angles free. The edges $\overline{AA'}$ and $\overline{BB'}$ are kept parallel and at fixed distance a , while the attach angle θ are free.

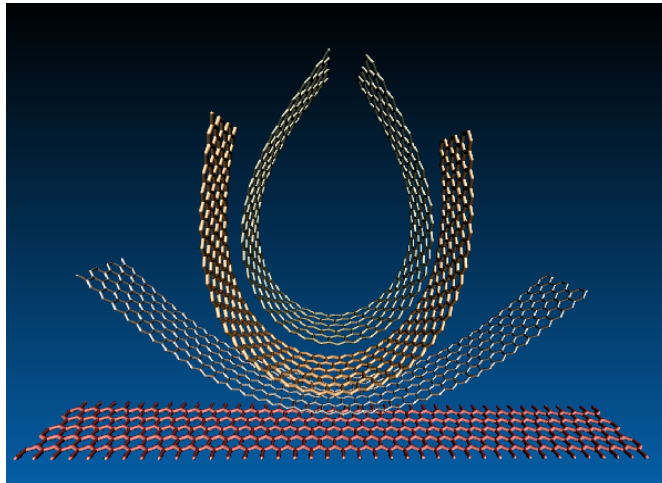


Figure 8.5: Several nanoribbons of graphene with different distances between edges are shown, which are build The reference configuration starting from the same flat reference configuration (the red lower one).

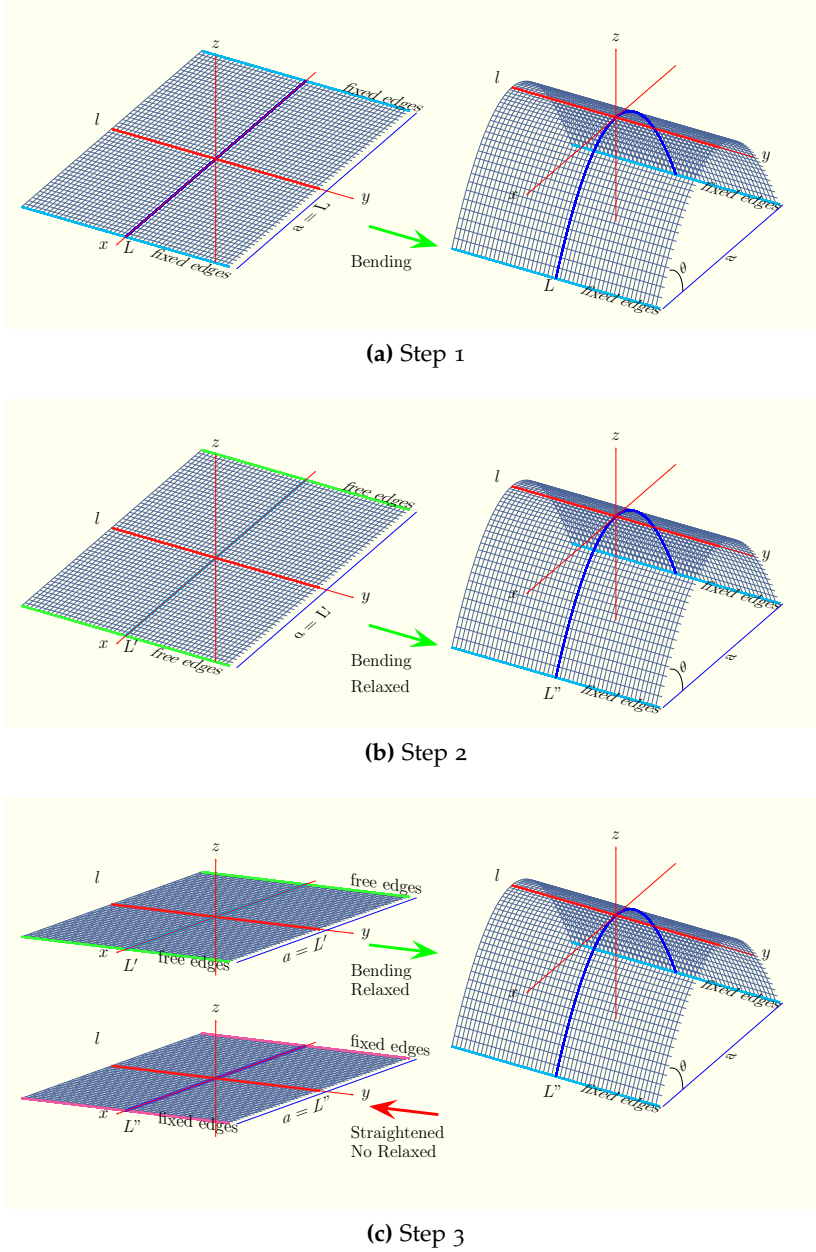


Figure 8.6: Panel(a) In the continuum picture the (pure) bending energy is $U_b = E_0^{\text{bended}} - E_0^{\text{flat}}$, here E_0^{flat} is the total energy of the equilibrium (flat) configuration, and E_0^{bended} is the total energy of the bended unrelaxed configuration. Panel (b) Taking into account full relaxation of the internal degrees of freedom of the bended systems, we evaluate the new bending rigidity κ by means of the energy $U_b = E_{\text{relaxed}}^{\text{bended}} - E_{\text{relaxed}}^{\text{flat}}$, where $E_{\text{relaxed}}^{\text{flat}}$ is the energy of a flat ribbon after a full relaxation, and $E_{\text{relaxed}}^{\text{bended}}$ is the energy of a full relaxed bended ribbon. Panel (c) we have defined a virtual process of straightening of a given relaxed and bended ribbon, thus the bending rigidity κ can be consequently determined by using $U_b = E_{\text{relaxed}}^{\text{bended}} - E_{\text{straightened}}^{\text{flat}}$.

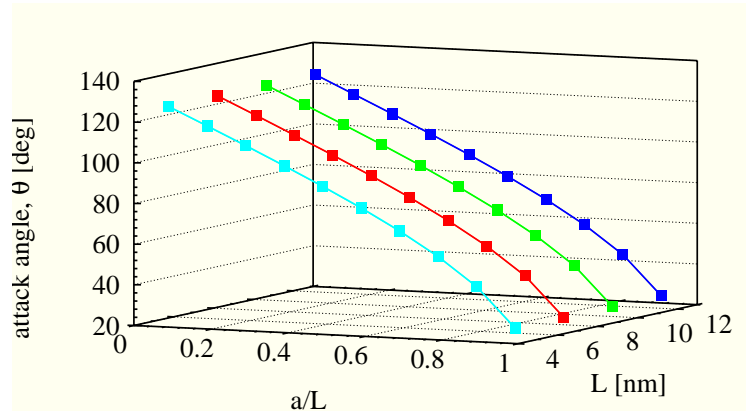


Figure 8.7: The theoretical results for the values of the attack angles θ (circles), predicted from Eq. (8.11) for several ribbon with different width L , each at different edge-distances a , are compared with the corresponding data from atomistic simulations (crosses).

value for κ must be independent of the actual configuration since the deformation is a pure bending one.

8.3 SIMULATION PROTOCOL AND THE CALCULATED BENDING FEATURES

Accordingly to the scheme outlined in the previous Section, we have firstly evaluated the (pure) bending energy as $U_b = E_0^{\text{bended}} - E_0^{\text{flat}}$, where E_0^{bended} and E_0^{flat} represent the TB-AS total energy of the bended (but not relaxed) and equilibrium (flat) configurations, respectively. The atomistic results for κ are reported in Fig. 8.3 (symbols) as function of the a/L ratio and for different width L . We estimate an average value $\kappa_{\text{ave}} = 1.40$ eV. While the reported values of κ (for nanotubes) vary in the range $1 \text{ eV} \lesssim \kappa \lesssim 2 \text{ eV}$, [15], we remark the most reliable *ab-initio* data $\kappa = 1.40$ eV [114], and $\kappa = 1.46$ eV [83], are in excellent agreement with our prediction, a feature standing for the reliability of the present computational procedure.

Although reassuring, the above picture must be refined in order to properly take into account atomic-scale features. Therefore, full relaxation of the internal degrees of freedom of the bended systems is performed by zero temperature damped dynamics until interatomic forces resulted not larger than $\sim 10^{-5} \text{ eV}/\text{\AA}$. We have so generated a new set of configurations where bending and stretching features are entangled. During the relaxation, the positions of the atoms belonging to the edges (i.e. atoms with $x = 0$ or $x = a$, see Fig. 8.2) are fixed and, therefore, the distance a between the edges remained constant. Overall we observed that the geometry is only marginally affected by relaxation as shown

Simulation protocol:
Step 1

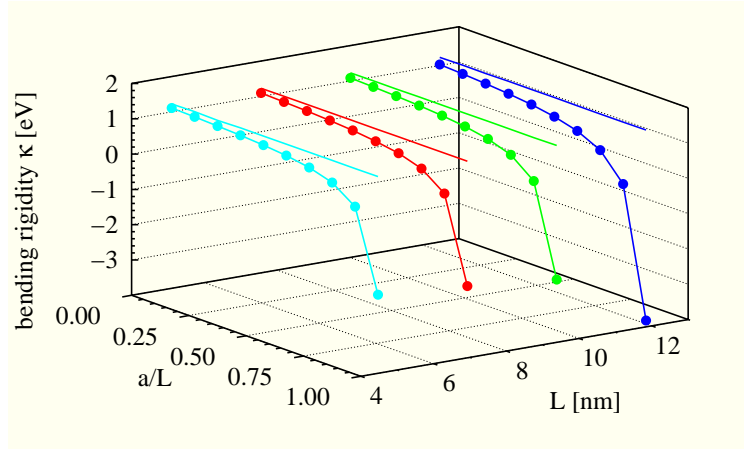


Figure 8.8: Bending rigidity κ computed by means of $U_b = E_{\text{relaxed}}^{\text{bended}} - E_{\text{relaxed}}^{\text{flat}}$ (full circles). Straight lines correspond to the average value $\kappa_{\text{ave}} = 1.40$ eV as deduced from Fig.1.

in Fig. 8.7. Here we compare the attack angle θ predicted from Eq. (8.11) versus the ratio a/L with the corresponding values obtained from the relaxed configurations. We note that, for $a/L \rightarrow 0$, we obtain the universal value 130.709° as previously discussed. As a matter of fact, after the relaxation, the attack angle θ do not change and the maximum variation of L was as little as 0.005 nm, corresponding to a variation of the integral \mathcal{J} smaller than 0.01%. Nevertheless, even for such minor relaxations the energetics of the fully relaxed systems is expected to sizeably differ from the purely bended case, because of the extraordinary large value of the graphene Young modulus (Chapter 5). It is therefore important to provide a new estimation of the bending energy for the fully relaxed configurations.

Following the above argument, we evaluated the new bending rigidity κ by means of the energy $U_b = E_{\text{relaxed}}^{\text{bended}} - E_{\text{relaxed}}^{\text{flat}}$ and Eq. (8.3), where $E_{\text{relaxed}}^{\text{bended}}$ is the energy of a relaxed bended ribbon and $E_{\text{relaxed}}^{\text{flat}}$ is the energy of a flat ribbon after a full relaxation (different from the energy of the infinite graphene sheet because of the edge effects). In this case, we have found a variation of κ upon a/L as shown in Fig. 8.8 (full circles). This result suggests that atomic-scale relaxations upon bending have induced as expected an additional field of in-plane stretching, which provides new energy contributions as reported in Eq. (8.1). It is interesting to observe that the largest differences between the unrelaxed and relaxed configurations are found for $a/L \simeq 1$. In fact, in this case the forces exerted by the constraints (maintaining the distance a between the edges) are almost parallel to the graphene sheet, favoring the stretching emergence.

This intriguing result opens the problem of how to disentangle bending and stretching features. As shown in Fig. 8.8, this is es-

*Simulation protocol:
Step 2*

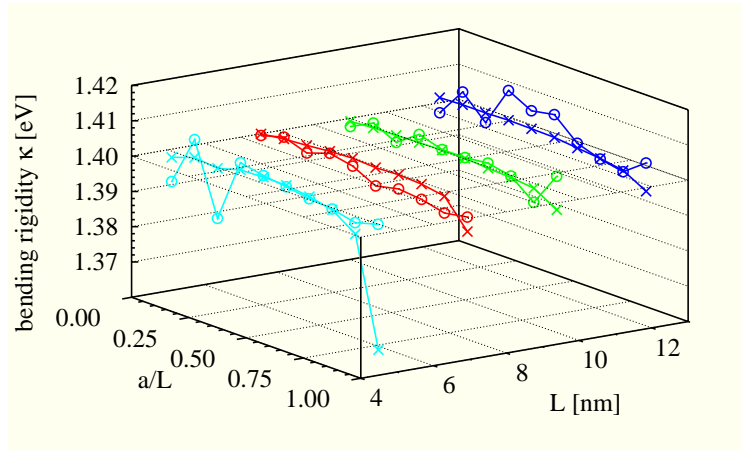


Figure 8.9: Comparison between the bending rigidity κ computed through $U_b = E_o^{\text{bended}} - E_o^{\text{flat}}$ (open circles) and $U_b = E_{\text{relaxed}}^{\text{bended}} - E_{\text{straightened}}^{\text{flat}}$ (crosses). The maximum deviation is less than the 1.5%.

pecially important in the limit of small deformations, a situation of considerable practical interest. To this aim we have defined a proof-of-concept computational procedure based on the virtual process of straightening (or unbending) of a given relaxed and bended ribbon: atoms are projected from such a configuration onto a plane by conserving all the first next neighbor bond lengths and all the second next neighbor planar angles. The process recovers a planar configuration, still maintaining all the details about any possible stretching (in-plane strain field); the corresponding energy $E_{\text{straightened}}^{\text{flat}}$ is straightforwardly evaluated by means of TB-AS. The bending rigidity κ can be consequently determined by using $U_b = E_{\text{relaxed}}^{\text{bended}} - E_{\text{straightened}}^{\text{flat}}$: the results are shown in Fig. 8.9 (crosses) where we also report κ as obtained by $U_b = E_o^{\text{bended}} - E_o^{\text{flat}}$ (open circles). The comparison points out a good agreement between the two different approaches since stretching features are either at all non considered (open circles) or included in both the bended and flat configurations (crosses) so as to compensate. It is interesting to note that the constant trend of κ versus a and L has been found similar to Fig. 8.3. In other words, we have proved that the evaluation of κ through the energy term $U_b = E_{\text{relaxed}}^{\text{bended}} - E_{\text{relaxed}}^{\text{flat}}$ is not correct since it is corrupted by a strain energy amount which is not directly related to the bending process. The energy due to the sole stretching field (induced by the bending process) can be accordingly defined as $E_{\text{straightened}}^{\text{flat}} - E_{\text{relaxed}}^{\text{flat}}$. The demonstration that such an energetic contribution corresponds only to stretching relies on the fact that both the terms $E_{\text{straightened}}^{\text{flat}}$ and $E_{\text{relaxed}}^{\text{flat}}$ have been evaluated on flat ribbons through TB atomistic simulations.

Simulation protocol:
Step 3

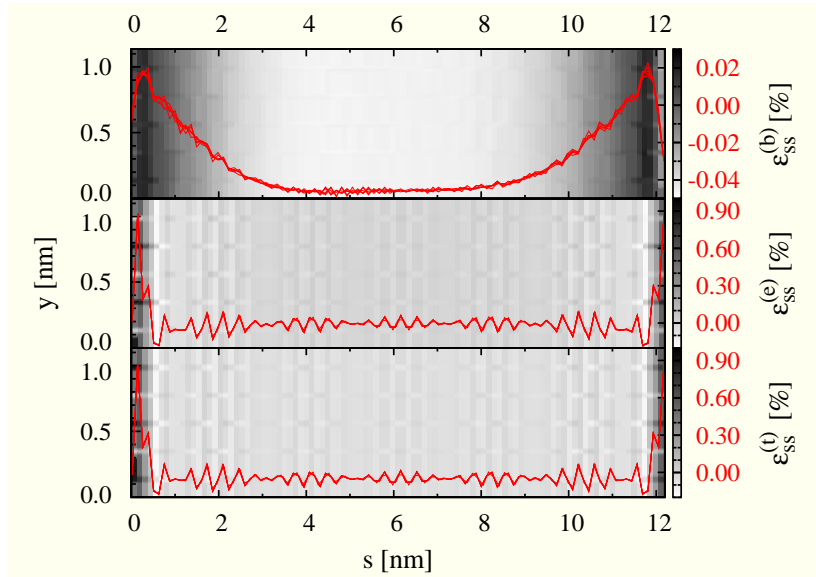


Figure 8.10: $\varepsilon_{ss}^{(b)}$ (strain induced by the bending), $\varepsilon_{ss}^{(e)}$ (strain induced by the edges) and $\varepsilon_{ss}^{(t)}$ (total strain) versus s (red curves). The gray scale map in background represents the same quantities in the sy -space for $L = 12$ nm and $a/L = 0.95$

A further evidence of the stretching emergence can be derived from Fig. 8.10 where the strain is calculated along the arc of length L (corresponding to the dashed line in Fig. 8.2), labeled by the coordinate s . We can calculate three strain fields $\varepsilon_{ss}^{(b)}$, $\varepsilon_{ss}^{(e)}$ and $\varepsilon_{ss}^{(t)}$ which are respectively defined as the relative difference between: (i) the relaxed and straightened configuration (energy $E_{\text{straightened}}^{\text{flat}}$) and the flat relaxed configuration (energy $E_{\text{relaxed}}^{\text{flat}}$); (ii) the flat relaxed configuration (energy $E_{\text{relaxed}}^{\text{flat}}$) and the flat unrelaxed configuration (energy E_o^{flat}); (iii) the relaxed and straightened configuration (energy $E_{\text{straightened}}^{\text{flat}}$) and the flat unrelaxed configuration (energy E_o^{flat}). While the strain $\varepsilon_{ss}^{(b)}$ is only due to bending, the term $\varepsilon_{ss}^{(e)}$ is induced by the presence of the edges (finite nanoribbon) in a flat configuration. The quantity $\varepsilon_{ss}^{(t)}$ represents the total strain induced by the relaxation of the bended ribbon with reference to the ideal graphene sheet. We observed with good accuracy the validity of the relation $\varepsilon_{ss}^{(t)} = \varepsilon_{ss}^{(b)} + \varepsilon_{ss}^{(e)}$, further proving that the total strain in a bended ribbon is the sum of two different contributions: the first one ($\varepsilon_{ss}^{(b)}$) is directly related to the bending process and the second one ($\varepsilon_{ss}^{(e)}$) is originated by edges effects, i.e. by the finite size of the nanoribbon. Although the first term seems to be quite negligible with respect to the second one, the previous energetic analysis reveals that both contributions are essential in order to explain the discrepancies between continuum and atomistic results.

Strain field along the arc of length

In conclusion, we offered robust arguments suggesting that the correct value for the bending rigidity of a carbon nanoribbon corresponds to $\kappa = 1.40$ eV, as calculated either through $U_b = E_0^{\text{bended}} - E_0^{\text{flat}}$ or through $U_b = E_{\text{relaxed}}^{\text{bended}} - E_{\text{straightened}}^{\text{flat}}$. On the other hand, the relation $U_b = E_{\text{relaxed}}^{\text{bended}} - E_{\text{relaxed}}^{\text{flat}}$ leads to incorrect results because of the emergence of a stretching field $\varepsilon_{ss}^{(t)}$. We have further proved that such an in-plane strain field can be decomposed in a first contribution $\varepsilon_{ss}^{(b)}$ due to the actual bending and a second one $\varepsilon_{ss}^{(e)}$ due to the edges effects.

Part III

APPENDIX

Contents

A.1	Derivative of a volume integral	137
A.2	Derivative of a surface integral	139
A.3	Novozhilov formulation of Lagrangian equations of motion.	141
A.4	Crystal symmetry condition	143
A.5	Virial stress and Periodic Boundary Conditions	145
A.6	Symmetry of the elastic moduli of Graphane conformers	147
A.6.1	Young Modulus	147
A.6.2	Poisson Ratio	151
A.7	Bending rigidity in nanotubes	153
A.8	Minimal surface of a bended membrane	157

A.1 DERIVATIVE OF A VOLUME INTEGRAL

We consider a subset $\mathcal{P}_t \subset \Omega_t$ which is the time deformed version of $\mathcal{P}_0 \subset \Omega_0$. We search a property giving the time derivative of an arbitrary volume integral. In this context, the symbol d/dt can be used when it is applied to a quantity depending only on the time t . In fact, in this case, there is no ambiguity. As before we consider a scalar field ϕ and, through a change of variables between Eulerian and Lagrangian coordinates, we obtain

$$\frac{d}{dt} \int_{\mathcal{P}_t} \phi d\mathbf{x} = \frac{d}{dt} \int_{\mathcal{P}_0} \phi J d\mathbf{X} \quad (\text{A.1})$$

where J is the determinant of the deformation gradient

$$J = \det \frac{\partial \mathbf{x}}{\partial \mathbf{X}} = \det \hat{\mathbf{F}} \quad (\text{A.2})$$

Then, the time derivation can enter the integral written in the reference configuration

$$\frac{d}{dt} \int_{\mathcal{P}_t} \phi d\mathbf{x} = \int_{\mathcal{P}_0} \frac{d}{dt} (\phi J) d\mathbf{X} = \int_{\mathcal{P}_0} (\dot{\phi} J + \phi \dot{J}) d\mathbf{X} \quad (\text{A.3})$$

The derivative of a determinant follows the rule

$$\frac{d}{dt} \det \hat{\mathbf{F}} = (\det \hat{\mathbf{F}}) \operatorname{tr} \left(\dot{\hat{\mathbf{F}}} \hat{\mathbf{F}}^{-1} \right) \quad (\text{A.4})$$

From Eq.(4.20) we obtain $\dot{\hat{\mathbf{F}}} \hat{\mathbf{F}}^{-1} = \hat{\mathbf{L}}$ and, therefore, we have

$$\dot{J} = J \operatorname{tr} (\hat{\mathbf{L}}) = J \nabla_{\mathbf{x}} \cdot \mathbf{v} \quad (\text{A.5})$$

So

$$\frac{d}{dt} \int_{\mathcal{P}_t} \phi \, d\mathbf{x} = \int_{\mathcal{P}_0} (\dot{\phi} + \phi \nabla_{\mathbf{x}} \cdot \mathbf{v}) J \, d\mathbf{X} = \int_{\mathcal{P}_t} (\dot{\phi} + \phi \nabla_{\mathbf{x}} \cdot \mathbf{v}) \, d\mathbf{x} \quad (\text{A.6})$$

Since $\dot{\phi} = \frac{\partial \phi}{\partial t} + \frac{\partial \phi}{\partial \mathbf{x}} \cdot \mathbf{v}$ we obtain

$$\frac{d}{dt} \int_{\mathcal{P}_t} \phi \, d\mathbf{x} = \int_{\mathcal{P}_t} \left(\frac{\partial \phi}{\partial t} + \nabla_{\mathbf{x}} \phi \cdot \mathbf{v} + \phi \nabla_{\mathbf{x}} \cdot \mathbf{v} \right) \, d\mathbf{x} \quad (\text{A.7})$$

or, finally

$$\frac{d}{dt} \int_{\mathcal{P}_t} \phi \, d\mathbf{x} = \int_{\mathcal{P}_t} \left[\frac{\partial \phi}{\partial t} + \nabla_{\mathbf{x}} \cdot (\phi \mathbf{v}) \right] \, d\mathbf{x} \quad (\text{A.8})$$

This property has been called Reynolds theorem or transport theorem. It is the most important result used to obtain the balance equations for continuum materials. If $\phi = 1$ we obtain

$$\frac{d}{dt} \int_{\mathcal{P}_t} d\mathbf{x} = \int_{\mathcal{P}_t} \nabla_{\mathbf{x}} \cdot \mathbf{v} \, d\mathbf{x} \quad (\text{A.9})$$

which represent the rate of variation of the volume of the region \mathcal{P}_t .

A.2 DERIVATIVE OF A SURFACE INTEGRAL

We begin by describing the deformation of a given surface moving from the reference to the current configuration. We therefore consider a surface $\mathbf{X} = \mathbf{X}(\alpha, \beta)$ in the reference configuration described in parametric form by two parameters α and β . The deformed surface in the current configuration is given by $\mathbf{x} = \mathcal{F}_t(\mathbf{X}(\alpha, \beta))$. We define \mathbf{NdS} and \mathbf{nds} as the unit normal vector multiplied by the area element in the reference and in the current configuration, respectively. From standard differential geometry we have

$$\mathbf{NdS} = \frac{\partial \mathbf{X}}{\partial \alpha} \wedge \frac{\partial \mathbf{X}}{\partial \beta} d\alpha d\beta \quad (\text{A.10})$$

The deformed version can be straightforwardly obtained as

$$\begin{aligned} \mathbf{nds} &= \frac{\partial \mathbf{x}}{\partial \alpha} \wedge \frac{\partial \mathbf{x}}{\partial \beta} d\alpha d\beta = \left(\frac{\partial \mathbf{x}}{\partial \mathbf{X}} \frac{\partial \mathbf{X}}{\partial \alpha} \right) \wedge \left(\frac{\partial \mathbf{x}}{\partial \mathbf{X}} \frac{\partial \mathbf{X}}{\partial \beta} \right) d\alpha d\beta \\ &= \left(\hat{\mathbf{F}} \frac{\partial \mathbf{X}}{\partial \alpha} \right) \wedge \left(\hat{\mathbf{F}} \frac{\partial \mathbf{X}}{\partial \beta} \right) d\alpha d\beta \end{aligned} \quad (\text{A.11})$$

The last expression can be written component by component

$$n_i ds = \epsilon_{ijk} F_{js} \frac{\partial X_s}{\partial \alpha} F_{kt} \frac{\partial X_t}{\partial \beta} d\alpha d\beta$$

and it can be multiplied by F_{ir} on both sides

$$F_{ir} n_i ds = \epsilon_{ijk} F_{ir} F_{js} F_{kt} \frac{\partial X_s}{\partial \alpha} \frac{\partial X_t}{\partial \beta} d\alpha d\beta$$

Since $\epsilon_{ijk} F_{ir} F_{js} F_{kt} = \det \hat{\mathbf{F}} \epsilon_{rst}$ we obtain

$$F_{ir} n_i ds = J \epsilon_{rst} \frac{\partial X_s}{\partial \alpha} \frac{\partial X_t}{\partial \beta} d\alpha d\beta$$

or

$$\hat{\mathbf{F}}^T \mathbf{nds} = J \frac{\partial \mathbf{X}}{\partial \alpha} \wedge \frac{\partial \mathbf{X}}{\partial \beta} d\alpha d\beta = J \mathbf{NdS} \quad (\text{A.12})$$

and finally we have obtained the relationship between \mathbf{NdS} and \mathbf{nds}

$$\mathbf{nds} = J \hat{\mathbf{F}}^{-T} \mathbf{NdS} \quad (\text{A.13})$$

This property has been called Nanson theorem. Now, it is interesting to evaluate the time derivative of the surface integral of a vector field \mathbf{a} . It can be brought back to the reference configuration as

$$\begin{aligned} \frac{d}{dt} \int_{S_t} \mathbf{a} \cdot \mathbf{nds} &= \frac{d}{dt} \int_{S_0} \mathbf{a} \cdot J \hat{\mathbf{F}}^{-T} \mathbf{NdS} \\ &= \int_{S_0} \left[\dot{\mathbf{a}} \cdot J \hat{\mathbf{F}}^{-T} + \mathbf{a} \cdot \dot{J} \hat{\mathbf{F}}^{-T} + \mathbf{a} \cdot J \dot{\hat{\mathbf{F}}}^{-T} \right] \mathbf{NdS} \end{aligned} \quad (\text{A.14})$$

Now $\dot{\mathbf{j}} = \text{Jtr}(\hat{\mathbf{L}}) = \text{J}\nabla_{\mathbf{x}} \cdot \mathbf{v}$ and $\dot{\hat{\mathbf{F}}}^{-\text{T}} = -\hat{\mathbf{F}}^{-\text{T}}\dot{\hat{\mathbf{F}}}\hat{\mathbf{F}}^{-\text{T}}$ and therefore

$$\begin{aligned} \frac{d}{dt} \int_{S_t} \mathbf{a} \cdot \mathbf{n} ds &= \int_{S_0} \left[\dot{\mathbf{a}} \cdot \hat{\mathbf{F}}^{-\text{T}} + \mathbf{a} \cdot \text{J}\nabla_{\mathbf{x}} \cdot \mathbf{v} \hat{\mathbf{F}}^{-\text{T}} - \mathbf{a} \cdot \hat{\mathbf{F}}^{-\text{T}} \dot{\hat{\mathbf{F}}}\hat{\mathbf{F}}^{-\text{T}} \right] \mathbf{N} dS \\ &= \int_{S_0} \left[\dot{\mathbf{a}} + \mathbf{a} \nabla_{\mathbf{x}} \cdot \mathbf{v} - \hat{\mathbf{L}}\mathbf{a} \right] \cdot \hat{\mathbf{F}}^{-\text{T}} \mathbf{N} dS \end{aligned} \quad (\text{A.15})$$

where the relation $\dot{\hat{\mathbf{F}}} = \hat{\mathbf{L}}\hat{\mathbf{F}}$ has been used. Finally, coming back to the current configuration we obtain

$$\frac{d}{dt} \int_{S_t} \mathbf{a} \cdot \mathbf{n} ds = \int_{S_t} \left[\dot{\mathbf{a}} + \mathbf{a} \nabla_{\mathbf{x}} \cdot \mathbf{v} - \hat{\mathbf{L}}\mathbf{a} \right] \cdot \mathbf{n} ds \quad (\text{A.16})$$

Since the material derivative is given by $\dot{\mathbf{a}} = \frac{\partial \mathbf{a}}{\partial t} + \frac{\partial \mathbf{a}}{\partial \mathbf{x}} \cdot \mathbf{v}$, we obtain

$$\frac{d}{dt} \int_{S_t} \mathbf{a} \cdot \mathbf{n} ds = \int_{S_t} \left[\frac{\partial \mathbf{a}}{\partial t} + \frac{\partial \mathbf{a}}{\partial \mathbf{x}} \cdot \mathbf{v} + \mathbf{a} \nabla_{\mathbf{x}} \cdot \mathbf{v} - \hat{\mathbf{L}}\mathbf{a} \right] \cdot \mathbf{n} ds \quad (\text{A.17})$$

It is simple to verify that $\nabla_{\mathbf{x}} \wedge (\mathbf{a} \wedge \mathbf{v}) + \mathbf{v} \nabla_{\mathbf{x}} \cdot \mathbf{a} = \frac{\partial \mathbf{a}}{\partial \mathbf{x}} \cdot \mathbf{v} + \mathbf{a} \nabla_{\mathbf{x}} \cdot \mathbf{v} - \hat{\mathbf{L}}\mathbf{a}$ and therefore we can write

$$\frac{d}{dt} \int_{S_t} \mathbf{a} \cdot \mathbf{n} ds = \int_{S_t} \left[\frac{\partial \mathbf{a}}{\partial t} + \nabla_{\mathbf{x}} \wedge (\mathbf{a} \wedge \mathbf{v}) + \mathbf{v} \nabla_{\mathbf{x}} \cdot \mathbf{a} \right] \cdot \mathbf{n} ds \quad (\text{A.18})$$

The Nanson relation $\mathbf{n} ds = \hat{\mathbf{F}}^{-\text{T}} \mathbf{N} dS$ can be also applied in order to obtain the so-called Piola identity. To this aim we use the standard divergence theorem

$$\int_{\partial \mathcal{P}_t} \Psi \mathbf{n}_i ds = \int_{\mathcal{P}_t} \frac{\partial \Psi}{\partial x_i} d\mathbf{x} \quad (\text{A.19})$$

if $\Psi = 1$ identically, we obtain $\int_{\partial \mathcal{P}_t} \mathbf{n}_i ds = 0$ and, therefore

$$\int_{\partial \mathcal{P}_t} \mathbf{n} ds = \int_{\partial \mathcal{P}_0} \hat{\mathbf{F}}^{-\text{T}} \mathbf{N} dS = \int_{\mathcal{P}_0} \nabla_{\mathbf{X}} \cdot (\hat{\mathbf{F}}^{-1}) d\mathbf{X} = 0 \quad (\text{A.20})$$

which means

$$\nabla_{\mathbf{X}} \cdot (\hat{\mathbf{F}}^{-1}) = 0 \Rightarrow \frac{\partial}{\partial X_j} \left(\text{J} \frac{\partial X_j}{\partial x_i} \right) = 0 \quad (\text{A.21})$$

This relation will be useful to obtain the balance equations of the continuum mechanics in the Lagrangian description.

A.3 NOVOZHILOV FORMULATION OF LAGRANGIAN EQUATIONS OF MOTION.

We consider the standard base of unit vectors \mathbf{E}_1 , \mathbf{E}_2 and \mathbf{E}_3 in the point \mathbf{X} of the reference configuration. Since the motion is controlled by the transformation $\mathbf{x} = \mathcal{F}_t(\mathbf{X})$, the unit vectors \mathbf{e}_i in the deformed configuration are given by the direction of the deformed coordinate lines

$$\mathbf{e}_i = \frac{\frac{\partial \mathcal{F}_t(\mathbf{X})}{\partial X_i}}{\left\| \frac{\partial \mathcal{F}_t(\mathbf{X})}{\partial X_i} \right\|} = \frac{\hat{\mathbf{F}}\mathbf{E}_i}{\|\hat{\mathbf{F}}\mathbf{E}_i\|} \quad (\text{A.22})$$

We remark that they do not form an orthogonal base. First of all, we simply obtain the norm of $\hat{\mathbf{F}}\mathbf{E}_i$

$$\|\hat{\mathbf{F}}\mathbf{E}_i\| = \sqrt{(\hat{\mathbf{F}}\mathbf{E}_i) \cdot (\hat{\mathbf{F}}\mathbf{E}_i)} = \sqrt{F_{ki}F_{ki}} = \sqrt{(\hat{\mathbf{F}}^T \hat{\mathbf{F}})_{ii}} = \sqrt{C_{ii}} \quad (\text{A.23})$$

where $\hat{\mathbf{C}}$ is the right Cauchy tensor. We define the unit vectors \mathbf{n}_1 , \mathbf{n}_2 and \mathbf{n}_3 perpendicular to the planes $(\mathbf{e}_2, \mathbf{e}_3)$, $(\mathbf{e}_1, \mathbf{e}_3)$ and $(\mathbf{e}_1, \mathbf{e}_2)$. It means that we can write

$$\mathbf{n}_k = \frac{1}{2} \eta_{kij} \frac{\mathbf{e}_i \wedge \mathbf{e}_j}{\|\mathbf{e}_i \wedge \mathbf{e}_j\|} = \frac{1}{2} \eta_{kij} \frac{(\hat{\mathbf{F}}\mathbf{E}_i) \wedge (\hat{\mathbf{F}}\mathbf{E}_j)}{\|(\hat{\mathbf{F}}\mathbf{E}_i) \wedge (\hat{\mathbf{F}}\mathbf{E}_j)\|} \quad (\text{A.24})$$

Now, we start with the calculation of $\|(\hat{\mathbf{F}}\mathbf{E}_i) \wedge (\hat{\mathbf{F}}\mathbf{E}_j)\|$

$$\begin{aligned} \|(\hat{\mathbf{F}}\mathbf{E}_i) \wedge (\hat{\mathbf{F}}\mathbf{E}_j)\| &= \sqrt{\eta_{kst} F_{si} F_{tj} \eta_{kab} F_{ai} F_{bj}} \\ &= \sqrt{(\delta_{sa} \delta_{tb} - \delta_{sb} \delta_{ta}) F_{si} F_{tj} F_{ai} F_{bj}} \\ &= \sqrt{C_{ii} C_{jj} - C_{ij}^2} \end{aligned} \quad (\text{A.25})$$

We can also write

$$\frac{ds_k}{dS_k} = \sqrt{C_{ii} C_{jj} - C_{ij}^2} \quad (\text{A.26})$$

where the indices i and j are complementary to k and dS_k and ds_k are the surface elements in the reference and current configuration having unit normal vector \mathbf{n}_k . Since $(\hat{\mathbf{F}}\mathbf{E}_i) \wedge (\hat{\mathbf{F}}\mathbf{E}_j) = \eta_{qst} F_{si} F_{tj} \mathbf{E}_q$, we therefore obtain

$$\mathbf{n}_k = \frac{1}{2} \eta_{kij} \frac{\eta_{qst} F_{si} F_{tj} \mathbf{E}_q}{\sqrt{C_{ii} C_{jj} - C_{ij}^2}} \quad (\text{A.27})$$

Since $\eta_{qst} F_{si} F_{tj} F_{qa} = J \eta_{aij}$ we can simply write $\eta_{qst} F_{si} F_{tj} = J \eta_{aij} (\hat{\mathbf{F}}^{-1})_{aq}$; this result can be used in Eq.(A.27) to yield

$$\mathbf{n}_k = \frac{1}{2} \eta_{kij} \frac{J \eta_{aij} (\hat{\mathbf{F}}^{-1})_{aq} \mathbf{E}_q}{\sqrt{C_{ii} C_{jj} - C_{ij}^2}} \quad (\text{A.28})$$

When k is fixed the indices i and j can assume two couples of values [if $k=1$ we have $(i,j)=(2,3)$ or $(3,2)$, if $k=2$ we have

(i,j)=(1,3) or (3,2) and if $k=3$ we have (i,j)=(2,1) or (1,2)] and the index a must assume the value k . At the end we eventually obtain

$$\mathbf{n}_k = \frac{J(\hat{\mathbf{F}}^{-1})_{kq} \mathbf{E}_q}{\sqrt{C_{ii}C_{jj} - C_{ij}^2}} = \frac{dS_k}{ds_k} J(\hat{\mathbf{F}}^{-1})_{kq} \mathbf{E}_q \quad (\text{A.29})$$

where the indices i and j are complementary to k (there is not the sum on k). We may consider the forces acting on the three deformed coordinate planes $(\mathbf{e}_2, \mathbf{e}_3)$, $(\mathbf{e}_1, \mathbf{e}_3)$ and $(\mathbf{e}_1, \mathbf{e}_2)$ (having normal unit vectors \mathbf{n}_1 , \mathbf{n}_2 and \mathbf{n}_3 , respectively) through the expressions

$$\mathbf{Tn}_k = \frac{J(\hat{\mathbf{F}}^{-1})_{kq} \mathbf{T}\mathbf{E}_q}{\sqrt{C_{ii}C_{jj} - C_{ij}^2}} = \frac{dS_k}{ds_k} J(\hat{\mathbf{F}}^{-1})_{kq} \mathbf{T}\mathbf{E}_q \quad (\text{A.30})$$

These vectors can be represented on both the base \mathbf{E}_i and \mathbf{e}_i as follows

$$\mathbf{Tn}_k = \sigma_{sk}^E \mathbf{E}_s \quad (\text{A.31})$$

$$\mathbf{Tn}_k = \sigma_{sk}^e \mathbf{e}_s \quad (\text{A.32})$$

where, since $\mathbf{E}_1, \mathbf{E}_2$ and \mathbf{E}_3 is an orthonormal base, we have

$$\sigma_{sk}^E = \mathbf{Tn}_k \cdot \mathbf{E}_s = \frac{dS_k}{ds_k} J(\hat{\mathbf{F}}^{-1})_{kq} \mathbf{T}\mathbf{E}_q \cdot \mathbf{E}_s = \frac{dS_k}{ds_k} J(\hat{\mathbf{F}}^{-1})_{kq} T_{sq} \quad (\text{A.33})$$

Moreover, we have the following relation between σ_{sk}^E and σ_{sk}^e

$$\sigma_{sk}^E = \mathbf{Tn}_k \cdot \mathbf{E}_s = \sigma_{jk}^e \mathbf{e}_j \cdot \mathbf{E}_s = \sigma_{jk}^e \frac{\hat{\mathbf{F}}\mathbf{E}_j \cdot \mathbf{E}_s}{\sqrt{C_{jj}}} = \frac{1}{\sqrt{C_{jj}}} F_{sj} \sigma_{jk}^e \quad (\text{A.34})$$

The representations σ_{sk}^E and σ_{sk}^e have been introduced by Novozhilov in his pioneering book on nonlinear elasticity. The Lagrangian equation of motion can be written as (see Eq.(4.68))

$$\frac{\partial}{\partial X_k} [J(\hat{\mathbf{F}}^{-1})_{kq} T_{sq}] + Jb_s = \rho Jv_s \quad (\text{A.35})$$

and then it can be expressed in terms of σ_{sk}^E

$$\frac{\partial}{\partial X_k} \left[\frac{ds_k}{dS_k} \sigma_{sk}^E \right] + Jb_s = \rho Jv_s \quad (\text{A.36})$$

or in terms of σ_{sk}^e

$$\frac{\partial}{\partial X_k} \left[\frac{ds_k}{dS_k} \frac{1}{\sqrt{C_{jj}}} F_{sj} \sigma_{jk}^e \right] + Jb_s = \rho Jv_s \quad (\text{A.37})$$

Finally, since it is evident that $\sqrt{C_{jj}} = dl_j/dL_j$, we can state the Lagrangian equations of motion in the Novozhilov form

$$\frac{\partial}{\partial X_k} \left[\frac{ds_k}{dS_k} \frac{dl_j}{dL_j} F_{sj} \sigma_{jk}^e \right] + Jb_s = \rho Jv_s \quad (\text{A.38})$$

A.4 CRYSTAL SYMMETRY CONDITION

The stiffness tensor $\hat{\mathbf{C}}$ has a symmetry with respect to a given orthonormal transformation \mathbf{A} if it does not change when subjected to that transformation. The matrices \mathbf{A} are so defined as the set of orthonormal transformations to which the elastic properties are invariant. In Cartesian coordinates the matrix \mathbf{A} is given by

$$\mathbf{A} = \begin{pmatrix} A_{11} & A_{12} & A_{13} \\ A_{21} & A_{22} & A_{23} \\ A_{31} & A_{32} & A_{33} \end{pmatrix}. \quad (\text{A.39})$$

that satisfy the orthogonality condition $\mathbf{A}^T \mathbf{A} = \mathbf{I}$, equivalent to $\mathbf{A}^T = \mathbf{A}^{-1}$.

Therefore the symmetry condition applied to the stress tensor can be written as

$$\hat{\mathbf{T}}' = \mathbf{A} \hat{\mathbf{T}} \mathbf{A}^T \quad (\text{A.40})$$

The stress tensor $\hat{\mathbf{T}}$ can be written in Voigt notation as $\mathcal{T} = (\mathbb{T}_{11} \ \mathbb{T}_{22} \ \mathbb{T}_{33} \ \mathbb{T}_{23} \ \mathbb{T}_{13} \ \mathbb{T}_{12})^T$ so that the Eq. (A.40) becomes

$$\hat{\mathcal{T}}' = \mathcal{A} \hat{\mathcal{T}} \quad (\text{A.41})$$

For conciseness, we fix the stress tensor elements as unity. We begin by writing the diagonal elements, namely $\mathbb{T}_{ij} = \delta_{iq} \delta_{qj}$, with $i, j, q \in \{1, 2, 3\}$, and, hence, we write the Eq. (A.40) as

$$\mathbb{T}'_{kl} = A_{ki} \mathbb{T}_{ij} A_{jl}^T = A_{ki} \delta_{iq} \delta_{qj} A_{lj} = A_{kq} A_{lq} \quad (\text{A.42})$$

The out-of-diagonal elements are $\mathbb{T}_{ij} = \delta_{in} \delta_{mj} + \delta_{im} \delta_{nj}$, so that

$$\begin{aligned} \mathbb{T}'_{kl} &= A_{ki} \mathbb{T}_{ij} A_{jl}^T = A_{ki} \delta_{in} \delta_{mj} A_{lj} + A_{ki} \delta_{im} \delta_{nj} A_{lj} \\ &= A_{kn} A_{lm} + A_{km} A_{ln} \end{aligned} \quad (\text{A.43})$$

Therefore we have obtained that \mathcal{A} in the Eq. (A.41) is

$$\left(\begin{array}{cccccc} A_{11}^2 & A_{12}^2 & A_{13}^2 & 2A_{12}A_{13} & 2A_{11}A_{13} & 2A_{11}A_{12} \\ A_{21}^2 & A_{22}^2 & A_{23}^2 & 2A_{22}A_{23} & 2A_{21}A_{23} & 2A_{21}A_{22} \\ A_{31}^2 & A_{32}^2 & A_{33}^2 & 2A_{32}A_{33} & 2A_{31}A_{33} & 2A_{31}A_{32} \\ A_{21}A_{31} & A_{22}A_{32} & A_{23}A_{33} & A_{22}A_{33} + A_{23}A_{32} & A_{21}A_{33} + A_{23}A_{31} & A_{21}A_{32} + A_{22}A_{31} \\ A_{11}A_{31} & A_{12}A_{32} & A_{13}A_{33} & A_{12}A_{33} + A_{13}A_{32} & A_{11}A_{33} + A_{13}A_{31} & A_{11}A_{32} + A_{12}A_{31} \\ A_{11}A_{21} & A_{12}A_{22} & A_{13}A_{23} & A_{12}A_{23} + A_{13}A_{22} & A_{11}A_{23} + A_{13}A_{21} & A_{11}A_{22} + A_{12}A_{21} \end{array} \right) \quad (\text{A.44})$$

which is the desired transformation matrix given in the Eq. (A.41). Thus, given a transformation matrix \mathbf{A} as in Eq. (A.39), whose entries are A_{ij} , the corresponding \mathcal{A} can be written using the Eq. (A.44).

Similarly we can derive the transformation matrix for the strain tensor. The invariance of the constitutive equation $\hat{\mathbf{T}} = \hat{\mathbf{C}}\hat{\boldsymbol{\varepsilon}}$ under such a transformation requires that

$$\mathcal{A}\hat{\mathbf{T}} = \hat{\mathbf{C}}(\mathcal{A}\hat{\boldsymbol{\varepsilon}}) \implies \hat{\mathbf{T}} = (\mathcal{A}^{-1}\hat{\mathbf{C}}\mathcal{A})\hat{\boldsymbol{\varepsilon}} \quad (\text{A.45})$$

Hence, using the definition of an orthonormal transformation

$$\hat{\mathbf{C}} = \mathcal{A}^{-1}\hat{\mathbf{C}}\mathcal{A} = \mathcal{A}^T\hat{\mathbf{C}}\mathcal{A} \quad (\text{A.46})$$

For a transversely isotropic material, the matrix \mathbf{A} has the simple form

$$\mathbf{A} = \begin{pmatrix} \cos\theta & \sin\theta & 0 \\ -\sin\theta & \cos\theta & 0 \\ 0 & 0 & 1 \end{pmatrix}. \quad (\text{A.47})$$

where the x_3 -axis is the axis of symmetry. The stiffness tensor remains invariant under rotation by any angle θ about the x_3 -axis. Using the specific values of θ in matrix \mathbf{A} , the stiffness tensor for transversely isotropic materials can be written as

$$\hat{\mathbf{C}} = \begin{pmatrix} C_{11} & C_{12} & C_{13} & 0 & 0 & 0 \\ C_{12} & C_{11} & C_{13} & 0 & 0 & 0 \\ C_{13} & C_{13} & C_{33} & 0 & 0 & 0 \\ 0 & 0 & 0 & C_{44} & 0 & 0 \\ 0 & 0 & 0 & 0 & C_{44} & 0 \\ 0 & 0 & 0 & 0 & 0 & (C_{11} - C_{12})/2 \end{pmatrix} \quad (\text{A.48})$$

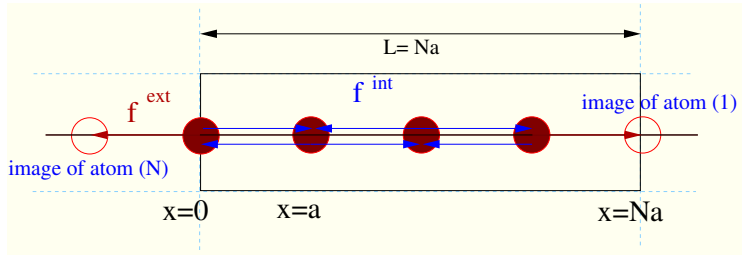


Figure A.1: One-dimensional chain of atoms subjected to nearest neighbors internal interaction, f^{int} , and to external forces f^{ext} . The Periodic Boundary Conditions are assumed.

A.5 VIRIAL STRESS AND PERIODIC BOUNDARY CONDITIONS

We present a brief discussion on the calculation of the atomic virial stress in a system under Periodic Boundary Conditions. The atomic virial stress is discussed in Section 4.9, where the virial is expressed in terms of the interatomic distances, Eq.(4.180), instead of the atomic positions as in Eq.(4.170). For simplicity, We consider the case of a one-dimensional chain of atoms at zero temperature. We assume that the system is subjected to nearest neighbors interactions of magnitude f^{int} . In Fig.A.1 the simulation cell of the one-dimensional system is shown. Each cell contains N particles with constant reciprocal distance, namely a , so that the period of the cell is $L = Na$, which is kept fixed by the external forces f^{ext} due to the interaction with the repeated cells along the chain. In such a case, the virial stress can be obtained by means of the Eq.(4.170) in terms of the atomic positions x_i :

$$T = \frac{1}{L} \sum_i^N x_i f_i^{\text{int}} = f^{\text{ext}} \quad (\text{A.49})$$

Note that, at the equilibrium, the total force on each atoms must be zero. Therefore, the internal force acting on the atom in x_N , i.e. $-f^{\text{int}}$, is equal in absolute value to the external one f^{ext} . As a consequence, the virial stress is null, as expected, only in absence of external forces.

On the other hand, in Molecular Dynamics simulations (typically) the system is not subjected to surface forces but the volume is fixed by means of the Periodic Boundary Conditions, i.e. by the interactions with the periodic images of the atoms (see Fig.A.1). In order to apply such conditions the interatomic distance x_{ij} have to be calculated by

$$x_{ij} \Big|_{\text{PBC}} = x_i - x_j - L \text{int} \left[\frac{(x_i - x_j)}{L} - \frac{1}{2} \right] \quad (\text{A.50})$$

In particular, this means that $x_{1N} \Big|_{\text{PBC}} = a$, being a the lattice parameter. In order to get the correct result obtained in Eq. (A.49)

The volume is fixed by external forces

The volume is fixed by the P.B.C.

Interatomic distances under Periodic Boundary Conditions

by means of the Eqs.(4.180), the boundary conditions must be properly considered. This can be done by calculating the virial stress in terms of the interatomic distances $x_{ij}|_{\text{PBC}}$

$$T = \frac{1}{L} \sum_{ij} x_{ij}|_{\text{PBC}} f_{ij} = f^{\text{ext}} \quad (\text{A.51})$$

which was to be demonstrated.

A.6 SYMMETRY OF THE ELASTIC MODULI OF GRAPHANE CONFORMERS

In accordance with the Hermann's theorem, the hexagonal crystals are transversally isotropic in their elastic properties. All the directions which make up one and the same angle with the principal symmetry axis are equal in their elastic properties, although for the hexagonal crystals these directions certainly crystallographically different. This is an example when the symmetry of a crystal properties is higher than the crystal itself.

Applying an axial tension σ along the arbitrary direction $\mathbf{n} = \cos \theta \mathbf{e}_x + \sin \theta \mathbf{e}_y$. Under this assumption we get $\hat{\mathbf{T}} = \sigma \mathbf{n} \otimes \mathbf{n}$ in terms of components as

$$T_{ij} = \sigma n_i n_j \quad (\text{A.52})$$

By inverting the constitutive equation, $\hat{\mathbf{T}} = \hat{\mathbf{C}}: \hat{\boldsymbol{\epsilon}} \implies \hat{\boldsymbol{\epsilon}} = \hat{\mathbf{S}}: \hat{\mathbf{T}}$, we find the corresponding strain tensor $\hat{\boldsymbol{\epsilon}}$ as follows

$$\epsilon_{ij} = s_{ijkl} T_{kl} = \sigma s_{ijkl} n_k n_l \quad (\text{A.53})$$

where s_{ijkl} is the compliance tensor. In particular, we easily get its longitudinal component $\epsilon_l = \mathbf{n} \cdot \hat{\boldsymbol{\epsilon}} \mathbf{n}$ along the direction \mathbf{n}

$$\epsilon_l = \epsilon_{ij} n_i n_j = \sigma s_{ijkl} n_k n_l n_i n_j \quad (\text{A.54})$$

as well as its transverse component $\epsilon_t = \mathbf{t} \cdot \hat{\boldsymbol{\epsilon}} \mathbf{t}$ along the direction $\mathbf{t} = -\sin \theta \mathbf{e}_x + \cos \theta \mathbf{e}_y$ (with $\mathbf{t} \cdot \mathbf{n} = 0$).

$$\epsilon_t = \epsilon_{ij} t_i t_j = \sigma s_{ijkl} n_k n_l t_i t_j \quad (\text{A.55})$$

A.6.1 Young Modulus

The \mathbf{n} -dependent Young modulus is defined as the ratio between the applied traction and the longitudinal extension $E_{\mathbf{n}} = \sigma / \epsilon_l$. Thus, the reciprocal Young modulus E^{-1} for the direction \mathbf{n} is given by

$$E^{-1}(\mathbf{n}) = s_{ijkl} n_k n_l n_i n_j \quad (\text{A.56})$$

This formula can be simplified by introducing the notation $n_i n_j = (\mathbf{nn})_{\lambda}$, where $ij \leftrightarrow \lambda = 1, \dots, 6$. Finally the Eq. (A.56) becomes

$$E^{-1}(\mathbf{n}) = s_{\lambda\mu} (\mathbf{nn})_{\lambda} (\mathbf{nn})_{\mu} \quad (\text{A.57})$$

The general formula for the reciprocal Young modulus $E^{-1}(\mathbf{n})$ can be written in terms of the Miller indices $h_i = h, k, l$ of the

Hermann's theorem.
If an r -rank tensor has an N -fold symmetry axis and $r < N$, then this tensor also has a symmetry axis of infinite order

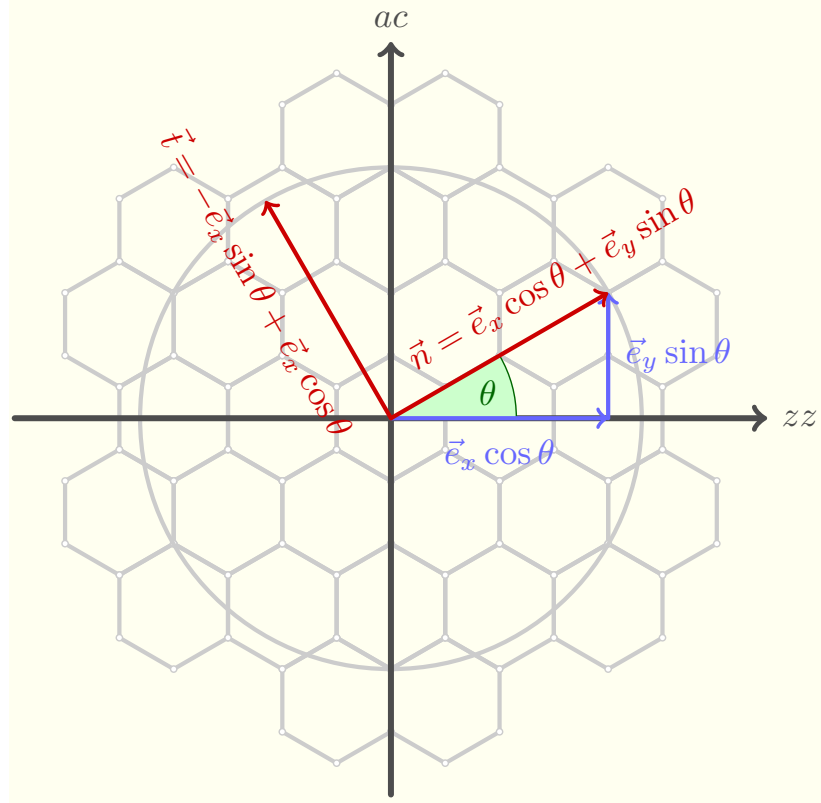


Figure A.2: By applying an axial tension σ along the arbitrary direction \vec{n} ($\theta = \vec{z}\vec{z} \angle \vec{n}$), the Cauchy stress tensor $\hat{T} = \partial U / \partial \hat{\epsilon}$ is $\hat{T} = \sigma \vec{n} \otimes \vec{n}$. By inverting the constitutive equation $\hat{T} = \hat{C} : \hat{\epsilon} \implies \hat{\epsilon} = \hat{S} : \hat{T}$ we find the corresponding strain tensor $\hat{\epsilon}$. $\epsilon_l = \vec{n} \cdot \hat{\epsilon} \vec{n}$ longitudinal component; $\epsilon_t = \vec{t} \cdot \hat{\epsilon} \vec{t}$ transverse component (with $\vec{t} \cdot \vec{n} = 0$). In particular, we easily get its longitudinal component $\epsilon_l = \vec{n} \cdot \hat{\epsilon} \vec{n}$ along the direction \vec{n} as well as its transverse component $\epsilon_t = \vec{t} \cdot \hat{\epsilon} \vec{t}$ along the direction $\vec{t} = -\sin \theta \vec{e}_x + \cos \theta \vec{e}_y$

crystallographic direction $[hkl]$ parallel to direction \mathbf{n} as the follows

$$E^{-1} = s_{\lambda\mu} Q_{\lambda} Q_{\mu} \quad (\text{A.58})$$

$$Q_{\lambda} = n_i n_j = \frac{A_{\alpha i} A_{\beta j} h_{\alpha} h_{\beta}}{g_{\gamma\eta} h_{\gamma} h_{\eta}} \quad (\text{A.59})$$

where $A_{\beta j}$ are the components of the the matrix of the expansion of vectorial basis \mathbf{a}_{α} of the crystal lattice with respect to mutually orthogonal unit vectors \mathbf{e}_i of the system of coordinates; the $g_{\gamma\eta}$ are the components of the metric tensor G (here Greek and Latin indices enumerate columns and rows, respectively). In the general case of the triclinic symmetry, we get

$$\begin{aligned} Q_1 &= q_1^2 = g^{-1} (ha \sin \beta - kb \sin \alpha \cos \gamma^{\dagger})^2 \\ Q_2 &= q_2^2 = g^{-1} \left(\frac{k}{b^{\dagger}} \right)^2 \\ Q_3 &= q_3^2 = g^{-1} (ha \cos \beta + kb \cos \alpha + lc)^2 \\ Q_4 &= q_2 q_3 = g^{-1} \left(\frac{k}{b^{\dagger}} \right) (ha \cos \beta + kb \cos \alpha + lc) \\ Q_5 &= q_3 q_1 = g^{-1} (ha \cos \beta + kb \cos \alpha + lc) (ha \sin \beta - kb \sin \alpha \cos \gamma^{\dagger}) \\ Q_6 &= q_1 q_2 = g^{-1} \left(\frac{k}{b^{\dagger}} \right) (ha \sin \beta - kb \sin \alpha \cos \gamma^{\dagger}) \\ g &= h^2 a^2 + k^2 b^2 + l^2 c^2 + \\ &\quad + 2klbc \cos \alpha + 2lhca \cos \beta + 2hkab \cos \gamma \end{aligned} \quad (\text{A.60})$$

where a, b, c are the lengths of the base vectors of the lattice and α, β, γ are the angles between them; $a^{\dagger}, b^{\dagger}, c^{\dagger}$ are the lengths of the reciprocal vectors and $\alpha^{\dagger}, \beta^{\dagger}, \gamma^{\dagger}$ are the angles between them, which are related as

$$\begin{aligned} a^{\dagger} &= \frac{\sin \alpha}{a\omega} \\ b^{\dagger} &= \frac{\sin \beta}{b\omega} \\ c^{\dagger} &= \frac{\sin \gamma}{c\omega} \end{aligned} \quad (\text{A.61})$$

$$\begin{aligned} \cos \alpha^{\dagger} &= \frac{\cos \beta \cos \gamma - \cos \alpha}{\sin \beta \sin \gamma} \\ \cos \beta^{\dagger} &= \frac{\cos \gamma \cos \alpha - \cos \beta}{\sin \gamma \sin \alpha} \\ \cos \gamma^{\dagger} &= \frac{\cos \alpha \cos \beta - \cos \gamma}{\sin \alpha \sin \beta} \end{aligned} \quad (\text{A.62})$$

where $\omega = \sqrt{1 - \cos \alpha^2 - \cos \beta^2 - \cos \gamma^2 + 2 \cos \alpha \cos \beta \cos \gamma}$

In the case of 2-dimensional systems as graphene and graphane, many terms of the Eqs.(A.60) becomes zero and we can neglect all the indices 3,4,5. Therefore the expansion of the Eq.(A.58) is reduced to

*2-dimensional
systems*

*Young modulus in
2-dimensional
systems*

$$E^{-1} = s_{11}Q_1^2 + s_{22}Q_2^2 + (s_{66} + 2s_{12})Q_1Q_2 \quad (\text{A.63})$$

*Hexagonal and
Trigonal lattices.*

The stiffness tensor \mathbf{C} for the hexagonal graphene (6/mmm) and trigonal chair graphane ($\bar{3}m$) 2D-lattice is the same

$$\mathbf{C} = \begin{bmatrix} c_{11} & c_{12} & 0 \\ c_{12} & c_{11} & 0 \\ 0 & 0 & c_{66} \end{bmatrix} \quad (\text{A.64})$$

as well as the compliance tensor \mathbf{S}

$$\mathbf{s} = \begin{bmatrix} s_{11} & s_{12} & 0 \\ s_{12} & s_{11} & 0 \\ 0 & 0 & s_{66} \end{bmatrix} = \begin{bmatrix} \frac{c_{11}}{c_{11}^2 - c_{12}^2} & -\frac{c_{12}}{c_{11}^2 - c_{12}^2} & 0 \\ -\frac{c_{12}}{c_{12}^2 - c_{11}^2} & \frac{c_{11}}{c_{11}^2 - c_{12}^2} & 0 \\ 0 & 0 & \frac{1}{c_{66}} \end{bmatrix} \quad (\text{A.65})$$

where in accord to the Cauchy relation we have that $s_{66} = 2(s_{11} - s_{12})$ or $c_{66} = \frac{1}{2}(c_{11} - c_{12})$. Reminding that in this case we have $a = b$, $\alpha = \beta = \frac{\pi}{2}$, $\gamma = \frac{2\pi}{3}$, the reciprocal Young modulus is simply given by

$$E^{-1} = s_{11} = \frac{c_{11}}{c_{11}^2 - c_{12}^2} \quad (\text{A.66})$$

*Orthorhombic
lattices.*

as we expect from an isotropic system.

The orthorhombic 2D-crystal symmetry (mmm) is no more isotropic. Its stiffness tensor \mathbf{C} is

$$\mathbf{C} = \begin{bmatrix} c_{11} & c_{12} & 0 \\ c_{12} & c_{22} & 0 \\ 0 & 0 & c_{66} \end{bmatrix} \quad (\text{A.67})$$

and the compliance tensor \mathbf{S} is given by

$$\mathbf{s} = \begin{bmatrix} s_{11} & s_{12} & 0 \\ s_{12} & s_{22} & 0 \\ 0 & 0 & s_{66} \end{bmatrix} = \begin{bmatrix} \frac{c_{22}}{c_{11}c_{22} - c_{12}^2} & -\frac{c_{12}}{c_{11}c_{22} - c_{12}^2} & 0 \\ -\frac{c_{12}}{c_{11}c_{22} - c_{12}^2} & \frac{c_{11}}{c_{11}c_{22} - c_{12}^2} & 0 \\ 0 & 0 & \frac{1}{c_{66}} \end{bmatrix} \quad (\text{A.68})$$

So the reciprocal Young modulus in the Eq.A.63 becomes

$$E^{-1} = \frac{(ha)^4 s_{11} + (kb)^4 s_{22} + (hkab)^2 (s_{66} + 2s_{12})}{((ha)^2 + (kb)^2)^2} \quad (\text{A.69})$$

where the basis vectors are all reciprocally orthogonal and $a \neq b$.

A.6.2 Poisson Ratio

In order to generalize the Poisson ratio ν formula for an anisotropic 2D-lattice, we can define it as a function of the deformation in two mutually orthogonal directions \mathbf{n} and \mathbf{m} .

$$\begin{aligned}\nu(\mathbf{n}, \mathbf{m}) &= -\epsilon_t/\epsilon_l = \\ &= -\frac{s_{\lambda\mu}(\mathbf{m}\mathbf{m})_\lambda(\mathbf{n}\mathbf{n})_\mu}{s_{\rho\sigma}(\mathbf{n}\mathbf{n})_\rho(\mathbf{n}\mathbf{n})_\sigma}\end{aligned}\quad (\text{A.70})$$

Poisson ratio can also be define using only one direction, because the perpendicularity condition impose that $m_i m_j = (\delta_{ij} - n_i n_j)$

$$\nu(\mathbf{q}) = -\frac{s_{ijkl}n_i n_j (\delta_{kl} - n_k n_l)}{s_{np rt}n_n n_p n_r n_t}\quad (\text{A.71})$$

that from the Eq.(A.56)

$$\begin{aligned}\nu(\mathbf{n}) &= \frac{s_{ijkl}n_i n_j n_k n_l}{s_{np rt}n_n n_p n_r n_t} - \frac{s_{ijkl}n_i n_j \delta_{kl}}{s_{np rt}n_n n_p n_r n_t} = \\ &= 1 - s_{ijkk}n_i n_j E(\mathbf{n}) =\end{aligned}\quad (\text{A.72})$$

$$= 1 - S_{ij}n_i n_j E(\mathbf{n})\quad (\text{A.73})$$

where S_{ij} are the components of the compressibility tensor defined by the strain under hydrostatic pressure p

$$\epsilon_{ij} = -S_{ij}p = -s_{ijkk}p\quad (\text{A.74})$$

Both for graphene and chair-graphane, the Poisson ratio is independent from the direction

$$\nu = -\frac{s_{12}}{s_{11}} = \frac{C_{12}}{C_{11}}\quad (\text{A.75})$$

While for the board-graphane with orthorhombic symmetry is quite different due to its anisotropy. From Eqs.(A.72), (A.60), and (A.69)

$$\begin{aligned}\nu(\mathbf{n}) &= 1 - ((s_{11} + s_{12})q_1^2 + (s_{22} + s_{12})q_2^2) n_i n_j E(\mathbf{n}) \\ &= 1 - \left(\frac{(ha)^2 s_{11} + (kb)^2 s_{22} + ((ha)^2 + (kb)^2) s_{12}}{((ha)^2 + (kb)^2)} \right) \\ &\quad \cdot \left(\frac{((ha)^2 + (kb)^2)^2}{(ha)^4 s_{11} + (kb)^4 s_{22} + (hkab)^2 (s_{66} + 2s_{12})} \right) \\ &= \frac{(hkab)^2 (s_{66} - s_{11} - s_{22}) - ((ha)^4 + (kb)^4) s_{12}}{(ha)^4 s_{11} + (kb)^4 s_{22} + (hkab)^2 (s_{66} + 2s_{12})}\end{aligned}\quad (\text{A.76})$$

Both the Young modulus and the Poisson ratio can be written in function of the angle θ between the direction \mathbf{n} and the basis vector \mathbf{a} (see Fig. A.2) carry on the Miller indices in terms of the cosine directors of \mathbf{n}

$$E^{-1}(\theta) = \cos(\theta)^4 s_{11} + \sin(\theta)^4 s_{22} + \cos(\theta)^2 \sin(\theta)^2 (s_{66} + 2s_{12})$$

*Poisson Ratio for
Hexagonal and
Trigonal lattices*

*Poisson Ratio for
boat-graphane*

(A.77)

$$\nu(\theta) = \frac{\tan(\theta)^2(s_{66} - s_{11} - s_{22}) - (1 + \tan(\theta)^4)s_{12}}{s_{11} + \tan(\theta)^4s_{22} + \tan(\theta)^2(s_{66} + 2s_{12})} \quad (\text{A.78})$$

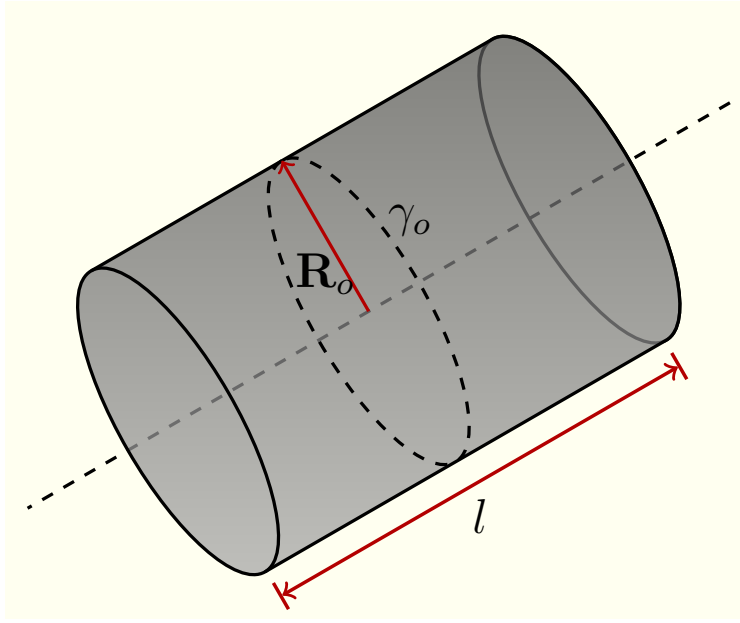


Figure A.3: A nanotube can be sketched as a simple cylinder. Here the radius R_o and circumference γ_o are referred to the reference configuration, while the length l is fixed by imposing the periodic boundary condition along the cylinder axis (dashed line).

A.7 BENDING RIGIDITY IN NANOTUBES

We have evaluate the bending rigidity κ of graphene, including relaxation effects, in Chapter 8. The same value $\kappa = 1.40$ eV has been obtained using carbon nanotubes instead nanoribbons. The nanotube, of course, do not show any edge effects, but the bending rigidity depends from the curvature, which in nanotubes is a geometric constant. In fact bond stretching is observed down to (15,0) nanotubes [101, 121, 122]. Including relaxation effects in function of the nanotube radius R it possible to extract the pure bending energy term by comparing the ray variation between the reference starting tube, which has all bonds equal to the perfect graphene, namely 1.41 \AA , and the full relaxed one.

In fact the cylindric geometry of a nanotube impose the Gaussian curvature null, $\mathcal{K} = 0$. Thus, the elastic energy density \mathcal{U} [eV \AA^{-2}] of a monoatomic layered membrane is defined as

$$\mathcal{U} = \frac{1}{2} \frac{E}{1+\nu} \text{Tr}(\hat{\epsilon}^2) + \frac{1}{2} \frac{E\nu}{1-\nu^2} [\text{Tr}(\hat{\epsilon})]^2 + \frac{1}{2} \kappa (2\mathcal{H})^2 \quad (\text{A.79})$$

depending on the mean curvature \mathcal{H} , and on the strain tensor $\hat{\epsilon}$.

To evaluate the only bending energy term \mathcal{U}_b , we impose strain $\hat{\epsilon} = 0$, so that the strain energy term go to zero, $\mathcal{U}_s = \frac{1}{2} \frac{E}{1+\nu} \text{Tr}(\hat{\epsilon}^2) + \frac{1}{2} \frac{E\nu}{1-\nu^2} [\text{Tr}(\hat{\epsilon})]^2 = 0$. The only bending energy den-

sity \mathcal{U}_b [$\text{eV}\text{\AA}^{-2}$] of a general given surface can be written as

$$\mathcal{U} = \frac{1}{2}\kappa(2\mathcal{H})^2 - \bar{\kappa}\mathcal{K} \quad (\text{A.80})$$

where the mean curvature is $\mathcal{H} = \frac{k_1+k_2}{2}$ [m^{-1}] and the Gaussian curvature is defined as $\mathcal{K} = k_1k_2$ [m^{-2}], here $k_1 = \frac{1}{R_1}$ and $k_2 = \frac{1}{R_2}$ are the principal curvatures, while R_1 and R_2 are the local principal radii of curvature. We have chosen a cylindric configuration that involving only one curvature $k_1 = \frac{1}{R_1}$ (i.e. $k_2 = 0$), therefore the mean curvature is $\mathcal{H} = \frac{k_1}{2}$, while the Gaussian curvature is null, $\mathcal{K} = 0$. Thus in the case of cylindric geometry, the bending energy density \mathcal{U}_b is given by

$$\mathcal{U} = \frac{1}{2}\kappa k_1^2 \quad (\text{A.81})$$

To obtain the total bending energy, we have to integrate the bending energy density on the reference surface Σ_o $\mathcal{U}_b = \int \int_{\Sigma_o} \mathcal{U} d\sigma = \frac{1}{2}\kappa l \int_{\gamma_o} k_1^2 ds$ where $\Sigma = L_o l$ being the total area of the reference system, $\gamma_o = 2\pi R_o$ is the circumference of the cylinder with radius R_o , and s is the arc length ($0 < s < L_o$). Note that the reference surface Σ_o is defined as the surface of the corresponding rectangular flat slice which we have rolled to build the nanotubes, i.e. the unstrained graphene nanoribbon wherein all the bond length are equal to the equilibrium distance $d_{C-C} = 1.41\text{\AA}$ between a pair of carbon atoms. The solution of the integral is as follows

$$\mathcal{U}_b = \int \int_{\Sigma_o} \mathcal{U}_b d\sigma = \frac{1}{2}\kappa l \int_{\gamma_o} k_1^2 ds \quad (\text{A.82})$$

$$= \frac{1}{2}\kappa l \int_{\gamma_o} (R)^{-2} ds \quad (\text{A.83})$$

$$= \frac{1}{2}\kappa l \frac{2\pi R_o}{R^2} \quad (\text{A.84})$$

Here the nanotube length l is constant due to the periodic boundary condition imposed along the axis of the cylinder. If the bending does not involve stretching, the radius R after the relaxation of the nanotube have to be equal the reference cylinder radius R_o . Therefore the bending energy can be simplified as

$$\mathcal{U}_b = \lim_{R \rightarrow R_o} \frac{1}{2}\kappa l \frac{2\pi R_o}{R^2} = \frac{\pi\kappa l}{R_o} \quad (\text{A.85})$$

Because of the bending energy can be computed by atomistic simulation as difference between the total energy of the nanotube E_o^{tube} and the corresponding reference flat system E_o^{flat} , namely $\mathcal{U}_b = E_o^{\text{tube}} - E_o^{\text{flat}}$, the bending rigidity κ of a nanotube with radius R_o is given by

$$\kappa = \frac{R_o}{\pi l \mathcal{U}_b} \quad (\text{A.86})$$

in absence of stretching on the surface.

Moreover, when a relaxation of the structure is allowed a variation of radius R is observed down to a certain dimension of the nanotube. In these cases besides the bending energy is given by the solution in Eq. (A.82) with $R \neq R_o$, it needs to take in account the no longer negligible stretching term in the Eq. (A.79). Thus we have to integrate also the stretching energy density u_s as follows

$$\begin{aligned} u_s &= \iint_{\Sigma_o} u_s d\sigma = \iint_{\Sigma_o} \left(\frac{1}{2} \frac{E}{1+\nu} \text{Tr}(\hat{\epsilon}^2) + \frac{1}{2} \frac{E\nu}{1-\nu^2} [\text{Tr}(\hat{\epsilon})]^2 \right) d\sigma \\ &= \frac{1}{2} \frac{E}{1+\nu} \iint_{\Sigma_o} \left(\text{Tr}(\hat{\epsilon}^2) + \frac{\nu}{1-\nu} [\text{Tr}(\hat{\epsilon})]^2 \right) d\sigma \end{aligned}$$

We can consider only strain $\hat{\epsilon} = \begin{pmatrix} \zeta & 0 \\ 0 & 0 \end{pmatrix}$ along the circumference, because the length l is fixed by the periodic boundary conditions. So that

$$\begin{aligned} u_s &= \frac{1}{2} \frac{E}{1+\nu} \iint_{\Sigma_o} \left(\zeta^2 + \frac{\nu}{1-\nu} \zeta^2 \right) d\sigma \\ &= \frac{1}{2} \frac{E}{1+\nu} \iint_{\Sigma_o} \left(\frac{\zeta^2}{1-\nu} \right) d\sigma \end{aligned}$$

$$\text{but } \zeta = \frac{\gamma - \gamma_o}{\gamma_o} = \frac{R - R_o}{R_o},$$

so that

$$\begin{aligned} u_s &= \frac{1}{2} \frac{El}{1-\nu^2} \left(\frac{R - R_o}{R_o} \right)^2 \int_{\gamma_o} ds \\ &= \frac{1}{2} \frac{El}{1-\nu^2} \left(\frac{R - R_o}{R_o} \right)^2 (2\pi R_o) \end{aligned}$$

(A.87)

Obviously when $R \rightarrow R_o$, the stretching energy goes to zero, $u_s = 0$.

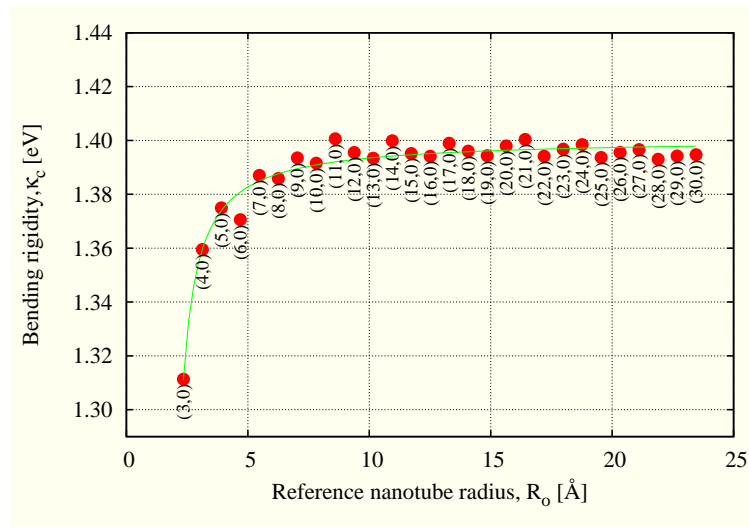


Figure A.4: Bending rigidity κ in function of the radius of a set of zig-zag nanotubes in the range of (3,0)-(30,0). The symbols show the value of the bending rigidity, as defined in the Eq. (A.85), obtained by tight-binding simulations. Note that down to the (15,0) a deviation from the constant value is observed. This fact is due to the rising of stretching bond effects due to the curvature. The asymptotic value is $\kappa = 1.40$ eV, exactly as obtained from the nanoribbons experiments discussed in the Chapter 8

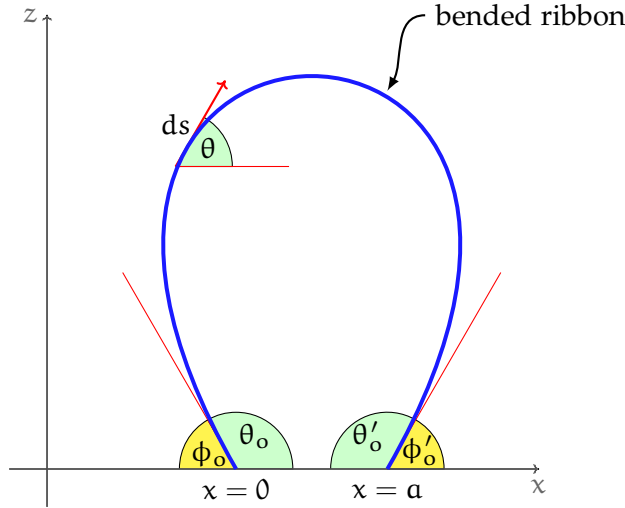


Figure A.5: A cross-section of a bended ribbon (blue curve) with parallel edges at fixed distance a . The ribbon width L and the edges distance a are taken constant, while the attack angles θ_0 and $\theta'_0 = -\theta_0$ (or ϕ and ϕ') are free up.

A.8 MINIMAL SURFACE OF A BENDED MEMBRANE

In the Sec. 8.2 we have discussed the problem of a bended nanoribbon. We show in this Appendix a more detailed discussion about the minimization the energy functional in Eq.(8.5) by the method of Lagrange multipliers λ , i.e. the solution of the Eq. (8.6)

A variational approach

$$\int_0^a dx \left[\frac{\dot{z}^2}{(1 + \dot{z}^2)^{\frac{5}{2}}} + \lambda \sqrt{1 + \dot{z}^2} \right], \tag{A.88}$$

enforcing the absence of any in-plane stretching under the follows boundary conditions:

$$\begin{aligned} \text{a constrained width,} & \quad L = \int_0^a dx \sqrt{1 + \dot{z}^2}, \\ \text{a fixed parallel edges,} & \quad z(0) = z(a) = 0, \\ \text{a free attack angle,} & \quad \theta = \arctg\left(\frac{dz}{dx}\right), \quad \dot{z}(0) = \dot{z}(a) = 0 \end{aligned} \tag{A.89}$$

Eulero-Poisson equation

The above integral can be written in the general form

$$G(z) = \int_0^a dx \mathcal{F}(z, \dot{z}, \ddot{z}, x)$$

which is the solution of the Euler-Poisson differential equation

$$\frac{\partial \mathcal{F}}{\partial z} - \frac{d}{dx} \frac{\partial \mathcal{F}}{\partial \dot{z}} + \frac{d^2}{dx^2} \frac{\partial \mathcal{F}}{\partial \ddot{z}} = 0 \tag{A.90}$$

PROOF: We can define the function $G(z, h)$

$$G(z, h) = \lim_{\alpha \rightarrow 0} \frac{G(z + \alpha h) - G(z)}{\alpha} = \frac{d}{d\alpha} G(z + \alpha h) \Big|_{\alpha \rightarrow 0} \quad (\text{A.91})$$

The derivative of the function $G(z + \alpha h) = \int_0^a dx \mathcal{F}(z + \alpha h, \dot{z} + \alpha \dot{h}, \ddot{z} + \alpha \ddot{h}, x)$ is given by

$$\begin{aligned} \frac{d}{d\alpha} G(z + \alpha h) \Big|_{\alpha \rightarrow 0} &= \int_0^a dx \frac{d}{d\alpha} \mathcal{F}(z + \alpha h, \dot{z} + \alpha \dot{h}, \ddot{z} + \alpha \ddot{h}, x) \\ &= \int_0^a dx \left(\frac{\partial \mathcal{F}}{\partial z} h + \frac{\partial \mathcal{F}}{\partial \dot{z}} \dot{h} + \frac{\partial \mathcal{F}}{\partial \ddot{z}} \ddot{h} \right) \\ &= \text{[by parts]} = \int_0^a dx \left(\frac{\partial \mathcal{F}}{\partial z} - \frac{d}{dx} \frac{\partial \mathcal{F}}{\partial \dot{z}} + \frac{d^2}{dx^2} \frac{\partial \mathcal{F}}{\partial \ddot{z}} \right) h \\ &\quad + \left(\frac{\partial \mathcal{F}}{\partial \dot{z}} - \frac{d}{dx} \frac{\partial \mathcal{F}}{\partial \ddot{z}} \right) h \Big|_0^a + \ddot{h} \frac{\partial \mathcal{F}}{\partial \ddot{z}} \Big|_0^a = 0 \end{aligned} \quad (\text{A.92})$$

Thus, imposing the follows constrains

$$\begin{aligned} \text{a fixed parallel edges,} \quad & z(0) = z(a) = 0 \Rightarrow h(0) = h(a) = 0 \\ \text{a free attack angle,} \quad & \dot{z}(0) = \dot{z}(a) = 0 \Rightarrow \frac{\partial \mathcal{F}(0)}{\partial \dot{z}} = \frac{\partial \mathcal{F}(a)}{\partial \dot{z}} = 0 \\ \text{or a fixed attack angle,} \quad & \dot{z}(0) = \dot{z}(a) = 0 \Rightarrow \dot{h}(0) = \dot{h}(a) = 0 \end{aligned} \quad (\text{A.93})$$

we get the Euler-Poisson Eq. (A.90), q.e.d.

The corresponding Hamiltonian can be written as follows

$$H = \mathcal{F} - \dot{z} \left(\frac{\partial \mathcal{F}}{\partial \dot{z}} - \frac{d}{dx} \frac{\partial \mathcal{F}}{\partial \ddot{z}} \right) - \ddot{z} \frac{\partial \mathcal{F}}{\partial \ddot{z}} \quad (\text{A.94})$$

Moreover we can proof that $\frac{dH}{dx} = \frac{d\mathcal{F}}{dx}$. By deriving the Eq. (A.94) and by using the Eq. (A.90)

$$\begin{aligned} \frac{dH}{dx} &= \frac{d\mathcal{F}}{dx} - \dot{z} \left(\frac{\partial \mathcal{F}}{\partial \dot{z}} - \frac{d}{dx} \frac{\partial \mathcal{F}}{\partial \ddot{z}} \right) \\ &\quad - \dot{z} \left(\frac{d}{dx} \frac{\partial \mathcal{F}}{\partial \dot{z}} - \frac{d^2}{dx^2} \frac{\partial \mathcal{F}}{\partial \ddot{z}} \right) - \ddot{z} \frac{\partial \mathcal{F}}{\partial \ddot{z}} - \dot{z} \frac{d}{dx} \frac{\partial \mathcal{F}}{\partial \ddot{z}} \\ &= \frac{d\mathcal{F}}{dx}, \quad \text{q.e.d.} \end{aligned}$$

In our case the function $\mathcal{F}(z, \dot{z}, \ddot{z}, x)$ is given by

$$\mathcal{F} = \frac{\ddot{z}^2}{(1 + \dot{z}^2)^{\frac{5}{2}}} + \lambda \sqrt{1 + \dot{z}^2} \quad (\text{A.95})$$

Thus the partial derivatives $\frac{\partial \mathcal{F}}{\partial x} = \frac{\partial \mathcal{F}}{\partial z} = 0$ have to be null. We introduce two parameters, C_1, C_2 to solve the Hamiltonian, Eq. (A.94), and the Euler-Poisson equation, Eq. (A.90), as follows

$$\begin{aligned} \mathcal{F} - \dot{z} \left(\frac{\partial \mathcal{F}}{\partial \dot{z}} - \frac{d}{dx} \frac{\partial \mathcal{F}}{\partial \ddot{z}} \right) - \ddot{z} \frac{\partial \mathcal{F}}{\partial \ddot{z}} &= -C_2 \\ -\frac{d}{dx} \frac{\partial \mathcal{F}}{\partial \dot{z}} + \frac{d^2}{dx^2} \frac{\partial \mathcal{F}}{\partial \ddot{z}} &= C_1 \\ \therefore \mathcal{F} + \dot{z} C_1 - \ddot{z} \frac{\partial \mathcal{F}}{\partial \ddot{z}} &= -C_2 \end{aligned} \quad (\text{A.96})$$

Replacing in the Eq. (A.96) the Eq. (A.95) and its derivative $\frac{\partial \mathcal{F}}{\partial z}$ we obtain

$$-\frac{\dot{z}^2}{(1+\dot{z}^2)^{\frac{5}{2}}} + \lambda\sqrt{1+\dot{z}^2} + \dot{z}C_1 = -C_2 \quad (\text{A.97})$$

We have to impose the boundary condition as in Eqs. (8.7). First of all, by the attack angle definition we get

$$\begin{aligned} \dot{z} &= \tan \theta \\ \ddot{z} &= \frac{1}{\cos^2 \theta} \frac{\partial \theta}{\partial x} \end{aligned} \quad (\text{A.98})$$

Introducing the arc length $s = \int_0^x dx \sqrt{1+\dot{z}^2}$ we get

$$\begin{aligned} \frac{\partial s}{\partial x} &= \sqrt{1+\tan^2 \theta} = \frac{1}{\cos \theta} \\ \frac{\partial \theta}{\partial x} &= \frac{\partial \theta}{\partial s} \frac{\partial s}{\partial x} = \frac{1}{\cos \theta} \frac{d\theta}{ds} \end{aligned} \quad (\text{A.99})$$

Thus, the Eq. (A.97) can be written as

$$-\frac{1}{\cos \theta} \left(\frac{d\theta}{ds} \right)^2 + \frac{1}{\cos \theta} \lambda + \frac{\sin \theta}{\cos \theta} C_1 = -C_2 \quad (\text{A.100})$$

Second, by the conditions for the fixed edges and the free attack angles, we get that $\frac{d\theta}{ds} = 0$ at $s = 0$ and $s = L$. Furthermore, the symmetry of the cylinder surface leads to $\theta(0) = \theta_o$ and $\theta(L) = -\theta_o$. So that deriving the Eq. (A.100)

$$\begin{aligned} \left. \frac{d\theta}{ds} \right|_{\theta_o} &= -\sqrt{\lambda + C_1 \sin \theta_o + C_2 \cos \theta_o} = 0 \\ \therefore \quad \lambda &= -C_1 \sin \theta_o - C_2 \cos \theta_o \quad (\text{A.101}) \\ \left. \frac{d\theta}{ds} \right|_{-\theta_o} &= -\sqrt{-2C_1 \sin \theta_o} = 0 \\ \therefore \quad C_1 &= 0 \end{aligned}$$

Therefore the Eq. (A.100) has been simplified as follows

$$\begin{aligned} \frac{d\theta}{ds} &= -\sqrt{C(\cos \theta - \cos \theta_o)} \\ S &= \int_0^s ds = \int_{\theta_o}^{\theta(s)} \frac{d\theta}{-\sqrt{C(\cos \theta - \cos \theta_o)}} \end{aligned} \quad (\text{A.102})$$

where $C \equiv C_2$ as well as in the following. Finally, we use the fixed length $L = \int_0^L dx \sqrt{1+\dot{z}^2}$ to obtain the parameter C as follows

$$\begin{aligned} L &= \int_{-\theta_o}^{\theta_o} \frac{d\theta}{\sqrt{C(\cos \theta - \cos \theta_o)}} \quad (\text{A.103}) \\ \therefore S &= L \frac{\int_{\theta(s)}^{\theta_o} \frac{d\theta}{\sqrt{C(\cos \theta - \cos \theta_o)}}}{\int_{-\theta_o}^{\theta_o} \frac{d\theta}{\sqrt{C(\cos \theta - \cos \theta_o)}}} \quad (\text{A.104}) \end{aligned}$$

In order to turn back in Cartesian coordinates, we observe that $\frac{dx}{ds} = \cos \theta$, and $\frac{dz}{ds} = \frac{dz}{dx} \frac{dx}{ds} = \sin \theta$,

$$\begin{aligned} x &= \int_{\theta(s)}^{\theta_0} \frac{\cos \theta d\theta}{\sqrt{C(\cos \theta - \cos \theta_0)}} \\ z &= \int_{\theta(s)}^{\theta_0} \frac{\sin \theta d\theta}{\sqrt{C(\cos \theta - \cos \theta_0)}} \end{aligned} \quad (\text{A.105})$$

and reminding that the edges of the nanoribbon is at fixed distance, i.e. $x(L) = a$, we can write

$$\begin{aligned} a &= \int_{-\theta_0}^{\theta_0} \frac{\cos \theta d\theta}{\sqrt{C(\cos \theta - \cos \theta_0)}} \\ &= L \frac{\int_{\theta(s)}^{\theta_0} \frac{\cos \theta d\theta}{\sqrt{(\cos \theta - \cos \theta_0)}}}{\int_{-\theta_0}^{\theta_0} \frac{d\theta}{\sqrt{(\cos \theta - \cos \theta_0)}}} \end{aligned} \quad (\text{A.106})$$

which give us θ_0 for any given edges distance a and nanoribbon length L . Therefore we have obtained the parametric form of the minimized surface

$$\begin{aligned} x &= L \frac{\int_{\theta(s)}^{\theta_0} \frac{\cos \theta d\theta}{\sqrt{(\cos \theta - \cos \theta_0)}}}{\int_{-\theta_0}^{\theta_0} \frac{d\theta}{\sqrt{(\cos \theta - \cos \theta_0)}}} \\ z &= L \frac{\int_{\theta(s)}^{\theta_0} \frac{\sin \theta d\theta}{\sqrt{(\cos \theta - \cos \theta_0)}}}{\int_{-\theta_0}^{\theta_0} \frac{d\theta}{\sqrt{(\cos \theta - \cos \theta_0)}}} \end{aligned} \quad (\text{A.107})$$

As shown in Sec. 8.2, we eventually obtain the final geometry in parametric representation $[x(s), z(s)]$

$$\frac{x}{L} = \frac{E(q) - \mathcal{E}(\text{am}\{\mathbf{K}(q)(1 - 2\frac{s}{L})\}, q)}{\mathbf{K}(q)} - \frac{s}{L} \quad (\text{A.108})$$

$$\frac{z}{L} = \frac{q}{\mathbf{K}(q)} \text{cn}\left\{\mathbf{K}(q)\left(1 - 2\frac{s}{L}\right)\right\} \quad (\text{A.109})$$

where s is the arc length ($0 < s < L$), $q = \sin \frac{\theta}{2}$ is the elliptic modulus and θ is the attack angle given by

$$\frac{a}{L} = 2 \frac{E(q)}{\mathbf{K}(q)} - 1. \quad (\text{A.110})$$

The quantities $E(q)$ and $\mathbf{K}(q)$ are the complete elliptic integrals, defined as [115, 116]

$$E(q) = \mathcal{F}\left(\frac{\pi}{2}, q\right), \quad \mathbf{K}(q) = \mathcal{E}\left(\frac{\pi}{2}, q\right) \quad (\text{A.111})$$

where the functions $\mathcal{F}(v, q)$ and $\mathcal{E}(v, q)$ are incomplete elliptic integrals of the first and second kind, respectively [115, 116]

$$\begin{aligned} \mathcal{F}(v, q) &= \int_0^v \frac{d\alpha}{\sqrt{1 - q^2 \sin^2 \alpha}} \\ \mathcal{E}(v, q) &= \int_0^v \sqrt{1 - q^2 \sin^2 \alpha} d\alpha. \end{aligned} \quad (\text{A.112})$$

Moreover, by considering $u = \mathcal{F}(v, q)$ we define the inverse relation (with fixed modulus q) $v = \text{am}\{u\}$, which is called Jacobi amplitude function. Further, $\text{cn}\{u\} = \cos v = \cos(\text{am}\{u\})$ and $\text{sn}\{u\} = \sin v = \sin(\text{am}\{u\})$ are the Jacobi elliptic functions.[116] Interesting enough, one can prove for a given (L, a) that $\lim_{a/L \rightarrow 0} \theta = 2.2813\text{rad} = 130.709^\circ$, an universal value of the attack angle found whenever $a = 0$ or L is very large.

An universal attack angle.

BIBLIOGRAPHY

- [1] P. R. Wallace. *Phys. Rev.*, 71,622. (1947). (Cited on page 1.)
- [2] Aziz A. Ahmadiéh and Hamid A. Rafizadeh. *Phys. Rev. B*, 7,4527. (1973). (Cited on page 1.)
- [3] A. Bosak and M. Krisch. *Phys. Rev. B*, 75,153408. (2007). (Cited on page 1.)
- [4] L.-F. Wang and Q.-S. Zhenga. *Applied Phys. Lett.*, 90,153113. (2007). (Cited on page 1.)
- [5] A. K. Geim S. V. Morozov D. Jiang Y. Zhang S. V. Dubonos I. V. Grigorieva K. S. Novoselov and A. A. Firsov. *Science*, 306. (2004). (Cited on pages 2 and 109.)
- [6] A. K. Geim S. V. Morozov D. Jiang M. I. Katsnelson I. V. Grigorieva S. V. Dubonos K. S. Novoselov and A. A. Firsov. *Nature*, 438,197. (2005). (Cited on page 2.)
- [7] V. P. Gusynin and S. G. Sharapov. *Phys. Rev. Lett.*, 95,146801. (2005). (Cited on pages 2 and 109.)
- [8] L. D. Landau. *Phys. Z. Sowjetunion*, 11,26. (1937). (Cited on page 2.)
- [9] R. E. Peierls. *Ann. I. H. Poincare* 5, 5,177. (1935). (Cited on page 2.)
- [10] N. D. Mermin. *Phys. Rev.*, 176,250. (1968). (Cited on page 2.)
- [11] J. H. Los A. Fasolino and M. I. Katsnelson. *Nature Materials*, 6,858. (2007). (Cited on page 3.)
- [12] X. Wei W. Kysar C. Lee and J. Hone. *Science*, 321,385. (2008). (Cited on pages 4, 5, 7, 77, 82, 83, 85, 86, 87, 105, and 110.)
- [13] V. M. Pereira and A. H. Castro Neto. *Phys. Rev. Lett.*, 103, 046801. (2009). (Cited on pages 4, 7, 110, and 120.)
- [14] M. Arroyo and T. Belytschko. *Phys. Rev. B*, 69,115415. (2004). (Cited on pages 4, 77, and 86.)
- [15] Z. C. Ou-Yang and Z. C. Tu. *J. Comput. Theor. Nanosci.*, 5, 422. (2008). (Cited on pages 4, 77, and 130.)
- [16] H.W. Zhang, J.B. Wang, and X. Guo. *Journal of the Mechanics and Physics of Solids*, 53,1929. (2005). (Cited on page 5.)

- [17] M. Y. Han, B. Özyilmaz, Y. Zhang, and P. Kim. *Phys. Rev. Lett.*, 98,206805. (2007). (Cited on pages 5 and 110.)
- [18] F. Sols, F. Guinea, and A. H. Castro Neto. *Phys. Rev. Lett.*, 99,166803. (2007). (Cited on pages 5, 7, and 110.)
- [19] E. R. Mucciolo, A. H. Castro Neto, and C. H. Lewenkopf. *Phys. Rev. B*, 79,075407. (2009). (Cited on pages 5 and 110.)
- [20] K. Nakada, M. Fujita, G. Dresselhaus, and M. S. Dresselhaus. *Phys. Rev. B*, 54,17954. (1996). (Cited on pages 5 and 110.)
- [21] B. Jørgensen L. Nilsson M. Andersen E. Rienks M. Bianchi M. Fanetti E. Lægsgaard A. Baraldi S. Lizzit Z. Slijivancanin F. Besenbacher B. Hammer T. G. Pedersen P. Hofmann R. Balog and L. Hornekær. *Nature*, 9. (2010). (Cited on pages 5 and 110.)
- [22] A. S. Chaudhari J. O. Sofo and G. D. Barber. *Phys. Rev. B*, 75,153401. (2007). (Cited on pages 6, 89, 90, and 94.)
- [23] M. I. Katsnelson D. W. Boukhvalov and A. I. Lichtenstein. *Phys. Rev. B*, 77,035427. (2008). (Cited on pages 6, 89, and 90.)
- [24] R.R. Nair T. M. G. Mohiuddin S. V. Morozov P. Blake M. P. Halsall A. C. Ferrari D. W. Boukhvalov M. I. Katsnelson A. K. Geim D. C. Elias and K.S. Novoselov. *Science*, art. 610. (2009). (Cited on pages 6 and 90.)
- [25] O. Leenaerts, H. Peelaers, A. D. Hernández-Nieves, B. Partoens, and F. M. Peeters. *Phys. Rev. B*, 82,195436. (2010). (Cited on pages 6 and 107.)
- [26] M. Topsakal, E. Akturk, and S. Ciraci. *Phys. Rev. B*, 79, 115442. (2009). (Cited on pages 6, 90, 92, and 93.)
- [27] Y. Ma J. Kasim Y. H. Wu Z. H. Ni H. M. Wang and Z. X. Shen. *ACS Nano*, 2. (2008). (Cited on pages 7, 110, and 117.)
- [28] P. Shemella and S.K. Nayak. *Appl. Phys. Lett.*, 94. (2009). (Cited on pages 7 and 110.)
- [29] Y. Zhao H. Jang S. Y. Lee J. M. Kim K.S. Kim J. H. Ahn P. Kim J. Y. Choi K. S. Kim and B. H. Hong. *Nature*, 457. (2009). (Cited on pages 7, 110, and 117.)
- [30] T. Yu Y. H. Lu Y. Y. Wang Y. P. Feng Z. H. Ni and Z. X. Shen. *ACS Nano*, 2. (2008). (Cited on pages 7, 110, and 117.)
- [31] A. H. Castro Neto V. M. Pereira and N. M. R. Peres. *Phys. Rev. B*, 80,045401. (2009). (Cited on pages 7, 110, 114, and 115.)

- [32] T. Wassmann, A. P. Seitsonen, A. M. Saitta, M. Lazzeri, and F. Mauri. *Phys. Rev. Lett.*, 101,096402. (2008). (Cited on page 7.)
- [33] K. A. Ritter and J. W. Lyding. *Nature Materials*, 8,235. (2009). (Cited on page 7.)
- [34] V. B. Shenoy, C. D. Reddy, A. Ramasubramaniam, and Y. W. Zhang. *Phys. Rev. Lett.*, 101,245501. (2008). (Cited on page 7.)
- [35] P. Koskinen, S. Malola, and H. Häkkinen. *Phys. Rev. Lett.*, 101,115502. (2008). (Cited on page 7.)
- [36] A. K. Geim M. I. Katsnelson K. S. Novoselov T. J. Booth J. C. Meyer and S. Roth. *Nature (London)*, 446,60. (2007). (Cited on pages 7 and 121.)
- [37] J. H. Chen W. G. Cullen M. S. Fuhrer M. Ishigami and E. D. Williams. *NanoLetters*, 7,1643. (2007). (Cited on pages 7 and 121.)
- [38] F. Guinea N. M. R. Peres K. S. Novoselov A. H. Castro Neto and A. K. Geim. *Rev. Mod. Phys.*, 81,109. (2009). (Cited on pages 8, 109, and 121.)
- [39] A. M. van der Zande S. S. Verbridge I. W. Frank D. M. Tanenbaum J. M. Parpia H. G. Craighead J. S. Bunch and P. L. McEuen. *Science*, 315,490. (2007). (Cited on pages 8 and 122.)
- [40] A. Isacsson J. Atalaya and J. M. Kinaret. *NanoLetters*, 8,4196. (2008). (Cited on pages 8 and 122.)
- [41] K. N. Kudin J.-L. Li R. K. Prud'homme R. Car D. A. Saville H.C. Schniepp and I. A. Aksay. *ACS Nano*, 2,2577. (2008). (Cited on pages 8 and 122.)
- [42] A. L. Higginbotham A. Sinitskii J. R. Lomeda A. Dimiev B. K. Price D. V. Kosynkin and J. M. Tour. *Nature (London)*, 458,872. (2009). (Cited on pages 8 and 122.)
- [43] L. Chico H. Santos and L. Brey. *Phys. Rev. Lett.*, 103,086801. (2009). (Cited on pages 8 and 122.)
- [44] P. O. Löwdin, *J. Mol. Spectr.* 3, 46 (1959). (Cited on page 15.)
- [45] L. Colombo, *Tight-binding molecular dynamics: A primer*, La Rivista del Nuovo Cimento Vol. 28, N. 10 (2005). (Cited on page 16.)
- [46] J. C. Slater and G. F. Koster. *Phys. Rev.*, 94,1498. (1954). (Cited on pages 17 and 18.)

- [47] W. A. Harrison. *Electronic Structure and the Properties of Solids*. Dover Publications, New York. (1989). (Cited on page 19.)
- [48] R. P. Feynman, *Phys. Rev.* **56**, 340 (1939). (Cited on page 21.)
- [49] P. Pulay, *Mol. Phys.* **17**, 197 (1969). (Cited on page 21.)
- [50] C. Z. Wang C. T. Chan C. H. Xu and K. M. Ho. *Journal of Physics: Condensed Matter*, **4**,6047. (1992). (Cited on pages 21, 22, 23, 84, 110, 126, and 127.)
- [51] L. Goodwin, A. J. Skinner, and D. G. Pettifor, *Europhys. Lett.* **9**, 701 (1989). (Cited on page 21.)
- [52] R. Dreizler and E. Gross. *Density Functional Theory*. New York. (1995). (Cited on page 25.)
- [53] R.G. Yang and W. Parr. *Density-Functional Theory of Atoms and Molecules*. New York. (1989). (Cited on page 25.)
- [54] P. Hohenberg and W. Kohn. *Phys. Rev.*, **136**,B864. (1964). (Cited on page 25.)
- [55] W. Kohn and L. J. Sham. *Phys. Rev.*, **140**,A1133. (1965). (Cited on pages 25, 26, and 28.)
- [56] E.P. Wigner. *Trns. Faraday soc.*, **34**,678. (1938). (Cited on page 29.)
- [57] D. Ceperley. *Phys. Rev. B*, **18**,3126. (1978). (Cited on page 29.)
- [58] D. M. Ceperley and B. J. Alder. *Phys. Rev. Lett.*, **45**,566. (1980). (Cited on page 29.)
- [59] J. P. Perdew and A. Zunger. *Phys. Rev. B*, **23**,5048. (1981). (Cited on page 29.)
- [60] J. P. Perdew and Y. Wang. *Phys. Rev. B*, **45**,13244. (1992). (Cited on pages 30 and 31.)
- [61] Y. Wang and J. P. Perdew. *Phys. Rev. B*, **44**,13298. (1991). (Cited on page 30.)
- [62] J. P. Perdew, J. A. Chevary, S. H. Vosko, K. A. Jackson, M. R. Pederson, D. J. Singh, and C. Fiolhais. *Phys. Rev. B*, **46**,6671. (1992). (Cited on pages 30 and 31.)
- [63] A. D. Becke. *Phys. Rev. A*, **38**,3098. (1988). (Cited on pages 30 and 31.)
- [64] J. P. Perdew, K. Burke, and M. Ernzerhof. *Phys. Rev. Lett.*, **77**,3865. (1996). (Cited on page 31.)

- [65] C. Lee, W. Yang, and R. G. Parr. *Phys. Rev. B*, 37,785. (1988). (Cited on page 31.)
- [66] M. C. Payne, M. P. Teter, D. C. Allan, T. A. Arias, and J. D. Joannopoulos. *Rev. Mod. Phys.*, 64,1045. (1992). (Cited on page 33.)
- [67] R. M. Pick, M. H. Cohen, and R. M. Martin. *Phys. Rev. B*, 1, 910. (1970). (Cited on page 33.)
- [68] X. Gonze. *Phys. Rev. A*, 52,1096. (1995). (Cited on page 34.)
- [69] S. Baroni, S. de Gironcoli, A. Dal Corso, and P. Giannozzi. *Rev. Mod. Phys.*, 73,515. (2001). (Cited on pages 34 and 93.)
- [70] X. Gonze and J.-P. Vigneron. *Phys. Rev. B*, 39,13120. (1989). (Cited on page 34.)
- [71] A. K. Subramaniyan and C.T. Sun. *International Journal of Solids and Structures*, 45,4340. (2008). (Cited on pages 70 and 71.)
- [72] A. G. McLellan. *Am. J. Phys.*, 42,239. (1974). (Cited on page 70.)
- [73] R. J. Swenson. *Am. J. Phys.*, 51,940. (1983). (Cited on page 70.)
- [74] R. Clausius. *Phil. Mag.*, 40,122. (1870). (Cited on page 70.)
- [75] J.C. Maxwell. *Transactions of the Royal Society of Edinburg XXVI*, art. 1. (1870). (Cited on page 70.)
- [76] M. Zhou. *Proc. R. Soc. Lond. A*, 459,2347. (2003). (Cited on pages 70, 85, and 86.)
- [77] G.L. Gray F. Costanzo and P.C. Andia. *Modelling and Simulation in Materials Science and Engineering*, 14,741. (2006). (Cited on page 71.)
- [78] G.L. Gray F. Costanzo and P.C. Andia. *International Journal of Solids and Structures*, 42,6409. (2005). (Cited on page 71.)
- [79] J.H. Weiner and J. Gao . *Macromolecules*, 20,2520. (1987). (Cited on page 71.)
- [80] D. Frenkel and B. Smit, *Understanding Molecular Simulation* (Academic Press, San Diego, 1996). (Cited on page 74.)
- [81] K. Kern M. Burghard and C. Gómez-Navarro. *Nano Letters*, 8,2045. (2008). (Cited on page 77.)
- [82] J. Zhou and R. Huang. *Journal of the Mechanics and Physics of Solids*, 56,1609. (2008). (Cited on pages 77 and 86.)

- [83] G. E. Scuseria K. N. Kudin and B. I. Yakobson. *Phys. Rev. B*, 64,235406. (2001). (Cited on pages 77, 85, 86, 93, and 130.)
- [84] L. Colombo. *Riv. Nuovo Cimento*, 28,1. (2005). (Cited on pages 77 and 126.)
- [85] L. D. Landau and E. M. Lifschitz. *Theory of Elasticity*. Butterworth Heinemann, Oxford. (1986). (Cited on pages 79, 96, 122, and 123.)
- [86] M. Łopuszyński and J. A. Majewski. *Phys. Rev. B*, 76,045202. (2007). (Cited on page 83.)
- [87] O. H. Nielsen. *Phys. Rev. B*, 34,5808. (1986). (Cited on page 83.)
- [88] K. H. Michel and B. Verberck. *Phys. Stat. Sol. (B)*, 245,2177. (2008). (Cited on pages 85 and 86.)
- [89] F. Liu, P. Ming, and J. Li. *Phys. Rev. B*, 76,064120. (2007). (Cited on pages 85, 86, and 93.)
- [90] J. Li G. Gui and J. Zhong. *Phys. Rev. B*, 78,075435. (2008). (Cited on pages 85, 86, 93, and 114.)
- [91] D. Sánchez-Portal, E. Artacho, J. M. Soler, A. Rubio, and P. Ordejón. *Phys. Rev. B*, 59,12678. (1999). (Cited on pages 85 and 86.)
- [92] H. Gao and M. Buehler. *Natur*, 439,307. (2006). (Cited on page 85.)
- [93] K. Y. Volokh. *J. Mech. Phys. Solids*, 55,2237. (2007). (Cited on page 85.)
- [94] R. Al-Jishi and G. Dresselhaus. *Phys. Rev. B*, 26,4514. (1982). (Cited on page 86.)
- [95] B. Peng, M. Locascio, P. Zapol, S. Li, S. L. Mielke, G. C. Schatz, and H. D. Espinosa. *Nature Nanotechnology*, 3,626. (2008). (Cited on page 86.)
- [96] S. Lebègue, M. Klintonberg, O. Eriksson, and M. I. Katsnelson. *Phys. Rev. B*, 79,245117. (2009). (Cited on page 90.)
- [97] M. A. Nkansah I. J. Hutchinson K. E. Evans and S. C. Rogers. *Nature*, 353. (1991). (Cited on page 92.)
- [98] QUANTUM-ESPRESSO is a community project for high-quality quantum-simulation software, based on density-functional theory, and coordinated by P. Giannozzi. See <http://www.quantum-espresso.org> and <http://www.pwscf.org>. (Cited on page 92.)

- [99] D. Vanderbilt. *Phys. Rev. B*, 41,7892. (1990). (Cited on page 92.)
- [100] V. I. Artyukhov and L. A. Chernozatonskii. *J. Phys. Chem. A*, 114. (2010). (Cited on pages 94 and 96.)
- [101] G. Dresselhaus R. Saito and M. S. Dresselhaus. *Physical Properties of Carbon Nanotubes*. Imperial College Press, London. (1998). (Cited on pages 94 and 153.)
- [102] H. B. Huntington. *The elastic constants of crystals*. Academic Press, New York. (1958). (Cited on pages 96 and 104.)
- [103] K. E. Evans and A. Alderson. *Adv. Mat.*, 12,617. (2000). (Cited on page 101.)
- [104] G. Montambaux, F. Piéchon, J.-N. Fuchs, and M. O. Goerbig. *Phys. Rev. B*, 80,153412. (2009). (Cited on pages 109 and 115.)
- [105] Z. Jiang Y. Zhang S. V. Morozov H. L. Stormer U. Zeitler J. C. Maan G. S. Boebinger P. Kim K. S. Novoselov and A. K. Geim. *Science*, 315,1379. (2007). (Cited on page 109.)
- [106] P. Dietl, F. Piéchon, and G. Montambaux. *Phys. Rev. Lett.*, 100,236405. (2008). (Cited on page 115.)
- [107] Y. Hasegawa, R. Konno, H. Nakano, and M. Kohmoto. *Phys. Rev. B*, 74,033413. (2006). (Cited on page 115.)
- [108] E. Cerda and L. Mahadevan. *Phys. Rev. Lett.*, 90,074302. (2003). (Cited on page 120.)
- [109] Y. W. Wong and S. Pellegrino. *J. Mech. Mater. Struct.*, 1,25. (2006). (Cited on page 120.)
- [110] F. Miao Z. Chen H. Zhang W. Jang C. Dames W. Bao and C.N. Lau. *Nature Nanotech.*, 4,562. (2009). (Cited on page 120.)
- [111] A. K. Geim and K. S. Novoselov. *Nature Materials*, 6,183. (2007). (Cited on page 121.)
- [112] A. E. Green and W. Zerna. *Theoretical Elasticity*. Oxford. (1954). (Cited on page 122.)
- [113] M. P. do Carmo. *Differential Geometry of Curves and Surfaces*. New York. (1976). (Cited on page 123.)
- [114] Q. Lu, M. Arroyo, and R. Huang. *Journal of Physics D: Applied Physics*, 42,102002. (2009). (Cited on pages 123 and 130.)

- [115] I. S. Gradshteyn and I. M. Ryzhik. *Table of integrals, series and products*. San Diego. (1965). (Cited on pages 126 and 160.)
- [116] M. Abramowitz and I. A. Stegun. *Handbook of Mathematical Functions*. New York. (1970). (Cited on pages 126, 160, and 161.)
- [117] A. J. Skinner L. Goodwin and D. G. Pettifor. *Europhys. Lett.*, 9,701. (1989). (Cited on page 126.)
- [118] G. Galli C. Bostedt T. W. van Buuren J.-Y. Raty and L. J. Terminello. *Phys. Rev. Lett.*, 90,037401. (2003). (Cited on page 127.)
- [119] L. Colombo P. Piseri L. Ravagnan Y. Yamaguchi and P. Milani. *Phys. Rev. B*, 76,134119. (2007). (Cited on page 127.)
- [120] M.P. Bogana and L.Colombo. *Appl. Phys. A*, 86,275. (2007). (Cited on page 127.)
- [121] L. Shen and J. Li. *Phys. Rev. B*, 71,165427. (2005). (Cited on page 153.)
- [122] T. Chang and H. Gao. *Journal of the Mechanics and Physics of Solids*, 51,1059. (2003). (Cited on page 153.)

INDEX

- Beltrami Saint-Venant equation, 56
Bloch sum, 14
Born-Oppenheimer, 14, 33
Cauchy stress tensor, 43, 66
Cayley-Hamilton theorem, 52
compliance tensor, 58
deformation gradient, 36
Density functional theory, 25
Dirichlet elastic problem, 59
Euler-Poisson, 126, 157
Eulerian coordinate, 36
Fermi-Thomas-Dirac exchange energy, 29
frozen core approximation, 32
Generalized Gradient Approximation, 28
generalized Hooke's law, 57
Harrison rule, 19
Hartree-Fock, 28
Hellmann-Feynman theorem, 21, 33
Hermann's theorem, 147
Hohenberg and Kohn lemma, 25
hopping integrals, 17
Kirchhoff theory, 123
Kohn-Sham equations, 26
Löwdin theorem, 15
Lagrangian coordinate, 36
Local Density Approximation, 28
Navier equation, 59
Neumann elastic problem, 59
Novozhilov equations, 141
Piola transformation, 48
Piola-Kirchhoff stress tensor, 45
pseudopotential, 31
Pulay force, 21
Rayleigh-Ritz variational principle, 26
Reynolds theorem, 46
Schrödinger equation, 14, 25
Sietz radius, 29
stiffness tensor, 57
theorem, $(2n + 1)$, 34
Tight Binding, 13
two center approximation, 17
Voigt notation, 60

EMILIANO CADELANO
GRAPHENE UNDER STRAIN

